QUANTUM CASCADE LASER: from 3 to 26 mum

DISS. ETH NO. 24571

QUANTUM CASCADE LASER: from 3 to 26 μm

A thesis submitted to attain the degree of

DOCTOR OF SCIENCES of ETH ZURICH

(Dr. sc. ETH Zurich)

presented by

JOHANNA MARIA WOLF

Master of Science ETH in Physics

born on 26.05.1983

citizen of Germany

accepted on the recommendation of

Prof. Dr. Jérôme Faist, examiner
Prof. Dr. Joachim Wagner, co-examiner

2017

Contents

List of Symbols and Acronyms

Symbols

$J_{\max}$	maximum current density
J_{thres}	threshold current density
J_{trans}	transparency current density
T_0	desc
α_{M}	total mirror losses
α_{tot}	total optical losses
α_{WG}	total waveguide losses
η_{inj}^{LLL}	injection efficiency into the lower laser level
η_{inj}	injection efficiency into the upper laser level
n_{LLL}	population of the lower laser level
η_{tr}	differential efficiency of laser transition
n_{ULL}	population of the upper laser level
n_{eff}	effective refractive index
$n_{\text{LLL}}^{\text{therm}}$	thermal population of the upper laser level
τ_{eff}	effective upper laser lifetime
τ_{LLL}	lifetime of lower laser level
τ_{trans}	effective transport time
$\tau_{\text{U,L}}$	scattering time from upper to lower laser level
τ_{ULL}	lifetime of upper laser level

Acronyms

AlAs	Aluminium Arsenide
AlInAs	Indium Aluminium Arsenide
AlN	Aluminium Nitride
BiBH	buried inverted buried heterostructure
CF_4	Tetrafluoromethane
CO	Carbon Monoxide
CO_2	Carbon Dioxide
DFB	Distributed-Feedback
DM	Density Matrix
FGR	Fermi Golden Rule
FP	Fabry-Perot
GIV	gain-current density-voltage curve
iBH	inverted buried heterostructure
ICL	Interband Cascade Laser
ICP	Inductively Coupled Plasma-etching
IFR	interface roughness
IGS	injector ground state
InGaAs	Indium Gallium Arsenide
InP	Indium Phosphide
IV	current density-voltage curve
LI	light-current density curve
LIV	light-current density-voltage curve
LLL	lower laser level
MBE	Molecular Beam Epitaxy
mid-IR	Mid-Infrared
MIS	main injector state
ML	Monolayer
MOVPE	Metalorganic Vapor Phase Epitaxy

N_2O	Nitrous Oxide
NDR	negative differential resistance
NEGF	Non-Equilibrium Green's Function
NUL	next upper level
PI	pocket injector
QCL	Quantum Cascade Laser
SEM	Scanning Electron Microscope
SiN	Silicon Nitride
SiO_2	Silicon Oxide
SO_2	Sulfur Dioxide
SO_3	Sulfur Trioxide
TEM	Transmission Electron Microscopy
THz	Terahertz
ULL	upper laser level

Abstract

Absorption spectroscopy of gases and liquids is amongst the most widely used methods to measure molecular concentrations. It is used in various fields, amongst them are industrial leak testing, medical analysis and surgery, process control and monitoring. Trace gas analysis of low-mass molecules is preferably performed in the mid-IR wavelength region, where the line strength for many molecules are high. With the QCL, invented in 1994, this spectral range has a laser source that delivers sufficient output power in continuous-wave operation. The semiconductor laser is robust and operates in a wide temperature range. This work is dedicated to explore the capabilities of QCLs and improve their performance in the wavelength region from 3 to 26 μm.

Our active region simulations are based on a Density Matrix model. The choice of basis wavefunctions is verified and a method to find the optimal injection barrier is presented. The influence of different interface roughness models is discussed. Our model agrees well with the full quantum Non-Equilibrium Green's Function model and with experiments.

In this thesis we explore the short wavelength boundary of QCLs. Lasing emission around 3.3 μm requires highly strained

active region material. We investigate in detail active region designs, growth optimization, the impact of intervalley scattering and interface roughness. We present a device emitting at 3.4 μm with dissipation values of only 250 mW and threshold currents as low as 16 mA in pulsed operation. A boxcar experiment with a 5.6 μs long pulse shows stable spectral behaviour of DFB devices, an important requirement for spectroscopic applications.

We perform genetic optimizations of devices in the range from 4 to 26 μm and investigate active region design parameters. The optimizations are performed on "seed" designs of published devices and designs from our own group. The current record design in wallplug efficiency for 9 μm is optimized. The design was extracted from literature and processed along with the optimized structure. Comparing the measurements, we improve the slope efficiency from 1.9 to 2.5 W/A, the wallplug efficiency from 9 to 12 % and the dynamical range from 1.5 to 2.1. For all optimizations, the seed and optimized structures are compared, resulting in some common strategies for optimization.

The active region designs are explored experimentally as single stacks and broadband designs. Heterogeneous stacking is discussed and application examples for DFB, external cavity and comb operation are shown. An attempt for spectral coverage of a full octave is presented. We show laser emission spanning from 1090 to 1960 cm^{-1} at 80 K.

Zusammenfassung

Absorptionsspektroskopie von Gasen und Flüssigkeiten sind unter den am weitesten verbreiteten Methoden zur Messung von molekularen Konzentrationen. Es gibt verschiedene Anwendungsgebiete, darunter industrielle Dichtheitsprüfung, medizinische Analyse und Chirurgie, Prozesskontrolle und -überwachung. Das Messen von Spurengasen leichtgewichtiger Moleküle wird bevorzugt im Mittel-infraroten Wellenbereich durchgeführt, da in diesem Bereich die Linienstärke für viele Moleküle hoch ist. Mit dem Quantenkaskadenlaser, erfunden im Jahre 1994, gibt es in diesem spektralen Bereich eine Laserquelle die ausreichend Leistung im Dauerstrichbetrieb liefert. Der Halbleiterlaser ist robust und operiert in einem weiten Temperaturbereich. Diese Arbeit widmet sich dem Erforschen der Möglichkeiten von Quantenkaskadenlasern und der Verbesserung ihrer Leistungsfähigkeit im Wellenbereich von 3 bis 26 μm.

Unsere Simulationen der aktiven Region basieren auf dem Density Matrix model. Die Wahl der Basisfunktionen wird geprüft und eine Methode um die optimale Barrierendicke des Einspeisers wird vorgestellt. Der Einfluss von unterschiedlichen Modelen für die Rauigkeit von Materialschnittstellen wird

diskutiert. Unser Model stimmt gut mit dem vollen Quantenmodel Non-Equilibrium Green's Function und mit Experimenten überein.

In dieser Arbeit erforschen wir die Grenze von Quantenkaskadenlasern hin zum kurzwelligen Wellenlängenbereich. Laseremission um 3.3 μm erfordert Materialien in der aktiven Region, die unter hoher Spannung stehen. Wir untersuchen im Einzelnen die Entwürfe für aktive Regionen, Wachstumsoptimierung, den Einfluss von Streuung zwischen Energietälern und Rauigkeit an den Materialschnittstellen. Wir präsentieren einen Laser, dessen Emission bei 3.4 μm liegt, er hat eine Verlustleistung von nur 250 mW und einen Grenzstrom von nur 16 mA in gepulster Operation. Ein Boxcar Experiment mit 5.6 μs langem Puls zeigt für einen Laser mit Rückkopplungsgitter ein stabiles spektrales Verhalten. Dies ist eine wichtige Voraussetzung für spektroskopische Anwendungen.

Wir führen genetische Optimierungen im Bereich 4 bis 26 μm durch und untersuchen die Kenngrössen der aktiven Zone. Die Optimierungen werden an 'Keimen' (Ausgangsstrukturen) durchgeführt, diese stammen von Veröffentlichungen oder aus unserer eigenen Forschungsgruppe. Der aktuelle Rekordhalter für den Wirkungsgrad im Emissionsbereich um 9 μm wurde optimiert. Der Ausgangsentwurf für die aktive Zone wurde von der Veröffentlichung extrahiert und zusammen mit dem optimierten Entwurf prozessiert. Ein Vergleich der Messungen ergibt eine Verbesserung der Steigungseffizient von 1.9 zu 2.5 W/A, des Wirkungsgrades von 9 zu 12 % und des dynamischen Bereichs von 1.5 zu 2.1. Für alle Optimierungen werden die Ausgangs- und optimierte Struktur verglichen. Dies führt zu einen gemeinsamen Stategien für die Optimierung.

Die Entwürfe für die aktiven Zonen werden experimentell

untersucht, wobei die aktive Zone aus einem oder mehreren Entwürfen zusammengesetzt wird. Heterogene Stapel Aktiver Zonen werden diskutiert und Anwendungsbeispiele für Laser mit Rückkopplungsgitter, externer Resonatoren und optische Frequenzkämme werden präsentiert. Ein Versuch eine volle Oktave im spektralen Bereich zu überdecken wird gezeigt. Wir präsentieren Laseremission von 1090 bis 1960 cm^{-1} bei einer Temperatur von 80 K.

Acknowledgments

First of all i would like to thank my physics teacher at the Upper Vocational School in munich who awoke my enthusiasm for physics. It was due to the inspiring work of all my teachers there, that studying was quite fun. They certainly shaped my career.

My supervisor Prof. Dr. Jérôme Faist assigned me for an interesting master thesis. Thank you for this opportunity, a project which i followed with much enthusiasm. I am very grateful to him for offering me a PhD position in his group. He shaped my PhD with a well balanced mixture of constructive criticism and outstanding enthusiasm. I am very grateful for his support and belief in me. The positive atmosphere in our research group is also due to his emphasis on good scientific work and collegial behaviour.

Thanks to Prof. Dr. Wagner for being co-examiner of this work.

I would like to thank Dr. Alfredo Bismuto for his committed supervision during my master thesis. I am grateful for the shared knowledge about QCL, fabrication and measurements. He shared with me the secrets of iBH processing, enabling me to achieve outstanding results at short wavelength region.

Thanks to Mattias Beck for his excellent work and commitment. Not only did he supply me with high quality MBE material, but also with a calm and structured work ethic, when everyone else is getting nervous. And for knowing exactly when to ask: ”Hanna, how are you?”.

I am grateful to Dr. Romain Terazzi for all his advise on the theory and simulations and for taking the time to answer all my questions. My deep gratitude to Dr. Martin Süess and Dr. Pierre Jouy for advising me on processing, measurements, physics and how to survive a PhD. Thanks also for the nice projects we could collaborate on, it was a pleasure to work with you, my friends. Thankfully i had colleagues like Dr. Borislav Hinkov, Dr. Valeria Liverini, Dr. Keita Ohtani and Dr. Martin Frankié, who were always willing to give advise. It was my pleasure to work with such gifted people, especially also my former master student, Nadja Walti, which got rewarded for an outstanding master thesis with the ETH medal.

Many thanks to my former and current office mates Dr. Christopher Bonzon, Dr. Dana Nevou, Lorenzo Bosco and Bo Meng. It was a pleasure to share the office with you whether for discussions on physics, taking a break or organizing a barbecue at the lake. I really enjoyed the calm and constructive atmosphere.

Thanks to all my current and former colleagues, for such a nice atmosphere inside and outside of ETH: Dr. Markus Rösch, Cristina Benea-Chelmus, Dr. Gustavo Villares, Dr. Federico Valmorra, Dr. Curdin Maissen, Dr. Sabine Riedi, Dr. Giancarlo Cerulo, Dr. Romain Peretti, Selam Nida, Dr. Camille Ndebeka-Bandou, Dr. Yong Liang, Dr. Laurent Nevou, Johannes Hillbrand, Matthew Singleton, Shima Rajabali, Elena Mavrona, Filippos Kapsalidis, Dr. Mehran Shahmohammadi, Gianlorenzo Paravincini Bagliani, Janine Keller, Dr. Giacomo Scalari, Dmtry

Kazakov, Dr. Peter Liu, Felice Appugliese, Yves Bideaux, Andreas Forrer, Dr. Markus Geiser, Dr. Andreas Hugi, Tudor Olariu and Francesca Settembrini.

Thanks to Erna Hug for helping me with european timesheets and so many other things and questions that she patiently took care of.

The QOE group is not only a place for high quality research, but also a group where you can listen to the musical talents of your colleagues (thanks to Markus Röesch, Dr. Giacomo Scalari and Jérôme Faist) have a swim in the lake or a barbecue. A place where you can find friends, thank you all for this!

I acknowledge my project collaborators Prof. Dr. A. Wacker, Prof. Dr. J. Wagner and Dr. Ralf Ostendorf for the fruitful collaboration within the MIRIFISENS project.

I would like to thank the physics workshop and the electronics laboratory team, especially Andreas Stucker and Lukas Gautschi for their patience, insights and ideas on my designs. Your excellent work made my life in the laboratory much easier.

The FIRST cleanroom is an excellent institution which allowed me to process my sample with a high quality. Thanks to all the team members for the maintenance of a constructive, well organized working environment. Thanks to Dr. Emilio Gini for his outstanding work with the MOVPE, Dr. Yargo Bonetti for his manifold help with cleanroom equipment, Dr. Silke Schön for giving me the opportunity to mentor new cleanroom members. Many things to experienced FIRST users, that helped me throughout the years, namely Dr. Diego Marti, Dr. Ralf Flückiger, Tamara Popovic and Wei Quan I am grateful to the physics department for giving me the opportunity to study and for the resources i had available.

Thanks to my family for all their support and love. Luckily i had parents who gave all their children the possibility to follow their dreams. I am very grateful for the support of my brother Thomas and his family, if everything seems to be only about physics anymore, a visit at the chiemsee with Thomas, Steffi and Muk helped me take my mind of it.

Special thanks to Sam, a true friend and namorado during sun and rain, hot times (Vinzenz) and freezing temperatures (Thórsmörk). Looking forward to 1302!

Chapter 1

General Introduction

The social and technical evolution of humankind advanced well beyond the caveman so far, and we are not yet done. The first industrial revolution started in 1760 [1], and was driven by water-powered machinery. It was followed by the steam-powered and electrified technology. After the forth industrial revolution, the motorization, we arrived now in the digital industrial revolution. The advantages and possibilities of the 21st century are striking. Video calls in HD quality between individuals all over the world is readily available, as are fast transport technologies on land, rail, sea and air. Just now, the door opens to even visit the outer space. The industry sector can deliver nearly anything, from laser cutting of high precision parts, all-automatized assembly and robots that interact with humans. And in case one needs something that is not yet on the market, it can be printed on a 3D printer. Medical services are so advanced, that even difficult operations might be performed with minimal invasion. Therefore the recreation process of the patient is shortened significantly. The sequencing of DNA opened the pathway to new biological and medical research and is also widely used in forensics.

As all revolutions before, the positive effects are accompanied

by negative impacts as well. Deforestation, Desertification, global warming, accumulation of non-decaying waste on land in sea and space, as well as other environmental damages pose a political and social challenge. Start-ups and well established companies are trying to tackle the issue with renewable energy source, decomposable plastic, carbon storage and exhaust filtering, to name just a few.

One of the main challenges is to monitor, control and subsequently to reduce greenhouse gas emission, air pollution and toxic substances. Examples thereof are carbon dioxide measurements at power plants, sulfur dioxide from combustion engines, nitrogen dioxide emission from cooking gas stoves or methane emission from livestock.

A demanding task is to measure low densities of low-mass molecules in gaseous and liquid form. To this end we will investigate the appropriate spectral range for gas (liquid) sensing and the possible laser sources. As it will turn out the Mid-Infrared Quantum Cascade Laser is a well suited emission source, with applications far beyond spectroscopy. In this work we will study in detail the properties and optimization possibilities of these lasers.

1.1 Mid-Infrared Spectral Region

The Mid-Infrared (mid-IR) wavelength region (3-50 μm) gives access to the fundamental roto-vibrational transitions of many low-molecular mass gas species (see Figure 1.1). Compared to the near-infrared spectral region (below 2.5 μm), the line strength is typically about two orders of magnitude higher. Therefore, in this spectral region the absorption coefficient is high, allowing highly accurate spectroscopy measurements. Gas spectroscopy is concentrating more and more on this wavelength region to

carry out trace gas analysis [2] at the ppb and ppt level [3–5], isotope measurements [6, 7] and isotopomere composition analysis [8]. In Figure 1.2 we present the spectral fingerprint of the isotopes of methane, as well as the isotopomeres of Nitrous Oxide (N_2O), which can be distinguished with gas spectroscopy. There are two atmospheric windows in the mid-infrared range, namely from 3 - 5 μm and from 8 - 14 μm indicated in Figure 1.1. They are beneficial for environmental gas sensing and free space communication. Possible applications are furthermore in the fields of medical [9] and industrial leak trace gas sensing, process control, petrochemical contamination tests as well as laser surgery and countermeasures.

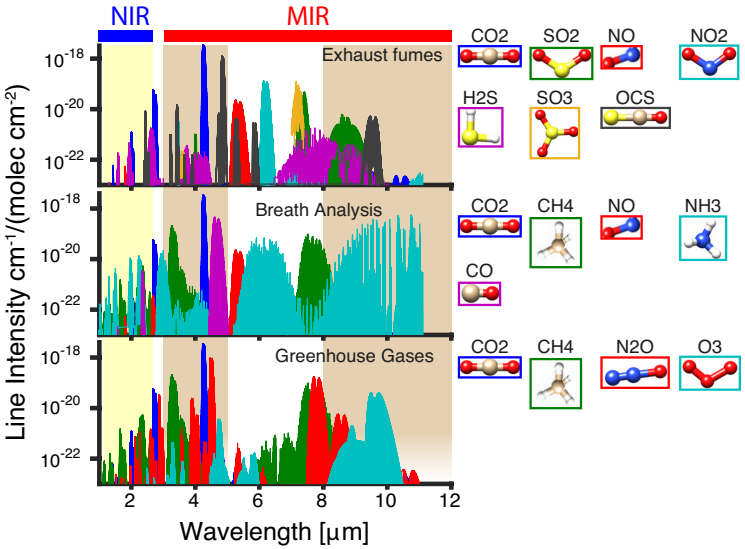

Figure 1.1: Line intensity of several gases in the near and mid-infrared. The first and second atmospheric windows are marked in brown. The near-infrared region is marked in yellow. Data from Ref. [10].

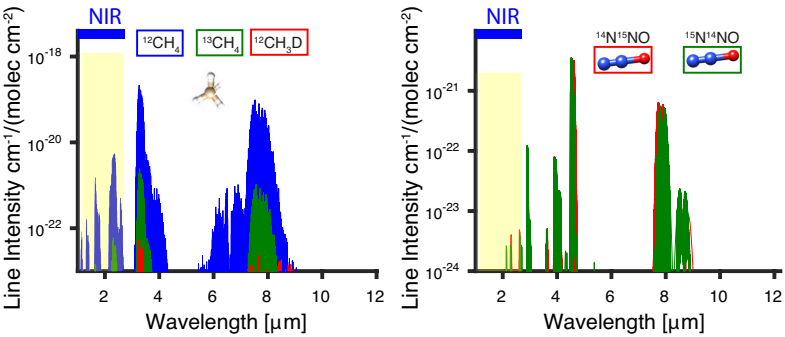

Figure 1.2: Line intensity of a) CH_4 and its isotopes and b) the Isotopomeres of N_2O: $^{14}N^{15}NO$, $^{15}N^{14}NO$. Data from Ref. [10].

1.2 mid-IR Applications and Performance Goals

In the following we will concentrate on spectroscopic applications. Further information on countermeasures or free space communication can be found in Refs. [11–15].

Molecules allow various optical transitions, which depend strongly on the structure and atom composition of the molecule. All these optical resonances make up a unique fingerprint which can be probed optically with absorption spectroscopy. Such a measurement setup consists of at least three parts: an emission source, an interaction area with the gas or liquid and a detector. A schematic setup is presented in Figure 1.3, where driver electronics and optical elements are omitted for clarity. The emitted light beam is directed into the interaction area, there, the light is absorbed depending on the absorption cross section of the gas molecules and the transmitted light is measured with a detector. Alternatively, one can measure the scattered light of the acoustic wave generated in the cell. In order to quantify a certain gas species in the infrared it's roto-vibrational resonances are probed as seen in the inset of Figure 1.3.

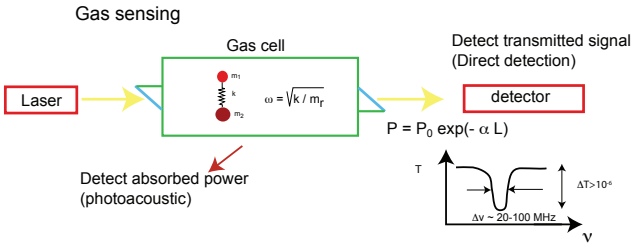

Figure 1.3: Schematic diagram of a generic gas sensing system. A laser is tuned across a roto-vibrational line of a molecule at frequency ω. In the direct absorption technique, the transmitted power is measured as a function of laser frequency. In photoacoustic technique, the laser is modulated and the acoustic wave generated by the absorbed power in the gas is measured. Figure taken from Ref. [16].

In this work we are interested in the emitter of such a setup. It should exhibit a low power dissipation, so that active cooling units can be avoided. For high precision trace gas measurements the laser should deliver high duty cycles or high output power. If the signal-over-noise is increased due to high output powers, the restrictions of the detector needs to be taken into account. Furthermore (quasi-)continuous-wave emission is required to make the spectroscopical detection system both electrically simple and small. Spectral tuning is necessary to align the emission wavelength and the roto-vibrational resonance. It is also used to tune in and out of the resonance in order to get a sample measurement as well as a reference measurement. The simultaneous detection of several gas species is performed with a tunable emission source, or with a broadband emitter and a spectrally resolved detection.

1.3 Mid-IR Sources

Semiconductor laser sources emitting in the mid-IR wavelength region include Interband Cascade Lasers (ICLs), Interband Diode

Lasers and Quantum Cascade Lasers (QCLs) [16]. QCLs are beneficial for spectroscopic applications as, with heterogeneous stacking, they can span a broad wavelength range in one single laser. A group of Northwestern University published spectral coverage of over $760\,\mathrm{cm}^{-1}$ for a single chip [17]. Several examples of broad QCL stacks will be given in Chapter 8.

The threshold current density can be fitted by $J_{\mathrm{thres}} = J_0 \exp(T/\mathrm{T}_0)$ where T is the temperature of the heatsink and T_0 the characteristic temperature of the laser with values well over 200K [18] for QCLs. Such a small thermal dependence of the threshold current density enables the laser to operate in a wide temperature range. This can be exploited for thermal tuning of the optical mode and for operation under rough environmental conditions.

The most widely used material system for QCLs is InGaAs/AlAs/AlInAs on InP substrate. It is well-developed in terms of fabrication technologies. This is partially due to their widespread use in the telecommunication industry. Because of the extensive research and favorable material properties, high quality growth of quantum wells is achieved today. QCL fabrication can furthermore use the well-established buried heterostructure technique which enables low-loss devices, high-duty cycle operation and excellent themperature management. Episide-down mounting further improves heat dissipation. We present power dissipation down to 250 mW for emission around $3.4\,\mu$m in Section 6. At long wavelengths a dissipation below 1 W is reachable [19, 20].

A strong research interest goes towards field-deployable, low footprint systems; for example the minituarization of the external cavity cavity setup Ref. [21]. Recent developments enabled handheld QCL-based systems, that are commercially available

[22, 23]. A very interesting miniaturization is the combination of laser, interaction area and detector on a single chip, as shown by the research group of Gottfried Strasser. The reader is referred to the following publications for more information [24, 25].

1.3.1 Narrow Bandwidth Devices

Single mode emitters are sucessfully accomplished using a Distributed-Feedback (DFB) grating, which is embedded into the waveguide. This fabrication technique is simple, robust and reliable. Such a chip does not require a broad gain spectrum ($\gtrsim$100 cm^{-1}) and the design can concentrate on devices with high gain and wallplug efficiency. The thermal tunability of the optical mode is a few wavenumbers, more precisely the emission wavelength tunes by a factor of 6.5-9 e-5 $1/\mathrm{K}$ [16]. This thermal tuning occurs also during a long driving pulse, the optical mode shifts by about 2 cm^{-1} during the first μs of the electrical pulse. It is used in the intermittent modulation concept [26, 27], to spectrally scan the trace gas resonance and beyond in one shot (few μs). Therefore the sample and reference measurement can be taken in a single measurement. A suitable single mode emitter and its long-pulse behavior is shown in Section 6.5.2.

Multi-mode emitters can be used to trace several gases with one setup. They are achieved by DFB arrays, multi-section DFBs or Vernier gratings. Due to the heterogeneous stacking, the resonance frequencies can be separated by several hundred wavenumbers. These devices require equalized gain at the requested emission wavelengths, but a flat gain in between those resonance frequencies is not necessary. In Section 8.1 we present a multi-section DFB, where the spectral emission is 90 cm^{-1} apart. In Section 8.2.2 we achieved surface emission from DFB arrays.

1.3.2 Broad Bandwidth Devices

Spectroscopy on continuously tunable broad spectral emitters is done in DFB arrays or in a external cavity configuration [28, 29]. External cavity setups achieve sequential single mode emission via external feedback. A rotating grating is place in front of the laser facet, depending on the position of the grating the losses of the spectral modes inside the laser cavity are changed. A broad, equalized gain is required to achieve sequential single mode emission over a wide range of the gain curve. A hand-held version of this, usually bulky, system was developed by the "Fraunhofer-Institut für Angewandte Festkörperphysik" and will be presented in Section 8.2.1.

Frequency combs [30–32] deliver equally spaced modes which can be recorded with a spectrometer. QCL frequency combs give the opportunity of spectrally broad spectroscopy in the mid-IR without any moving parts. Additionally to the required broad gain spectrum, these devices need high output power which is equally distributed on the Fabry-Perot modes and continuous-wave operation. In Figure 1.4 we present a schematic dual-comb setup which is able to take reference and measurement simultaneously. This field got a lot of interest in recent years and some of the designs discussed in this work are designed and used for comb operation, see Section 8.1 and Refs. [33–35].

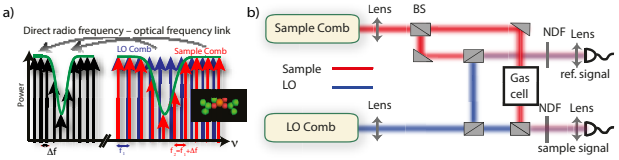

Figure 1.4: Principle of dual-comb spectroscopy. (a) A multi-heterodyne beat of two frequency combs with slightly different comb spacings is created on a fast detector, generating a direct link between the optical and the RF domain. The multi-heterodyne beat signal contains information on the sample absorption. (b) Schematic view of the dual-comb spectroscopy set-up based on QCL frequency combs. One comb is used as a local oscillator (LO), while the other probes the gas cell. BS: 50:50 Antireflection-coated beam splitter, NDF: neutral density filter. Adapted from Ref. [33].

Chapter 2

Simulation Tools

In this chapter, a theoretical description of Quantum Cascade Lasers (QCLs) is given. We describe the most important simulation models used to predict the spectral properties and output performance of such a system. A first overview of genetic optimizations is presented.

2.1 Description of the Active Region

A QCL [16] consists of epitaxially grown layers of different semiconductor materials; these layers make up the quantum wells and quantum barriers of the active region which is designed to emit at a predefined wavelength. The band diagram and the electron wavefunctions are presented in Figure 2.1. A laser consists of several active region periods (around 50), which are separated by the injection barrier. Three of them are presented in Figure 2.1 (green area). As we see, each period contains a part where the optical transition takes place and an extractor / injector part which forms a miniband. In the latter the electron is extracted from the lower laser level (LLL), cooled, and then injected into the upper laser level (ULL) of the following active

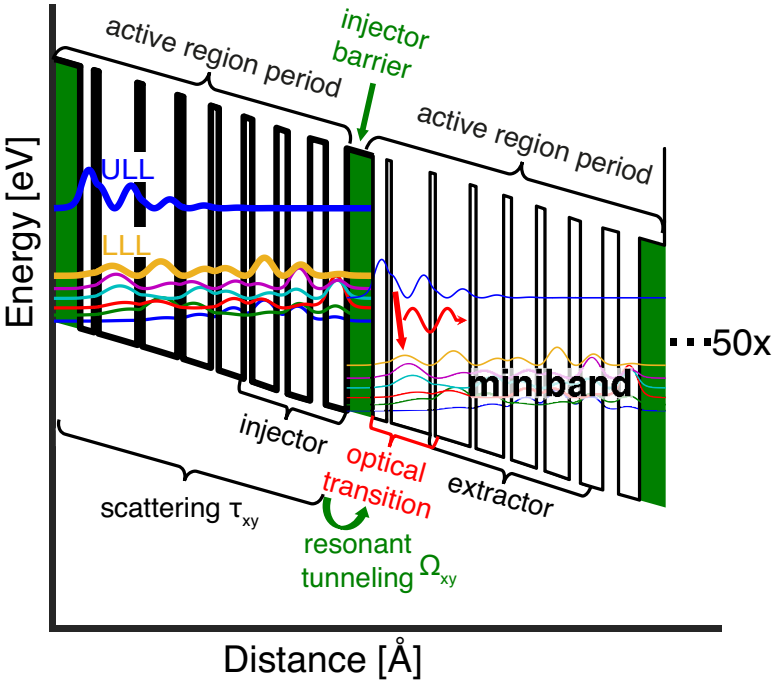

Figure 2.1: Band diagram and the squared electron wavefunctions offset by their energy. Indicated are the different parts of the active region period like optical transition, extractor and injector. The scattering mechanisms for the DM model are indicated at the bottom.

period, where it can undergo the next transition. The electron can be seen as cascading down the potential landscape (shown in black in Figure 2.1), emitting up to one photon per active region period.

The emission of a photon takes place as electrons are undergoing the intersubband transitions from ULL to LLL, the device is unipolar. The emission wavelength is defined by the energy levels of these states and therefore is given by the layer thicknesses and can be engineered easily. In this work, if not stated

otherwise, the material system for the active region is Indium Gallium Arsenide (InGaAs) for wells and Indium Aluminium Arsenide (AlInAs) or Aluminium Arsenide (AlAs) as potential barriers. These are grown on Indium Phosphide (InP) substrate.

The quantum theoretical description for a single electron is represented by the following Hamiltonian:

$$\begin{aligned} H\Psi(\mathbf{r}) &= E\Psi(\mathbf{r}) \\ H &= H_0 + H_{\text{scatt}} + H_{\text{int}} \\ H_0 &= \frac{p^2}{2m_0} + V_{\text{crystal}}(\mathbf{r}) + V_{\text{electric Field}} + V_{\text{Hartree}} \\ H_{\text{scatt}} &= H_{\text{IFR}} + H_{\text{AD}} + H_{\text{DOP}} + \cancel{H_{\text{EE}}} + && \text{(elastic)} \\ &\quad H_{\text{LO phonon}} + \cancel{H_{\text{LA phonon}}} && \text{(inelastic)} \\ H_{\text{int}} &= -ep_z/(m\omega)E_0 sin(\omega t); \end{aligned} \tag{2.1}$$

Where we separated the bare Hamiltonian due to the electron kinetic energy, crystal structure and the applied field (H_0), the scattering Hamiltonian (H_{scatt}) and the interaction between the optical field and the material using the electric dipole Hamiltonian in the Coulomb gauge (H_{int}). The scattering terms are due to interface roughness (IFR), alloy disorder (AD), dopants / ions (DOP), electron-electron interaction (EE), longitudinal optical (LO) phonons or longitudinal acoustic (LA) phonons, where the electron-electron scattering and the LA phonon scattering terms are neglected in this work. Electron-electron interaction is partially included as a mean-field theory in V_{Hartree}. e is the electron charge, p_z the momentum, m the effective electron mass, ω the frequency of the optical field.

2.1.1 Electron Wavefunctions

The electron wavefunctions and the band diagram can be calculated self-consistently for H_0. The basis wavefunctions can be retrieved via the k·p method with an effective two band Kane model in the envelope approximation:

$$\begin{aligned} H_0\Psi_{n,\mathbf{k}}(\mathbf{r}) &= E_{n,\mathbf{k}}\Psi_{n,\mathbf{k}}(\mathbf{r}) \\ \Psi_{n,\mathbf{k}}(\mathbf{r}) &= \exp(i\mathbf{kr})u_{n,\mathbf{k}}(\mathbf{r}) \\ (\frac{p^2}{2m_0} + \frac{\hbar}{m_0}\mathbf{kp} + \frac{\hbar^2k^2}{2m_0} + & \\ V_{\text{crystal}}(\mathbf{r}) + V_{\text{electric Field}} + V_{\text{Hartree}})u_{n,\mathbf{k}}(\mathbf{r}) & \\ = E_{n,\mathbf{k}}u_{n,\mathbf{k}}(\mathbf{r}) & \end{aligned} \tag{2.2}$$

$$\begin{aligned} u_{n,\mathbf{k}}(\mathbf{r}) &= a_c(\mathbf{k})u_{c,\mathbf{0}}(\mathbf{r}) + a_v(\mathbf{k})u_{v,\mathbf{0}}(\mathbf{r}) \\ \begin{pmatrix} E_c + \frac{\hbar^2k^2}{2m_0} & \frac{\hbar}{m_0}\mathbf{kp} \\ \frac{\hbar}{m_0}\mathbf{kp} & E_v + \frac{\hbar^2k^2}{2m_0} \end{pmatrix} & \begin{pmatrix} a_c(\mathbf{k}) \\ a_v(\mathbf{k}) \end{pmatrix} = E_{n,\mathbf{k}} \begin{pmatrix} a_c(\mathbf{k}) \\ a_v(\mathbf{k}) \end{pmatrix} \end{aligned} \tag{2.3}$$

Here $\Psi_{n,\mathbf{k}}$ is the electron wavefunction for the band n and wavevector $\mathbf{k}$, p is the momentum operator and u is the bloch wavefunction. In the two-band model (valence and conduction band) the bloch wavefunction can be identified by the amplitudes a_v and a_c, respectively. With the transfer matrix method, the wavefunctions for one or several active region periods are found: The active region is split into thin layers. Within this thin layer the basis function is propagating as an exponential or sinusoidal plane wave. For each layer the transfer function is calculated. The boundary conditions between the layers are given by the continuity equations. Through scanning the relevant energy-values for the active region period(s), we can determine the self-energies and the electron wavefunctions of the active region: $\Psi_i(z)$.

Within a self-consistent loop the Hartree potential is calculated from the Poisson equation (Equation 2.4), then the population is

recalculated, until convergence over the energies of the basis states is reached.

$$\begin{aligned} \rho(z) &= eN_D(z) - e\sum n_i|\Psi_i(z)|^2 \\ \frac{\partial^2}{\partial z^2}V_{\text{Hartree}} &= -\rho(z)/\varepsilon \end{aligned} \tag{2.4}$$

ρ is the net charge density, N_D the donor density, ε the permittivity and n_i the population of state i.

For precise Mid-Infrared (mid-IR) calculations the non-parabolicity of the conduction band is not negligible as its effect increases with energy [36]. The effective two-band model takes into account the effect of the split-off band, without increasing the complexity of the equations. The valence band wave function is approximated as a mixture of light-hole and split-off band with the coefficients $\sqrt{2/3}$ and $\sqrt{1/3}$, respectively. With this transformation the two valence bands are no longer coupled and the band "$\sqrt{1/3}$ light-hole + $\sqrt{2/3}$ split-off" can be neglected. The effect of this effective two-band model is reduced to a effective mass term.

The kinetic energy of the conduction band is then:

$$E(k) = \frac{\hbar^2 k^2}{2m^*}(1 - \gamma k^2) \tag{2.5}$$

Here $\gamma = \hbar^2/(2m^*E_g)$ is the non-parabolicity constant, $m^* = m_0/(1 + E_P/E_g)$ the effective mass, E_P is the Kane energy and E_g is the bandgap.

2.1.2 Simulation Models

We will briefly discuss the most important models to solve Equation 2.1, namely the classical rate equations, the semiclassical Density Matrix (DM) approach, the Ensemble Monte-Carlo and the

full quantum calculation via Non-Equilibrium Green's Function (NEGF). For a detailed description the reader is referred to the literature. This paragraph is based on the implementations of Prof. Dr. Harrison (Rate Equations) [37, 38], Dr. Mátyás (Ensemble Monte-Carlo) [39], Dr. Terazzi (DM) [36], Prof. Dr. Wacker (NEGF) [40].

All these implementations do not embed fitting parameters but rather physical properties of the materials which are well known. Only the effective mass and band discontinuity of strained materials and the interface roughness are not precisely known and will be discussed later. As input, the layer sequence, the material, the material's composition and the band discontinuity are used. A summary of the simulation models is given in Table 2.1.

For the carrier transport in QCL active region designs we will find that coherent transport, namely sequential resonant tunneling and incoherent transport induced by scattering contribute to the current density.

Rate Equation While the first part of the Hamiltonian H_0 is used to deduce the wavefunctions of one active region period, the scattering Hamiltonian H_{scatt} is evaluated perturbatively via the Fermi Golden Rule (FGR) to deduce the scattering rates τ_i between the states. Using the Boltzmann equation and this scattering rates the population change can be evaluated. The carrier transport into the active region period must be set manually or via evaluation of the scattering from one active region period to the next. The difference between outgoing and incoming scattering events leads to the current density [38]. In the latter case, it is possible to predict the current-voltage behavior, but numerical instabilities occur at the fields where wavefunctions cross. The rate equations for N

states and manually set current densities are given by:

$$\begin{aligned} \dot{\boldsymbol{n}} &= -1/\tau\ \boldsymbol{n} + \boldsymbol{J}/e \\ \begin{pmatrix} \dot{\boldsymbol{n}}_1 \\ \dot{\boldsymbol{n}}_2 \\ ... \\ \dot{\boldsymbol{n}}_N \end{pmatrix} &= \begin{pmatrix} -1/\tau_1 & 1/\tau_{2,1} & ... & 1/\tau_{N,1} \\ 1/\tau_{1,2} & -1/\tau_2 & ... & 1/\tau_{N,2} \\ ... & ... & ... & ... \\ 1/\tau_{1,N} & 1/\tau_{2,N} & ... & -1/\tau_N \end{pmatrix} \begin{pmatrix} \boldsymbol{n}_1 \\ \boldsymbol{n}_2 \\ ... \\ \boldsymbol{n}_N \end{pmatrix} + \begin{pmatrix} J_1/e \\ J_2/e \\ ... \\ J_N/e \end{pmatrix} \end{aligned} \tag{2.6}$$

Here n_i, τ_i and J_i are the population, the lifetime and the injected current of state i, $\tau_{i,j}$ is the scattering rate from level i to j, e is the electron charge. Reducing the system to a 3 state-laser and adding a photon flux S and gain and loss contributions [16] leads to:

$$\begin{aligned} \frac{\mathrm{d}n_{\mathrm{ULL}}}{\mathrm{d}t} &= \eta_{\mathrm{inj}}\frac{J}{e} - \frac{n_{\mathrm{ULL}}}{\tau_{\mathrm{ULL}}} - S g_c(n_{\mathrm{ULL}} - n_{\mathrm{LLL}}) \\ \frac{\mathrm{d}n_{\mathrm{LLL}}}{\mathrm{d}t} &= \eta_{\mathrm{inj}}^{LLL}\frac{J}{e} + \frac{n_{\mathrm{ULL}}}{\tau_{\mathrm{U,L}}} + S g_c(n_{\mathrm{ULL}} - n_{\mathrm{LLL}}) - \frac{n_{\mathrm{LLL}} - n_{\mathrm{LLL}}^{\mathrm{therm}}}{\tau_{\mathrm{LLL}}} \\ \frac{\mathrm{d}S}{\mathrm{d}t} &= \frac{c}{n_{\mathrm{eff}}}(S g_{\mathrm{c}}(n_{\mathrm{ULL}} - n_{\mathrm{LLL}}) - S\alpha_{\mathrm{tot}}) + \beta\frac{n_{\mathrm{ULL}}}{\tau_{\mathrm{sp}}} \end{aligned} \tag{2.7}$$

Here n_i are the populations of ULL or LLL, η_{inj} and $\eta_{\mathrm{inj}}{}^{LLL}$ the injection efficiency into the upper and lower laser level, g_c the gain coefficient, $n_{\mathrm{LLL}}^{\mathrm{therm}}$ the thermal population of the LLL and τ_{sp} the spontaneous lifetime of the ULL. n_{eff} and α_{tot} are the effective refractive index and the total loss of the optical beam, respectively.

For a steady state system with gain-clamping $g_c(n_{\mathrm{ULL}} - n_{\mathrm{LLL}}) = \alpha_{\mathrm{tot}}$ we can calculate the slope efficiency:

$$\frac{dP}{dI} = N\hbar\omega\alpha_{\mathrm{M}}\frac{dS}{dI} = \frac{N\hbar\omega}{e}\frac{\alpha_{\mathrm{M}}}{\alpha_{\mathrm{tot}}}\frac{\tau_{\mathrm{eff}}}{\tau_{\mathrm{eff}} + \tau_{\mathrm{ULL}}}, \tag{2.8}$$

where N is the number of periods, ω the emission frequency, α_M and α_{tot} the mirror and total optical losses, $\tau_{eff} = \tau_{ULL}(1 - \tau_{LLL}/\tau_{U,L})$ the effective transition time.

DM The density matrix formalism can be seen as an extension of the rate equations, where coherent transport through the barrier and broadening of the laser transition is taken into account. The rate equation model is used to describe the transport of carriers between the states within the active region period. The transport between two active region periods is calculated using the tight binding approach which includes the dephasing terms. Dephasing is due to intrasubband scattering events, and reduces the transport through the injection barrier due to loss of coherence. The population of the state is not changed but the dephasing contributes considerably to the broadening of the state. For the lasing transition, the broadening is given by the lifetime of the upper state and the dephasing time between the upper and lower laser level.

The DM is working with 0-dimensional states and enables access on the total state population. The electron temperature can be defined manually, alternatively it is possible to deduce a typical in-plane wavevector with the "kinetic energy balance". For this the electron temperature and subsequently the scattering rates are varied until a balance between events that increase or decrease the kinetic energy is reached. At long wavelengths the use of the self-consistent kinetic balance model can be skipped to spare computational resources. An efficient thermalization of electrons in the injector is given through phonon scattering in a high density of electron states. In the active region, a simple argument shows that during the transport time of an electron approximately 250 meV ($\approx$5 μm) can be absorbed by optical phonon scatting. This leads to the conclusion that only for wavelength λ shorter

than 5 μm, electrons are not efficiently cooled and kinetic balance needs to be taken into account. For all other structures as long as the electron reservoir coincides with the lower states in the simulations (e.g. the injector ground state) the self-consistent computation-intensive kinetic balance can be avoided.

In general, thermalized population in the structure is assumed for the self-consistent potential. While this is a good approximation in most cases where the carriers are concentrated in the injector region close to the doped layers, this assumption fails in the case of carrier accumulation in other parts of the structure. In the latter, it is necessary to use a "super-self" algorithm for the convergence of the self-consistent potential. Instead of thermalized distribution of the carriers in the structure, the population of each state is defined through transport calculations. Therefore band bending is modeled correctly.

The model takes coherent and incoherent transport into account. The scattering Hamiltonian H_{scatt} is evaluated perturbatively via the FGR to deduce the scattering rates τ_i. Transport within the local basis (one active region period, if not stated otherwise) is achieved on basis of these scattering rates (incoherent scattering). Between the local basis states (between active region periods) transport is calculated through the tight binding model (coherent transport). This will be discussed further in Section 5.1. In a two level system, where the states are coupled by a barrier, with an energy detuning of Δ and a coupling energy of Ω, we have the Liouville von Neumann

equation:

$$
\begin{aligned}
i\hbar\dot{\rho} &= [H_0,\rho] + \left.\frac{\partial\rho}{\partial t}\right|_{\text{coll}} = (\mathcal{L}_0 + \mathcal{L}')\rho \\
\rho &= (\rho_{11},\rho_{12},\rho_{21},\rho_{22}) \\
\mathcal{L}_0 &= i\hbar \begin{pmatrix} 0 & i\Omega & -i\Omega & 0 \\ i\Omega & -i\Delta & 0 & -i\Omega \\ -i\Omega & 0 & i\Delta & i\Omega \\ 0 & i\Omega & -i\Omega & 0 \end{pmatrix} \\
\mathcal{L}' &= i\hbar \begin{pmatrix} -1/\tau_1 & 0 & 0 & 1/\tau_2 \\ 0 & -1/\tau_{\shortparallel} & 0 & 0 \\ 0 & 0 & -1/\tau_{\shortparallel} & 0 \\ 1/\tau_1 & 0 & 0 & -1/\tau_2 \end{pmatrix}
\end{aligned}
\tag{2.9}
$$

Where ρ_{ii} is the state population ρ_{ij} is the coherence and $\tau_{\shortparallel}$ is the dephasing time. The current density through the structure can be evaluated using the average over the velocity operator:

$$
J = eN_D \langle V \rangle = eN_D \langle \dot{Z} \rangle = Tr\big(eN_D/(i\hbar)\rho\,[H,Z]\big) \tag{2.10}
$$

Here V is the velocity operator and Z is the position operator. In the last part we used the average values in density matrix formalism where the average over an operator A is given by: $\langle$A$\rangle$ = Tr(ρ A). The time-derivative is evaluated with the Heisenberg equation of motion: $\dot{A}$ = i/$\hbar[H,A]$.

This leads to the current contribution given by the resonant tunneling, it was first presented by Kazarinov and Suris [41].

$$
J = \frac{2 * e * \tau_{\shortparallel} * \Omega^2}{1 + \Delta^2\tau_{\shortparallel}^2 + 4 * \Omega^2\tau_{\shortparallel}\tau_{\text{ULL}}} = \frac{2 * e * \hbar\Omega^2}{\hbar}\frac{\gamma}{(\hbar\Delta)^2 + \gamma^2}\Delta n \tag{2.11}
$$

Δn is the population difference between two states coupled by resonant tunneling, γ the broadening due to scattering, therefore:

$2\gamma = \hbar/\tau_{\shortparallel}$. In this equation the current is driven by the population difference. This assumption already fails in the case of a superlattice structure at resonance. Even as the population difference is zero it is clear that carrier transport takes place. The model leading to Equation 2.11 is based on momentum conserving state transitions, as given by the resonant tunneling. If we expand this to energy-preserving scattering events as occurring due to interface roughness, we get the second order current contribution, see Figure 2.2.

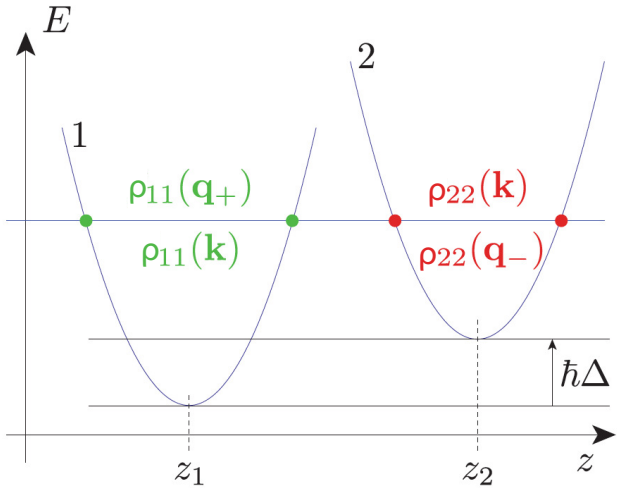

Figure 2.2: The second-order formula for the current density is illustrated. Two subbands 1 and 2 are considered with same mass. The detuning energy $\hbar\Delta$ is reported. The population-difference terms $\rho_{22}(k) - \rho_{11}(q_+)$ and $\rho_{22}(q_-) - \rho_{11}(k)$ are reported on an absolute energy scale, showing that the population difference is evaluated at a constant energy rather than at a constant wave-vector. The values of the momentum are given by: $q_\pm(k) = 1/\hbar\sqrt{2m(\pm\hbar\Delta + E(k)}$, where $E(k) = \hbar^2k^2/2m$ is the kinetic energy. Figure taken from Ref. [36].

$$J = 2 * e * \hbar\Omega^2 \frac{\gamma^1(k)\big(\rho_{22}(k) - \rho_{11}(q_+)\big) + \gamma^2(k)\big(\rho_{22}(q_-) - \rho_{11}(k)\big)}{(\hbar\Delta)^2 + \big(\gamma^1(k) + \gamma^2(k)\big)^2} \tag{2.12}$$

The subscript on the broadening term γ specifies the subband in which the elastic scattering takes place.

The gain is evaluated as negative absorption in a homogeneously filled material. The photon-absorption rate of a incoming beam at angle ψ is evaluated using the FGR and the electrical dipole approximation. The fraction of absorption with respect to the total field intensity gives the absorption (negative gain) of the structure.

$$\begin{aligned} R &= \frac{\pi}{2\hbar} \sum | < i|H_{\text{int}}|f > |^2 \rho(E_f - E_i - \hbar\omega) \\ I &= \frac{1}{2}\varepsilon_0 n_{\text{refr}} c E^2 cos(\psi) \\ \alpha(\omega) &= \frac{R\hbar\omega sin^2(\psi)cos(\psi)}{IL_p} = -g(\omega) \\ g(\omega) &= -\frac{2\pi e^2 z_{\text{if}}^2(\rho_{ii} - \rho_{ff})}{\varepsilon_0 n_{\text{refr}} \lambda L_p} \frac{\gamma}{(E_f - E_i - \hbar\omega)^2 + \gamma^2} \end{aligned} \tag{2.13}$$

R is the absorption rate, i and f the initial and final state, $\hbar\omega$ the energy between these states, n_{refr} the effective refractive index, E the electric field, L_p the length of the active region period and z the dipole matrix element. The linewidth of the optical transition γ takes the ULL lifetime and the dephasing time between ULL and LLL into account:

$$\gamma = 1/(2\tau_{\text{ULL}}) + 1/\tau_{\text{ll}} \tag{2.14}$$

In the same way as elastic scattering (mainly due to interface roughness) needed to be taken into account for the carrier transport, it also influences the gain calculations. In Figure 2.3 the second order gain contribution is illustrated: Additionally to the emission of energy $\hbar\omega$ an energy-conserving scattering event takes place. In the expression for the gain the population difference is modified from

$$(\rho_{ff} - \rho_{ii}) \Rightarrow \gamma^1(\rho_{ff}(k) - \rho_{ii}(q+)) + \gamma^2(\rho_{ff}(q_-) - \rho_{ii}(k)), \quad (2.15)$$

where $q_\pm = 1/\hbar\sqrt{2m(\hbar^2k^2/(2m) \pm (\hbar\Delta - \hbar\omega)}$. The first term indicates a second order process consisting of a photon emission from the upper subband followed by elastic scattering into the lower subband, the second term is due to elastic scattering from the upper subband followed by a photon emission into the lower subband.

Ensemble Monte-Carlo In the Ensemble Monte-Carlo simulation model published by Mátyás [39] the electron wavefunctions are calculated for 5 subsequent periods. The wavefunctions and bandstructures are computed super-self-consistently with a Schrödinger-Poisson solver. The scattering Hamiltonian H_{scatt}, including the e-e interaction term, is treated as perturbation where the scattering probabilities are extracted with the FGR. Only incoherent scattering is taken into account. Coherent tunneling effects, which are known to influence the current of QCLs [42], are neglected. Ensemble Monte-Carlo includes also the in-plane dynamics of electrons, and delivers a space dependent current density for the analyzed structure in growth direction. The main difference to the other models presented here is that the electron transport through the structure is evaluated

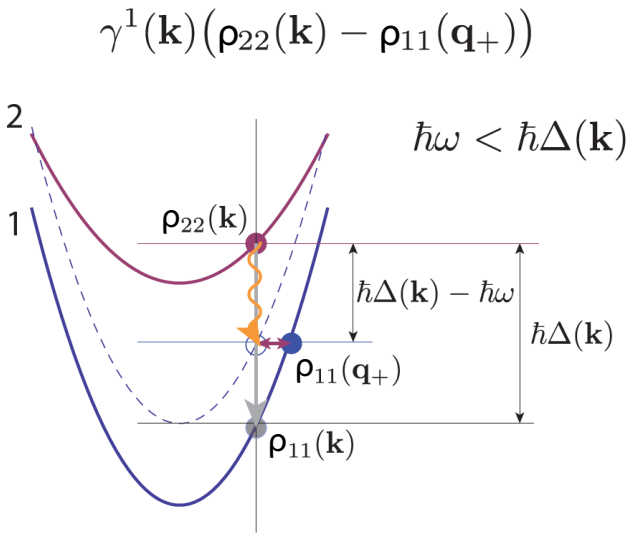

Figure 2.3: The first population term of Equation 2.15 is illustrated between a pair of subbands with non-parabolicity. The intra-subband scattering potential (inside γ^1) enables transitions from the upper subband (2) to the lower subband (1) out of the resonance condition: $\hbar\omega < \hbar\Delta(k)$. These transitions are allowed as the conservation of the momentum has been relaxed in optical transitions. In the figure the first-order transition is also represented in grey. The transition occurs at the detuning energy: $\hbar\omega = \hbar\Delta(k)$. Figure taken from Ref. [36].

statistically. A statistical distribution of a fixed number of electrons is taken as a starting point: each electron of the ensemble is transported through the active region structure with respect to the corresponding scattering rates. The optical field is evaluated using the FGR and the electrical dipole approximation. The linewidth of this optical transition is given by the scattering rates of the states, ignoring the contribution from the dephasing time. This simulation model enables straightforward implementation of electron-electron scattering as a two-body problem. The semiclassical solution of the Hamiltonian (Equation 2.1) takes the non-parabolic dispersion relation into account.

NEGF The NEGF simulations use a non-equilibrium green's function to model the QCL active region in a full quantum mechanical picture without perturbative parts in the Hamiltonian. The wavefunctions are Wannier states calculated in a band potential of 11 periods, non-parabolicity is taken into account. The wavefunctions are calculated as eigenfunctions of H_0, neglecting the Hartree Potential and without bias. Instead of the wavefunctions, the populations are calculated self-consistently, taking into account not only H_0 but the full Hamiltonian. The transport is calculated for a non-equilibrium, but stationary state system. The scattering is implemented at the same level as the bandstructure potential using its self-energies. Therefore it automatically includes coherent and incoherent scattering. The approximations are reduced to the use of a typical momentum wavevector for evaluating the scattering self-energies. The k dependent electron density distribution is accessible. The NEGF model of A. Wacker was extended to include the optical field ([43]) of a QCL and results for a lasing device will be given in Section 5.3.

The high level of complexity is accompanied with large computational costs; a simulation of a typical mid-infrared QCL might take 10 hours ($\approx$ 100 cores). Here we assume, that the current density-voltage curve (IV) (without lasing operation), light-current density-voltage curve (LIV) and field-dependent gain spectra are simulated. By contrast, the Ensemble Monte-Carlo model and DM take only about 10 minutes ($\approx$ 100 cores). This number scales mainly with the number of electron states and therefore strained materials with high band discontinuities and many bound states are computationally more demanding.

	EMC	DM	NEGF
wavefunction			
k · p method (transfer-matrix, shooting method)	x	x	x
extent of basis function [periods]	5	1	11
Wannier-Stark basis: eigenfunction of H_0	x	x	
Wannier basis: eigenfunction of H_0^*			x
self-consistent solver			
Schrödinger-Poisson solver	x	x	
non-parabolicity			
effective two-band Kane model	x	x	x
population: self-consistent solver			
H_0 + self-energies			x
transport			
incoherent scattering	x	x	x
coherent transport through injector barrier incl second order current		x	
coherent transport			x
scattering rates via FGR	x	x	
scattering rates via self-energies			x
e-e scattering	x		
e-e scattering via mean-field theory		x	x
equation of motion			
Boltzmann equation	x		
density matrix equation		x	
Dyson equation			x
population of wavefunction	$\Psi_{i,(kx,ky)}(z)$	$\Psi_i(z)$	$\Psi_{i,(kx,ky)}(z)$
second order gain		x	x
linewidth broadening			
lifetime	x	x	x
dephasing time		x	x
optical field			
FGR, dipole approximation	x	x	
AC field component in Green's function			x
full computation time [hours]	0.17	0.17	10

Table 2.1: Summary of the simulation models. Where H_0^* is H_0 without $V_{\text{electric Field}}$ and V_{Hartree}.

2.2 Genetic Optimization

Since the first realization of the QCL [16], the optimization of the design, growth and processing steps of active region designs have been a lively field of research. Early on, the focus was on the active region design, which quickly branched from the three quantum well active region [44] towards the double phonon extraction [45], the bound-to-continuum [46], the continuum-to-bound [47] and also the continuum-to-continuum [48] approach. Apart from that, the optimization of scattering times, the extraction of carriers from the LLL, the injector region and the semiconductor material system are ongoing [49–54]. We have also been exploring genetic algorithms as a tool to optimize active regions. Our group presented the pocket injector which was the result of early genetic optimizations [55].

Several automated optimization algorithms have been developed so far and can be used universally for fields as different as economics, genetics, radiotherapy and physics. They include genetic/evolutionary algorithms, swarm optimization, simulated annealing and others [56, 57]. While optimization algorithms are in widespread use today in various fields, it is not yet the case for the design of QCL active regions in the terahertz and mid-infrared spectral region. Some exceptions can be found in Refs. [55, 58–60].

The low computational cost of the DM model combined with the high capability to predict correctly the active region performance (see Chapter 5) makes it suitable for automatized optimization. As described in Chapter 7 our genetic optimization tool typically performs more than 400'000 active region simulations before reaching convergence. This is possible due to the fast computation of the DM model and the use of the

ETH CLUSTER BRUTUS. The results of one active region design (LIV,gain-current density-voltage curve (GIV), gain spectrum) are given after 10 minutes. This enables us to do automatized active region designs. The goal is on one side to improve the performance or perform spectral shifts of existing devices, according to application requirements. It might also lead to new design ideas and different optimization approaches.

The genetic algorithm used in this work is based on an in-house software package [55,61]. We use 40'000 active region samples per generation and extract 32 of the best designs, according to their merit function. They are used as seed structures for creating the subsequent generation. The active region samples are generated by varying the layer thicknesses by at most 0.1 %. The injector barrier thickness, the electron sheet density levels and the material system of the structures are kept constant.

The merit function is one of the most important parts of genetic optimizations and has been modified compared to the optimization done in Ref. [55]. Our aim is to efficiently remove pathological cases and numerical exceptions from the structure pool. To this aim, we simulate the sample structures for a part of the light-current-voltage curve, instead of one random point as done previously. The merit function consists of the mean average of the wallplug efficiency of the structure over 4 successive fields. If within the simulated field-range the field-to-field points show large variations (more than 1 %) in wallplug efficiency, the sample is excluded from the optimization. The field-range is chosen before the optimization, for example in order to favour devices which operate at low fields and subsequently improve wallplug efficiency. Additionally, structures where the peak of the gain spectrum is not within a given range are discarded.

The software continues to produce and simulate sample

generations until convergence is achieved, meaning the best structures are drifting around a common value of the merit function. This can be seen after 10 - 15 generations. The convergence and the exclusion of numerically unstable structures was investigated for the optimization run of Section 7.3.1. The first and second best samples of some generations were analysed in detail. These structures are very similar in terms of basis functions, gain spectrum, wallplug-light-current density-voltage curve dependency and the optical parameters of the structures. They do not exhibit unphysical electron transport properties or unphysical gain maxima.

In a previous work [55], the very best structures of each generation were about 2-5 % higher in merit function than the following ones and were discarded as pathological cases. In order to benchmark our modified merit function, we compare the new optimization algorithm (see Section 7.3.1) to the last generation of Ref. [55]. The latter is shown as a red dashed curve in Figure 2.4. Using our new merit function, we see good convergence from the 10th generation onwards and also the best structures can be taken into account. The structure which was finally selected is the best-merit candidate from the 16th generation (see green curve and cross in Figure 2.4).

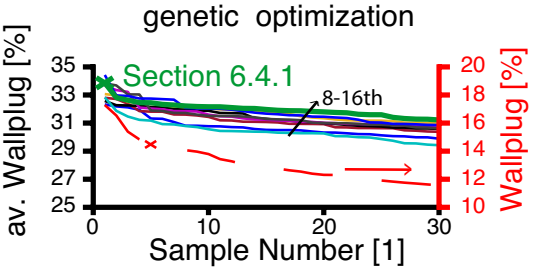

Figure 2.4: Merit function results for the best 30 samples of generation 8 to 16 are presented for the optimization done in Section 7.3.1. The dashed red line gives the last generation for Ref. [55] plotted on the right axis. The structure finally chosen for Section 7.3.1 and Ref. [55] are indicated with a cross.

2.3 Simulation Parameters

The input to our simulation model contains besides the active region specification (layer thickness, material, electron sheet density) also the temperature of the crystal lattice, the total losses of the optical mode and others. In order to be able to compare different simulations but also to keep reasonable values for specific wavelengths, we fix the simulation parameters as shown in Table 2.2. It should be noted, that this parameters might differ from real devices, but merely used to find the optimized design for a reasonable, fixed set of parameters.

The total optical losses, for example, are set to $7.5\,\mathrm{cm}^{-1}$ for the wavelength range from 5 to 12 μm. We can calculate the losses for a 3 mm long cavity with high-reflective coating at the back and an overlap factor of 0.6, using an optimized waveguide design adapted to the emission wavelength. The total modal losses are between 5 and $10\,\mathrm{cm}^{-1}$ for devices ranging from 5 to 12 μm.

These parameters are used throughout this work, if not stated otherwise. In case the measured data is directly compared to the

wavelength		**3-5 μm**	**5-12 μm**	**26 μm**
optical mode losses/Γ	1/cm	3	7.5	70
mirror losses (wallplug efficiency)	1/cm	3	7.5	–
lattice temperature	K	293	293	100
electron temperature	K	kinetic balance	380	150
device dimension	mm x μm	1.5 x 4.0	1.5 x 4.0	1 x 60.0
periods	1	30	30	30
facet reflectivity	1	0.25	0.25	0.25

Table 2.2: Parameters for active region simulations for different emission wavelength range. Γ is the modal overlap.

simulation results we adopted the parameters accordingly. This will be clearly stated in the text. Therefore we hope to facilitate both, the comparison of different designs with each other, and also the comparison of designs and measured data.

Chapter 3

Active Region Design

In the previous chapter we presented the simulation models for Quantum Cascade Lasers (QCLs). Here we present simulation outputs like scattering times or oscillator strengths and their role for the active region design. Later this knowledge will help us to create designs which for example cover a broad spectral range, have low power dissipation or a high wallplug efficiency.

3.1 Active Region Evaluation

3.1.1 Basis Function and Parameters of the Optical Transition

To illustrate the important parameters in the active region design, we present in Figure 3.1 the band diagram and the electron wavefunctions of a laser at 10.4 μm (Ref. [29], Appendix A.1.2). The computation of this data was already described in Section 2. In Figure 3.1 a) to d) we show some essential parameters for active region evaluation. All numbers are given just below threshold to remove the effect of photo-driven transport.

Figure 3.1 a) shows optical transition parameters, we find

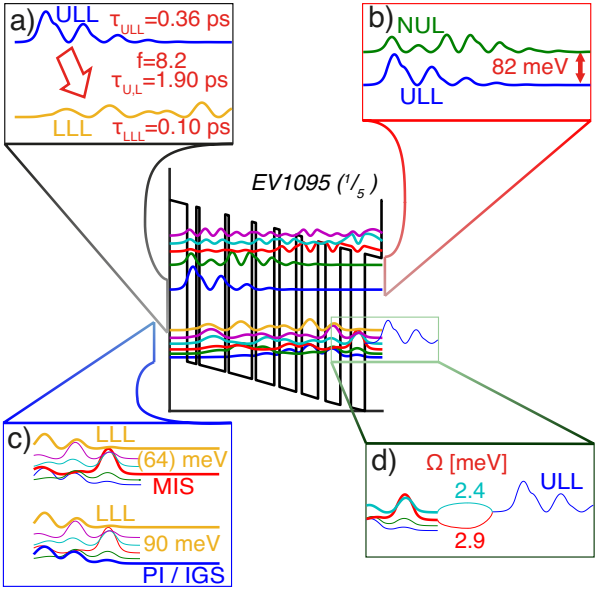

Figure 3.1: Bandstructure of a QCL and its performance parameters. The active region design is grown as 1 out of 5 stacks in "EV1095". Presented is the band diagram and the squared electron wavefunctions offset by their energy with respect to the distance in growth direction. a) to d) Parameters of the lasing transition, the energy distance to the excited state, the energy separation of the miniband and the oscillator strength to the next period. d) We shifted the ULL of the next period to the right for clarity. Details can be found in the text.

the lifetimes of the upper and lower laser states and the scattering time between them abbreviated by τ_{ULL},τ_{LLL} and $\tau_{U,L}$, respectively (compare also Equation 2.7). Together they make up the effective transition time

$$\tau_{eff} = \tau_{ULL}(1 - \tau_{LLL}/\tau_{U,L}) \tag{3.1}$$

and the transition efficiency

$$\eta_{tr} = \tau_{eff}/(\tau_{eff} + \tau_{LLL}), \tag{3.2}$$

which are directly proportional to the population inversion and the slope efficiency (see Equation 2.8), respectively. They are to be maximized. The oscillator strength of the transition (f) is proportional to the gain and should be maximized to increase the gain of the active region.

In a vertical transition design high performance is attempted by increasing the dipole matrix element of the transition, but as a consequence the ratio of upper to lower level lifetime deteriorates, and subsequently the population inversion decreases. For diagonal designs the lifetimes are optimized to increase τ_{eff} and η_{tr}, but the dipole matrix element is considerably lower than for vertical designs (around 14Å instead of over 20Å). They deliver good performance even at high currents and show a broader gain spectrum compared to vertical transitions, due to increased interface roughness scattering. Examples will be given in Chapter 7. If the application goal is more directed towards a broad gain spectrum or good performance at high currents, a diagonal design should be preferred. It also features more tuning with increased voltage.

Figure 3.1 b) presents the energy difference between the upper laser level (ULL) and the next upper level (NUL) (state above ULL) (82 meV). This separation needs to be large to prevent electron leakage through NUL [49, 54], while taking into account that the excited states are also necessary to provide oscillator strength from the ULL to lower states, especially the lower laser level (LLL). The population of NUL increases in designs with electric field and electron temperature. We opt for a energy separation between ULL and NUL of 70-100 meV, depending on the electron temperature and the electric field.

Figure 3.1 c) gives the energy difference between the LLL and the main injector state (MIS) (64 meV). It should be small to reduce

the voltage drop of one period, and therefore the power dissipation of the resulting laser. On the other hand, the thermalized electrons in the injector need to be energetically separated from the LLL to avoid thermal backfilling. The thermal occupation of states in the miniband up to the LLL leads to a considerable performance decrease. Therefore the energy separation of the miniband (distance between the LLL and the injector ground state (IGS), 90 meV) should be 90-120 meV, depending on the electron temperature of the active region. Due to non-radiative transitions from the ULL, electrons with a kinetic energy equal to the optical transition energy populate the miniband. Therefore the miniband thickness should scale also with transition energy and the inverse wallplug efficiency. The color-code of this values (see Figure 3.1 c)) corresponds to the LLL. The separation between the LLL and the MIS will be written in brackets throughout this work. We found it is an advantage to add a pocket injector (PI) below the MIS, to reduce the thermal backfilling while maintaining a low voltage drop. Due to the existence of the PI, we differenciate between the IGS, as the lowest state in the injector and the MIS as the state mainly contributing to the injection towards the next periods. IGS and MIS can be the same state.

Figure 3.1 d) we see the coupling energies Ω to the ULL (see Section 2.1.2). They will be discussed in detail in Section 5.2. The coupling energies are presented for two states in this example. The color (see Figure 3.1 d)) is set with respect to the corresponding injector state.

3.1.2 Wallplug Efficiency

The wallplug efficiency is given by $\eta = P/(V * J)$ where P is the output power normalized by the device surface, V the applied voltage and J the current density. The maximum wallplug

efficiency for a device with threshold current density J_{thres} and maximum current density J_{max} at a voltage of V_{max} is then [16]:

$$\eta = \frac{dP}{dJ} \frac{J_{\text{max}} - J_{\text{thres}}}{J_{\text{max}} * V_{\text{max}}}. \tag{3.3}$$

The slope efficiency dP/dJ can be calculated from the rate equations (Equation 2.8) and is inverse proportional to the total losses of the optical mode. These losses can be approximated by the free carrier losses. Assuming that the values for the sheet electron density, the number of periods and the mirror losses are optimized, the wallplug efficiency reaches a value given by [62]:

$$\eta = \eta_{\text{tr}}(1 + \frac{\Delta}{\hbar\omega})^{-1} \frac{(\sqrt{g^*\tau^*} - 1)^2}{g^*\tau} \tag{3.4}$$

$$g^* = 1/2\, \omega^2 \tau_{\perp}^2 f m^* \tag{3.5}$$

$$\tau^* = \tau_{\text{eff}} / \tau_{\text{trans}} \tag{3.6}$$

Where Δ is the energy difference between LLL and MIS, ω the emission wavelength, m^* the relative effective electron mass and τ_{trans} the transport time of an electron through the structure. In order to increase the wallplug efficiency [62], one needs to increase the transition efficiency η_{tr} and the product $f\tau_{\text{eff}}$. The comparison of best wallplug device analysed in Ref. [16] gives a clear preference for devices with high values of η_{tr} in contrast to designs with high values of $f\tau_{\text{eff}}$. Devices with a long ULL lifetime and a short LLL lifetime exhibit not only large values of η_{tr} but also strong photo-induced transport, further increasing the device performance.

3.2 Influence of the transparency current density

A topic which is scarcely discussed in literature, but very essential is the transparency current of QCLs. It defines the boundary between absorption and gain, where population inversion is reached. This transparency current exists as the upper state population needs to compensate the non-zero population of the lower state. We will consider direct injection from the MIS to the LLL and backfilling. Backfilling can be described by a thermal population of the miniband: $n_{\mathrm{LLL}}^{\mathrm{therm}} = n_g exp(-\Delta/kT)$. A more precise calculation goes beyond an effective one-subband model of the miniband, assuming multiple equally spaced subbands [51]. The transparency current density leads to additional dissipation of the device and decreases the maximum output power.

The threshold of a laser is given by equation 3.7:

$$\begin{aligned} g_c \Delta n &\stackrel{!}{=} \alpha_{\mathrm{tot}} \\ g_c \left(J_{\mathrm{thres}}/e(\eta_{\mathrm{inj}}\tau_{\mathrm{eff}} - \cancel{\eta_{\mathrm{inj}}^{LLL}\tau_{\mathrm{LLL}}}) - n_{\mathrm{LLL}}^{\mathrm{therm}} \right) &= \alpha_{\mathrm{M}} + \alpha_{\mathrm{WG}} \end{aligned} \tag{3.7}$$

where

$$\Delta n = J/e(\eta_{\mathrm{inj}}\tau_{\mathrm{eff}} - \cancel{\eta_{\mathrm{inj}}^{LLL}\tau_{\mathrm{LLL}}}) - n_{\mathrm{LLL}}^{\mathrm{therm}} \tag{3.8}$$

where g_c is the gain cross section (modal gain), Δn the population inversion. The total optical losses α_{tot} consist of the mirror losses α_{M} and the waveguide losses α_{WG}. J is the current density with J_{thres} being the threshold current density. τ_{eff} is the efficient transition time, τ_{LLL} the LLL lifetime and η_{inj} the injection efficiency into the ULL. The contribution of the injection efficiency into the LLL (or any state below) $\eta_{\mathrm{inj}}^{LLL}$ was calculated with the density matrix model. At threshold it is found to be below 2 % for structures emitting at different wavelength. We will neglect this contribution in the following. The thermal population of the

LLL $n_{\mathrm{LLL}}^{\mathrm{therm}}$ can be interpreted as additional loss term (resonant absorption) or as an additional current (transparency current) $J_{\mathrm{trans}} = e n_{\mathrm{LLL}}^{\mathrm{therm}} / (\eta_{\mathrm{inj}} \tau_{\mathrm{eff}})$.

It can be measured by plotting the device threshold current densities in dependence of the device mirror losses α_{M}=$1/(2L)\, ln(R_1 R_2)$ (see Figure 3.2) for an uncoated and a high-reflective coated backfacet. At the point where the linear extrapolation of these points crosses 0, we find the threshold current density of a device with no mirror losses. Therefore, moving then further to the point x=-α_{WG}, we find the threshold current density of a device without mirror and without waveguide losses: the transparency current density.

In our example we used a wide and narrow miniband device (see Table 3.1). The structures are lattice matched designs at 8.5 μm and described in detail in Section 7.2.2, where information about the growth, waveguide and mounting as well as the light-current density-voltage curve (LIV) measurement of the devices can be found. These active region designs show the same slope in Figure 3.2, which is equivalent to a similar gain coefficient and modal overalp. We see a clear improvement in the transparency current for the wide miniband device. These results agree well with the simulations (see Table 3.1). The contribution of the injection efficiency is equal for the two designs (0.91) presented in this section. In a later example (see Section 7.3.1) we will present the limitations of this simplified model in case of efficient depopulation of the LLL.

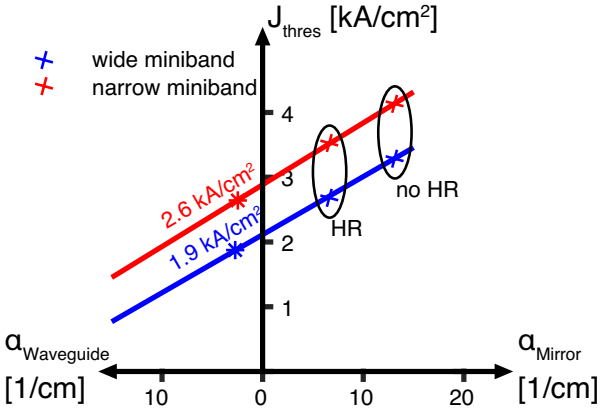

Figure 3.2: Device threshold current density as a function of mirror/waveguide losses at 20 °C. The crosses represent the measured threshold current densities with and without high-reflectivity coating on the backfacet. The lines are the linear extrapolation. The transparency current is then located on the x-axis at -α_{WG}, indicated by the star.

		seed (7.2.2, B.14)	*genetic* (7.2.2, B.15)
Δ	meV	109	97
J_{trans}	kA/cm^2	0.65	0.83
$J_{trans}^{\mathbf{meas}}$	kA/cm^2	**1.9**	**2.6**
Gain Coefficient	cm/kA	14.9	13.9
Gain Coefficient$^{\mathbf{meas}}$	cm/kA	**16.9**	**15.1**

Table 3.1: Data from simulations and measurements of 8.5 μm lattice matched designs.

3.3 Gain Spectrum

One of the main goals of this work is to achieve powerful broadband devices which are used as external cavity, multi-wavelength Distributed-Feedback (DFB) or frequency comb devices. At the level of active region design this requires a flat, broad gain spectrum at all wavelength positions of interest. For this we use heterogeneous stacking, a powerful advantage

of intersubband emission. By stacking several different active regions with different emission wavelengths we can broaden the gain spectrum considerably to values exceeding 59 % around the center wavelength [17]. These stacked active regions should be designed to minimize cross absorption and equalize the total modal gain at the requested wavelengths. Good knowledge of the spectral position and the broadenings of the optical transition and absorptions are required. The optical emission of all stacks should occur in the same current range.

In Figure 3.3 we present an example for a heterogeneous stacking of two active region designs (see Section 8.2.2). The simulated total gain spectrum is shown versus emission wavenumber. The red rectangles below the curve represents 70 % of the peak gain value, usable within an external cavity setup or as DFB devices. Here one can expect devices in the emission range from 915 to 1000 cm^{-1} and from 1090 to 1215 cm^{-1}. For higher wavenumbers absorption takes place, which is due to transitions from the miniband to states above the lasing transition. In case the presented design should be expanded by a third active region stack, positioned at 1700 cm^{-1}, an additional absorption of 4 cm^{-1} needs to be taken into account (see Figure 3.3). A reduction of cross absorption can be achieved by spatially separating the corresponding wavefunctions or by shifting the spectral position of the absorption.

Gas sensing applications are either broadband or concentrating on one or few absorption lines. In the latter case DFB devices are favoured. The spectral precision of simulations and the reproducibility is an important task. In order to produce high-efficiency single/multi-mode devices, the measured gain needs to peak at the required emission wavelength(s). A discrepancy between the simulated and measured gain curve

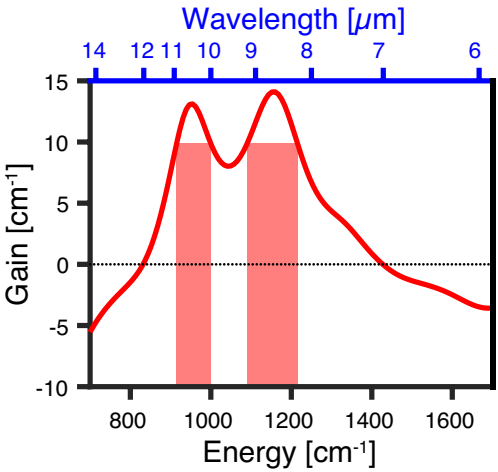

Figure 3.3: Gain spectrum simulation at 2.5 kA/cm^2. The dual-stack active regions will not be continuously tunable.

might be attributed to inaccuracy of design parameters.

The band discontinuity for strained, ternary material is based on the physical properties of the binary bulk materials, the deformation potential is then calculated using a linear approximation between two binary materials. This model might not be accurate enough for thin film layers as used in QCLs, where layer thicknesses can be as thin as a monolayer. Additionally the treatment of electrons with a high in-plane kinetic energy is not well represented using a constant subband temperature (see Section 5.3).

In Figure 3.4 we present the gain spectrum for band discontinuities of 720 and 800 meV which results in a shift of 100 cm^{-1} (more than 8 % around the center wavelength). Furthermore, as seen in Section 5.2, an emission through the injector barrier can occur if this barrier is too thin. This emission,

typically from MIS to the ULL, is not predicted by our simulation, where the electron wavefunctions are cut in the injector barrier. In Section 5.2 we present a method to predict this transitions with electron wavefunctions cut in the extractor/injector region and avoid them by using thicker injector barriers.

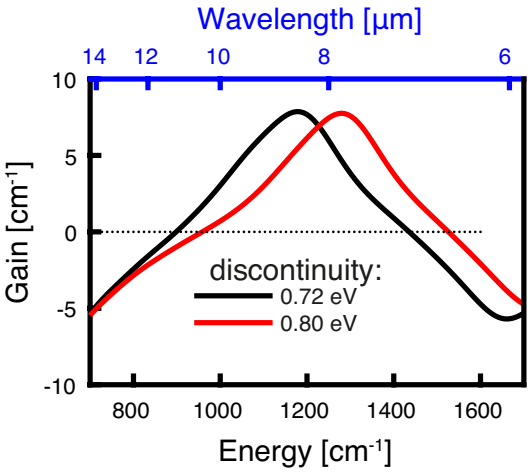

Figure 3.4: Shift in gain peak position due to different discontinuities. Here: $100\,\mathrm{cm}^{-1}$

The emission wavelength is given by the layer sequence of the active region period. In our simulation tool these layer thicknesses values can be arbitrarily chosen, the change of material is abrupt. This stands in contrast to the growth of QCL active regions, where in the ideal case a monolayer should be completed before a new material is grown. If the layer thicknesses are not a multiple of the monolayer thickness, the semiconductor plane at interfaces will incorporate a mix of the two different materials. The interface fluctuations can be as thick as 4 monolayer, see Ref. [63]. This problem is discussed in Section 6.4.

Slight shifts of the gain spectrum can result from inaccuracies in the growth, especially the uncertainty of shutter opening times. Designs for short wavelengths or strained active regions are especially susceptible as they often contain layers with only few monolayers of thickness, which might have a considerable influence on the emission wavelength. Nevertheless the comparison of regrown active region designs show a excellent uniformity: the lattice matched structure at 8.5 μm from Section 7.2.2 (*seed*) shifted by 30 cm^{-1} the strained design at the same wavelength, found in Section 7.3.1 (*seed*) shifted by 20 cm^{-1}. For active regions emitting around 3.3 μm (see Section 6.6) the shift is 45 (70) cm^{-1} where the value in brackets corresponds to a growth with decreased arsenic flow.

Chapter 4

Laser Fabrication and Measurements

4.1 Fabrication

Besides the important role of the active region design and growth, the processing of Quantum Cascade Laser (QCL) chips is a key factor for the laser performance and its reproducibility. It is responsible for uniform current injection into the active region and guiding of the mode while maintaining low waveguide losses and efficient heat transport. For strained material, careful processing is needed to avoid relaxation of the material, especially during the regrowth steps in a Metalorganic Vapor Phase Epitaxy (MOVPE) where the wafer is heated to 630 °C. In the following we will describe the recently optimized buried inverted buried heterostructure (BiBH) [64] procedure, which is based on the established inverted buried heterostructure (iBH) process steps [65]. The new processing workflow was developed to improve the etching profile of the active region, reduce the leakage current through the ridge sidewalls and to improve the epitaxial growth quality. We will give an overview of the workflow and then the improved processing steps are presented in more detail.

The active region periods are grown by Molecular Beam

Epitaxy (MBE) on an InP Substrate (see Figure 4.1 a)), the electron sheet density is around 1-2 $\times 10^{17}$ cm^{-3} for the substrate and 1 $\times 10^{17}$ cm^{-3} (10 $\times 10^{10}$ cm^{-2}) for the active region. The active core is sandwiched in a 200 - 400 nm InGaAs cladding layer (0.4-0.6 $\times 10^{17}$ cm^{-3}), which can incorporate a grating defined by dry or wet-etching. Subsequently, a MOVPE regrowth step of 400 - 500 nm of InP ("planarization") is performed (see Figure 4.1 b)). The ridges are defined with a Silicon Oxide (SiO_2) or Silicon Nitride (SiN) hardmask (see Figure 4.1 c)) and etched (see Figure 4.1 d)). The recipes are found in Table 4.1. For the etching step we either use a fast wet-etching solution which is further described below, or an Inductively Coupled Plasma-etching (ICP) dry-etching process followed by a $\approx 2\,\mu$m deep etch to smoothen the sidewalls and generate an undercut below the hardmask. Dry etching has the advantage of well defined and uniform ridge width [64] and is the preferred solution for high-yield single-mode devices. On the sides of the active region a layer of insulating InP:Fe (0.6 $\times 10^{17}$ cm^{-3}) the so-called "lateral" regrowth is grown by MOVPE (see Figure 4.1 e)). With this step the active region is buried in InP material. After removing the hardmask, the last MOVPE regrowth is done to complete the cladding on top of the active region (see Figure 4.1 f)). A metallization layer is deposited and the lasers are electrically separated from each other. After this the substrate is thinned down to about 220 μm and a metalization layer is deposited on the backside of the chip (see Figure 4.1 g)) and mounted episide-up or episide-down.

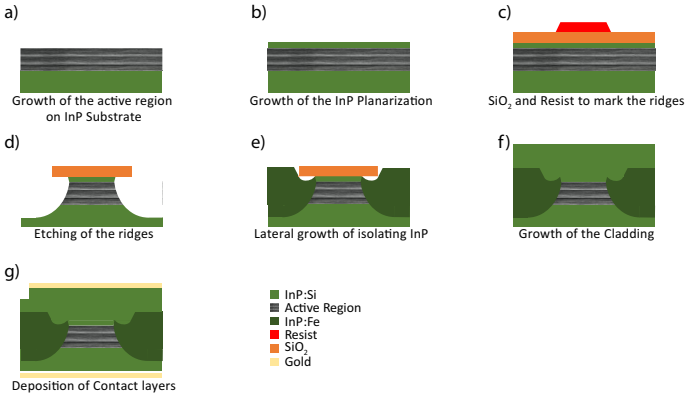

Figure 4.1: Schematic drawing of the active region fabrication steps with BiBH technique. a) Growth of the active region on InP:Si substrate. Optional: etching of grating into InGaAs surface. b)MOVPE growth of the planarization layer. c) Definition of the ridges with a SiO_2 mask. d) Etching of the ridges. e) lateral regrowth. f) Cladding regrowth. g) Thinning down of the substrate and metallization on top and bottom of the chip.

PECVD		
SiH_4 (2.5 % N_2)	sccm	340
N_2O	sccm	710
Temperature	°C	300
Pressure	mTorr	900
RF power	W	20
RF time	s	10
LF power	W	30
LF time	s	5
deposition rate	nm/min	45

RIE		
Ar	sccm	25
CHF_3	sccm	25
Temperature	°C	18
Pressure	mTorr	30
RF power	W	70
RF time	s	60
DC bias	V	350
repetition		22
etching depth	nm	450

Table 4.1: Recipe for SiO_2 deposition and etching.

4.2 Measurement

The processed wafer is cleaved into bars or single ridges of 0.25 to 6 mm length. They are mounted epilayer-up on copper blocks or epilayer-down on NS submounts. The latter technique is described in detail in Ref. [66]. Devices, that are used for measuring

spontaneous luminescence might be mounted with the ridge parallel to the edge, the measurement is then taken perpendicular to the ridge. Subsequently coatings might be applied using a Univex 500 electron-beam evaporator. The measurements are performed on a Peltier cooler. Light-current curves are recorded using a calibrated thermopile detector. Continuous-wave measurements are done with a Keithley 2420 sourcemeter and the Wavelength Electronics QCL 2000. Spectral measurements are performed with a resolution of $0.075\,\mathrm{cm}^{-1}$ and taken by fourier transform infrared spectroscopy(FTIR). Spontaneous luminescence is recorded with a resolution of 16 or $32\,\mathrm{cm}^{-1}$ and a mercury cadmium telluride (MCT) photovoltaic detector. The far-fields were recorded using a goniometer assembly and a pyroelectric detector. For the far-field measurements the device was driven in a micro-macro scheme: A burst of 4807 pulses with a pulse width of 208 ns and 2 % duty-cycle where send to the device at an overall repetition rate of 10 Hz. The 10 Hz frequency was used for the lock-in detection.

The Keithley sourcemeter gives current spikes when the current is switched on / off, leading to detrimental voltage applied on our short wavelength (3.36 μm) lasers. Therefore, to avoid current spikes, later measurements are performed with a Wavelength Electronics QCL 2000. The QCL 2000 delivers an "open circuit" error at currents below 5 mA due to the high resistance of the device. Light-current density-voltage curves (LIVs) are therefore recorded only for higher currents.

4.3 Gratings with a Feature Size of 250 nm

In most spectroscopy applications wavelength selection for one or several modes is essential for high-precision measurements. This is often achieved by etching corrugations into the InGaAs cladding

layer close to the active region, forming Distributed-Feedback (DFB) gratings. The feature size (1/2 of the period length) of a first order DFB grating has the length of $\Lambda/2 = \lambda/(4 \times n_{\text{eff}})$ for emission at wavelength λ. Assuming an effective refractive index n_{eff} for the optical mode of 3.36, leads to half-periodicities of 246 nm for the region around 3.3 μm. This is close to the emission wavelength (220 nm) of our deep-UV lithography, and much smaller than the wet-etching resist thickness (AZ1505, 500-600 nm). We will describe in the following the fabrication of such narrow gratings. This work is part of the publication [67], further details can be found in Section 6.6.

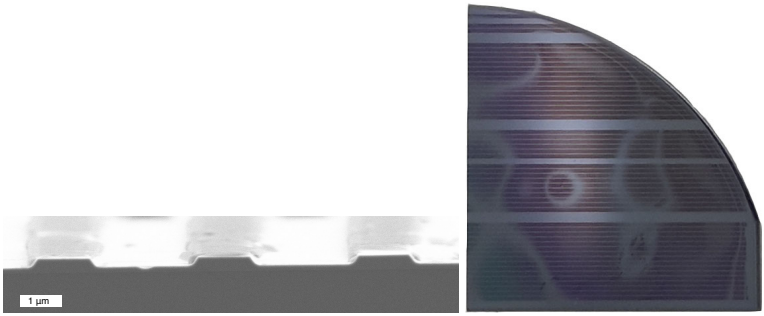

Figure 4.2: SEM pictures. a) A cross section of the grating etch. It shows the grating with an etching depth of 200 nm and a resist thickness of roughly 70 nm. b) Top view of the processed wafer, the grating was etched uniformly, indicated by the near absence of Newton's rings. Figure b) taken from Ref. [64].

A new lithography recipe enabled us to keep the optical lithography step in contrast to the more time-consuming alternative of e-beam lithography. The resist was diluted with EBR (AZ1505:EBR = 1:4), giving a resist thickness of 70 nm (Table 4.2). This thickness is suitable for optical patterning and also withstands the wet etching step. In Figure 4.2 a) we see the cross section of the grating. The etching depth is 200 nm. In Figure 4.2 b) we see the topview on the processed quarter of the wafer after the etching

step. The grating pattern is very uniform with few Newton's rings visible.

Resist	AZ1505:EBR = 1:4
Exposure Dose	7 mJ/cm^2
Exposure Wavelength	220 nm
Developer	1 M KOH:H2O = 1:8
Developing Time	35s

Table 4.2: Lithography recipe for 70 nm resist thickness.

4.4 Etching of Ridges

The shape of the ridge profile is defined by the etching step. On the planar active region material, ridges are defined by lithography on a SiO_2 or SiN hardmask and then etched away. Dry etching or wet etching are possible. The first option leads to straight, but rough sidewalls (strongly dependent on the hardmask quality) without undercut below the hardmask, therefore a subsequent smoothing etch is necessary. By contrast, wet etching is done with an isotropic etchant, leading to smooth, but trapezoidal shapes.

The ridge profile is important for obtaining high performance devices. We opt for vertical sidewalls, where the width of the ridge is similar for all active region periods. Therefore, during operation at a specific current, all active region periods are at the same point in the gain-current density-voltage curve (GIV). In this case, the crossing from absorption to gain takes place in all periods simultaneously and cross-absorption is avoided.

After etching the ridges, an undercut on each side of the SiO_2 hard mask of 0.4 $\times$ etching depth (about 2 μm) is needed to regrow a thick, planar InP:Fe layer on the sides of the ridges, while avoiding fast growth on the edge of the ridge ("rabbit ears", [68]).

This topic will be refined further in the next section.

The sidewall roughness is an important performance factor [69]. In the Mid-Infrared (mid-IR) QCLs the interface roughness is the main contribution to the broadening of states and scattering losses. Additionally sidewall roughness has a strong impact on regrowth quality. A smooth and oxide-free interface is needed to avoid dislocation and polycrystalline defects as well as holes.

Up to now, the current regrowth quality and trapezoidal shaped ridges are decreasing device performance, to this end we present the improvement of the wet etching recipe [64]. We investigate two etching solutions, which uniformly etch Indium Phosphide (InP), Indium Gallium Arsenide (InGaAs), Indium Aluminium Arsenide (AlInAs) and Aluminium Arsenide (AlAs), where the last 3 are compounds of the QCL active region. HBr:HNO3:H2O (1:1:10) is the standard iBH etching solution, the etching rate of which is stable only after an "aging" time of about 2 weeks and is about 0.01 μm/s. This etching solution is sensitive to contamination and both visible and ultraviolet light. It is diffusion-limited and therefore the flow of the etching solution needs to be precisely controlled to achieve a good etching profile. Non-uniform etching of the different active region materials has led in the past to sidewall roughness and fault propagation during the regrowth as seen in Figure 4.3a) and b). Nevertheless this solution can lead to reproducible, nearly rectangular ridges with a smooth surface as shown in Ref. [64,67,70,71].

In order to overcome the shortcomings of the aforementioned solution, for the BiBH instead we use HBr:Br:H2O (17:1:10). It etches the QCL semiconductor materials uniformly, leading to smooth sidewalls. In general, increasing the etching depth to more than twice the active region thickness ($>5\,\mu$m) leads to vertical sidewalls seen in Figure 4.3 c).

The etching rate on the InP-substrate, is somewhat slower which might lead to a small kink between the two materials; nonetheless - up to now - no stacking fault has been observed at this point. The faster etch rate of 0.13 μm/s might lead to less sensitivity to contamination.

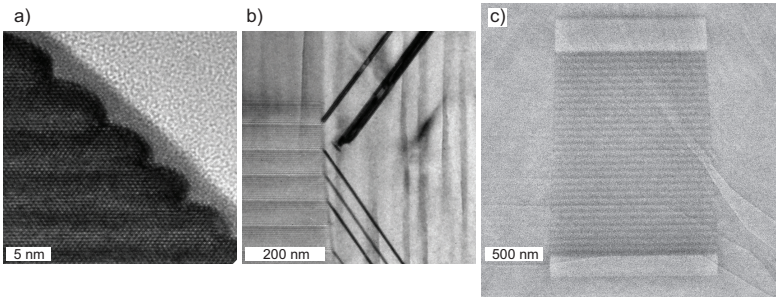

Figure 4.3: a),b) TEM images of the buried active region, etching was realized with HBr:HNO3:H2O. c) SEM image of a ridge cross section, etching was realized with HBr:Br:H2O. a) Small sidewall roughness on *EV2071* (emission around 3.4 μm, Section 6.1). The etching rate discrepancy is due to high Al content in some layers. b) Propagating defects due to rough surface. The active region design is at 4.5 μm, not presented in this work. c) Etch profile of active region emitting at 3.3 μm (copy of [72]) shows vertical sidewalls. The etching depth is 10 μm. Active Region is surrounded by InP. Figures taken from Ref. [64].

4.5 Leakage Management

In this section we will discuss the adaptations with respect to leakage management for the iBH and the BiBH process. In Figure 4.4 a) we see a schematic view of a processed ridge cross section (color-code as in Figure 4.1; AlInAs layers in grey). The BiBH and iBH are placed on the left and right side, respectively. Figure 4.4 b) compares the Scanning Electron Microscope (SEM) picture of processed samples.

The lateral insulating material is InP:Fe, regrown by MOVPE.

This material creates mid-gap traps for electrons, situated approximately 0.59 eV [73] below the conduction band. As a consequence the Fermi-level is fixed in the bandgap region and electron transport is forbidden. The bulk leakage of this i-InP was investigated in Refs. [64,66,74]. The lateral InP:Fe isolation layer in the iBH process is sandwiched in four AlInAs barriers (20 nm) to further reduce leakage (see grey lines in Figure 4.4 a)). We observe from SEM images, that these AlInAs layers are not continuous close to the active region, and carriers might leak through part of the ridge. This is indicated with the red line in Figure 4.4 a). In the BiBH process we decided to remove the AlInAs layers grown above the substrate. This way the bulk leakage current should still be below $1 \times 10^{-3}\,\mathrm{A/cm^2}$ (below 1 mA for a typical device), while the number of interfaces is reduced leading to a better growth quality. In order to reduce leakage, adaptations need to be made above the lateral regrowth.

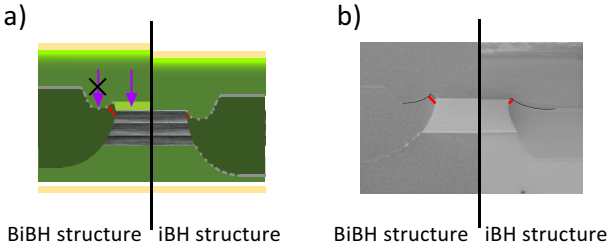

Figure 4.4: a) Schematic comparison of the BiBH(left) and the iBH(right) process. The ridge cross section is presented, color-code is taken from Figure 4.1; grey is used for AlInAs. The red line indicates the shortest leakage path, the violet arrow the direction of current flow. Different electron sheet density levels are indicated by shades of green, light green is used for high doping. b) SEM picture of the ridge cross section for the two different process flows, the interface between the "lateral" and "cladding" layer is emphasized with a black line, the red line shows the shortest leakage path.

In the iBH process the InP:Fe regrowth fills up the lateral side of the active region and the InGaAs top cladding (200 to 400 nm). In the BiBH process the lateral regrowth thickness was increased by 500 nm due to the introduction of a planarization layer (see beginning of this chapter). As a consequence the shortest leakage path (red line in Figure 4.4 a) and b)) increased from 0.3 μm to 0.66 μm. For deep etched active regions with nearly rectangular shape this distance was further improved to 1 μm.

To investigate the current leakage we performed one-dimensional calculations of the conduction band edge along the conduction and leakage path. We assume the parameters given in Table 4.3 and 4.4. The conduction band edge discontinuity between InP and InGaAs is 220 meV and the fermi level of the iron doped InP is set 590 meV below the conduction band [75]. For the other materials the fermi-level is calculated according to their doping, following the equation n=N_c exp($E_C - E_F/(k_B$T)) where n is the doping level, N_c the effective electron density of states, E_C the energy of the conduction band, E_F the fermi energy, k_B the Boltzmann constant and T=300K. Complete ionization of the carriers and traps is assumed, the degeneracy of the trap states is set to 2 in contrast to 0.45 used in Ref. [74]. As we are interested in the electron transport before the active region, we approximate the QCL periods with InGaAs material. Two dimensional simulations, including the structure of the active region, applied field and modeling of the iron states as trap states as well as electron recombination centers can be found in Refs. [74, 75].

The conduction band edge versus distance for the conduction and leakage path is shown in Figure 4.5. The planarization layer allows for a higher doping level directly on top of the active region. The doping level is indicated by light green color in Figure 4.4 a) and in the inset of Figure 4.5. The InP layer directly

material	m^*	ε_r	mobility[$cm^2/(Vs)$]
InP	0.08	12.5	5400
InGaAs	0.043	3.9	12000
AR	0.043	3.9	

Table 4.3: Material parameters for the conduction band edge calculation.

conduction path			leakage path		
material	dop[$1/cm^3$]	[μm]	material	dop[$1/cm^3$]	[μm]
InP	2e16	0.5	InP	2e16	1.1 (1.5)
InP	5e16 (2e16)	0.5	InP:Fe	6e16	0.66 (0.3)
InGaAs	4e16	0.3			
AR	2e16	2.1	AR	2e16	1.7
InGaAs	4e16	0.3	InGaAs	4e16	0.3
InP	1e17	0.3	InP	1e17	0.3

Table 4.4: Layer sequence for the conducting path and the leakage path. If not stated otherwise the dopant is Si.

above the active region is therefore more conductive, funneling the current into the InGaAs cladding layer(indicated by violet arrows in Figure 4.4 a)). The funneling effect can be verified in the conduction band diagram. The blue curve in Figure 4.5 a) gives the band edge from cladding layer through the active region and finally into the substrate (the path is indicated in the inset). The conduction band discontinuity due to the increased doping in the planarization layer is about 24 meV.

The conduction band diagram through the lateral regrowth is illustrated in the red curves in Figure 4.5 b) (the path is indicated in the inset), where we neglected the AlInAs barriers above the iron doped InP, as this layer is not continuous close to the active region. Due to the pinning of the fermi-level a barrier in the conduction band is generated in the iron doped layers. We assumed full ionization of the trap states, whereas a more detailed analysis

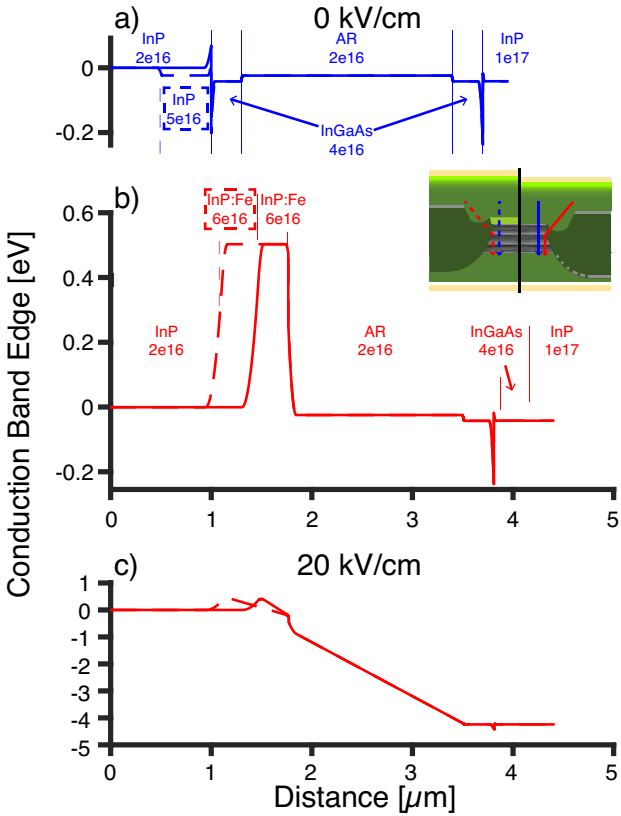

Figure 4.5: Conduction band edge at a electric field of a), b) 0 kV/cm and c) 20 kV/cm versus distance. The different paths are indicated in the inset for the BiBH in dashed lines and for the iBH in continuous lines. The AlInAs layers in the lateral regrowth are omitted. The carrier path is presented through the cladding in a) (blue color) and the leakage path through the lateral regrowth in b) and c) (red color). The material sequence and doping is indicated above and below the band diagram in a) and b). In case the material differs between the BiBH and iBH fabrication technique the BiBH values are framed with a dashed line. If not stated otherwise the dopant is Si.

should take into account a spin-degeneracy of only 0.45 and the iron states acting as recombination centers, a detailed model is described in Ref. [75]. In our case the region of band bending is

about 50 nm thick, whereas the calculations in Ref. [75] give over 100 nm.

In Figure 4.5 c) we present the conduction band edge under a bias of 20 kV/cm (around 4 V). As the QCL active region core can be seen as a superlattice extended by an extractor and injector part, it is expected that the bias drop occurs mainly in the active region instead of the cladding and the substrate. To verify this, we assume a laser ridge with the dimensions 3 mm $\times$ 6 μm and typical values for the BiBH process, namely a chip width of 400 μm, substrate thickness of 200 μm and a cladding height of 4 μm. We find that the combined resistance from the substrate, the InGaAs cladding and the InP cladding amounts to less than 0.026 Ω. The total resistance on a processed device is around 90 Ω, as was calculated from measurements of the genetic device in Section 7.3.1. Therefore we neglect the bias drop in the InP:Si and InGaAs cladding layer for Figure 4.5 c). For low fields the formation of electric field domains within the active region core can be neglected (see Ref. [16]) and we assume a constant electric field in this region. The different electric field in the iron doped layers (24, 11 kV/cm) is due to the different path length. Carrier diffusion and other field-effects in the iron doped layers are neglected [75]. We can see that due to the applied bias the effective barrier height and width are reduced, whereas the barrier for the sample with planarization layer is about 250 μm wider (measured at the 0 eV base line).

The BiBH process shows a reduced number of crystaline defects after processing which we assume is due to the pure InP surface present at the last cladding regrowth step. This differs from the iBH process, which exhibits a InGaAs layer on top of the active region and InP surface otherwise. At the intersection point of these materials, we often observe crystalline defects.

The measured LIV of a wafer processed with and without

the planarization layer is presented in Figure 4.6. The active region is a copy of [76] and the seed structure for the genetic optimization in Section 7.2.2, lasing emission is around 8.5 μm. We show several devices of 1 mm length with high reflectivity coating on the back facet. They are mounted epi-side up on copper submounts and power measurements are taken with a thermopile detector. The dotted line and continuous lines represent the lasers with and without planarization, respectively. The current density-voltage curve (IV) of non-planarized devices do not overlap with each other, which is a clear sign of carriers bypassing parts of the active region. Different regrowth quality, with crystalline defects and stacking faults result in an additional current that depends on the wafer position. As the slope efficiency is similar for these devices, a defect within the active region can be excluded. In the measurements with planarization layer the IVs overlap, as expected. The leakage current for low fields is clearly reduced for the BiBH, leading to a twofold reduction in threshold. This result could quantitively be reproduced in several active regions and different BiBH process runs, showing a clear reduction in leakage for low currents.

The iBH technique can result in low-leakage devices, as seen in Refs. [64, 67, 70, 71]. Nevertheless the BiBH process is less susceptible to defects on the sidewall, polycrystalline defect growth and leakage. On average we achieve better fabrication quality with the BiBH protocol.

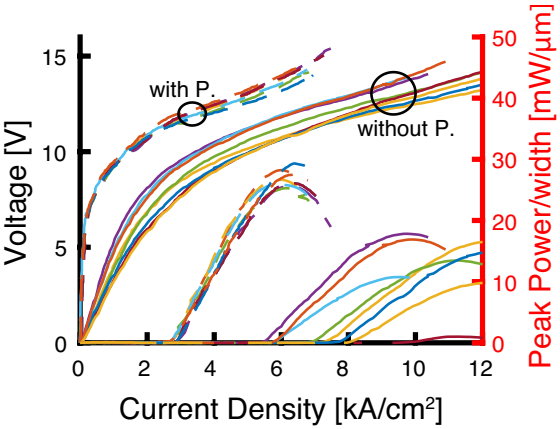

Figure 4.6: Comparison with and without planarization layer in pulsed operation with 1 % duty-cycle. Several measurements for HR coated 1 mm long devices at 20 °C.

Chapter 5

Validation of the Simulation Model

5.1 Choice of Basis: A Dependency Study

The electron wavefunctions presented in this thesis are calculated with the Density Matrix (DM) formalism in one active region period, the borders of the active region banddiagram are defined by barriers with high conduction band discontinuity. The continuum states are approximated as bound states above the active region period. With this method it is possible to normalize the wavefunctions. The beginning and end of the period is usually set at the injection barrier, the thickest barrier layer in the structure. This is reasonable, if mixing between the states from different periods can be neglected. The choice of boundary conditions has an impact on the electron basis wavefunction and the carrier transport.

The electron wavefunction of the main injector state (MIS) and the upper laser level (ULL) are represented by $|\Psi_{MIS}\rangle$ and $|\Psi_{ULL}\rangle$, the coupling between them is treated via the tight-binding model and included into the density matrix model, whereas the diagonalized basis of the Hamiltonian would be a mixture between those two states. Through the injection barrier, in between two

periods, we apply the tight binding model. At the alignment field this leads to sequential resonant tunneling between MIS and ULL and non-resonant tunneling for the other states, for example from the MIS to the lower laser level (LLL). This might underestimate the current. Optical transitions through the barrier are not calculated, especially the transition from the injector ground state to the LLL. We will investigate the discrepancy in current and gain contribution for simulating one, two and three subsequent periods. For two subsequent periods the tight binding model will be applied for the first injection barrier at the beginning of the structure whereas at the second injection barrier the wavefunctions are not localized anymore on the two sides of the injection barrier and coherent transport as well as incoherent scattering is taken into account. In the case of three subsequent periods, the tight-binding model is calculated at the first injection barrier, coherent and incoherent transport is modeled for the subsequent two injection barriers.

Simulating two or more subsequent periods will lead to a current accumulation before each injector barrier. In order to take into account the effect of carriers in the middle of the local basis, the self-consistent potential needs to be calculated on the transport populations. This is done with the super-self algorithm as described in Section 2.1.2.

In Figure 5.1 we see the basis wavefunctions for two subsequent periods (color-coded) and for one period (thin black curves). The active region design is found in Appendix B.15. While we see a splitting for the wavefunctions across the barrier at 63 kV/cm (ULL and ULL', indicated in Figure 5.1) the wavefunctions at 70 kV/cm (and 50 kV/cm, not shown) are localized and show only one ULL. Our simulation model cannot fully account for the correct charge distribution, therefore the ULL population and the

potential of subsequent periods are slightly non-periodic (<12 % variation for n_{ULL}). In the case of two and three subsequent periods, we build the average of the optical parameters over the subsequent periods, which are shown in Figure 5.2. We compare the results for 2 (red) and 3 (blue) active region periods compared to the simulations with 1 active region period (green). The current density is increased when scattering across the enclosed injection barriers is included. The oscillator strength of the transition is slightly decreased as part of the oscillator strength is shifted to the transition of the injector ground state to LLL. These two parameters vary by about 15 % as indicated by the green shade. The gain spectrum, normalized by the current density, is shown in Figure 5.2. Except for a slight blueshift due to a shifted ULL, the gain shape and intensity agree with each other. Therefore we can conclude that treating the MIS and ULL as a mixed state $1/\sqrt{2}\,\psi_{ULL} \pm 1/\sqrt{2}\,\psi_{MIS}$ or in the tight binding scheme has an insignificant impact on the gain spectrum. The influence on the current and optical parameters is small and predictable. The tight binding approach is therefore well suited for generating and modifying designs, as long as the injection barrier is thick enough to separate the injector and laser states sufficiently. The optimal injection barrier thickness will be studied further in Section 5.2.

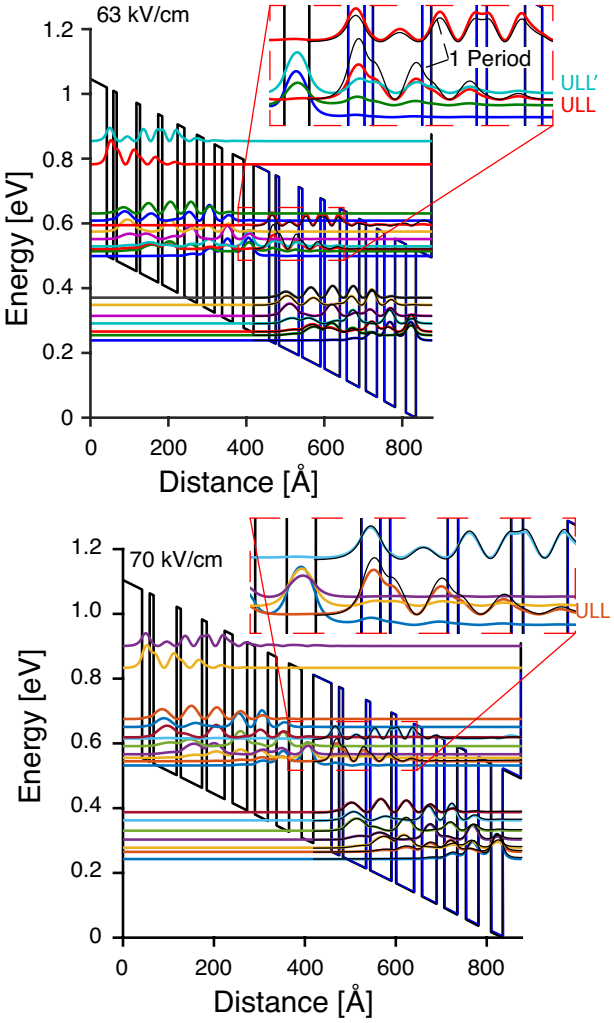

Figure 5.1: The basis wavefunctions at a bias of 63 and 70 kV/cm. For each bias we present the wavefunctions for two subsequent periods(color-coded), overlayed in black thin lines are the wavefunctions of a single period. A zoom of the injector and precedent active wells is shown on the top.

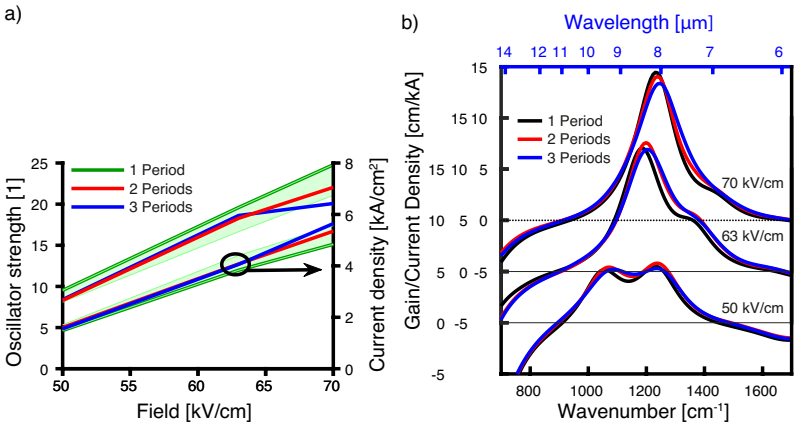

Figure 5.2: a) Oscillator strength and current density versus field for 1, 2 and 3 subsequent periods. 15 % deviation of the 1-Period value is indicated in shaded green. b) Gain spectrum for the fields 50,63 and 70 kV/cm evaluated for 1, 2 and 3 subsequent periods. The gain was normalized by the current density and is offset by 5 cm^{-1} for clarity. A black dotted line indicates the 0-gain position.

5.2 Influence of Injector Barrier Thickness

The current through the active region is given by $J = en/\tau_{\text{trans}}$, where n is the carrier density and τ_{trans} is the average transport time through the active region period. Where τ_{trans}=$\tau_{\text{ULL}} + \tau_{\text{cool}} + \tau_{\text{inj}}$ is the sum of upper laser level (ULL) lifetime, cooling time of electrons within the active region period and the tunneling time through the injection barrier. The cooling of electrons mainly occurs due to optical phonon (about 34 meV) scattering, with a scattering time of 0.2 ps. As Quantum Cascade Lasers (QCLs) show a wallplug efficiency of less than 50 % at typical operation temperatues (above -20 °C), most electrons undergo non-radiative transitions and the cooling is fixed by the energy distance between the ULL and the main injector state (MIS). The tunneling time can be engineered by changing the injection barrier. The effects of changing the injector barrier width was previously investigated by Ref. [77] using a Terahertz (THz) active region design. An experimental study for a AlGaAs/GaAs design in the Mid-Infrared (mid-IR) is presented by Ref. [78].

The current due to resonant tunneling can be approximated by the Kazarinov and Suris formula (Ref. [41], Equation 2.11). In the strong coupling regime, where $4\Omega^2\tau_{||}\tau_{\text{ULL}} \gg 1$, the states on each side of the thin injector barrier mix. In a typical QCL with a dephasing time of 70 fs and a τ_{ULL} of 0.4 ps the boundary is at a splitting energy Ω of 2 meV. The current at resonance is $J_{max} = n * e/(2 * \tau_{\text{ULL}})$ and depends only on the τ_{ULL}, but not on the barrier thickness. This regime is not well described by our density matrix simulations, as our choice of basis does enables mixing between injector states and states of the next active region period only to first order, as given by the tight binding model. We will work closer to the weak coupling regime, where the maximum current is given by $J_{max} = e * n * \tau_{||} * \Omega^2$, with a square dependence

on the coupling energy. In this regime we can tune the maximum current independently from the τ_{ULL}. Electron transport through the barrier is slower than in the strong coupling regime due to a thicker barrier, which also implies that the transition from the injector states to the lower laser level (LLL) is reduced.

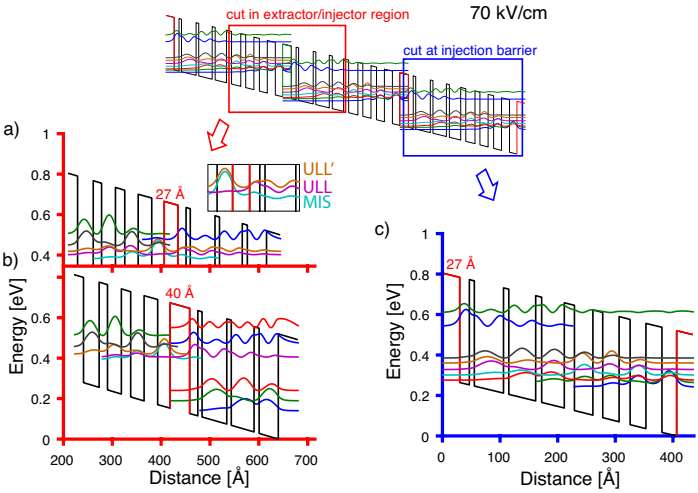

Figure 5.3: Basis Functions at 70 kV/cm cut in the in the extractor/injector region barrier (left) and injector barrier (right). Top: sketch showing the different cutting locations. a), b) Barrier thickness 27 and 40Å cut in the extractor/injection region, c) Barrier thickness 27Å basis cut at injector barrier. In a) the lowest 3 wavefunctions are removed for simplicity. The injector barrier is marked in red.

Carrier transport through thick barriers is calculated well with the tight-binding model while incoherent scattering between states is a reasonable approximation for thin barriers. We will compare both transport methods at the injection barrier, to identify more precisely the optimal thickness thereof. The simulations are presented for the genetically optimized structure of Section 7.2.2. The electron wavefunctions are cut at the injection barrier (see Figure 5.3 c)) as already seen in the previous section. This results

will be compared with electron wavefunctions where the band diagram was cut in the middle of the extractor/injector region (see Figure 5.3 a), b)). To clarify the boundary conditions, a sketch on top of Figure 5.3 a) and c) shows three subsequent active region periods with the cut used in the simulations indicated below in a red and blue rectangle, respectively. The cut in Figure 5.3 a), b) is positioned after the ULL, so that the optical transition stays nearly undisturbed, the potential is calculated with the super-self convergence similar to the Section 5.1. In this case the injector / extractor region is not represented well, as mixing between the states before and after the cut is inhibited. Due to the mixing of the MIS and the ULL our basis now might show two upper lasing states ULL and ULL' (see Figure 5.3 a)).

For increasing injector barrier thickness the states of the injector and ULL localize. To quantify this, the Figure 5.4 a) gives the coupling regime criterion $4\Omega^2\tau_{\shortparallel}\tau_{\mathrm{ULL}}$ and the coupling energies Ω towards the ULL and towards the LLL for selected barrier thickness. The coupling criterion changes strongly for thin barriers. The 27Å thick barrier is clearly in the strong coupling regime, from 38Å onwards a crossing from strong to weak coupling takes place. At the same time the coupling energies are reduced. If we identify the leakage current with $J_{\mathrm{leak}} = e * n * \tau_{\shortparallel} * \Omega_{LLL}^2$, we see in Figure 5.4 a) that a significant leakage is to be expected from thin barriers.

The Figure 5.4 b) gives the oscillator strength for wavefunctions cut at the injector barrier (blue) and in the extractor/injector region (red) for different barrier thicknesses. As expected, when the wavefunctions are cut in the injector barrier, the optical transition parameters do not depend on the barrier thickness. For example the oscillator strength stays constant at 24.5. If the wavefunctions are cut in the extractor/injector, anticrossing takes

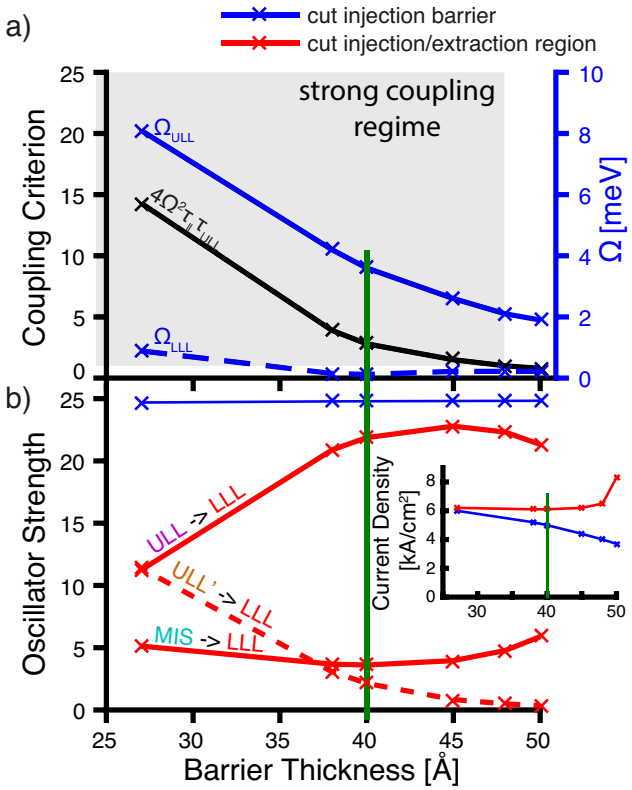

Figure 5.4: a) Coupling criterion and coupling energies towards ULL and LLL with respect to barrier thickness. b) Oscillator strength in dependence of barrier thickness for ULL and MIS. Blue: wavefunctions cut at the injector barrier, red: wavefunctions cut in the injection/extraction region. Inset of b) Current density for the same dataset. All results are taken at 70 kV/cm. The optimal barrier thickness of 40Å is marked with a green line.

place across the injection barrier. We see from Figure 5.3 a), b) the light blue and magenta states are the best candidates for MIS and ULL, respectively. The contribution of the state ULL' is small except for thin barriers (Figure 5.4 b)). Again, we see the most significant change for the barrier thickness increasing from 27Å

to 38Å. The ULL candidate gains in oscillator strength as the wavefunction shifts more to the optical transition region, at the same time the MIS candidate has a reduced oscillator strength as it shifts to the injection region.

For 40Å the oscillator strength is close to the one calculated for the cut in the injection barrier, which validates that the latter is a reasonable choice of basis in this coupling regime. The current density is shown in the inset of Figure 5.4 b). Cutting the structure through the injection barrier leads to current density which decreases with increasing barrier thickness. This is in agreement with the discussion above. When the structure is cut through the injector/extractor region the barrier for the resonant tunneling and current density evaluation is not the injection barrier, but the fourth barrier of the structure. Therefore increasing the thickness of the injection barrier does not change the current density. This is a unphysical result and shows the breakdown of the rate equation model for thick barriers.

For barrier thicknesses from 40 to 50 Å, the oscillator strength of the MIS candidate increases due to an increase in the dipole matrix element from 12.7 to 15Å. At the same time, the current density increases by $1.4\,\mathrm{kA/cm^2}$. The comparison of the electron wavefunctions for the injector barrier of 45 and 50 Å is presented in Figure 5.5. For the thicker injector barrier, the MIS state has a higher probability on the right side of the injector barrier. This unphysical result is due to the resonance of the ULL and MIS. These unphysical results also occur in the rate equation model (see Section 2.1.2). To avoid these resonances, our group implemented the treatment of the injector barrier via the tight-binding model as described in Ref. [36].

The decreasing oscillator strength of the MIS candidate with increasing barrier width can also clearly be seen in

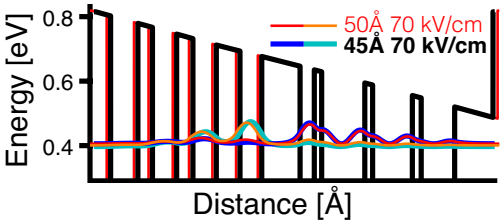

Figure 5.5: Comparison of the wavefunctions for the MIS and ULL candidate for barrier thickness of 45 and 50Å. For the thicker barrier, the MIS candidate (orange line) has a slightly higher probability after the injection barrier compared to the thinner barrier (light blue curve).

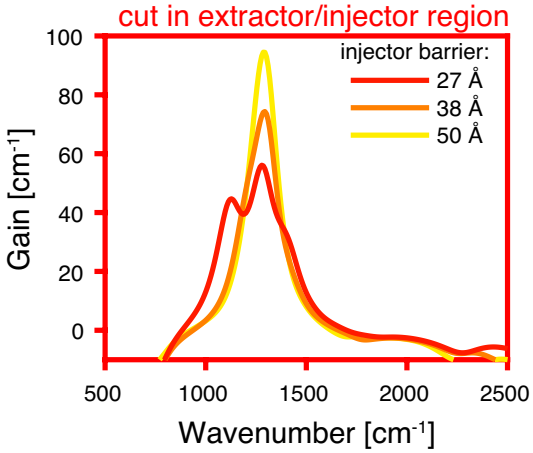

Figure 5.6: Gain spectrum at 70 kV/cm for the basis wavefunctions are cut in the extractor/injector region. The low-energy emission from the MIS candidate disappears with increasing barrier thickness.

Figure 5.6, where we plot the gain spectrum of the structure for different barrier thicknesses. The wavefunctions are cut in the extractor/injector region. The change is once again most prominent between the barrier thicknesses of 27 and 38 Å, where

we see an additional, redshifted emission from the MIS candidate and a small blueshifted contribution from ULL'. The shape of the gain spectrum does not change significantly for further increase of the barrier thickness.

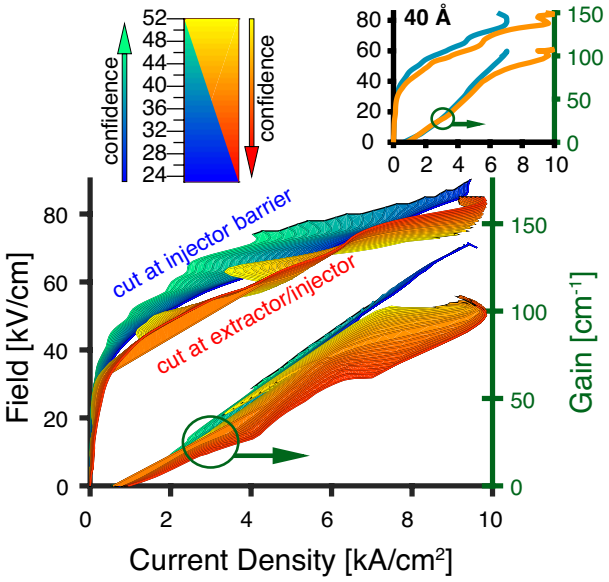

Figure 5.7: GIV for several injector barrier thicknesses. The width is color-coded with thicker barriers in lighter colors. Blue to green: wavefunctions cut at the injector barrier, red to yellow: wavefunctions cut in the injection/extraction region. The inset gives the data for the injector width of 40Å.

In Figure 5.7 we see the gain-current density-voltage curve (GIV) of this structure evaluated for an injection barrier thickness ranging from 24 to 52Å. The barrier thickness is color-coded with thicker barriers in lighter colors. The yellow curves represent the data from the electron wavefunctions cut in the injector/extractor region, the blue curves the electron wavefunctions cut at the injection barrier. For the latter we see that the gain does not

depend strongly on the barrier thickness, as the oscillator strength between the injector state and the LLL is neglected. The maximum current density decreases with increasing barrier thickness, as predicted by the Kazarinov and Suris formula. For the cut in the extractor/injector region we see, as expected, a significant increase of peak gain for increasing barrier thickness. This is due to the oscillator strength shifting towards the lasing transition. The current density-voltage curve (IV) shows more resonances(for example at 63 and 45 kV/cm), which are the alignments of the different extractor/injector states. The field of 70 kV/cm for this study was choosen to avoid these resonances.

In order to separate the injector state reasonably well from the lasing transition while keeping the current density and therefore n_{ULL} as high as possible, we decided for a 40Å thick injection barrier. As seen in the inset of Figure 5.7 the GIV of the two variations of basis wavefunctions are in good agreement.

In Figure 5.8 we present the gain spectrum for the choosen injector barrier thickness of 40Å. The gain is normalized by the current density. It shows a blueshift for the structure cut in the extractor/injector region compared to the cut at the injection barrier. This is not due to a shift of the ULL, but a result of a downward shift of the LLL in the absence of the other states of the extractor/injector region.

From the example shown, it becomes clear that the injector barrier thickness is an important parameter for the maximum current density and the injection efficiency of the structure. A thin barrier can lead to parasitic emission from the MIS and carrier leakage, whereas a thick barrier will decrease the maximum current density. We presented a way to optimize the injector barrier thickness with our simulation tool, resulting in a width of 40Å for structures around 8.5 μm. Additionally we showed that inhibiting

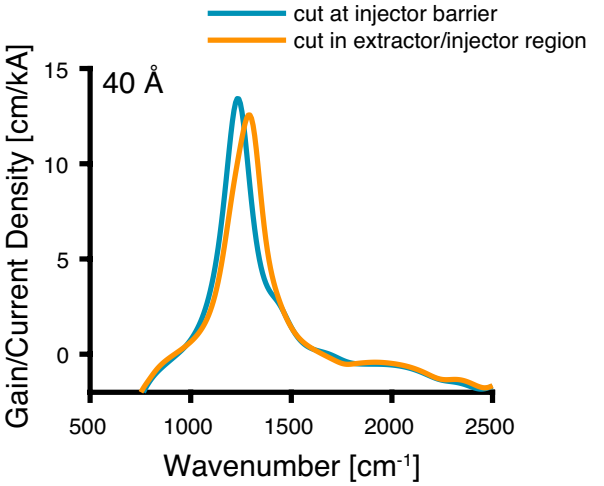

Figure 5.8: Gain spectrum, normalized by the current density at 70 kV/cm, the barrier thickness is 40Å. The current density is 5.0 and 6.1 for the cut at the injector barrier and the extractor/injector region, respectively

the mixing of states through the injector barrier has only small influence on the simulation results in this regime.

5.3 Comparison Density Matrix (DM) and Non-Equilibrium Green's Function (NEGF)

Our DM simulations were compared with measurements of QCLs which were fabricated and measured within our group [42, 55]. This comparison showed good agreement. In collaboration with the PSI Institute and the Rzeszow University we have presented good overlap between gain measurements and NEGF results. Moreover the DM model has given reasonable agreement [79]. The validation of our model is a necessary requirement for the following chapters, where the DM simulations are used to

optimize and predict the QCL performance. We rely on a realistic prediction of electrical, optical and spectral results. As a next step, we will compare our DM model with the NEGF simulation as well as with measurements for another design in terms of gain, IV and light-current density-voltage curve (LIV). With this approach we can verify the validity of our DM model. We will additionally present the distribution and subband temperature of the carriers in a typical QCL structure.

The work was done in collaboration with LUND university and III-V Lab. It is published in Ref. [80]. We consider two implementations of the DM model, where the first (DM simp., III-V Lab) uses the first order current only, while the second one (DM 2nd, ETH), described in Refs. [36, 61] and Section 2, includes the second order current following Ref. [42]. These are directly compared with the NEGF model described in Ref. [40]. The results are compared with experimental data from Ref. [76] and a regrowth from a different facility. The active region design is a 8.5 μm lattice matched QCL (Appendix B.14, Section 7.2.2).

All basic parameters, such as band gaps, effective masses and optical properties of the QCL materials, are the same in all models. For instance, all models use the same Gaussian interface roughness correlation length of 9 nm and height of 0.1 nm. The validation of this interface roughness parameters will be discussed in the next Section. The lattice temperature is 300 K. In the DM models, the electron temperature is fixed to 430 K.

The structure with the Wannier-Stark states is shown in Figure 5.9, together with the carrier densities, which have a shift with respect to the Wannier-Stark states caused by impurity scattering [81]. These shifts, only obtained with the NEGF model, mainly result from the real parts of the self-energies, which are of the order of 14 meV. They are similar for all states, so that they

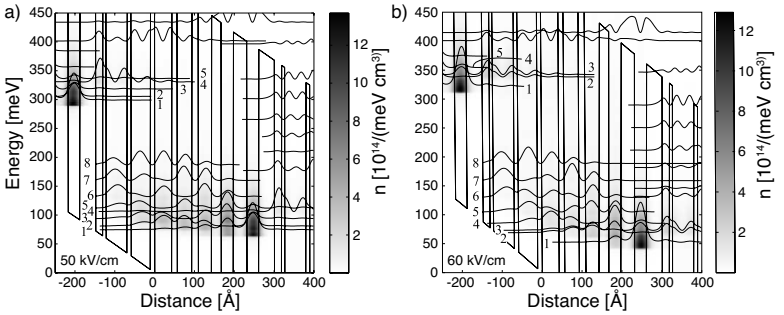

Figure 5.9: Carrier densities and the square of the wave functions, calculated in the NEGF model, for different electric fields near threshold (a) and far above threshold (b). The numbers label the injection level (1), the ULLs (4 in (a), 2 and 3 in (b)), and the lower laser level (8). Figure taken from Ref. [80].

hardly affect the tunneling resonances.

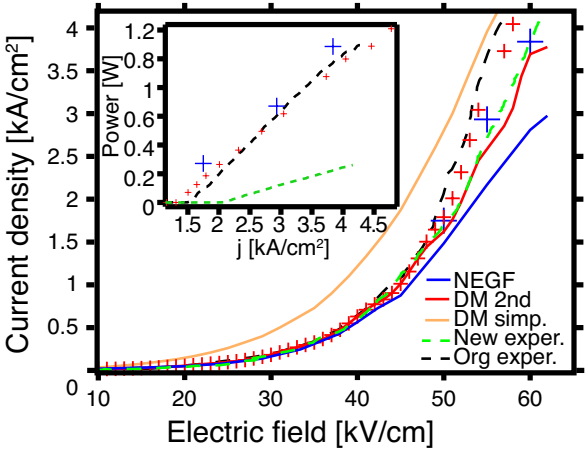

Figure 5.10: Current-field characteristics for the different simulation models and experimental measurements. The field of the experimental data is obtained from the bias divided by the nominal length. Simulations under lasing conditions are given by large blue crosses for the NEGF and small red crosses for the DM model. The inset shows the measured and calculated output power as a function of the current density. Figure taken from Ref. [80].

Figure 5.10 shows the current densities vs. applied electric field. The dashed lines show the experimental data for the original device and our regrowth, which agree until threshold (J_{thres}=1.5 kA/cm^2 and 2 kA/cm^2 of the original and regrown device, respectively). This reflects the reproducible growth quality as verified by X-ray measurements determining the actual period of 44.6 nm for the original and 44.7 nm for the regrown device (nominal 44.9 nm). In addition, the peak currents are comparable. The full lines give the simulation results of the different models without lasing. We see a good agreement between the NEGF model and the DM 2nd model for fields below $\approx$ 52 kV/cm, which both reproduce the experimental data below threshold. In contrast, as expected [61], the DM simp. model provides a much larger current density, which shows the importance of including the second order current in the calculations.

The simulated gain spectra, taken in the limit of a vanishing lasing field, are shown in Figure 5.11, near threshold a) and far above threshold b). The results of the DM 2nd and NEGF models agree near threshold while the DM simp. model shows a slightly larger gain with a blue-shift, coming from the approximation of constant effective mass in the gain calculation within this model. This trend is also seen in Figure 5.11 c) for a wide range of electric fields, where the peak positions for both the NEGF and DM 2nd models agree qualitatively with the measurements. As the electric field increases, the gain evaluated by the two DM models increases strongly, while the NEGF model provides a significantly lower gain. This discrepancy most likely comes from the approximation of constant subband temperatures used in the DM models, while increasing electron temperatures provide detrimental occupation of higher levels at larger fields in the NEGF simulations. A highly non-thermal population is also predicted by the NEGF simulation

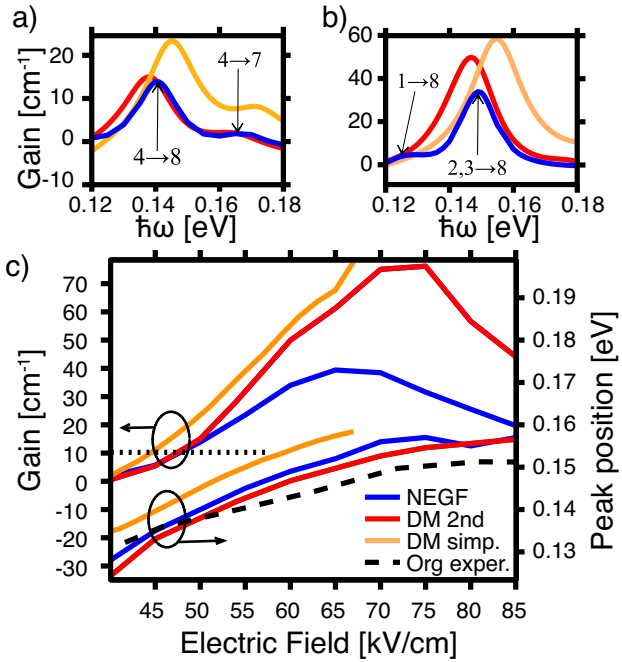

Figure 5.11: Simulated gain spectrum at electric fields of (a) 50 kV/cm and (b) 60 kV/cm. The gain is calculated in the off-state of the laser. In (a) and (b), the transitions of the respective gain peaks in the NEGF simulations are indicated. (c) Peak values and positions vs. electric field. The horizontal dotted line shows the computed threshold gain for the original experiment. The experimental peak position (black dashes) is taken from the electroluminescence spectrum of Ref. [76]. Figure taken from Ref. [80].

in Ref. [82]. In Figure 5.11 b) the NEGF predicts a side peak from the transition 1 to 8, which is not visible in the DM models. This is due to the restriction of the basis states to one period in the DM models (see Section 5.1). The NEGF predicts a peak gain of only 4.4 cm^{-1} for the transition 1 to 8. This contribution cannot explain the gain discrepancy at the laser transition energy of 16 cm^{-1}. The transition strength of 1 to 8 is expected to decrease with increasing field, but the gain discrepancy between the DM and

NEGF are increasing as seen in Figure 5.11 c). In the NEGF model the relevant ULL at threshold is level 4 (see Figure 5.9 a)), and at the higher field, the two resonant levels 2 and 3 (see Figure 5.9 a)), whose coherence is taken into account in the NEGF model. As we saw in Section 5.1 the electron wavefunctions in the DM model do not mix between the periods, therefore for all fields one ULL is present.

The waveguide losses α_{WG} for the device in Ref. [76] are reported to be 2.8 cm^{-1}. With a mirror loss of α_{M}=3.3 cm^{-1} and a mode confinement factor of Γ=0.63, a gain $G_{\mathrm{thres}} \approx 10\,\mathrm{cm}^{-1}$ is required in the QCL active region for achieving lasing. From Figure 5.11 c), it is seen that in the DM 2nd and NEGF models, G_{thres} is reached at electric fields of 47.3 kV/cm and 47.6 kV/cm, respectively. This is in very good agreement with the experimental value of 48 kV/cm. For this field, the NEGF model provides a threshold current density of 1.2 $\mathrm{kA/cm}^2$, and the DM 2nd model gives 1.3 $\mathrm{kA/cm}^2$ (Exp. 1.5 $\mathrm{kA/cm}^2$). Again, the DM simp. model differs, giving a threshold field of 44 kV/cm with the corresponding current density of 1.7 $\mathrm{kA/cm}^2$. As the new device was processed using a double trench waveguide instead of the buried heterostructure technique used in the original device, the losses for this sample are higher. The observed threshold field of 52 kV/cm and threshold current of $\approx$2 $\mathrm{kA/cm}^2$ reflect the trend for the gain simulations.

Under laser operation, an maximum output power of P=1 W was reported in Ref. [76]. The conversion of output power into an AC field inside of the cavity, is given by the relation for a traveling wave [43]

$$P = (F_{\mathrm{ac}})^2 \frac{n_{\mathrm{eff}} c \varepsilon_0 A (1-R)}{2\Gamma}, \tag{5.1}$$

where n_{eff} is the refractive index of the gain medium, A is the facet area, and R is the reflectivity, we obtain an ac field inside the active region of strength $F_{ac} \approx 30\,\text{kV/cm}$. This is a significant amount compared with the dc field under operation $F_{dc} \approx 58\,\text{kV/cm}\,(13\,\text{V})$. This AC field is affecting the transport

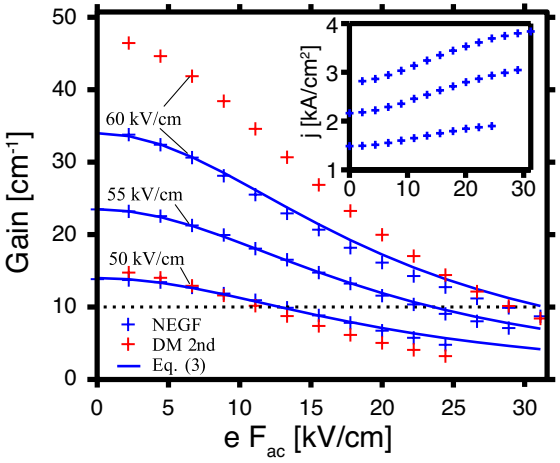

Figure 5.12: Gain vs. applied AC field strength for different DC fields, simulated in the NEGF and DM models, compared to the relationship 5.2. The inset shows the current density in the NEGF model. The horizontal dotted line shows the threshold gain of the original sample. Figure taken from Ref. [80].

by increasing the current density above threshold, as expected in the case of photon-driven transport [83]. The simulated transport under an applied ac field is shown in Figure 5.12, where an increasing F_{ac} results in an increased current density and a decreasing gain. For F_{dc}=50 kV/cm, the NEGF results agree well with the DM model. Again, for F_{dc}=60 kV/cm, the gain is higher for the DM model. The dotted line in Figure 5.12 indicates G_{thres} for the original device. Its intersection with the gain determines the ac field where gain and losses compensate.

For these ac fields, Figure 5.10 shows with crosses the NEGF and DM current densities under lasing operation. As expected, this is in much better agreement with the experimental current density as compared to the simulations without a laser field which neglects the photon-driven transport. The corresponding power output (inset of Figure 5.10) calculated from Eq. 5.3 for the NEGF model also agrees well with this experimental data as well as the DM model. The experimental data shows higher threshold and lower slope efficiency for the new devices compared to the original publication. This is a consequence of higher waveguide losses, as mentioned above.

Now, we show that the gain in the NEGF model follows the semiclassical rate equation, given by Equation 2.13. Where z_{if}=2.2 nm is the dipole matrix element and 2γ=14 meV is the FWHM of the gain spectrum from Figure 5.11(a). Extracting the values for the population inversion, the emission wavelength λ, and z_{if} from the NEGF simulations, we calculate for electric fields of 50 and 60 kV/cm a peak gain of 16 and 43 cm^{-1} , respectively, agreeing reasonably well with Figure 5.11(a) and Figure 5.11(b). Thus, the gain can be solely explained by the relationship 2.13, where Δn_{fi} accounts for the largest fraction of the variation in gain. This, together with the fact that the frequency of peak gain agrees with the energy difference between the peaks in the spectral function, shows that in this particular case, complex effects such as dispersive gain [84,85] and depolarization shifts [86,87] are not of relevance, in agreement with Refs. [77,88]. The differences in gain between the NEGF and the DM model for high dc fields can be attributed to the differences in Δn_{fi} addressed above.

The semiclassical saturation equation gives [16]

$$G(F_{\mathrm{ac}}) = \frac{G_0}{1 + \frac{(½\varepsilon_0 c n_{\mathrm{refr}} F_{\mathrm{ac}})^2}{I_s}} \quad \text{with } I_s = \frac{\hbar \varepsilon_0 c n_{\mathrm{refr}} \gamma}{e^2 z_{fi}^2 \tau} \tag{5.2}$$

For z_{fi}=2.2 nm and τ=0.47 ps (approximate lifetime of the ULL), we obtain a value for the saturation flux I_s of 1.8e10 W/m^2. Figure 5.12 shows that Equation 5.2 reproduces the full NEGF calculations.

From the NEGF modeling results, the carrier densities for each level and in-plane momentum can be extracted. Fitting to a Fermi distribution function, the subband temperatures T_a can be extracted. In Table 5.1 these temperatures are presented at a bias of 55 kV/cm with and without lasing field. The electron temperature for the structure (not single subbands) can also be evaluated with the DM model, when the kinetic balance is evaluated. The results thereof are added into Table 5.1. If the lasing field is included, the electron temperature evaluated with DM decreases, which is expected from energy conservation. For the NEGF the temperature increases, which is due to an increase in non-thermal population of the subbands in accordance with the result above[1]. The DM calculations shown above are performed with a fixed electron temperature of 430 K which is in good agreement with the results shown in Table 5.1.

In conclusion, we have presented simulations of a QCL both with and without a laser field, based on DM and NEGF models, and compared these results to experimental data from two separate growths. The transport and gain characteristics are well explained by simple relations, and thus, the DM model reproduces

[1] In the publication [80] the electron temperature from the injector ground state (IGS) is erroneously referenced as LLL. Here we state the correct version.

	without lasing	with lasing
NEGF: ULL [K]	398	512
NEGF: MIS [K]	345	411
DM (kinetic balance) [K]	467	452

Table 5.1: Subband temperature for the NEGF model for ULL and the MIS and for the DM model with kinetic balance (for all subbands). The lattice temperature is 300 K.

the experimental data as well as the NEGF model. However, the NEGF model predicts significantly lower gain and current for large dc fields close to the current density peak. We also find that the DM simp. model overestimates the current density in the devices, confirming the importance of taking the second order current into account. Finally, electron temperatures from the DM model with kinetic balance and the NEGF model vary by 60 to 70 K. For lasing operation the population in the NEGF model becomes non-thermal.

5.4 Impact of interface roughness distributions

As the interfaces between semiconductor layers are never entirely perfect (see Figure 5.13), the lateral translational invariance is broken and interface roughness scattering becomes inevitable. Several studies have focused on its relevance for the lifetime of the ULL [89–93], which is a key element for the lasing performance. Furthermore, interface roughness is relevant for the broadening of tunneling transitions [94, 95] in QCLs. The deviations from an ideal interface are treated statistically, where the spatial correlation function of the height fluctuations contains the relevant information to evaluate the scattering matrix elements.[2]

[2]Correlations between different interfaces are of minor importance as they are washed out under typical growth conditions unless barriers are very thin [90].

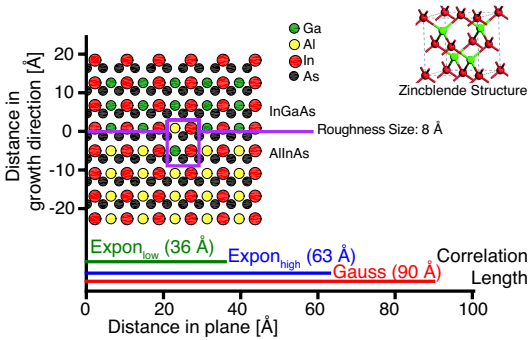

Figure 5.13: Visualization of roughness in epitaxially grown semiconductor layers and the correlation length.

It is common to model this correlation function by a Gaussian with two fit parameters "although there is no definite physical ground" [96]. In this paper such a Gaussian correlation function is compared to an exponential fit and calculations for a mid-IR-QCL are presented. We present results from the NEGF and DM models. The Gaussian distribution suppresses scattering at high momentum transfer which enhances the lifetime of the ULL in mid-IR lasers. Furthermore we discuss the implementation of interface roughness within a two band model. The work described here is published together with LUND University [97].

Interface roughness is the main scattering contribution of mid-IR QCL but up-to-date quantitative measurements of the interface roughness are not conclusive. The central assumption for modeling interface roughness is that the position of the interface between two materials is fluctuating by $\eta(\mathbf{r})$, where $\mathbf{r}$ is a two-dimensional vector in the $x-y$ plane of the heterostructure

layers. The scattering rate from subband ν to μ is given by:

$$\begin{aligned}
\Gamma_{IFR}^{\nu->\mu} &= 2\pi \sum_k \langle |\langle \mu k' | H_{\mathrm{IFR}} | \nu k \rangle|^2 \rangle \delta(E_\nu(k) - E_\mu(k') - E_{\nu\mu}) \\
\langle \mu k' | H_{\mathrm{IFR}} | \nu k \rangle &= \int d^2 r F_{\mu\nu} \eta(\mathbf{r}) exp(i\mathbf{q}\mathbf{r}) \\
\Gamma_{IFR}^{\nu->\mu} &= 2\pi F_{\mu\nu}^2 \frac{1}{A} \int \mathrm{d}^2 r \int \mathrm{d}^2 r' e^{\mathrm{i}\mathbf{q}\cdot(\mathbf{r}-\mathbf{r}')} \eta(\mathbf{r}) \eta(\mathbf{r}') \\
&= 2\pi F_{\mu\nu}^2 \frac{1}{A} \int \mathrm{d}^2 r \; e^{\mathrm{i}\mathbf{q}\cdot\mathbf{r}} \int \mathrm{d}^2 r_0 \eta(\mathbf{r}_0 + r) \eta(\mathbf{r}_0) \\
&= 2\pi F_{\mu\nu}^2 \frac{1}{A} \int \mathrm{d}^2 r e^{\mathrm{i}\mathbf{q}\cdot\mathbf{r}} \langle \eta(\mathbf{r}) \eta(0) \rangle \\
&= 2\pi F_{\mu\nu}^2 f(\mathbf{q}), \qquad (5.3)
\end{aligned}$$

where A is the sample area, $F_{\mu\nu}$ is the interaction strength. For clarity in the last part we omitted the energy conservation factor and the integral over all possible momentum exchange vectors **q**= **k** - **k**'. The Fourier transformation of the spatial correlation function $\langle \eta(\mathbf{r}) \eta(0) \rangle$ for the fluctuations is commonly assumed to be a Gaussian distribution [96] with

$$\begin{aligned}
\langle \eta(\mathbf{r}) \eta(0) \rangle &= \delta^2 \mathrm{e}xp\left(-\frac{|\mathbf{r}|^2}{\Lambda^2} \right) \\
\rightarrow \quad f(\mathbf{q}) &= \pi \delta^2 \Lambda^2 \mathrm{e}xp\left(-\frac{\Lambda^2 |\mathbf{q}|^2}{4} \right). \qquad (5.4)
\end{aligned}$$

Alternatively, the idea, that there is a constant likelihood to be at the rim of a roughness plateau, suggests an exponential distribution:

$$\begin{aligned}
\langle \eta(\mathbf{r}) \eta(0) \rangle &= \tilde{\delta}^2 \mathrm{e}xp\left(-\frac{|\mathbf{r}|}{\tilde{\Lambda}} \right) \\
\rightarrow \quad f(\mathbf{q}) &= \frac{2\pi \tilde{\delta}^2 \tilde{\Lambda}^2}{\left(1 + \tilde{\Lambda}^2 |\mathbf{q}|^2\right)^{3/2}} \qquad (5.5)
\end{aligned}$$

The average fluctuation height δ and the spatial correlation length Λ can be measured for example by Transmission Electron Microscopy (TEM), STM and Atomprobe, the values for the Gaussian distribution used in this work are deduced from Ref. [63]. There are experimental indications for an exponential distribution for several material systems such as Si/SiO_2 [98]; InAs/GaSb [99], InAs/GaInSb [100]; GaAs/InGaAs [101]. For GaAs/ or InGaAs/AlInAs interfaces, relevant for QCL structures, less information is available. Ref. [63] reports lateral fluctuations of 10 nm for an InGaAs/AlInAs QCL but does not provide a distribution function, while Ref. [102] reported values of 10-20 nm for a GaAs/AlGaAs superlattice. Ref. [91] used a Gaussian distribution with $\Lambda = 6$ nm and $\delta = 0.15$ nm, to fit their data for a $GaAs/Al_{0.33}Ga_{0.67}As$ QCL. Recently, $\langle \eta(\mathbf{r})\eta(0)\rangle$ has been measured for a GaAs/InGaAs QCL, where three different Gaussians were required to fit the data [103].

It is meaningless to compare the Gaussian and an exponential distribution with the same set of parameters, i.e. setting $\tilde{\delta} = \delta$ and $\tilde{\Lambda} = \Lambda$, as in this case the exponential distribution would result in twice the scattering of the Gaussian one at $\mathbf{q} \approx 0$. Rather, Λ and δ should be changed as to achieve similar scattering rates in a wide range of $\mathbf{q}$, in order to quantify the difference using either distribution. Provided the dominating scattering events have small $\mathbf{q}$, both distributions are expected to provide similar results with the translation

$$\text{Expon}_{\text{low q}} \quad \tilde{\Lambda} = \Lambda/\sqrt{6} \quad \text{and} \quad \tilde{\delta} = \sqrt{3}\delta \tag{5.6}$$

so that the functions $f(\mathbf{q})$ as well as their second derivatives coincide at the maximum $|\mathbf{q}| = q = 0$. We find, that the exponential distribution provides much stronger scattering for large $\mathbf{q}$ with this translation. A second natural translation is

given by requiring an identical average fluctuation height $\langle \eta(\mathbf{r} = 0)\eta(0)\rangle$ (large q) and identical $f(\mathbf{q} = 0)$ for the Gaussian and exponential distribution. This provides the translation

$$\text{Expon}_{\text{high q}} \quad \tilde{\Lambda} = \Lambda/\sqrt{2} \quad \text{and} \quad \tilde{\delta} = \delta \tag{5.7}$$

which better reproduces the fall-off at larger q-values but agrees less well for small q as can be seen in Figure 5.14. The corresponding functions $f(\mathbf{q})$ are displayed in Figure 5.14 for different roughness parameters.

Considering the case of an IR QCL, the non-radiative scattering from the ULL requires a particular large momentum transfer q, as the large energy mismatch between initial and final states (typically the lasing energy) must be transferred into in-plane kinetic energy for energy conservation. Assuming a lasing energy of $\hbar\omega = 150$ meV (8.3 μm), implies $\text{q}_{\text{lasing}} \approx 0.4\ \text{nm}^{-1}$. Miniband transitions needed to transport the carriers into the MIS are in the order of the LO phonon energy q_{LO}=0.2 nm^{-1}, both values are indicated in Figure 5.14. At q values which are important for scattering events in the miniband, the $\text{Expon}_{\text{low q}}$ and Gauss distribution overlap. At higher q values, especially at the momentum exchange vector q_{lasing}, $\text{Expon}_{\text{high q}}$ and the Gauss distribution overlap. The exponential distribution $\text{Expon}_{\text{low q}}$ shows increased non-radiative scattering at q_{lasing} (see Figure 5.14).

The algebraic decay of f(**q**) for the exponential distribution functions can be related to the behavior of $g(\mathbf{r}) = \langle \eta(\mathbf{r})\eta(0)\rangle$ for $r \to 0$. Standard rules of Fourier transformation provide the second derivative

$$\frac{\partial}{\partial \mathbf{q}} \cdot \frac{\partial}{\partial \mathbf{q}} g(\mathbf{r}) = -\frac{1}{4\pi^2} \int \mathrm{d}^2 q\, q^2 f(\mathbf{q}) \mathrm{e}^{\mathrm{i}\mathbf{q}\cdot\mathbf{r}}.$$

Assuming that $g(\mathbf{r}) = g(r)$ and $f(\mathbf{q}) = f(q)$ are rotationally invariant, the asymptotic behavior $f(q) \sim 1/q^3$ for large q

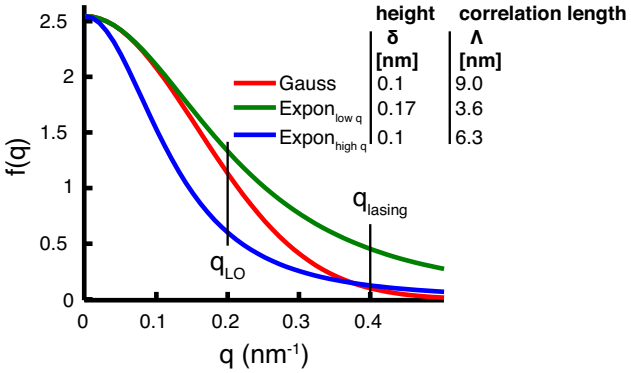

Figure 5.14: Fourier transforms $f(q)$ of the correlation functions for different roughness distribution functions. Figure taken from Ref. [97].

translates in real space to $\delta g(\mathbf{r}) \to \infty$ for $r \to 0$, which means that the gradient of $g(\mathbf{r})$ is discontinuous at the origin (this corresponds to the Fourier transform asymptotic behavior theorem in the one dimensional case discussed by [104]). Such a discontinuity naturally occurs, if $g(r)$ has a finite slope at $r = 0$ (which is the case for the exponential distribution in contrast to the Gaussian).

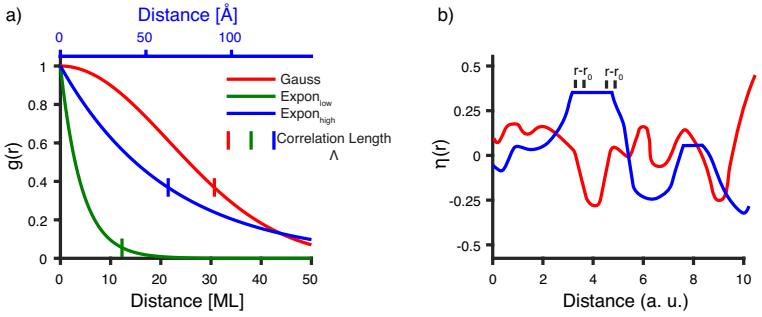

Figure 5.15: a) $g(\mathbf{r}) = \langle \eta(\mathbf{r})\eta(0) \rangle$ for different roughness distribution functions. The correlation length Λ is marked with a vertical line. b) Visualization of a sharp and smooth function for $\eta(r)$. blue: with a sharp drop, red: smooth function.

A (negative) slope of $g(r)$ at $r = 0$ (see Figure 5.15 a)) can be motivated by the following argument: We consider the product $\eta(\mathbf{r})\eta(\mathbf{r}_0)$ for a fixed reference point $\mathbf{r}_0$. This product is positive for $\mathbf{r} = \mathbf{r}_0$ and maintains its value as long as $\mathbf{r}$ is on the same plateau as $\mathbf{r}_0$. Crossing the rim of the plateau, $\eta(\mathbf{r})\eta(\mathbf{r}_0)$ more likely changes to a negative value as the average elongation $\langle \eta(\mathbf{r}) \rangle = 0$. As one averages over all reference points $\mathbf{r}_0$, there are some points, which are precisely on the rim of a plateau and thus $\langle \eta(\mathbf{r})\eta(0) \rangle$ is expected to have a finite negative slope in the direction of $\mathbf{r}$ for small r (see blue curve in Figure 5.15 b)). Note, that this argument requires a sharp drop of the scattering potential for the conduction band electrons at the rims between the plateaus. On the other hand, if the rims of the plateaus result in a smooth change of the potential landscape, there would be no such negative slope for small r (see red curve in Figure 5.15 b)), leading to a Gaussian distribution. To determine which behavior is the most accurate in a real situation would therefore require the precise measurement and interpretation of the actual potential landscape.

In order to demonstrate the relevance of the roughness distribution, we provide simulation results, in the case of one mid-IR QCLs using the interface roughness parametrizations shown in Figure 5.14.

In order to quantify the impact of different interface roughness distributions on the QCL performance, we simulate the mid-IR device [76] shown in Figure 5.9 with the DM model and the NEGF model. The comparison of the simulations is necessary, as the scattering is implemented differently in these models. A detailed discussion of the model differences is given in the previous section, where we applied the Gaussian roughness model with $\Lambda = 9$ nm and $\delta = 0.1$ nm. Here we compare these results with the two exponential models applying different translations of the

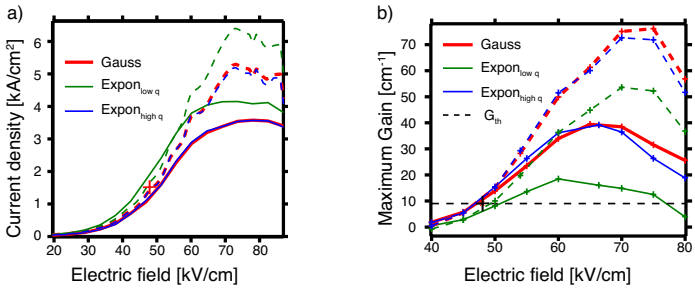

Figure 5.16: (a) Current-field characteristics of the QCL in Ref. [76] for the DM (dashed lines) and NEGF (full lines) simulation schemes and different roughness distributions given in Figure 5.14(a). (b) Peak gain vs. electric field. The dotted line denotes the gain required to compensate the losses. The crosses show the experimental threshold data in both panels. Figure taken from Ref. [97].

parameters as shown in Figure 5.14.

A comparison of the current-field characteristics is shown in Figure 5.16 (a). We find that the $\text{Expon}_{\text{low q}}$ roughness distribution provides generally higher currents than $\text{Expon}_{\text{high q}}$ and Gauss. This can be attributed to the shorter lifetime of the upper laser state due to enhanced roughness scattering with large momentum transfer, which facilitates the transfer of carriers through the device. The trend is the same in both simulation schemes, albeit the currents from the NEGF model are generally smaller than the DM results. Note that the field for the experimental data does not take into account any possible bias drop in contacting regions, which would reduce the field slightly. Thus, comparison with experiment cannot clearly support a certain model.

Now we consider the simulated peak value of the gain as a function of applied electric field, displayed in Figure 5.16 (b) and the gain spectrum presented in Figure 5.17, where we also show experimental results. Due to a lack of direct gain measurements, the experimental results are deduced from

luminescence measurements published in Ref. [76]. Here we find the highest gain for the Gaussian roughness, somewhat lower values for $\text{Expon}_{\text{high q}}$ and relatively low gain for $\text{Expon}_{\text{low q}}$. Again this can be directly attributed to the lifetime of the upper laser state, which is central for the inversion. Quantitatively, the NEGF model provides an inversion δn of 2.54, 1.14, and 2.33 $\times 10^9 \text{cm}^{-2}$ for the Gauss, $\text{Expon}_{\text{low q}}$ and $\text{Expon}_{\text{high q}}$ distribution, respectively, at an electric field of 50 kV/cm. The linewidth γ for NEGF and DM model, as well as for experimental data from Ref. [76] is presented in Figure 5.17. The key contribution to the gain $\delta n/\gamma$ suggests for the NEGF model a reduction in gain by 53% ($\text{Expon}_{\text{low q}}$) and an increase by 9% ($\text{Expon}_{\text{high q}}$) of the peak gain compared to the Gaussian distribution. This reflects the trend in the full NEGF calculations at 50 kV/cm, where the corresponding relative changes are a reduction by 42% ($\text{Expon}_{\text{low q}}$) and an increase by 10% ($\text{Expon}_{\text{high q}}$), respectively. γ is dominated by intra-subband scattering with low q, hence the similar γ for the Gauss and $\text{Expon}_{\text{low q}}$ distributions. $\text{Expon}_{\text{high q}}$ has a lower γ, as expected from the lower $f(q)$ at low q. From this reasoning, the $\text{Expon}_{\text{low q}}$ distribution is expected to have the largest γ, however this is only the case for the DM simulation. For the NEGF we find that Gauss results in a somewhat higher value, for which we currently have no clear explanation. The large γ values for the experimental data are not fully understood, we would therefore propose a comparison with direct gain measurements.

A gain of $\sim$9 cm^{-1} is required in order to overcome the total losses of the experimental sample [80], and this is observed at the experimental threshold field of 48 kV/cm. All three roughness distributions agree reasonably with the experimental threshold current density, the Gauss and $\text{Expon}_{\text{high q}}$ requiring slightly higher losses and the $\text{Expon}_{\text{low q}}$ slightly lower, and both

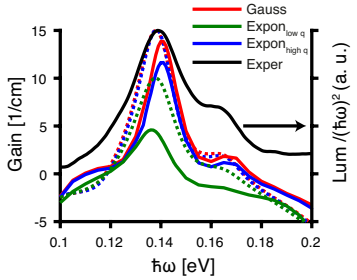

	NEGF γ [meV]	DM γ [meV]	Experiment γ [meV]
Gauss	14	17	
Expon low q	13	18	
Expon high q	12	15	
Exper.			25

Figure 5.17: Gain spectrum at 50 kV/cm of the QCL in Ref. [76] for the DM (dashed lines) and NEGF (full lines) simulation schemes and different roughness distributions given in Figure 5.14 a). The luminescence result from Ref. [76] (black) at 53 kV/cm is corrected using the einstein coefficients.

the DM and NEGF models provide the same threshold field when the same distribution is employed. Finally, we note that the DM model provides significantly larger gain than the NEGF model at higher fields. The reasons therefore are discussed in the previous section. Similar output powers are found if gain saturation is considered [80].

We have studied the relevance of different distribution functions for the interface roughness in QCLs. In principle, exponential distribution functions provide a slower decay of scattering with increasing transition wave-vector q, compared to Gaussians, which is a result of the finite slope of the spatial correlation function at the origin. We find that for mid-IR-QCLs, the scattering at large $q \gtrsim q_{\text{lasing}}$ values is most important and that the results for Gaussian and exponential distribution functions are comparable, if they provide similar matrix elements in this region. These findings are recovered by different simulation schemes, which demonstrates that they hold beyond specific approximations in the respective models.

Chapter 6

Short Wavelength: Active Region Design and Growth

The region from 3 μm to 5 μm, situated in the first atmospheric window, is of particular interest for spectroscopic applications. Trace gas detection with an accuracy of ppb or ppt is possible for nitrous oxide, nitrogen dioxide, carbon dioxide, carbon monoxide, hydrogen cyanide, formaldehyde and molecules containing the methyl group [105]. Hydrocarbons like methane, ethane or formaldehyde could be measured with a high sensitivity (ppt) at this frequency range. Applications for detecting propane and butane were demonstrated by EMPA using devices around 3.3 μm [106]. This short wavelength sources enhance the possibilities for leak detection in industry, environmental monitoring and sensing for medical purposes.

Semiconductor laser sources emitting in the 3 μm wavelength region include Interband Cascade Lasers (ICLs), Interband Diode Lasers and Quantum Cascade Lasers (QCLs) [16].

ICLs have made huge progress in terms of temperature performance, mode stability and threshold reduction. Single-mode emission for a temperature range of 60 °C [107], power

dissipation at threshold (134 A/cm^2, 400 mA) of 95 mW at room-temperature [108] and continuous-wave operation with 10 mW of output power [109] were presented around the 3.5 μm wavelength range. Interband cascade lasers (ICL) have been presented with distributed feedback (DFB) emitters [107]. The grating, placed on top of the waveguide, was fabricated using e-beam lithography.

Type I diode lasers have shown continuous-wave room-temperature emission [110, 111] with threshold current densities of 300 A/cm^2 (0.6 A) and output powers reaching more than 100 mW. They also achieved continuous-wave operation at 3.2 μm wavelength [112].

The devices mentioned above exploit interband emission, but the spectral range around 3 μm can be covered using intersubband transitions with a quantum cascade laser (QCL) [44] as well. QCLs have also been subject to performance improvements. One very attractive feature is the fact that the InGaAs/AlInAs material system on Indium Phosphide (InP) substrate is widely used in the telecommunication industry, processing techniques are now established and buried heterostructure techniques are well developed. Lasing operation has been shown at a wavelength around 3 μm by different groups using different material systems [113, 114]. Laser operation at 3.05 μm was shown at 80 K using different well materials for the upper and lower lasing state [115]. Emission down to 3.15 μm was reported [72, 116]. Lasers on a Sb-free material system showed watt-level emission at room-temperature. More recently, room-temperature continuous-wave operation was reported at 3 and 3.2 μm [117].

Output powers in pulsed operation have reached Watt level for QCLs working in this wavelength range [116, 118–121]. Pulsed lasing until 127 °C and continuous-wave operation until 55 °C was

presented [113,117,121]. A broad spectral coverage can be achieved with heterogeneous active regions, e.g. covering the spectral range from 3 to 4 μm [122].

In Section 6.1 we will investigate the growth quality and performance of different barrier designs for short wavelength emission. Different regrowth temperatures are tested in Section 6.2. Both projects were done in collaboration with Martin Süess, Selam Nida and Mattias Beck. Application examples of low dissipation lasers will be given in Section 6.5 and results from dual-grating designs are explored in Section 6.6.

6.1 Symmetric versus asymmetric quantum cascade laser design emitting at 3.2 μm

The short wavelength range (3 μm-5 μm; 250 to 410 meV) cannot be addressed by lattice matched materials. The conduction band offset of the Indium Gallium Arsenide (InGaAs)/Indium Aluminium Arsenide (AlInAs) material system amounts to 520 meV. In order to accommodate the optical transition and the miniband, a band offset exceeding 500 to 820 meV is needed. Therefore, in the design presented in Ref. [72] compressively (1.3 %) strained InGaAs(28 % Ga) and tensile (3.5 %) strained Aluminium Arsenide (AlAs) layers are used. The conduction band offset amounts to 1.4 eV.

As these two strained materials are grown right after each other, there is a high amount of local strain in the active region (bandstructure presented in Figure 6.1 a)). We propose a step-barrier design shown in Figure 6.1b). A 2-3Å lattice matched AlInAs buffer is inserted between the regions of high strain. The AlAs and InGaAs layers were adapted accordingly. The AlInAs buffer on each side of the AlAs barrier creates a

symmetric bandstructure (see Figure 6.1 b)) we will therefore call it "symmetric design". The reference structure in Figure 6.1 a) has AlInAs layers only on one side of the AlAs barriers for the extractor region and will be named "asymmetric design".

The additional barrier layer lead to a higher spatial separation of upper laser level (ULL) and lower laser level (LLL), and slightly more diagonal optical properties. The asymmetric design has a simulated gain coefficient of 1.4 cm/kA, slightly better than the symmetric design which shows 1.0 cm/kA. Additionally the threshold current density is decreased with 2.8 and 3.2 kA/cm^2 for the asymmetric and symmetric design, respectively. This can also be seen in the gain-current density-voltage curve (GIV) and light-current density-voltage curve (LIV) presented in Figure 6.2. A summary of the performance parameters is given in Table 6.1. The performance differences between the asymmetric and symmetric design are due to slight mismatch in the electron wavefunctions.

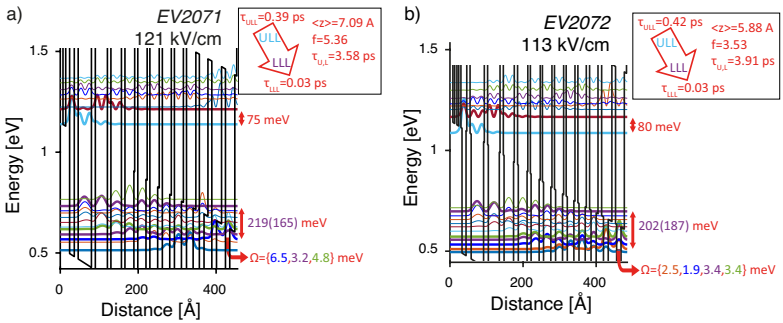

Figure 6.1: Band diagrams and the squared electron wavefunctions offset by their energy. Additional parameters of the design as described in Section 3.1.1. a) asymmetric 3.3 μm design (Appendix B.2). b) symmetric 3.3 μm design (Appendix B.3).

3.3 μm		asymmetric	symmetric
		EV2071	EV2072
electron sheet density	10^{10} cm^{-2}	50	50
period length	A	446	475
max WP	%	37.0	23.52
Slope Efficiency	W/A	11.00	10.09
Gain Coefficient	cm/kA	1.42	1.01
τ_{eff}	ps	0.39	0.42
η_{tr}		0.93	0.93
Transparency Current Density	kA/cm^2	0.96	0.94
Threshold Current Density	kA/cm^2	2.79	3.20
Jmax	kA/cm^2	>10.06	19.47
emission	μm	3.4	3.3

Table 6.1: Performance Parameter from Simulations.

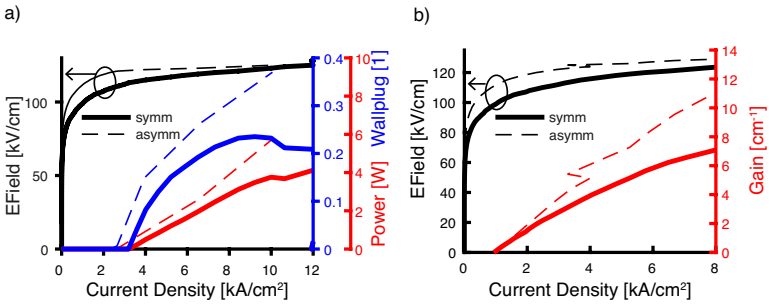

Figure 6.2: Simulated a) LIV and b) GIV for the asymmetric and symmetric design in dashed and continuous line, respectively.

6.1.1 Growth Analysis

The use of strain-compensated material demands a good growth quality. Since our first publication of 3.3 μm emission [72], we constantly improved strain compenzation and defect quality. The Transmission Electron Microscopy (TEM) analysis of grown layers delievered important information about material composition, interface quality and stacking faults [64]. Different seed areas of stacking faults could be identified (see Figure 6.3) and addressed

separately. Strain-balancing and growth temperature was further improved on the side of the Molecular Beam Epitaxy (MBE) growth.

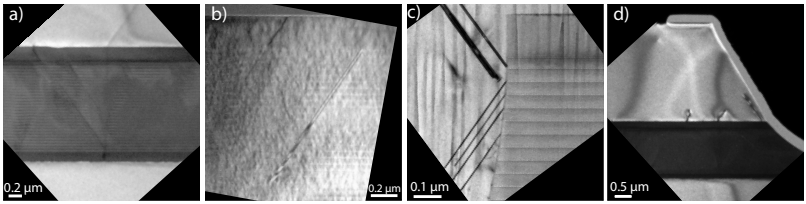

Figure 6.3: TEM images of dislocation defects. 1) at Beginning of growth, propagating through the QCL structure 2) in middle of structure 3) at lateral regrowth interface 4) at cladding regrowth interface. Figures courtesy of Martin Süess and Selam Nida.

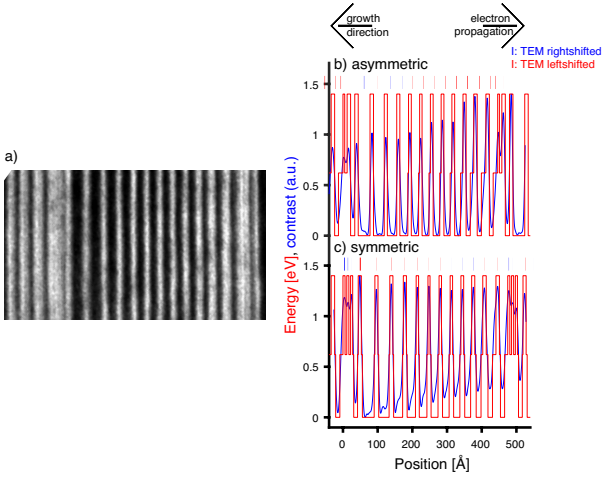

Figure 6.4: a) TEM picture of the asymmetric design. AlInAs layers are grey, InGaAs layers black. Figure taken from Ref. [64]. b) Averaged contrast from a) compared with the bandstructure design. c) same for the symmetric design. Over the barriers a blue/red bar indicates the shift of the micrograph with respect to the bandstructure design to the right and left respectively.

A TEM image of the asymmetric design is shown in

Figure 6.4a). All layers including the composite barriers (as small as 5Å) are distinguishable, the growth showed a low amount of defects. In both cases, the periodicity and the position of barriers and wells agree well with the design. We can connect the image contrast to either Ga or Al, the latter is chosen for its higher sticking coefficient. If we assume that the brightness is linearly connected with the Al-concentration of the layer, we can overlay averaged TEM-Data with the basis potential. This is seen in Figure 6.4b) and c) for asymmetric and symmetric design, respectively. As this measurement is dependant on the contrast setting and sample alignment of the TEM we restrict ourself to qualitative comparison. The symmetric design should lead to a lower skew factor of the wells and the barriers of the structure, additionally the highest contrast peak should be more centered in the composite barrier. The spatial difference between center of the barrier and contrast peak is shown as blue or red bar on top of the barriers in Figure 6.4b) and c). Both assumptions for the symmetrical design could not be conclusively verified on the dataset.

6.1.2 Results

In order to characterize this active region designs further, we measured the spontaneous electroluminescence from both wafers, processed in normal ridge configuration [65]. The active region contains 30 periods and is doped 66 and 64 $\times 10^{10}$ cm^{-2} for the symmetric and asymmetric sample, respectively. The cladding consists of (0.02 / 2.5 / 0.85) μm InP doped with (5 / 0.2 / 30) $\times 10^{17}$ cm^{-3}. For each wafer 380 μm long ridges from different wafer positions were measured below threshold. The result for the asymmetric sample is shown in Figure 6.5. The color corresponds to a radial region of the wafer which is indicated

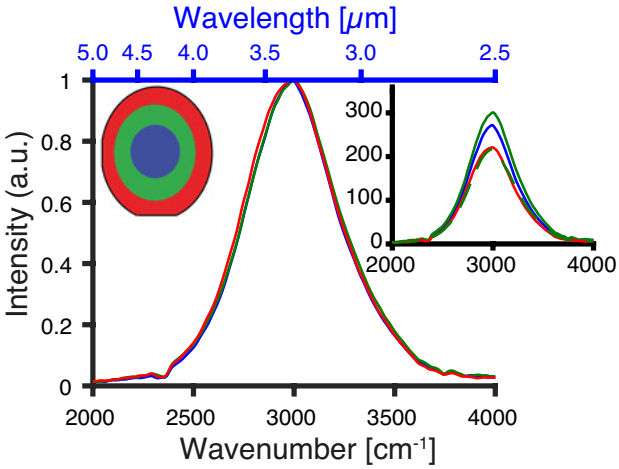

Figure 6.5: Measured spontaneous electroluminescence of asymmetric design at different positions of the wafer at 16 V. The emitters are 380 μm long normal ridge devices measured through the laser facet. The absolute intensity (inset) changes non-reproducibly with position.

in the wafer scheme. While normalized data is reproducible across the wafer for both samples, the absolute value of the spontaneous electroluminescence seems not to be comparable. The absolute intensity changes with the position on the wafer, but also within the radial position. The divergence with respect to wafer position might depend on thickness variations and local strain level. Interestingly the middle of the wafer does not give the highest absolute emission and a slightly broadened curve, even as the MBE growth quality is optimized at this region.

The shape of the electroluminescence gives valuable information about optical transitions [76]. In Figure 6.6 we see the normalized spontaneous electroluminescence of the symmetric and asymmetric sample. Apart from the main transition, the symmetric design shows additionally a small contribution at low

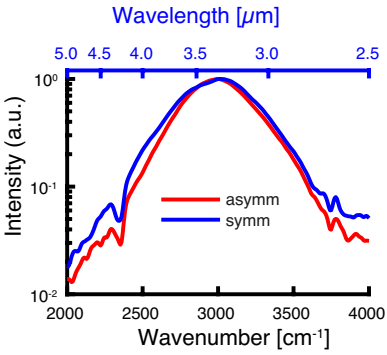

Figure 6.6: Measured spontaneous electroluminescence of asymmetric and symmetric design at 18 V. The emitters are 380 μm long normal ridge devices measured through the laser facet.

wavenumbers. This might be a contribution of the ULL to the state above the LLL (see Figure 6.1). Furthermore the interface quality is directly related with the width of the electroluminescence. As the symmetric sample has considerably more interfaces compared to the asymmetric one, we expect a broader electroluminescence curve. The measured data (shown in Figure 6.6) confirms this with a width of 630 cm^{-1} and 620 cm^{-1} for the symmetric and asymmetric sample, respectively.

While the simulation predict a small performance advantage for the asymmetric sample compared to the symmetric one, the measured LIV (Figure 6.7) shows a clear improvement. We would like to remind the reader that the simulations are done with the parameters indicated in Table 2.2, which do not coincide with the measured devices. Only comparative analysis is possible. The threshold of the asymmetric sample is less than half compared with the symmetric measurement. The slope efficiency is 780 mW/A and 203 mW/A, respectively. The symmetric sample shows the band alignment at a lower voltage, as

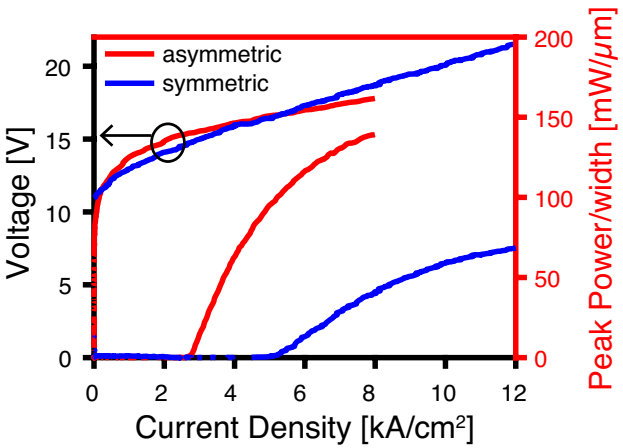

Figure 6.7: Measured LIV of the asymmetric and symmetric design at -20 °C in pulsed operation. The laser are processed in normal-ridge configuration, high-reflective-coated on the back facet, dimensions are (4.6 mm×23.5 μm) and (3.8 mm×18 μm) for the asymmetric and symmetric sample, respectively.

predicted by simulations, but also considerable more leakage with a rollover around 12 kA/cm^2 instead of 8 kA/cm^2. To overcome the leackage problem, further comparison was carried out at different Metalorganic Vapor Phase Epitaxy (MOVPE) growth temperatures.

6.2 Temperature study at 3.2 μm

The growth temperature of short wavelength QCL is 495 °C, as previous publications showed that higher temperatures lead to relaxed active region materials [116]. This temperature adaptation was a necessary step for showing the short wavelength laser emission on the InGaAs/AlInAs/AlAs material system [72] in our group. The performance impact of MOVPE regrowth temperature on the other hand is not published so far and will be studied in the following. We use the symmetric and asymmetric design

at 3.3 μm (Section 6.1) and processed them in normal ridge configuration, the process steps are presented in Ref. [65].

A elevated growth temperature during regrowth can lead to the propagation of dislocations and stacking faults in the heterostructure. The density of seed defects depends strongly on the total strain of the sample. Additionally, at the semiconductor interfaces interdiffusion can occur. The intermixing between barrier and well materials leads to a broadening of the optical transition. Smoothing of the interfaces on the other hand reduces the interface roughness.

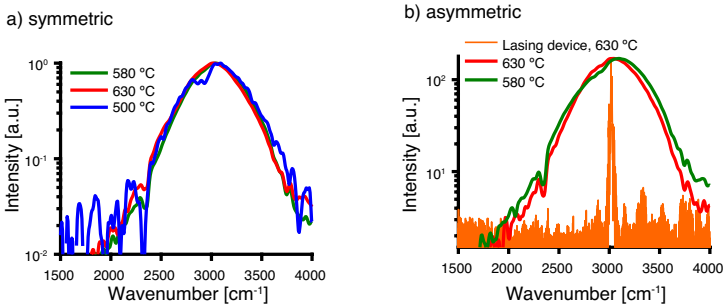

Figure 6.8: Measured spontaneous electroluminescence of a) symmetric and b) asymmetric design at different growth temperatures at 16 V. The emitters are 250 - 380 μm long normal ridge devices, measured perpendicular to the ridge, the side is lapped with a 45 ° angle to increase the signal. The device for the asymmetric sample at 630 °C is measured through the laser facet.

In Figure 6.8 a) the spontaneous emission for the symmetric design is shown, the cladding regrowth took place at three different temperatures: 500, 580 and 630 °C. All three samples are from the same MBE growth. Figure 6.8 b) gives the same results for the asymmetric active region design. For both, the symmetric and asymmetric design, the width of the emission is broader for the regrowth at 580 °C and in the symmetric case further broadened for the 500 °C regrowth. A narrow spontaneous emission is a

sign of good growth quality and low period to period variation, but a broadened emission can also be a sign of additional optical emission. The latter is excluded as the active region design and the driving conditions are the same.

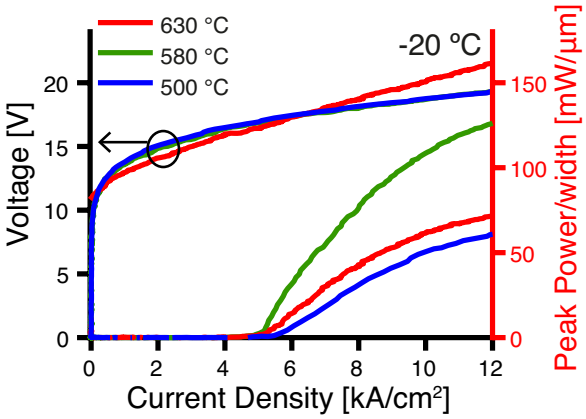

Figure 6.9: Measured LIV of symmetric design for different growth temperatures measured at -20 °C. The lasers are with high-reflectivity-coated back facet and have dimensions of (3.8 mm×18 μm), (3.37 mm×15 μm) and (3.0 mm×13 μm) for 630, 580 and 500 °C respectively.

The LIV of the symmetric design is shown in Figure 6.9. As seen in the previous section, the 630 °C measurements suffer from current leakage, the performance thereof is underestimated. For the symmetric design it seems that 580 °C is the optimum growth temperature, but for the asymmetric design the 580 °C process showed no lasing operation, even after high-reflectivity coating. Taking the leakage problem into account, a regrowth temperature of 630 °C gives the better results. For the asymmetric design we found better threshold current densities and slope efficiencies (see Figure 6.7), therefore we will keep the asymmetric design for the

rest of the chapter.

As the temperature adaptation of the MOVPE process is accompanied by adjusting many other process parameters like gas flows and it's ratios, we cannot completely exclude that these results are influenced by different regrowth qualities.

6.3 Leakage to X,L-Valleys

For the material system used in this chapter the X and L-Valley of the bandstructure are located 650 and 510 meV [123] above the conduction band edge, while the ULL is placed at 610 meV. As mentioned in Ref. [117] leakage into the X,L-valleys might lead to decreased performance.

The separation between the Γ and L-Valley is sensitive to the strain of the material and it increases in tensile strained thin InGaAs-Layers [124]. To investigate the influence on laser performance, we modify the injector region of a design lasing at 3.4 μm ("low strain"). In the last 4 Barriers, a submonolayer thickness of 1Å is transformed from AlInAs into AlAs. Due to the exchange of lattice matched AlInAs to tensile strained AlAs we change the average lattice strain, while keeping the electron wavefunctions nearly the same (see Figure 6.10). The optical properties changed by less than 5 %. As a consequence the simulated LIV of both designs overlap, as presented in Figure 6.11 a). In order to verify that the active region design is similar we kept the electron sheet density for both designs at 50×10^{10} cm^{-2} (continuous line). In grown structures the electron sheet density was 41.6×10^{10} cm^{-2} and 52.9×10^{10} cm^{-2} for the "low strain" and "high strain" sample. The material composition ($In_{0.72}Ga_{0.28}As/Al_{0.48}In_{0.52}As/AlAs$) and the active region thickness of the two samples is the same.

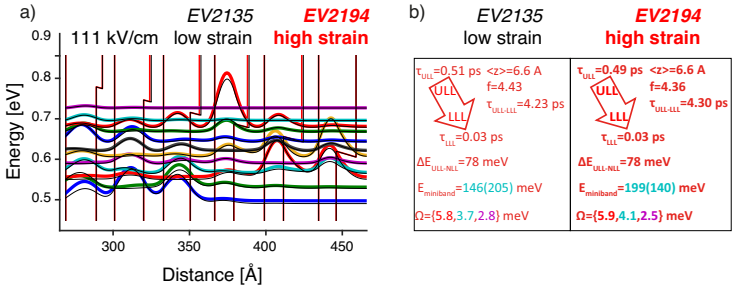

Figure 6.10: a) Band diagrams and the squared electron wavefunctions offset by their energy. The "high strain" sample is shown in thick, colored lines, the potential is shown in red. The "low strain" sample is overlayed in thin black lines for better comparison. Shown is only the injector, where 1Å of AlInAs is transformed into AlAs. b) Additional parameters of the designs as described in Section 3.1.1.

The samples are processed in buried inverted buried heterostructure (BiBH) configuration and mounted epi-side up on copper submounts. A high-reflective coating is applied on the front and back facets. Power measurements are taken with a thermopile detector.

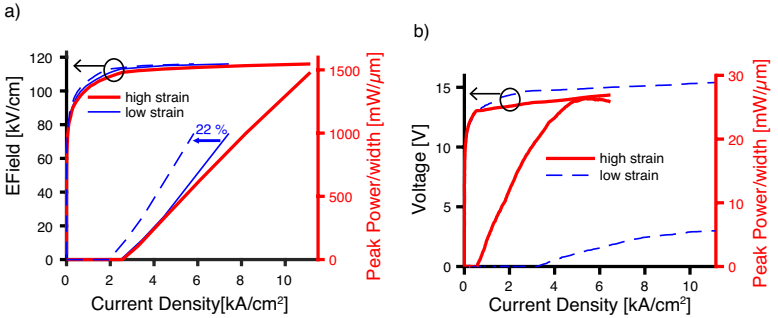

Figure 6.11: a) Simulated LIV of low strain and high strain sample with the same electron sheet density (50×10^{10} cm^{-2}). A 22 % reduction in current density is indicated in dashed blue line. b) Measured LIV at -20 °C for the "low strain" and "high strain" samples, the electron sheet density is 41.5 and 52.9×10^{10} cm^{-2} and the dimensions are (0.5 mm × 3 μm) and (1.5 mm × 4.0 μm), respectively. The power is normalized by the width of the device.

The comparison of the LIV measurements is shown in Figure 6.11 b). Despite the decrease in electron sheet density of 22 % the current of the "low strain" sample increased by a factor of 5. We suspect that part of the doping from the "high strain" device is occupying states in the X and L valley, therefore absorption to this states is reduced. The threshold current density of the "high strain" ("low strain") sample is 0.6 (3.0) kA/cm^2. The slope-efficiency, 650 (205) mW/A, and peak power increased significantly for the high strain sample. We attribute this to reduced current leakage into the X and L valley, the carriers are now available to populate the ULL and therefore increasing the efficiency of the laser. The simulation for the "low strain" design predict a linear increase in gain with respect to the current density up to 6 kA/cm^2. Nevertheless, assuming that a considerable amount of carriers escape from the ULL to the X and L valleys, the gain would be considerably reduced and gain starving of the "low strain" sample should be considered as well. In contrast to the simulations, the lasing threshold of the "low strain" sample might lie in the non-linear part of the GIV. Therefore sufficient gain for short and narrow devices is not available. The discrepancy between the doping density and the maximum current density was observed also for other growths emitting around 3 μm and is not fully understood.

6.4 Growth of full monolayer structures

The growth of III-V semiconductor material via MBE occurs due to the condensation of III-V compounds on the surface. The height of the smallest compound in the zincblende crystal structure is a Monolayer (ML) the thickness thereof is half a lattice constant. For lattice matched materials the ML thickness and lattice constant are given by 2.9344 and 5.8687Å. In case that the material is changed

while the surface plane is only partially filled with ML sized islets, the surface is filled up with the subsequent growth material. A sketch of this process is shown in Figure 6.12 where the grown atoms are presented as circles in a 2D projection, for simplicity we neglect non-uniformity due to strain. In the presented case at the interface only half a ML is filled by AlInAs, the rest is composed by InGaAs, the subsequent growth material. This might induce a significant amount of roughness, in the order of a ML height, as the plane perpendicular to the growth direction is filled with two, randomly distributed ternary materials. The interface between two materials in Figure 6.12 a) is located at 0, the orange line follows the roughness created there. Partially filled layers might cause significant scattering losses.

The period to period roughness might increase as well, if the total active region period thickness is not a multiple of the ML thickness. This will be explained in the following generic example illustrated in Figure 6.12 b). We investigate an active region design with period length N+3/4 ML, and the first layer in this period, named A, with a layer thickness of 1 ML. N is a integer number. We will investigate the interfaces of A over several active region periods, assuming that the growth starts on a planar layer and growth uncertainties can be neglected. At the beginning of the growth the two interfaces of A are perfectly filled ML, the interface roughness is only due to intermixing and defects. In the second period the previous layer occupies 3/4 of the ML surface, the layer A will fill the rest of the plane, as the layer is a full ML, we find that on both interfaces of the layer A the materials are distributed with a ratio of 1:3. The interface roughness increases due to the partially filled planes. At the beginning of the next period the filling level will be 1/2 of a ML, so both materials, from A and from the previous layer, can be found with a probability of 50 %.

For this filling level we expect the highest contribution of interface roughness due to partially filled ML. Even as the layer consists of ML thickness, the averaged interface roughness of the active region is increased compared to a full ML design. As the average layer thickness is not changed, we do not expect a shift of the gain peak, but a broadening of the lasing transition.

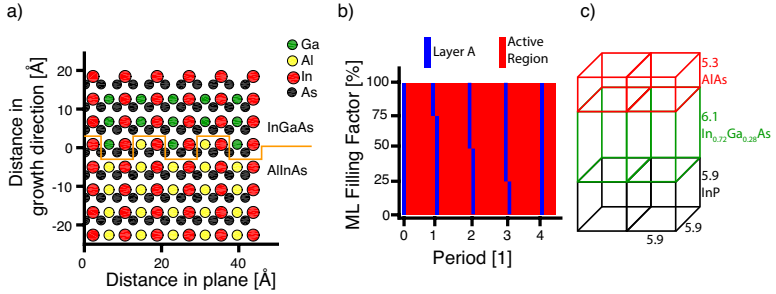

Figure 6.12: a) Schematic representation of a interface roughness. A 2D-projection of the growth cross section is shown with atoms represented as filled circles. The interface is located at 0 the material is color-coded with Indium in red, Gallium in pink, Aluminium in blue and Arsenic in black. The orange line follows the roughness around the interface. b) Schematic representation of period-to-period interface roughness fluctuations. c) Scheme of the unit cells for strained materials.

To verify this, we propose a sample specifically designed to completely fill the planar layers. Here we will neglect the restrictions of precision during the growth which are mainly given due to the shutter closing (about 0.2 s uncertainty), during this time 0.6Å can be grown. In the present case we use strained materials, therefore the in-plane lattice constant is matched with the lattice constant of InP, the ML height is calculated according to the material composition (see Table 6.2, Figure 6.12 c)). As reference we take the asymmetric design from Section 6.3 and present a similar full ML version, the bandstructure can be found in Figure 6.13. The well and barrier layers of the reference design are as thin as one ML, especially around the part where the optical

material	relaxed lattice constant	vertical extention on InP=2xML
InP	5.8687	5.8687
$In_{0.72}Ga_{0.28}As$	5.9449	6.1003
$Al_{0.48}In_{0.52}As$	5.8687	5.8687
AlAs	5.6608	5.2668

Table 6.2: Calculation of the out-plane lattice constants.

transition takes place. The performance and spectral parameters could not be matched completely in a full ML version. We see a difference especially in the ULL lifetime (Figure 6.13). There is a slight spectral shift of the gain peak position (not shown) from 3.4 to 3.5 μm for the full ML design. We present the LIV and GIV in Figure 6.14 a) and b). The power and gain dependence on current overlaps reasonably well for the two designs. Furthermore, as the miniband thickness varies, the ML design works at lower electric fields (Figure 6.14). Despite this small differences, we expect a clear difference in the width of the spontaneous emission of these structures and maybe also in the laser performance.

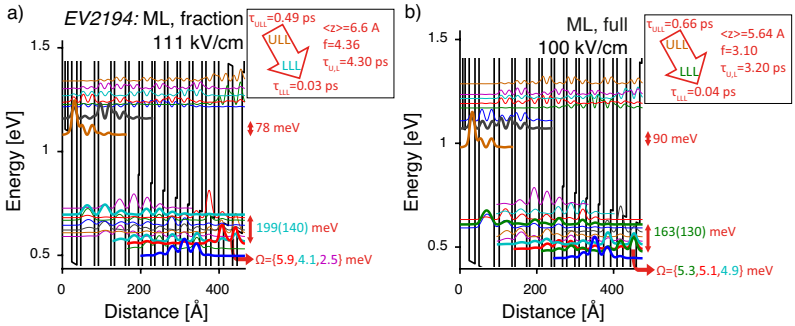

Figure 6.13: Band diagrams and the squared electron wavefunctions offset by their energy. Additional parameters of the design as described in Section 3.1.1. a)3.4 mum μm ML fractions (Appendix B.5). b) 3.4 mum μm full ML (Appendix B.6).

The active region has yet to be grown.

3.4 μm		ML fraction	full ML
electron sheet density	10^{10} cm^{-2}	50	50
period length	A	457	466
max WP	%	37.18	36.14
Slope Efficiency	W/A	12.12	12.05
Gain Coefficient	cm/kA	1.37	1.37
τ_{eff}	ps	0.49	0.65
η_{tr}		0.94	0.94
Transparency Current Density	kA/cm^2	1.46	0.46
Threshold Current Density	kA/cm^2	2.94	2.66
Jmax	kA/cm^2	>12.75	>11.15
emission	μm	3.4	3.5

Table 6.3: Performance Parameter from Simulations.

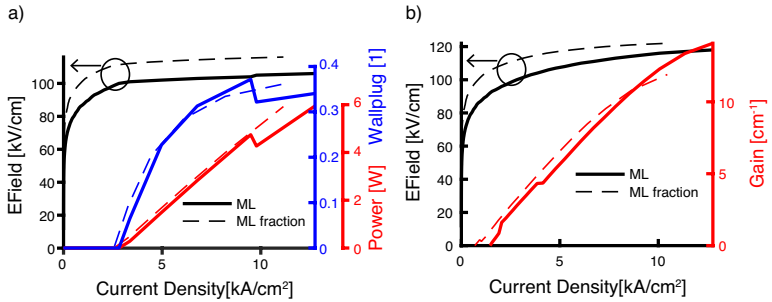

Figure 6.14: Simulated LIV and GIV for the ML fraction and full ML in dashed and continuous line, respectively.

6.5 3.36 μm Single-Mode Quantum Cascade Laser with a Dissipation below 250 mW

The performance improvements from this Chapter and Chapter 4 lead to a 3.36 μm BiBH distributed-feedback Quantum Cascade Lasers with a power dissipation at threshold below 250 mW and operation temperatures are as high as 130 °C. We will present the fabrication of ridge width as narrow as 1.7 μm. The optical performance and temperature dependence of our devices is shown in pulsed and continuous-wave operation. We

realized single-mode emission in pulsed and continuous-wave operation and present the single lobed laser far-field. Single-mode performance is demonstrated in long pulse (5.56 μs) operation. This work was published in Ref. [71].

For QCLs, mode selection was published by other groups at 3.36 μm [125], where a third-order buried DFB grating was corrugated on top of a InGaAs/AlAs (Sb) QCL active region. Single-mode ring-CSELs based on quantum cascade structures were presented with a radial second-order grating at 8 μm [126]. Fabrication was done using e-beam lithography. The devices showed a low beam divergence (8°). A third order unilateral grating has been used by [118] to reach 1 W of output power at room-temperature with a single-mode operation. The same group showed a third order buried grating on InGaAs/AlAs (Sb) [119].

As yet, QCLs suffer from high threshold currents and therefore high dissipation values which is a clear disadvantage for application in portable systems. Thresholds of 620 mA (1.66 kA/cm^2) in pulsed operation and 500 mA (1.4 kA/cm^2) in continuous-wave operation at 3.2 μm at a temperature of 25 °C were presented [117].

Small volume active regions together with optimized active region design and a high facet reflectivity are key factors for low dissipation values in QCLs [127]. Thermal management can be further optimized by using BiBH techniques to achieve low dissipation [19,20]. In the following, we present our new results, a combination of high power, low threshold currents and low power dissipation.

6.5.1 Methods

The QCL active region, presented in this section, is a strain compensated GaInAs/AlAs/AlInAs structure at 3.36 μm (Appendix B.5, grown as "EV2194"), in order to cover absorption lines of molecules containing the methyl group. The active region consists of 30 periods. The thickness of the InGaAs layer on top of the active region, used for the DFB grating, is 200 nm.

The ridges were etched with width from 1 to 4 μm. These narrow ridges help to improve thermal transport and to reduce the threshold currents. The grating was defined by a single optical lithography (deep-UV light at 220 nm wavelength) and wet etched. For an emission wavelength of 3.36 μm, we varied the grating period from 530 to 534 nm using an expected effective refractive index of 3.165. The duty cycle of the grating is 50 % to maximize the coupling strength. The different gratings are formed with one periodicity (single-grating) or as dual-grating (Section 4.3). In a dual-grating, two or more physical grating periodicities are used to form one effective optical grating periodicity, the simplest case of which would be two grating periodicities repeated one after the other, where the effective optical grating periodicity is the average of these two.

The structure was overgrown with an n-doped cladding deposited by Metal-Organic Vapor Phase Epitaxy and consists of several layers of n-doped InP:Si: (0.5 / 2 / 0.2 / 1.85) μm doped (1 / 2 / 50 / 70) $\times 10^{17}$ cm^{-3}. The lasers were processed using the BiBH technique (see Chapter 4, Ref. [64]). The cleaved devices were mounted epilayer-up on copper blocks. The high-reflectivity (HR) coating on the back facet of the lasers is composed of Al_2O_3/Au (300 nm/150 nm) and the front side coating, applied to most lasers, consists of

$Al_2O_3/Ge/Al_2O_3/Ge\,(400\ /\ 230\ /\ 400\ /\ 230)\,nm$ and show a measured reflectivity of 92 %. The measurements were performed on a Peltier cooler. Light-current curves were recorded using a calibrated thermopile detector. Continuous-wave measurements were done with a Keithley 2420 sourcemeter. With this sourcemeter we regularly had current spikes when the current was switched on / off, leading to detrimental voltage applied on our lasers. Therefore, to avoid current spikes, later measurements are performed with a Wavelength Electronics QCL 2000. Spectral measurements with a resolution of $0.075\,cm^{-1}$ were taken by fourier transform infrared spectroscopy(FTIR). The boxcar integrator measurements used a peltier cooled mercury cadmium telluride (MCT) photovoltaic detector exhibiting a cutoff frequency of 250 MHz. The far-fields were recorded using a goniometer assembly and a pyroelectric detector. For the far-field measurements the device was driven in a micro-macro scheme: A burst of 4807 pulses with a pulse width of 208 ns and 2 % duty-cycle where send to the device at an overall repetition rate of 10 Hz. The 10 Hz frequency was used for the lock-in detection.

6.5.2 Results

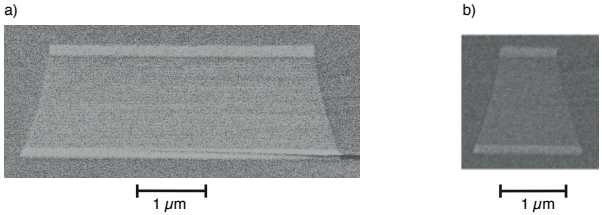

Figure 6.15: (a) SEM picture of the facet of a device with 4.075 μm width and 1.7 μm height. (b) SEM of a narrower device of 1.35 μm width. Figure taken from Ref. [71].

Figure 6.15 shows the front view of cleaved laser facets. In both

cases the height of the active region is 1.7 μm, the average width of the ridge in Figure 6.15(a) is 4.075 μm. The device in Figure 6.15(b) has a narrower ridge, more precisely 1.35 μm.

The narrowest ridge width which shows lasing is 1.13 μm the device is 2.5 mm long and high-reflectivity coated on the back. The threshold current amounts to 94 mA (3.3 kA/cm^2) at 20 °C.

Fabry-Perot Results

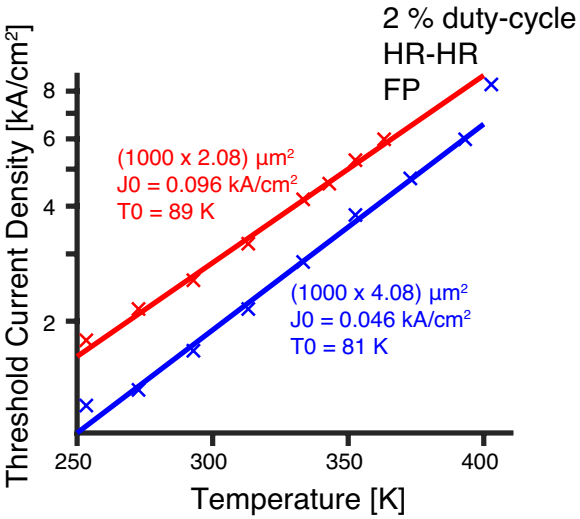

Figure 6.16: Threshold current density as a function of temperature for two Fabry-Perot device. Laser emission was up to 130 and 90 °C, respectively. Figure taken from Ref. [71].

For standard characterization, Fabry-Perot devices were measured. A device with dimensions of 1 mm x 4.08 μm was coated on both facets with high-reflectivity coating. Lasing operation was observed until 130 °C, as seen in Figure 6.16. The threshold data from -20 °C until 120 °C was fitted by the

exponential $J(T) = J_0 \exp(\frac{T}{T_0})$ [16]. The extracted T_0 amounts to 81 K, the J_0 is 46 A/cm^2. Shown is also a second device with a T_0 value of 89 K. The relatively low value of T_0 stands in contrast to much larger T_0 values usually published for QCL. The large discontinuity between the strained $In_{0.72}Ga_{0.28}As$ quantum wells and the AlAs barriers should prevent thermal carrier leakage. Additionally, we see no evidence of significant thermal broadening in the spontaneous emission. Therefore we attribute the low T_0 values to carrier losses towards the X- and L-valleys.

High Temperature Performance

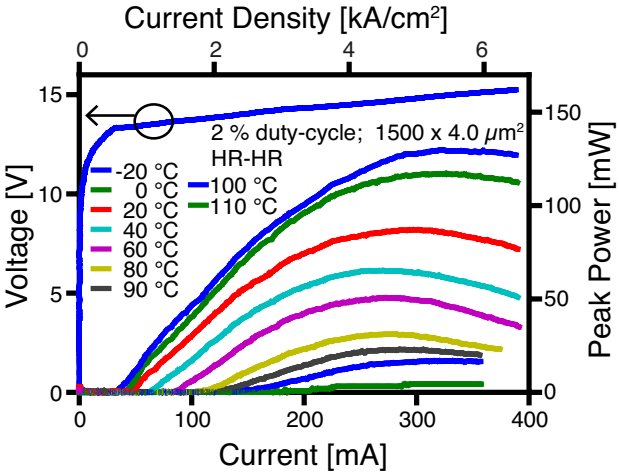

Figure 6.17: LIV of a DFB device for a temperature range of -20 °C to 110 °C in pulsed operation. The dissipation value at -20 °C amounts to 440 mW at a current of 33 mA. The dynamical range of the device at -20 °C amounts to nearly 9:1. Figure taken from Ref. [71].

Figure 6.17 shows the LIV of a pulsed laser over a temperature range of -20 °C to 110 °C. The device is 1.5 mm long and 4 μm wide, with a high-reflectivity coating on both facets. The

power dissipation at -20 °C amounts to 440 mW at threshold. The threshold current is 33 mA (current density of 0.55 kA/cm^2). The device reaches up to 3.8 % wallplug efficiency with a peak power of 130 mW. At 20 °C wallplug efficiency is still 2.9 % and the threshold current increases slightly to 47 mA (0.78 kA/cm^2). For 110 °C, the threshold is 186 mA. This threshold current is more than an order of magnitude lower compared to previously published QCL-devices in the 3 μm range [117,121]. The wallplug is comparable to previous results of 3.1 % at 25 °C for emission at 3.2 μm [117].

A kink in the current-voltage curve clearly indicates the onset of lasing and subsequently a large dynamical range of laser operation occurs, which hints to an efficient current-photon conversion due to photon driven transport. We define the dynamical range as: $(J_{max}(T) - J_{thres}(T))/J_{thres}(T)$ with J_{thres}, J_{max} the current density at threshold and maximum power, respectively. For -20 °C the dynamical range is 9:1 and for 110 °C it decreases to approximately 1:1. Previous devices show roughly a value of 3:1 or lower for the same temperature [67,116]. We attribute our improvement in dynamical range to a better strain-balanced epitaxial growth of the active region and to improvements of the processing which gave straight sidewalls resulting in a more homogeneous field distribution. The device includes a buried distributed-feedback grating (DFB), but due to the mismatch of the gain spectrum and the grating periodicity in this specific device, we observe lasing on FP modes (2720 - 2930 cm^{-1}) instead of the DFB mode (2970 cm^{-1}).

Low Dissipation

For smaller contact area devices the threshold current in pulsed operation is reduced even further, as shown in Figure 6.18. The device has 500 μm length and a laser ridge width of 2 μm.

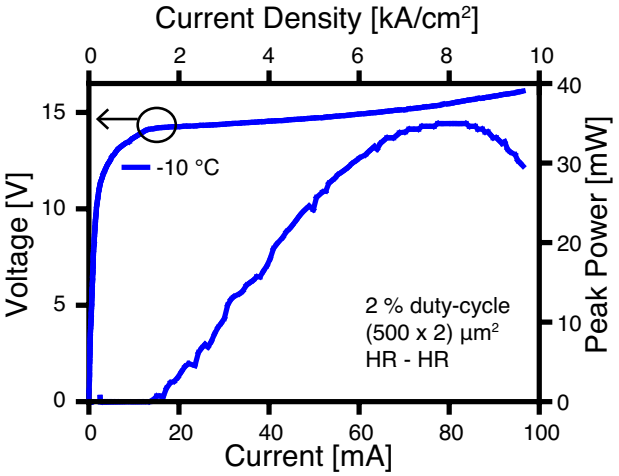

Figure 6.18: LIV in pulsed operation at -10 °C. Dissipation value at threshold is 230 mW for -10 °C. Figure taken from Ref. [71].

Front- and backside high reflectivity coating were applied. The threshold current at -10 °C is decreased to 16 mA (current density of 1.6 kA/cm^2) which corresponds to a dissipation of 230 mW at threshold. The output peak power is up to 35 mW.

Continuous-wave Operation

The lasers were also tested in continuous-wave operation. Figure 6.19 shows lasing up to 15 °C. The device is 613 μm long and 2 μm wide. The back facet of the device was coated with a high-reflectivity coating. The threshold current is 30 mA (2.4 kA/cm^2) at -20 °C and 48 mA (4.3 kA/cm^2) at 15 °C. Peak power is over 10 mW at -20 °C. Even though the thermal conductivity G_{thres} for several devices amounted to values above 1500 W/(K cm^2) and the ridges are very narrow, continuous-wave mode seems to be limited to temperatures below 15 °C. This stands in contrast to very high operation temperatures in pulsed mode.

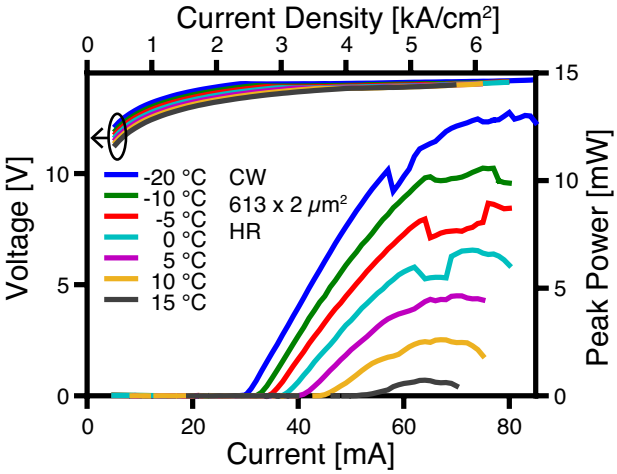

Figure 6.19: LIV in continuous-wave operation from -20 °C to 15 °C. Figure taken from Ref. [71].

We attribute this limitation to a combination of a low T_0-value of these devices and to a strong temperature gradient across the active region. Reaching the maximum operation temperature in the middle of the active region seems to have a detrimental effect on lasing. The maximum operating temperature is given by $T_{\max} = T_0 * \left(ln(T_0 * G_{\text{thres}}/(\delta * J_0 * V_{\text{thres}})) - 1\right)$ [16], where V_{thres} is the voltage at threshold. In our case it amounts to 320 - 340 K for continuous-wave and 650 - 670 K for pulsed operation with a duty-cycle of δ=2 %. Continuous-wave measurements conducted on wider ridges gave low threshold values of 90 mA (1.2 kA/cm^2) at -20 °C but laser operation was possible only until 0 °C, in agreement with our argument above. This problem can be adressed by reducing the number of active region periods. The overlap in the horizontal direction amounts to 80 %, which is higher than the optimum between a high total overlap and a high overlap for the single active region periods [16].

Emission Spectrum

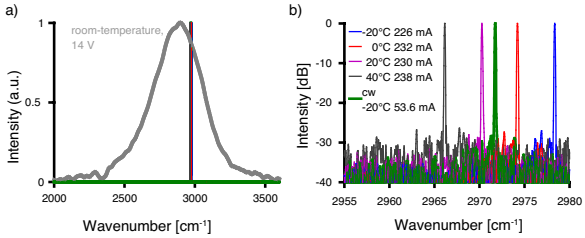

Figure 6.20: (a) Spontaneous emission of the active region at 14 V, measured at room-temperature (bold grey line). The device dimensions are 215 $\times$ 215 μm. Full-width-half-max of the emission amounts to 410 cm^{-1}. Emission spectra of a single-mode DFB laser around 2970 cm^{-1} are shown in linear scale. (b) Zoom of the single-mode spectra in dB-scale. Spectra were recorded up to 40 °C in pulsed operation (2 %) and continuous wave operation at -20 °C. The device is 750 μm long and 4 μm wide and high-reflectivity coating is applied to both facets. Figure taken from Ref. [71].

The bold grey line in Figure 6.20(a) shows the spontaneous emission which was measured on a square mesa. The dimensions of the mesa amounts to 215 $\times$ 215 μm and it was processed along with the lasers presented here. The boundaries of the mesa are etched instead of cleaved to avoid cavity effects. The Full-width-half-max of the spontaneous emission at 14 V is 410 cm^{-1} centered around 2900 cm^{-1} (3.45 μm).

Single-mode operation of the DFB lasers is presented in Figure 6.20(a) and (b). The device is 750 μm long and 4 μm wide. Emission spectra are shown for -20 °C up to 40 °C in pulsed operation and for continuous wave operation at -20 °C. The device is double-side coated with a high-reflectivity coating. The side mode suppression ratio is more than 20 dB. The presentation of single-mode DFB lasers fabricated as already demonstrated in Ref. [67] shows the reproducibility of using optical lithography with dual-grating technique for small periodicities. An effective

refractive index of 3.15 was calculated from several single-mode emitting devices using the relation $\Lambda = \frac{\lambda}{2 \times n_{eff}}$ where Λ is the grating periodicity, λ is the emission wavelength and n_{eff} is the effective refractive index.

Long Pulse Operation

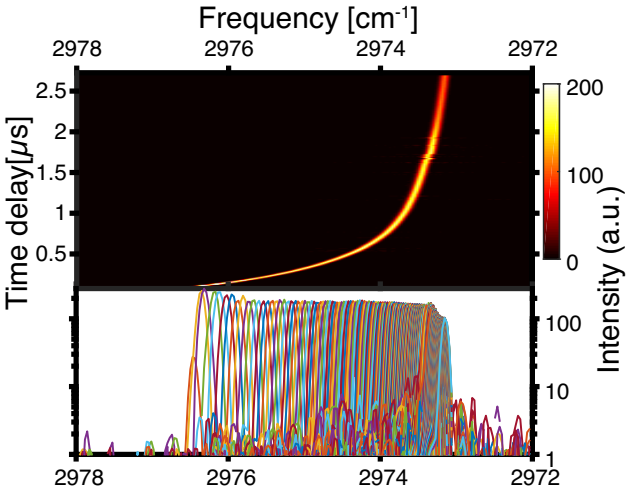

Figure 6.21: Single-mode long-pulse measurements at 10 % dc at a pulse width of 5.56 μs. The measurement was taken at -15 °C. The output power was stable for at least 2 μs and the emission wavelength tuned continuously from 2976 to 2973 cm^{-1}. Top: shows the tuning of the emission wavelength versus time delay (starting from pulse onset). The colorscale gives the signal intensity in arbitrary units. Bottom: Single spectra of the different time slices. Figure taken from Ref. [71].

A particularly interesting method of laser spectroscopy, the intermittent modulation concept [27] is a method whereby the shift of wavelength and long output power stability of a laser during a long pulse is used to scan over a resonance. The signal is recorded with high temporal precision and gives therefore a reference and absorption measurement at the same time.

In order to characterize the behavior of our lasers for longer pulse duration we performed a boxcar integrator experiment. The laser is operated with a long pulse width of 5.56 μs and 10 % duty-cycle. The submount temperature during the measurement was set to -15 °C and the driving conditions of the laser were 39 mA and 13.4 V. The output of the laser is fed through a FTIR and recorded with a MCT detector. A boxcar integrator is used to sample the signal into time slices of 10 ns and a variable delay. The sampled signals with different time delays are individually fed back to the FTIR for spectral measurements. In this way, we are able to get the spectral information attributed to only 10 ns time slices of a much longer pulse. In Figure 6.21 we see this time resolved spectral information. On top we present the frequency shift of the laser during the 5.56 μs pulse. In the first μs, the frequency shifts by more than 2 cm^{-1} due to the heating of the active region. For longer pulse duration the frequency stabilizes around 2973 cm^{-1}. In the bottom we see the time slices spectra plotted in the usual intensity versus frequency plot. The intensity of the spectra gives stable output power for about 2 μs and only then decreases by about one half.

These boxcar integrator measurements also help us to investigate the low maximum operation temperature in continuous-wave mode. By increasing the substrate temperature on the device shown in Figure 6.21 by 15 °C, the laser emission deteriorates quickly in intensity, after 400 ns laser emission ceases to exist. This again underlines our argument of detrimental heating effects.

Far-field Measurements

The far-field of a nearly quadratic ridge facet (1.35 μm width and 1.7 μm height) is shown in Figure 6.22(a). Figure 6.22(b)

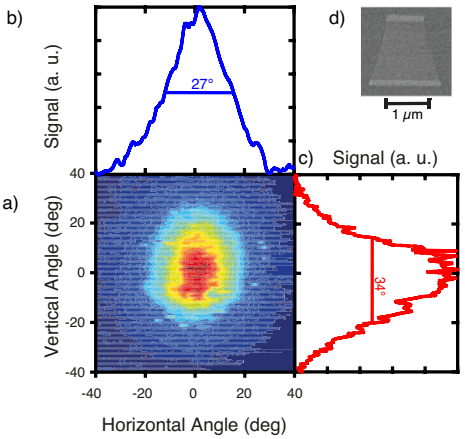

Figure 6.22: (a) Far-field, (b) horizontal cross section and (c) vertical cross section of a 4 mm long laser, (d) SEM picture of the facet. The facet has 1.35 μm width and 1.7 μm height. The laser was operated at -12 °C at 385 mA. The Far-field exhibits a full-width-half-max of 27° × 34°. Figure taken from Ref. [71].

is the horizontal cross-section and Figure 6.22(c) is the vertical cross-section of the far-field. Both subfigures are labelled with the full-width-half-max of the emission. Figure 6.22(d) shows a SEM picture of the laser facet. The far-field shows a single lobed emission with approximately gaussian shape. As expected, the facet exhibits a nearly symmetric far-field pattern with a full-width-half-max of 27° × 34°. Driving conditions were 385 mA at -12 °C. The current was delivered in a micro-macro pulse scheme, using 2 % duty cycle and a 10 Hz lock-in detection.

6.5.3 Conclusion

We present GaInAs/AlAs/AlInAs distributed-feedback QCLs with single-mode emission around 3.36 μm showing low dissipation and a large dynamical range. The devices show threshold current values of 16 mA at -10 °C with a threshold

power dissipation of 230 mW. Another device shows 0.55 kA/cm^2 threshold at -20 °C and still 0.78 kA/cm^2 at +20 °C which is 33 mA and 47 mA, respectively. These values are for pulsed operation, continuous-wave values are 90 mA (1.2 kA/cm^2) and 30 mA (2.4 kA/cm^2) at -20 °C measured on two different devices. Additionally we present single-mode emission on the DFB wavelength for different temperatures in pulsed and continuous-wave operation. Boxcar integrator measurements show mode stability in terms of single-mode operation and output stability during long pulses. The far-field of our narrow ridges give a symmetric pattern with a full-width-half-max of 27 ° × 34 °.

6.6 Distributed-feedback quantum cascade laser emitting at 3.2 μm

We present GaInAs/AlAs/AlInAs QCLs emitting from 3.2 to 3.4 μm. Single-mode emission is obtained using buried distributed-feedback gratings. Devices with single-mode emission down to 3.19 μm were achieved with peak power of up to 250 mW at -20 °C. A tuning range of 11 cm^{-1} was obtained by changing the device temperature between -30 °C and 20 °C. This work was published in Ref. [67]. The work and the publication was executed before the optimization of short wavelength devices presented in this chapter and the optimization of the fabrication (see Chapter 4).

For many spectroscopic applications, mentioned at the beginning of this chapter, a tunable single-mode emission at a previously determined wavelength is required. We present in this work QCL devices fabricated for output wavelength close to 3.3 μm. To achieve a better single-mode yield, a Distributed-Feedback (DFB) configuration with a first-order grating was chosen and realized by means of standard deep-UV contact lithography. This

technique can easily be transferred to industrial production.

6.6.1 Methods

The QCL active region is a copy of the strain compensated structure published in 2011 [72] on a GaInAs/AlAs/AlInAs material system and grown as "EV1695". The thickness of the InGaAs layer on top of the active region, used for the DFB grating, was changed to 200 nm.

The ridges were etched with width ranging from 3 to 7 μm. The grating was realized by partly etching the InGaAs layer. On the top of the etched grating, a n-doped cladding was deposited by MOVPE constituted by 3 μm of n-doped InP:Si (2×10^{17} cm^{-3}) followed by an 80 nm thick InGaAs:Si contact layer (6×10^{18} cm^{-3}). The lasers were processed using inverted buried heterostructure (iBH) technique [45, 76]. The cleaved devices were mounted epilayer-up on copper blocks. Measurements were performed on a Peltier cooler.

The gratings were defined by a single optical lithography (deep-UV light at 220 nm wavelength) and wet etching. They were designed for emission wavelengths between 3.2 and 3.45 μm and contain a quarter-wave shift placed in the center of each laser structure. Because of a mask fabrication resolution of about 10 nm (given by the photomask producer) the gratings for short wavelength devices needs to be adapted. We use only three different grating pitches, namely 2×250, 2×260 and 2×270 nm which would give an emission of 3.2, 3.3 and 3.4 μm, respectively. In order to obtain a specific effective grating period, a combination of two grating pitches ("dual gratings") can be used. For example, a 505 nm effective grating period(Λ_{eff}) could be obtained with 30 periods of a 500 nm grating followed by 10 periods of a 520 nm

grating. A sketch of this grating-design is presented in Figure 6.23.

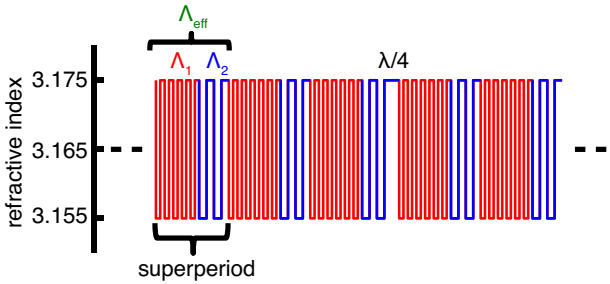

Figure 6.23: Sketch of a dual-grating. Using two grating periods to achieve an effective grating period Λ_{eff}.

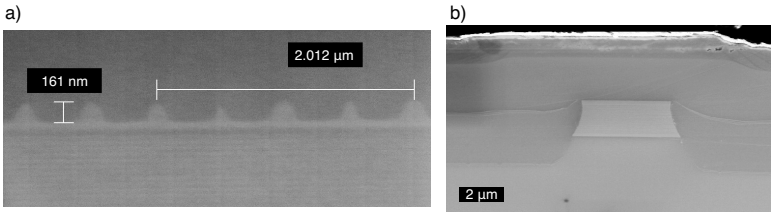

Figure 6.24: SEM pictures. a) A laser facet with a ridge width of 4.2 μm. b) A cross section of the waveguide along the ridge direction. It shows the grating on top of the active region with an etching depth of 160 nm. Figure taken from Ref. [67].

In Figure 6.24 we present the Scanning Electron Microscope (SEM) pictures of the grating (a)) and facet (b)) of a laser. In Figure 6.24 a), a device cleaved along the waveguide is shown it displays the grating on top of the active region. The grating depth is 160 nm and the duty cycle is 25 %. Compared to a 50 % duty cycle, this leads to a reduced coupling constant of the optical mode towards the grating [128]. As can be seen in Figure 6.24 b), the ridge cross section has a quasi-rectangular shape.

6.6.2 Results

The measured spontaneous emission of the active region is shown in Figure 6.25 along with the measured laser spectra from several devices. Spontaneous emission data was taken at room-temperature from a 1.6 mm long device. The device was measured perpendicular to the ridge with an applied voltage of 15.8 V. Laser spectra were measured under different driving conditions at 0 °C in pulsed operation. The spontaneous emission displays a full width half maximum of 621 cm^{-1}, in excellent agreement with the asymmetric sample presented in Section 6.1. The emission shows broad maxima from 3.15 to 3.34 μm. Laser emission ranged from 3.19 to 3.42 μm.

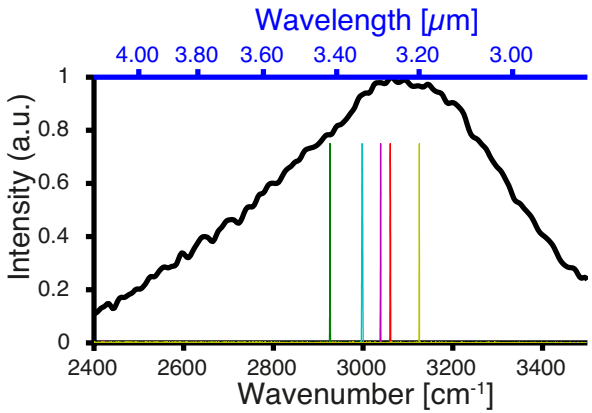

Figure 6.25: Room-temperature spontanous emission of the active region(black) showing a FWHM of 621 cm^{-1} at 15.8 V. Additionally lasing spectra of some devices in pulsed operation under different driving conditions at 0 °C are presented. Figure taken from Ref. [67].

In Figure 6.26 b) we show the stopband of one dual-grating laser with a quarter-wave shift in the middle of the structure. The 2.6 mm x 4 μm device was measured below threshold with

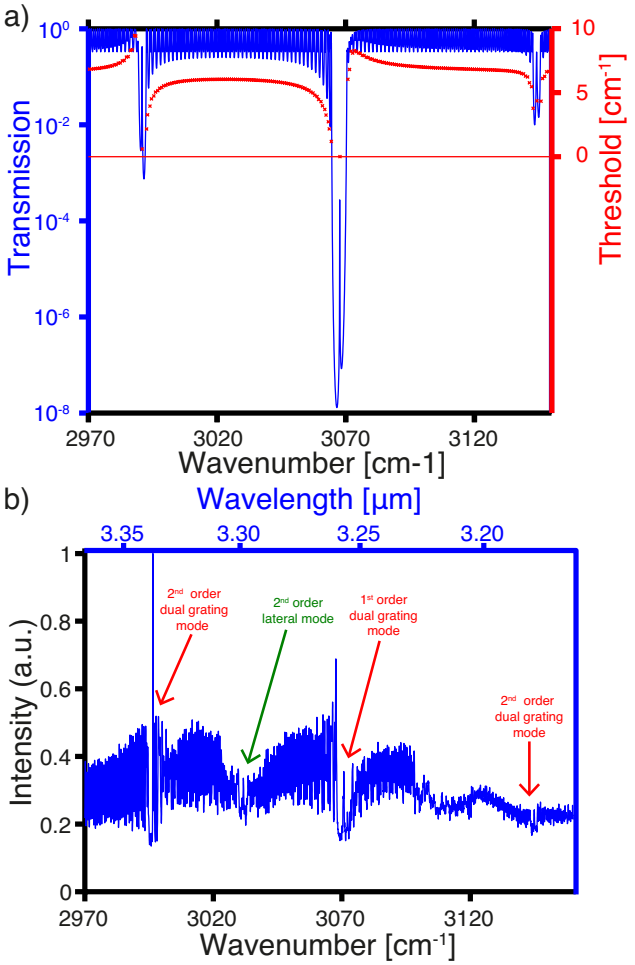

Figure 6.26: a) Transfer-matrix simulation of the transmission and threshold of a 2 mm long dual-grating DFB with an effective periodicity of 515 nm and effective refractive index of 3.165. b) Measured amplified spontaneous emission of a 2.6 mm x 4 μm lasing device with the same dual-grating as the simulation. Figure taken from Ref. [67].

an applied voltage of 14.8 V at 10 °C. It exhibits a spectral width of Δk =6.1 cm^{-1} at 3070 cm^{-1} with a quarter-wave shift mode in

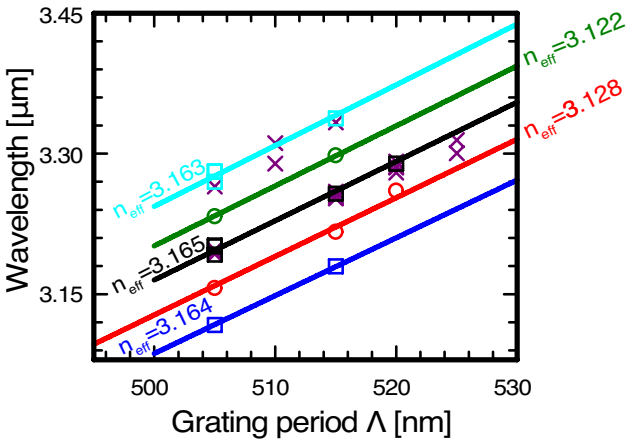

Figure 6.27: Plot of the quarter-wave shift mode wavelengths versus grating period showing the fundamental mode (black), 2nd order dual-grating modes (light blue and dark blue) and 2nd order lateral modes (red, green). The purple crosses mark the lasing wavelengths. Figure taken from Ref. [67].

its center, as predicted by theory [129]. The device was lasing at 3070 cm^{-1}, on the edge of the stopband and at a higher-order mode at 3000 cm^{-1}. The stopband width corresponds to a coupling constant of $\kappa = \pi\, n_{\mathrm{eff}}\, \Delta k\, sin(\pi\, \mathrm{DC}) = 43\,\mathrm{cm}^{-1}$ [128], where the effective reflective index n_{eff} is 3.2 and DC is the duty cycle of the grating. The coupling constant was not optimized for a value of κ L around 1 for the presented device length L, but rather adapted for losses of around 1 cm^{-1} obtained by transfer-matrix simulations.

The additional stopbands at 2990 and 3140 cm^{-1} are due to the design of the grating. The stopbands at 3032 and 3102 cm^{-1} are due to higher-order lateral modes. The presented example includes the periodicities 500 nm and 520 nm with a ratio of 10:30 leading to a superperiod of $L_{superperiod}$=20.6 μm. Therefore additional dual-grating modes of order n appear at wavenumbers of $\pm n \times \frac{1}{2 \times n_{\mathrm{eff}} \times L_{superperiod}} = \pm n \times 75.8\,\mathrm{cm}^{-1}$ around

the fundamental mode [130]. A 2 mm long device was used in the simulations having the same grating design as the device presented in the same figure. The separation to the higher-order dual-grating modes can be adjusted by changing $L_{superperiod}$.

Transfer-matrix simulations (see Figure 6.26 a)) reproduced the stopbands including their quarter-wave shift modes. Not predicted are the additional stopbands at 3032 cm^{-1} and 3102 cm^{-1}. These arise due to higher order lateral modes and as such cannot be retrieved by the 1-D simulation. In order to help distinguish the various mode types the amplified spontaneous emission data of several devices was analysed. Figure 6.27 illustrates the quarter-wave shift mode wavelengths versus grating periods. The 2nd order dual-grating mode has a lower coupling constant, and therefore, a narrower stopband. This is used for differentiating the 1st and 2nd order dual-grating mode. For the retrieval of the 2nd order lateral mode wavelengths, devices with only one grating period were analysed. In these cases the electroluminescence shows 1 or 2 stopbands, which correspond to 1st and 2nd order lateral modes. With this analysis we group the data and approximate with linear fits using the formula for the Bragg wavelength:

$$\lambda_B = 2{n_{\text{eff}}}^i \times (\frac{1}{\Lambda} + j \times \frac{1}{L_{superperiod}})^{-1} = 2{n_{\text{eff}}}^i \times \Lambda(1 + j \times \frac{1}{N_\Lambda})^{-1}$$

(j-th dual-grating mode; i-th lateral mode)

where Λ stands for the effective periodicity in the structure, N_Λ for the length of the superperiod divided by Λ, i = 1, 2 for the first and second-order lateral mode respectively, j = 0, ± 1 for the first and second-order dual-grating mode respectively.

The black line in Figure 6.27 is a linear fit for the fundamental dual-grating and the fundamental lateral modes. The 2nd order

dual-grating modes are fitted by the light blue and dark blue lines while the 2nd order lateral modes are fitted by the red and green lines. The effective refractive index deduced from Figure 6.27 is 3.165 for the fundamental lateral modes (fundamental and 1st order dual-grating modes) and 3.12 for the second-order lateral modes. Plotting the lasing frequencies versus the grating period (purple cross, Figure 6.27), we deduce that almost all devices are lasing on the fundamental mode. Few devices are lasing on the 2nd order dual-grating mode or on a combination of the first and second-order lateral mode. For all measured devices we found a single mode yield of about 80 %. We have not observed higher order lateral modes for ridge width narrower than 5 μm.

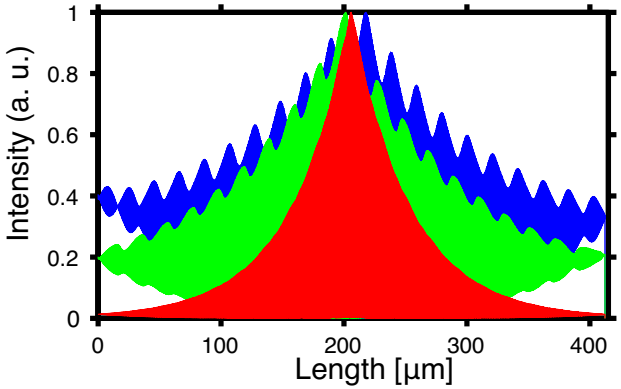

Figure 6.28: Simulation of the optical mode intensity along the ridge for a 412 μm long device made of periodicities of 500 nm and 520 nm with a superperiod of 20.6 μm and an effective periodicity of 515 nm. Red: Data evaluated at λ = 3.2594 μm which corresponds to the fundamental quarter-wave shift mode. Blue and Green: Evaluation at λ = 3.1803 μm and λ = 3.3436 μm which correspond to the 2nd order dual-grating mode. Figure taken from Ref. [67].

Calculations of the optical mode intensity profile along the ridge, given by the transfer-matrix method, show periodic modulations of the mode. Figure 6.28 shows the mode intensity

profile of the fundamental and the two 2nd order dual-grating modes. The periodicity along the ridge amounts to $\frac{2\pi}{\sqrt{\Delta\beta^2-\kappa^2}}$ [130], where the imaginary part of the coupling constant κ and the gain within the structure are neglected and $\Delta\beta = 2 \times \beta - \frac{2\times\pi}{\Lambda}$ is the detuning of the propagation constant β from the Bragg frequency. From coupled wave theory we know that the periodicities are given by the detuning from the Bragg frequency and amount to the imaginary part of $\frac{\pi}{s}$ where $s = \sqrt{\kappa\kappa^* - (\frac{1}{2}(\Delta\beta + ig))^2}$ is the complex propagation constant [130]. Here g is the gain coefficient inside of the structure. In the case presented, the transfer-matrix simulation gives a periodicity of 20.6 μm, equal to the result for the formula above. Spatially modulated injection, with the same periodicity as the optical mode, could be used for generating tunable single mode emission. We believe that this happened with one device which was lasing at 3.3 and 3.26 μm for different driving conditions.

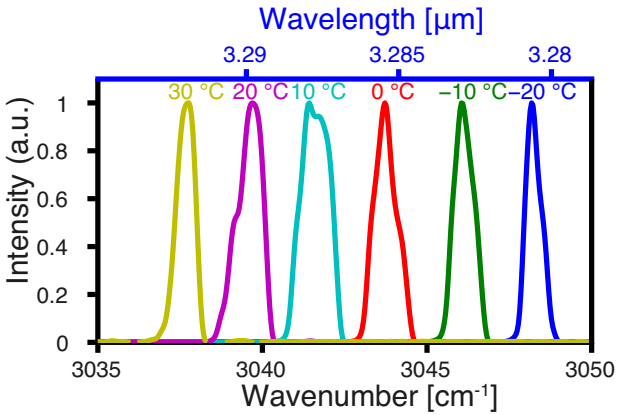

Figure 6.29: Spectra of an device emitting at 3.3 μm for various submount temperatures. Figure taken from Ref. [67].

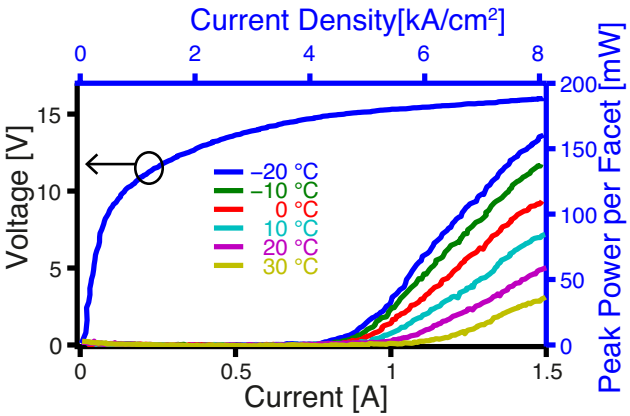

Figure 6.30: Power-current-voltage characteristics of the device shown in Figure 6.29. The slope efficiency is 284 mWA and the threshold current density is 4.7 kA/cm^2 at -20 °C. Figure taken from Ref. [67].

Figure 6.29 and 6.30 show a device emitting around 3.29 μm with a side-mode suppression ratio of over 20 dB. The ridge length is 2.64 mm and the width is 7 μm. The temperature tuning reached 10.5 cm^{-1} from -20 to 30 °C, giving a temperature tuning coefficient of 0.21 cm^{-1}/K. The threshold current density is 4.7 kA/cm^2. A slope efficiency of 284 mW/A was measured at -20 °C. The output power for the uncoated device per facet is 160 mW at -20 °C whereas the highest output power we achieved was 250 mW on a multimode device. Based on the transfer-matrix computations of the losses, the lowest cavity loss should be achieved on the defect mode in the center of the stopband, whereas we observed our lasers to operate mostly on the band edge mode. We attributed this to fabrication defects that affected most the modes that are highly confined in the center of the cavity.

6.6.3 Conclusion

We demonstrated single-mode lasing from 3.19 to 3.41 μm and the quarter-wave shift mode in the spontaneous amplified emission. Temperature tuning of the single-mode emission is 0.21 cm^{-1}/K, and the output power is sufficient for most spectroscopic applications. Because of the relatively large thermal dissipation at threshold, continuous-wave operation has not been achieved. The incorporated DFB grating was accomplished with standard deep-UV optical lithography using only three grating periodicities. The spectral spacing towards the higher-order dual grating modes is proportional to $\frac{1}{L_{superperiod}}$. Therefore lasing on the second-order grating modes could be avoided by using a shorter superperiod.

Chapter 7

Genetic Active Region Design

In the following section, genetic optimised active regions from 4 to 26 μm are presented in ascending order of their emission wavelength. The active regions, used for heterogeneous stacks are presented together. In some cases, we present measured results of single active region designs, but the measurements of multi-wavelength stacks are presented in the next chapter.

The designs, which were used as a starting point of the optimization process will be called *seed* and the resulting optimised design will be called *genetic* throughout the whole chapter. Therefore the names refer to the designs of the current section, if not stated otherwise.

Our simulation tool is used for wavelength as short as 3 μm (see Chapter 6), but these structures incorporate a high number of material layers and the need of kinetic balance calculations, both are increasing significantly the computational cost. Simulation results neglect the inter-valley scattering and suffer from uncertainties in the conduction band discontinuum for highly strained material. Growth restrictions, like Monolayer (ML) material thicknesses, critical thickness for non-relaxed material

and strain compensation needs to be adapted and controlled manually. Therefore we restrict ourselves to active regions with wavelength longer than 4 μm.

The longest wavelength presented here is 26 μm and therefore at the long-wavelength edge of the Mid-Infrared (mid-IR) wavelength region. We assume the calculation of the electronic wavefunctions and the corresponding optical properties like dipole moments in this wavelength region are in reasonable agreement with experimental data. Contrary to the Terahertz wavelength region, the effect of electron-electron interaction can still be approximated with thermalized subbands and a basis renormalization using the Hartree potential, neglecting the scattering contribution between different levels. For the designs presented here, the electron-electron scattering time from upper laser level (ULL) to lower laser level (LLL) is about 5-10 ps [16], about 10 times slower than the total scattering time of the optical transition. Simulations of the normalized gain are used to optimize a structure and will be presented in Section 7.4.

7.1 4 μm strained Active Region

The aim of this optimization run is to improve and shift the active region *seed* design (Appendix B.8), which is centered around 4.4 μm. This design is the result of an earlier optimization, the results are published in Ref. [55]. The second optimization with the improved software package (see Section 2.2) enables us to explore the impact of our adaptation. The shift in wavelength towards 4.6 μm is necessary as both, the *seed* and *genetic* design will be used in a broad heterogeneous stack for comb emission (see Section 8.1).

The basis wavefunctions and bandstructure of the *seed* and

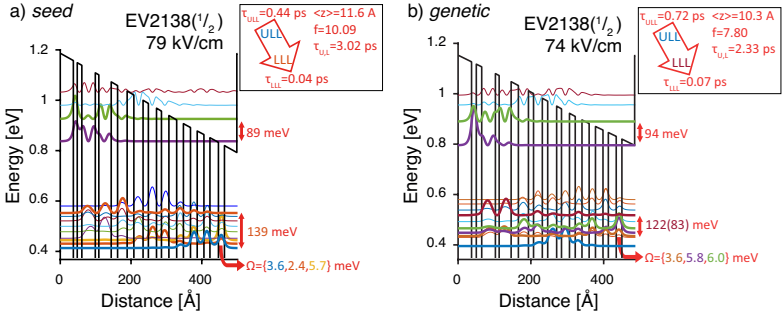

Figure 7.1: Band diagram and the squared electron wavefunctions offset by their energy with respect to the distance in growth direction. Additional parameters of the design as described in Section 3.1.1. a) *seed* structure [55] (Appendix B.8). b) *genetic* design (Appendix B.9).

4.3 - 4.6 μm		*seed*	*genetic*
electron sheet density	10^{10} cm^{-2}	10	10
period length	A	462	448
max WP	%	38.3	44.12
Slope Efficiency	W/A	9.05	9.16
Gain Coefficient	cm/kA	5.72	3.27
τ_{eff}	ps	0.43	0.70
η_{tr}		0.91	0.91
η_{inj}		0.64	0.68
Transparency Current Density	kA/cm^2	0.37	0.44
Threshold Current Density	kA/cm^2	1.03	1.10
Jmax	kA/cm^2	6.63	12.23
dyn Range	1	5.4	10.1
emission	μm	4.4	4.6

Table 7.1: Design, optical and electrical properties of the simulated structures.

genetic are shown in Figure 7.1, the evaluation parameters in Table 7.1 and the resulting gain-current density-voltage curve (GIV) and light-current density-voltage curve (LIV) in Figure 7.2. The *genetic* design is more diagonal with an increased τ_{ULL}. As the τ_{LLL} increased as well, the transition efficiency is 0.91 for both active regions and as a consequence the slope efficiencies are

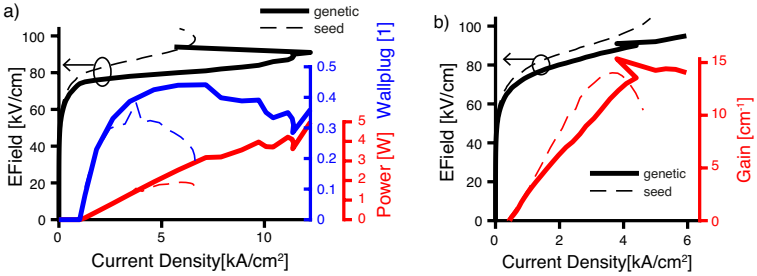

Figure 7.2: Simulated a) LIV and b) GIV for the *seed* and *genetic* design in dashed and continuous line, respectively.

similar. The *genetic* version takes advantage of a twofold increase in dynamical range. The larger maximal current in the genetic design (see Figure 7.2 b)) is due to larger coupling energies. From the LIV we see that the genetic design also gives significantly more photocurrent, leading to a further improvement in dynamical range. The genetic design works at lower field which is a result of a lower energy distance between the LLL and the main injector state (MIS) which was reduced from 139 to 83 meV. The energy separation from the ULL to the state above is increased to reduce leakage currents.

The *seed* and *genetic* were combined in a dual stack active region. The measured results are presented in Section 8.1.

7.2 Long Wavelength Lattice Matched Active Regions

In this section we present our efforts to create a broad flat emission in the long wavelength range with lattice matched materials . Therefore we propose 4 different active regions for a heterogeneous stack. They are used in two different projects which are further described in Chapter 8.2.1 and Chapter 8.2.2. Both projects aim at

the delivery of small and efficient spectroscopy devices which are able to detect several gas species at the same time. The requirement for the genetic optimization therefore are active regions that provide a good wallplug efficiency. With that the output power can be maximized while keeping the input power, and therefore the dissipation minimal.

The *seed* active regions were already used in a broadband device, published in Ref. [29]. The tuning was 39 % around the center frequency and a peak optical output power of 1 W in pulsed operation was presented. We optimised four lattice matched active regions around 7.3, 8.5 9.4 and 10.4 μm separately. The designs at 7.3 and 8.5 μm are presented here as optimization examples, the other two designs can be found in Section A.1.

7.2.1 Structure at 7.3 μm

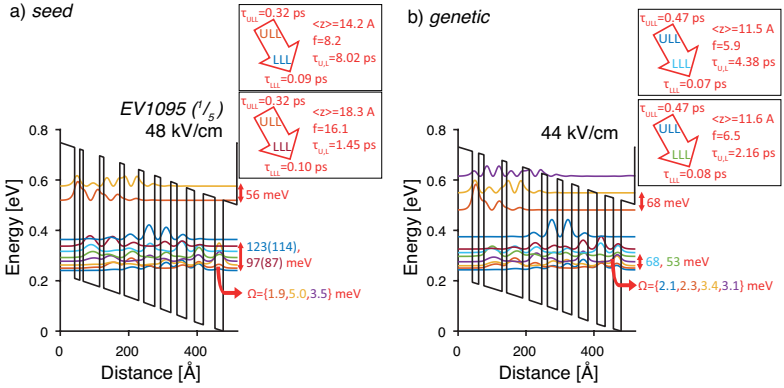

Figure 7.3: Band diagram and the squared electron wavefunctions offset by their energy with respect to the distance in growth direction. Additional parameters of the design as described in Section 3.1.1. a) *seed* design (Appendix B.11). b) *genetic* design (Appendix B.12)

The optimization around 7.3 μm is discussed in the following,

7.3 μm		*seed*	*genetic*
electron sheet density	10^{10} cm^{-2}	10	10
period length	A	474	478
maximum wallplug-efficiency	%	30.09	42.55
slope efficiency	W/A	2.10	2.74
gain coefficient	cm/kA	10.1	10.2
τ_{eff}	ps	0.32,0.30	0.46,0.45
η_{tr}		0.78,0.76	0.87,85
transparency current density	kA/cm^2	0.73	1.38
threshold current density	kA/cm^2	1.63	2.30
maximum current density	kA/cm^2	10.75	12.06
emission	μm	7.50	7.24

Table 7.2: Design, optical and electrical properties of the simulated structures.

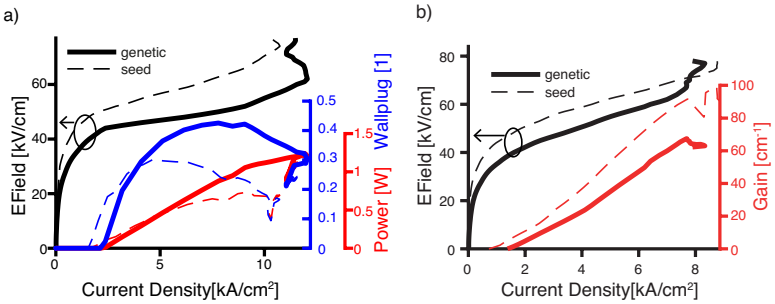

Figure 7.4: Simulated a) LIV and b) GIV for the *seed* and *genetic* design in dashed and continuous line, respectively.

the bandstructure of the *seed* and the *genetic* design is found in Figure 7.3. The *genetic* active region design is more diagonal than the *seed*, with a increased upper state lifetime and slightly decreased lower state lifetime. This leads to a increase in the slope efficiency from 2.1 (*seed*) to 2.7 W/A (see Figure 7.4 a)). The performance properties of the structure are summarized in Table 7.2.1. The energy separation between the LLL and the MIS and the miniband width is reduced for the *genetic* design, therefore the operation field is lower (see Figure 7.4 b)), but also the transparency current increased from 0.7 (*seed*) to 1.4 kA/cm^2.

The gain coefficient is similar around threshold (10 cm/kA), while for higher currents the vertical *seed* design shows a higher gain coefficient.This is an advantage of the vertical design, which leads to large oscillator strength values, even at high fields. The diagonal designs on the other hand maintain improved lifetimes and scattering times for high fields, which subsequently leads to good slope efficiency values.

In this example the optimization for wallplug efficiency was partially achieved by increasing the transparency current density. This increase directly translated into an increase in threshold current density, as we can see in Figure 7.4 a). Even as the resulting *genetic* design has a 41 % increase in wallplug efficiency, a low threshold current density is essential for continuous-wave operation and low dissipation. In Section 7.2.3 we will present a technique of combining high wallplug efficiencies with low threshold current densities based on the genetic optimization presented in this section.

7.2.2 Structure at 8.5 μm

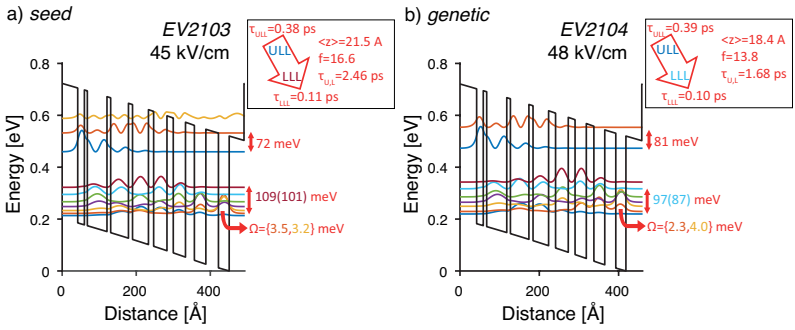

Figure 7.5: Band diagram and the squared electron wavefunctions offset by their energy with respect to the distance in growth direction. Additional parameters of the design as described in Section 3.1.1. a) *seed* design (Appendix B.14). b) *genetic* design (Appendix B.15)).

8.5 μm		*seed*	*genetic*
electron sheet density	10^{10} cm^{-2}	10	10
period length	A	449	417
max WP	%	20.87	26.74
Slope Efficiency	W/A	1.38	1.64
Gain Coefficient	cm/kA	14.9	13.9
τ_{eff}	ps	0.36	0.37
η_{tr}		0.77	0.79
Transparency Current Density	kA/cm^2	0.65	0.83
Threshold Current Density	kA/cm^2	1.31	1.55
Jmax	kA/cm^2	8.75	11.38
emission	μm	8.6	8.7

Table 7.3: Design, optical and electrical properties of the simulated structures.

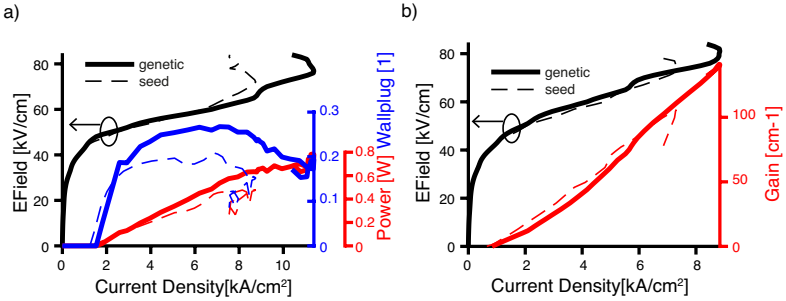

Figure 7.6: Simulated a) LIV and b) GIV for the *seed* and *genetic* design in dashed and continuous line, respectively.

The *seed* of the 8.5 μm optimization was published in Ref. [76]. We present the band diagramm and the electronic wavefunctions of both structures in Figure 7.5. The difference in state lifetimes and dipole matrix elements are not as pronounced as before. A lower energy separation between ULL to the MIS would lead to lower electric fields for the *genetic* design, but the effect is compensated by a shorter active region period. The *seed* and *genetic* were already presented in Section 3.2, where the effect of the miniband width is evaluated. We present the LIV and GIV in Figure 7.6 a) and

b), respectively. The increased coupling energies lead to a slight increase in maximum operation current (see Figure 7.6 b)) and as a consequence to a larger dynamical range in Figure 7.6 a). In this structure, the increase of the dynamical range, combined with a slight increase in η_{tr} is the key improvement factor.

The *seed* and *genetic* structure were grown by molecular beam epitaxy on InP substrate. The active core consists of 50 periods, the electron sheet density is $7.7 \times 10^{10}\,\mathrm{cm}^{-2}$. Both wafers are capped with a 300 nm InGaAs layer. Buried inverted buried heterostructure (BiBH) lasers were processed as described in Section 4. The cladding consists of differently doped InP:Si layers, the sequence is $(0.02/0.46/0.04/1.5/.2/0.5)\,\mu$m doped with $(1/0.5/1/0.2/0.5/30)\ \times 10^{17}\ \mathrm{cm}^{-3}$.

The cleaved devices were mounted epilayer-up on copper submounts and Peltier cooled. Light-Current curves were recorded using a calibrated thermopile detector. Pulsed measurements where performed with 1 % duty cycle and 104 ns pulse width. The measured power is corrected by collection efficiency.

In Figure 7.7 a) an b) the simulated and measured LIV of the processed *seed* and *genetic* active regions are presented. The parameters of the measured device were used for the simulation in Figure 7.7 a). The cladding design was not optimized for low optical losses, therefore the presented results do not show the full potential of the design. The maximum wallplug efficiency amounts to 6.2 and 8.1 % for *seed* and *genetic*, respectively. The maximum output powers (not shown) are 52 and 70 mW/μm. The trend of the measurement compares well with the simulation results, where the threshold of the *genetic* sample is slightly higher and the wallplug efficiency increased, while the operating field is the same. The discrepancy in absolute values between the simulations and the measurements might origin from leakage

current, resulting also in a less visible kink in the current density-voltage curve (IV), and a discrepancy in the modal overlap.

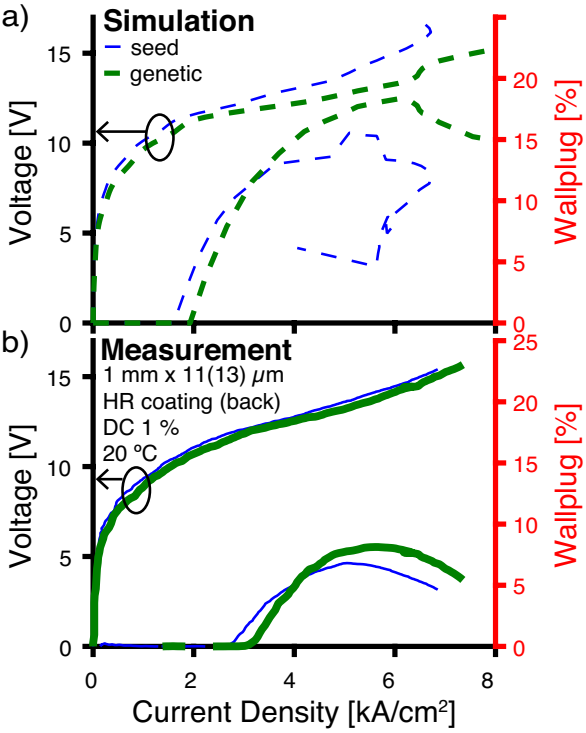

Figure 7.7: a) Simulated WIV of *seed* and *genetic* design, simulation parameters are adapted to the devices shown in b). b) Measured WIV of *seed* and *genetic* design at 20 °C in pulsed operation with a DC of 1 %. The devices are 1mm long and 11 (13) μm wide for *seed* (*genetic*). A high-reflectivity coating is applied on the backfacet.

7.2.3 Post-Selection: Low Threshold

The genetic optimization generates over 15 generations, as described in Section 2.2. From each generation the best samples are used to build the subsequent generation by modifying the well

and barrier thicknesses.

After the run is converged, the best merit samples can be investigated for the application requirements. Here we concentrate on the gain spectrum, but also at the threshold current density and the dynamical range. Due to the convergence (see Figure 2.4) the number of active regions with a similar merit function is big enough to do a post-selection without interfering in the optimization of the merit function.

We want to present a post-selection with respect to low dissipation devices. Our pool consists of 20 generations with the 20 best samples optimized for wallplug efficiency. The post-selection criteria is low threshold current density. The light-current density curves (LIs) of this pool are presented in Figure 7.8. As we see the threshold current density varies by $2\,\mathrm{kA/cm^2}$ the NDR shifts by $4\,\mathrm{kA/cm^2}$. From this pool the best threshold sample can be examined manually.

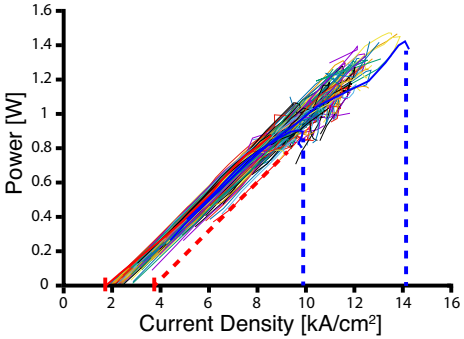

Figure 7.8: LI of the 20 best-merit samples for 20 generations. The threshold current densities vary by 2 $\mathrm{kA/cm^2}$, the NDR by $4\,\mathrm{kA/cm^2}$.

This post-selection was performed on the active regions at $7.3\,\mu\mathrm{m}$ (Section 7.2.1), $8.5\,\mu\mathrm{m}$ (Section 7.2.2) and

9.4 μm (Section A.1.1). We will present here the result for the shortest wavelength, the data for 8.5 μm is found in Appendix A.1.3. For the longest wavelength the design shown in Appendix A.1.1 (no post-selection) was kept. All three designs were combined in a heterogeneous active region and form part of a μ-External Cavity Quantum Cascade Laser (QCL) setup. The results of our collaborators thereof will be shown in Section 8.2.1

Structure at 7.3 μm

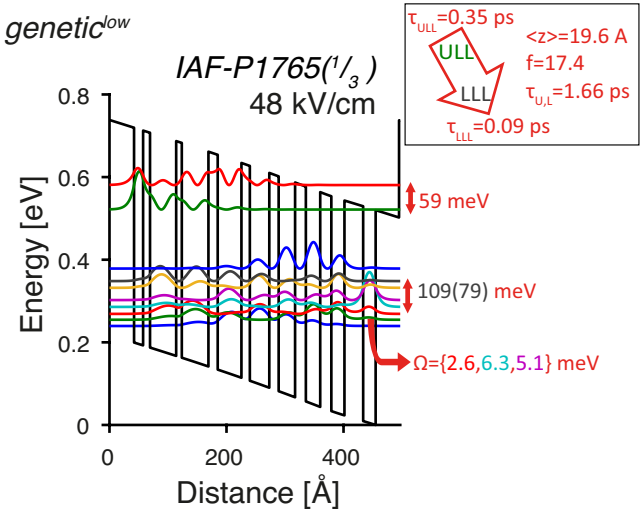

Figure 7.9: Band diagram and the squared electron wavefunctions offset by their energy with respect to the distance in growth direction for the *genetic* $^{\text{low}}$ design (Appendix B.13). Additional parameters of the design as described in Section 3.1.1.

The bandstructure of the low threshold post-selection (subsequently called *genetic* $^{\text{low}}$) is presented in Figure 7.9. The miniband width of the structure is 109, 97 and 53 meV for the *genetic* $^{\text{low}}$, the *seed* (Section 7.2.1) and the *genetic*

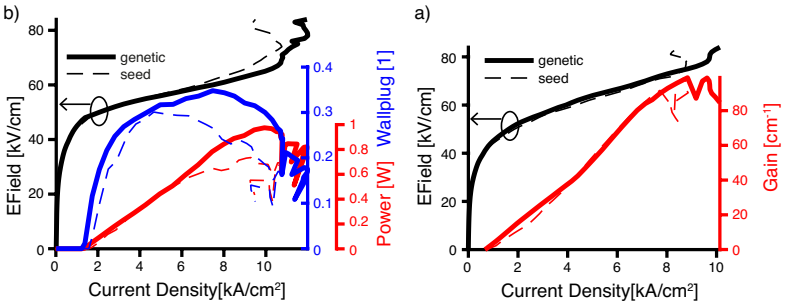

Figure 7.10: Simulated LIV and GIV for the low-threshold design (*genetic* ^{low}) in comparison with the *seed* presented in Section 7.2.1

(no post-selection, Section 7.2.1). This is in accordance with the threshold current densities of these devices which amount to 1.3, 1.6, 2.3 kA/cm^2, respectively. The optical transition is only slightly more diagonal than the *seed* and except for the change in miniband width very similar. The performance parameters are therefore similar to the *seed* structure as we can see in the LIV and GIV (see Figure 7.10 a) and b)). The sample presented in Section 7.2.1 has a clear advantage at higher currents, lower fields and a better slope efficiency, leading to higher output power and higher maximum wallplug efficiency. This is summarised in Table 7.4. It can be seen in Appendix A.1.3 that the post-selection can also lead to a good alternative, combining low threshold and high wallplug efficiency.

7.3 μm		*seed*	*genetic* $^{\text{low}}$	*genetic*
electron sheet density	10^{10} cm^{-2}	10	10	10
period length	A	474	453	478
max WP	%	30.09	34.81	42.55
Slope Efficiency	W/A	2.10	2.08	2.74
Gain Coefficient	cm/kA	10.10	11.83	10.2
τ_{eff}	ps	0.32,0.30	0.33	0.46,0.45
η_{tr}		0.78,0.76	0.79	0.87,85
J_{trans}	kA/cm^2	0.73	0.67	1.38
J_{thres}	kA/cm^2	1.63	1.33	2.30
J_{max}	kA/cm^2	10.75	11.98	12.06
emission	μm	7.5	7.1	7.2

Table 7.4: Design, optical and electrical properties of the simulated structures. Presented for the *seed* design, the *genetic* $^{\text{low}}$ design presented here and the *genetic* design (no post-selection, Section 7.2.1).

7.3 Middle and Long Wavelength Strained Active Regions

In order to explore the possibilities of strained active regions in the middle and long wavelength region, we used a reproduction of the design published in Ref. [52] as *seed* structure. In various genetically optimizations we derived *genetic* designs at shifted emission wavelengths of 6, 7, 8.5 and 9.6 μm. The shift in wavelength was performed by the optimization run itself with only rough layer thickness adaptations for the 6 and 9.6 μm design. This designs are later combined for a broadband design as described in Section 8.3.2. As the wavelength between the *seed* and *genetic* design varies strongly, we will present in the following only the comparison for the *genetic* design at 8.5 μm. The simulation results for all other wavelength can be found in the Appendix A.2.

7.3.1 8 μm strained Active Region

We present a detailed comparison between two strain compensated active regions, the *seed* design is extracted from the bandstructure presented in Ref. [52]. Up to date, this structure shows the highest wallplug efficiencies at an emission wavelength of 9 μm: 16 % for pulsed operation at 20 °C (see Section 7.5.2). We expect that the optimization of this active region further improves the performance. The *seed* and *genetic* designs are compared for their theoretical and experimental performance characteristics.

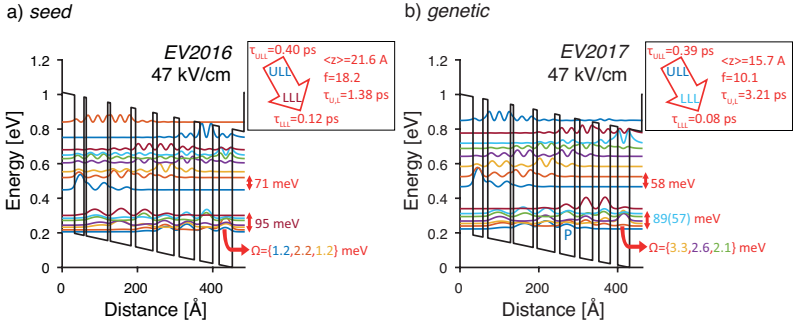

Figure 7.11: Band diagram and the squared electron wavefunctions offset by their energy with respect to the distance in growth direction. Additional parameters of the design as described in Section 3.1.1. a) *seed* design (Appendix B.24). b) *genetic* design (Appendix B.25).

As seen in Figure 7.11a) and b), one of the main differences between *seed* and *genetic* structure is the LLL and ULL lifetime. For the *genetic* structure the LLL lifetime was decreased substantially to 0.08 ps (*seed*: 0.12 ps), while the ULL lifetime is constant and is slightly increased for higher fields(not shown). This is beneficial for the population inversion and also for the photon driven transport [131]. The first barrier was increased from 6Å (*seed*) to 12.3Å(*genetic*) which increased the scattering time between ULL and LLL from 1.38 to 3.21 ps. From this we calculate that the

8.5 μm		*seed*	*genetic*
electron sheet density	10^{10} cm^{-2}	10	10
period length	A	450	428
max WP	%	17.2	36.48
Slope Efficiency	W/A	1.73	2.25
Gain Coefficient	cm/kA	16.0	11.5
τ_{eff}	ps	0.37	0.38
η_{tr}		0.76	0.83
Transparency Current Density	kA/cm^2	0.97	0.91
Threshold Current Density	kA/cm^2	1.54	1.67
Jmax	kA/cm^2	6.60	8.03
dynamical range		3.3	3.8
emission	μm	8.39	7.82

Table 7.5: Design, optical and electrical properties of the simulated structures.

transition efficiency η_{tr} improved from 0.76 to 0.83. The *genetic* design is a bound-to-continuum design where the LLL shows fast scattering towards the two states below (0.3 and 0.3 ps). On the other hand, the *seed* structure is showing bound-to-bound features where the scattering times (0.6 and 0.3 ps) are higher. As in our previous work [55], a state below the injector state is established, which we call pocket injector (marked with 'P' in Figure 7.11b)). Due to the more diagonal transition in the *genetic* design the dipole matrix element and oscillator strength are lower.

The simulated LIV for the *seed* and the *genetic* is shown in Figure 7.12a). The threshold is similar, but the *genetic* structure has a much higher predicted slope efficiency of 2.25 W/A (*seed*: 1.73 W/A) and a higher wallplug efficiency of 36.5 % (*seed*: 17.2 %). The *genetic* structure shows a change in the differential resistance at the onset of lasing which is a clear sign of photon-driven transport and leads to a dynamical range of 3.8 (*seed*: 3.3).

The *seed* and *genetic* structure were grown by molecular beam epitaxy on InP substrate. The active core consists of

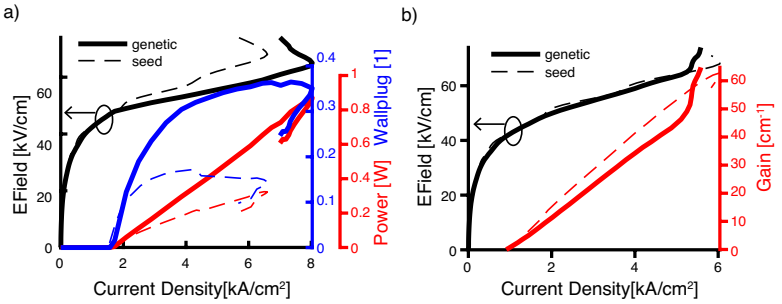

Figure 7.12: Simulated a) LIV and b) GIV for the *seed* and *genetic* design in dashed and continuous line, respectively.

45 periods, the electron sheet density is nearly the same with 10.4×10^{10} cm^{-2} (*seed*: 10.3×10^{10} cm^{-2}). Both wafers are capped with a 300 nm InGaAs layer. BiBH lasers were processed as described in Section 4. The cladding consists of differently doped InP:Si layers, the sequence is (0.02/0.46/0.04/1.5/2/0.5) μm Si-doped with (1/0.5/1/.2/0.5/30) $\times 10^{17}$ cm^{-3}.

The cleaved devices were mounted epilayer-down on AlN submounts and Peltier cooled. Light-Current curves were recorded using a calibrated thermopile detector. Pulsed measurements where performed with 1 % duty cycle and 104 ns pulse width. The measured power is corrected by collection efficiency and is always given as total output of both facets.

The measured Wallplug-(Light-)Current-Voltage curve is shown in Figure 7.13 b). The simulation shown previously (Figure 7.12) are performed with parameters comparable to the other simulations. Therefore we present in Figure 7.13 a) the simulations according to the measured devices (device dimension, mirror loss, total power).

The comparison of the *seed* and *genetic* structure gives a clear improvement, as can be seen in Figure 7.13. We show the wallplug

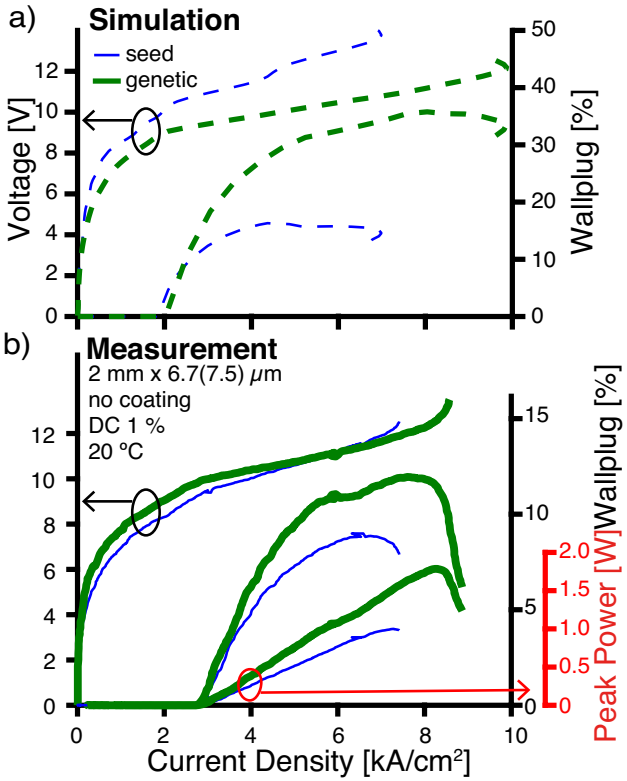

Figure 7.13: a) Simulated WIV for *seed* and *genetic* device using the device properties of b). b) Measured WIV comparison of *seed* and *genetic* structure. Output power given for two facets.

efficiency and total output power for the *seed* and the *genetic* structure versus current density at 20 °C. The devices are 2 mm long and 6.7 µm (*genetic*: 7.5 µm) wide. No coating was applied to the facets of the tested lasers. The dynamical range increased from 1.5 (*seed*) to 2.1(*genetic*) due to an increase in photo-driven current. This can be seen in the current-voltage curve of the *genetic*

structure as a clear change of slope at threshold in Figure 7.13, which we assign to a low LLL lifetime. For the same reason, the slope efficiency improves to 2.5 W/A (*seed*: 1.9 W/A) while the threshold current density is nearly the same for the two structures. The wallplug efficiency of the *genetic* sample reaches 12 % (*seed*: 9 %). All these improvements agree with the predictions from our simulations. The threshold of our devices is higher than expected and the total wallplug efficiency is much lower as seen in Figure 7.13. This might be due to high optical losses from the cladding and lower modal overlap.

From measurements we can also deduce the transparency current density and the gain coefficient. In Figure 7.14 we see the threshold current densities for devices of the *seed* and *genetic* structure versus mirror losses (blue and red crosses, respectively). Following the method described in Section 3.2 we arrive at a transparency current of 2.1 and 1.8 kA/cm^2 for *seed* and *genetic*, respectively. The extracted parameters are summarized in Table 7.6. The extracted gain coefficient and also the transparency current density is in good qualitative accordance to our simulation. Interestingly the measured gain coefficient is slightly higher than predicted, alternatively it could also be that the optical modal overlap was underestimated. A higher modal overlap is not in agreement with our result from Figure 7.13.

Notably, the values are in disagreement with the prediction from the miniband width: $J_{\text{trans}} = e n_{\text{LLL}}^{\text{therm}} / (\eta_{\text{inj}} \tau_{\text{eff}})$ where $n_{\text{LLL}}^{\text{therm}} = n_g exp(-\Delta/kT)$ (Section 3.2). Following this analysis, the transparency current density of the *seed* design should be around 70 % of the *genetic* value. This is not due to the effective one-subband approximation of the miniband, as the genetic design has fewer subbands below the LLL. The reduced lifetime of the LLL of 0.08 ps of the *genetic* design (*seed* design: 0.12 ps) might be

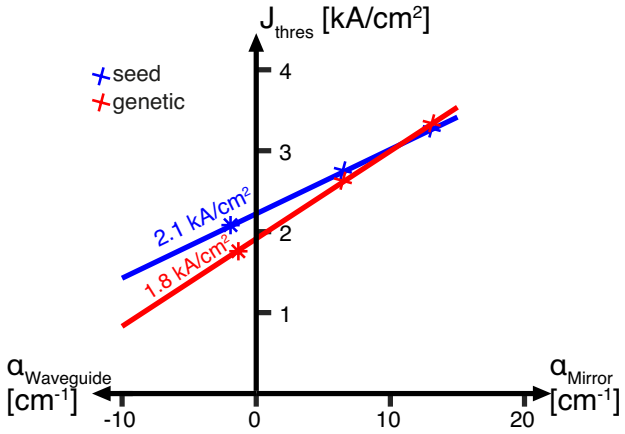

Figure 7.14: Device threshold current density as a function of mirror/waveguide losses. The crosses represent the measured threshold current densities with and without high-reflectivity coating. The lines are the linear extrapolation. The transparency current is then located on the x-axis at $-\alpha_{WG}$, indicated by the star. Device dimensions are (1 mm $\times$ 8.7 (9.6) μm for *seed* (*genetic*), respectively.

8.5 μm		*seed*	*genetic*
Δ	meV	95	89
J_{trans}	kA/cm^2	0.97	0.91
$J_{trans}^{\mathbf{meas}}$	kA/cm^2	**2.1**	**1.8**
Gain Coefficient	cm/kA	16.0	11.5
Gain Coefficient$^{\mathbf{meas}}$	cm/kA	**18.9**	**13.7**
η_{inj}		0.91	0.81

Table 7.6: Transparency current and gain coefficient from the simulations and extracted from Figure 7.14.

responsible for effectively transporting carriers away from the LLL. Additionally we need to take into account that the system is not in a thermally steady state, as assumed by the model from Section 3.2. In this case the prediction of our density matrix simulations are accurate, while the simplified thermal population model of the miniband fails to predict the transparency current.

7.4 Mid-Infrared meets Terahertz

The longest wavelength optimised with our software package is shown in this section. The *seed* design is a structure from Keita Othani with an emission wavelength around 31 μm on the material system $GaAs_{0.51}Sb_{0.49}/In_{0.53}Ga_{0.47}As$. It is similar to the structure published in Ref. [132]. The merit function uses peak gain divided by current density for optimization. The sliding window method is evaluated at higher electric field (20-25 kV/cm) than the operation bias of the *seed*. This lead to a *genetic* design working around 24 kV/cm, with a larger miniband and therefore reduced transparency current (see Figure 7.15, 7.16). The emission wavelength was reduced using the genetic optimization to 26 μm in the *genetic* design.

In Figure 7.15 we see the band diagram and the electron

26 μm		*seed*	*genetic*
electron sheet density	10^{10} cm^{-2}	25	25
period length	A	688	632
Gain Coefficient	cm/kA	48	98
τ_{eff}	ps	0.23	0.28
η_{tr}		0.48	0.52
Transparency Current Density	kA/cm^2	1.1	0.4
Jmax	kA/cm^2	5.1	5.6
emission	μm	26	31

Table 7.7: Design, optical and electrical properties of the simulated structures.

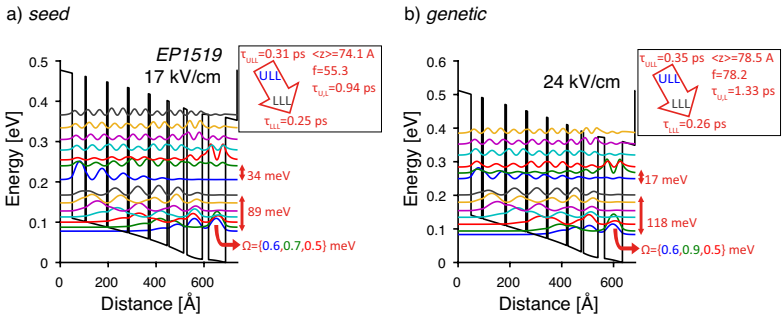

Figure 7.15: Band diagram and the squared electron wavefunctions offset by their energy with respect to the distance in growth direction. Additional parameters of the design as described in Section 3.1.1. a) *seed* (Appendix B.31). b) *genetic* (Appendix B.32).

wavefunctions of a) the *seed* and b) the *genetic* design. The dipole matrix element increased due to the optimization, which, combined with a decrease of emission wavelength, leads to an increase in gain coefficient from 48 to 98 cm/kA (see Table 7.7). The energy difference between the ULL and the excited state is reduced by half in the *genetic* design compared to the *seed*. But due to a poor overlap between this states we do not expect a performance decrease. The lifetimes of the ULL and LLL did not change significantly, but the scattering time between *seed* and *genetic* design increased from 0.9 to 1.3 ps, as a consequence of increased barrier thickness. As expected this results in a slight increase in τ_{eff} and η_{tr} (see Table 7.7).

In Figure 7.16 a) we see the GIV for the *seed* and *genetic* structure. The gain benefits from the higher gain coefficient, but also from a lower transparency current. In Figure 7.16 b) we see the gain spectrum for the two designs. As expected from the optical properties, only one optical transition is visible.

The *genetic* structure has yet to be grown.

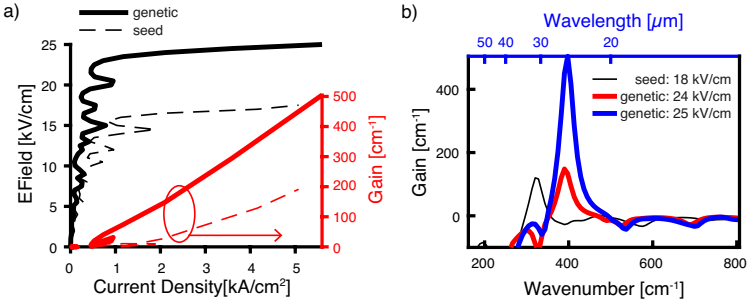

Figure 7.16: Simulated a) GIV and b) gain spectrum for the *seed* and *genetic* design in dashed and continuous line, respectively.

7.5 Conclusion

From the analysis of the optimizations described above and in the Appendix A, we can deduce some common optimization features. In general the designs become more diagonal, usually by increasing the barrier thickness separating ULL and LLL. They show a increased ULL lifetime and scattering time. Therefore the aim is a higher slope efficiency and not an increase in gain coefficient. In some cases the miniband was increased to reduce the transparency current, which also leads to a lower operating field. In most cases the active region performance was optimized at high current densities, therefore increasing the maximum wallplug efficiency. On the other hand this often leads to an increase in threshold current density.

7.5.1 Wallplug efficiency

The simulated wallplug efficiencies of the structures presented in this work are summarized in Figure 7.17. The green line represents the theoretical wallplug limit from Ref. [62] (see Section 3.1.2), where the parameters are adapted accordingly. As described in Section 3.1.2 the total losses are approximated by the free carrier

losses: $\alpha_{tot} \propto \lambda^2$, where λ is the emission wavelength. The *genetic* structures (marked with stars) exhibit consistently better wallplug efficiencies compared to the *seed* designs with only one exception: the lattice matched design at 9.3 μm (see Section A.1.1).

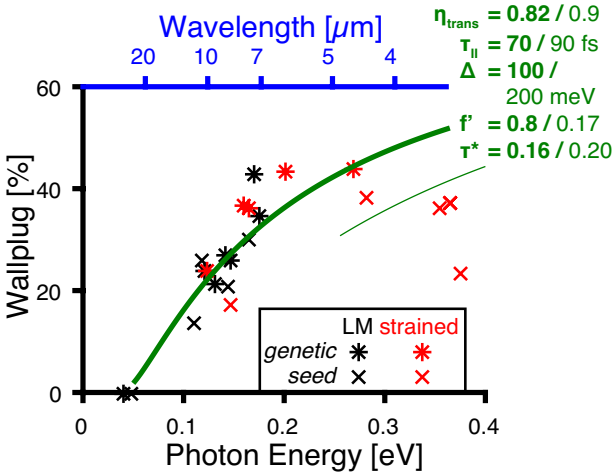

Figure 7.17: Simulated wallplug efficiency for the designs presented in this thesis. The green line is the theoretical limit from Ref. [62] adapted to our results. f'=fm*/m_0: reduced oscillator strength.

There is a clear discrepancy between the theoretical formula (green line in Figure 7.17) and the simulation results, whereas the latter value exceed the prediction by up to 10 %. Even as the wavelength dependence of the optical losses between 5 and 12 μm are neglected (the output power is calculated for optical losses of 7.5 cm^{-1}) our results follow the same wavelength dependance as the theoretical formula. We therefore conclude that the losses are mainly due to reabsorption from the miniband into the next upper level (NUL) or states above, giving a similar wavelength dependance. On the other hand, the theoretical

prediction is based on rate equations for the expression of dP/dJ, neglecting the positive effect of photon-driven transport for the wallplug efficiency.

The values taken for the theoretical wallplug efficiency (thick green line in Figure 7.17) are valid for structures around 8 μm and need to be adapted for the short wavelength region. The adapted curve is shown as a thin green line in Figure 7.17. Especially the lower oscillator strength (3 instead of 18), wider miniband and higher transition efficiency play a role.

7.5.2 Comparison with publications

Strained active materials(indicated in red in Figure 7.17) are necessary for short wavelength devices on the Indium Gallium Arsenide (InGaAs)/Indium Aluminium Arsenide (AlInAs) material system on Indium Phosphide (InP), where a larger band discontinuity is needed to incorporate the optical transition and the injector/extractor region. For long wavelength devices, lattice matched materials were assumed to be the better choice due to superior growth quality. A publication in 2010 [133] showed very good performance of strain-balanced QCL devices at wavelengths longer than 6 μm. Followed by 19 % of wallplug efficiency shown one year later [51] and Richard Leavitt et al. [134] published a direct comparison of lattice matched and strained active region design. The strained design showed better values for the threshold current density and the slope efficiency increased by 31 % at 25 °C, the measured T_0 value is 222 K compared to 194 K for the lattice matched sample. The higher energy separation from the ULL to the continuum is believed to reduce carrier leakage towards the continuum, even at high fields. The bandedge energy of the X and L-valley of InGaAs is increased, which was important for short wavelength designs shown in Chapter 6.

In Figure 7.18 we show the wallplug efficiency versus photon energy for selected publications from 3 to 11 μm. The numbers are given with respect to the total output at 20 °C in pulsed operation [18, 20, 49, 51–53, 71, 76, 117, 135–139]. The solid green and blue curves represent the theoretical limit for the wallplug efficiencies [62] for different injection efficiencies and a dephasing time of 70 fs.

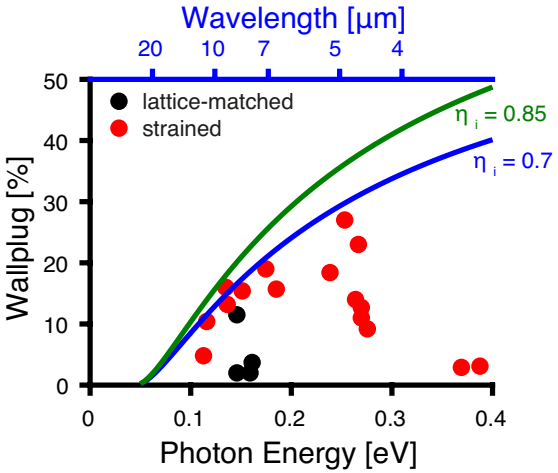

Figure 7.18: Wallplug efficiency for both facets at 20 °C in pulsed operation [18, 20, 49, 51–53, 71, 76, 117, 135–139]. Lattice-matched materials are shown in black, strained material systems in red.The solid green and blue curves represent the theoretical limit for the wallplug efficiencies [62] for different injection efficiencies and a dephasing time of 70 fs.

This overview shows better performance for strained designs throughout the mid-IR wavelength range. In contrast to this, the distinction between lattice matched and strained designs is not applicable for the simulated values (see Figure 7.17). Independent of the material system, very good wallplug efficiencies of over 40 % are reached.

Chapter 8

Broadband Active Regions And Their Application

Multi-species detection of trace gases throughout the mid-infrared is an active research-topic with applications ranging from 3 to 10 μm [140]. The advantage of Quantum Cascade Lasers (QCLs) is the engineering of the emission wavelength by adapting the semiconductor well thicknesses, which enables emission throughout the Mid-Infrared (mid-IR) and Terahertz (THz) wavelength region. Unlike interband devices, the gain of an intersubband laser like the QCL is delta-like and heterogeneous stacking can be used to stack different active region designs into one active core. Emission of several wavelengths potentially leads to bandwidth of over 760 cm^{-1} [17]. This feature strongly facilitates the spectroscopic setup as optical beam combining of different sources is not necessary.

The building blocks of the heterogeneous stacks are the active region designs, their proportion, the total number of active region periods, the doping level of the active region and the cladding design.

The design of a heterogeneous stacked active region need to

lead to a flat gain curve for all spectral positions of interest. Ideally all stacks reach the threshold condition at about the same current density to enable the full spectral width for low currents. In case of similar gain coefficients, the dynamical range of broad spectral emission can be maximized.

Cross absorption in the active region design appears between states of the miniband and from there to the excited states. This leads to absorption below and above the lasing transition, respectively. As the vertical extension of the active region core is limited to about 2 μm (about 50 periods), the overlap of each single wavelength stack is reduced. In order to reach the threshold condition sufficient gain is necessary.

In order to grow stacked active region designs spanning over a wide spectral range, the composition might need to be changed. This can be done either by interrupting the growth between active region stacks, to adapt the material composition or by using more than one cell for certain materials and switching in between these cells. An alternative method will be presented in Section 8.3.1.

8.1 Heterogeneous stack around 4 to 5 μm

The wavelength range around 4 μm has it's application in trace gas sensing of, amongst others, Sulfur Dioxide (SO_2) Sulfur Trioxide (SO_3), and Tetrafluoromethane (CF_4) Carbon Monoxide (CO), Nitrous Oxide (N_2O) and Carbon Dioxide (CO_2). Where it can also be used to distinguish the different isotopologues (e.g. for CO_2). It is important for environmental and medical sensing, industrial leak and fire detection. Additionally it can be used for petrochemical testing.

The *seed* and *genetic* active region designs presented in Section 7.1 were combined to deliver a broadband active region.

The number of periods are 17 and 18 for the *seed* (Appendix B.8) and the *genetic* design (Appendix B.9), respectively. The modal overlap with the active region periods results in 34 % and 40 %. The electron sheet density of the active region is 10×10^{10} cm^{-2}.

The active region was processed according to the buried inverted buried heterostructure (BiBH) protocol, the active region is sandwiched between 200 nm Indium Gallium Arsenide (InGaAs) layers. The data is taken from 3 different processes. The cladding for the hakki-paoli measurement is composed of $(0.020/0.360/0.020/0.4/\mathbf{0.04}/0.2/1.85)\,\mu$m InP doped $(5/1/5/2/\mathbf{5}/50/70) \times 10^{17}$ cm^{-3}, where the bold layer is InGaAsP which can be used as an etch stop, the active region is named EV2138. The light-current density-voltage curve (LIV) and dual-comb measurements are from a second Molecular Beam Epitaxy (MBE) growth (EV2139), the cladding is done with $(0.020/0.460/0.040/2.5/0.85)\,\mu$m InP doped $(5/1/5/0.2/30) \times 10^{17}$ cm^{-3}. All devices are mounted episide-down on Aluminium Nitride (AlN) submounts. The power is measured with a calibrated thermopile detector.

The hakki-paoli measurement of a device with dimensions (3.3 mm$\times$ 3 μm) is presented in Figure 8.1 a). The measurements were performed by Gustavo Villares. The gain spans nearly 600 cm^{-1} around 2270 cm^{-1}. The simulated and measured gain are compared in Figure 8.1 b). The simulation was adapted to the values of the measured device and the measurement was offset by the calculated waveguide and mirror losses. The modal overlap is taken into account. The bandwidth of the simulated emission spectrum is considerably broader than the measured gain, a possible reason for this is a high group delay dispersion in the real device. The spectral position of simulation and measurement are in good agreement.

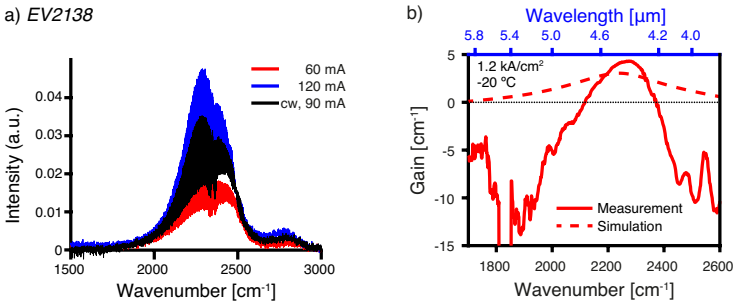

Figure 8.1: a) Hakki-paoli-measurement of a device with dimensions (3.3 mm$\times$ 3 μm) at different currents in pulsed operation and in continuous-wave operation at -20 °C. b) Comparison between hakki-paoli extracted gain-value from in pulsed operation and the simulated gain at -20 °C. The current density is 1.2 kA/cm^2 the total losses of the device and the overlap factor are taken into account. Data of the measured devices for a) and b) with courtesy from Gustavo Villares.

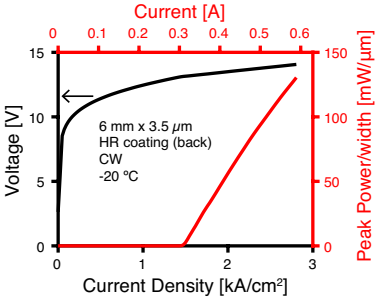

Figure 8.2: Measured LIV at -20 °C. The output power is normalised by the ridge width. The device has a high-reflective coating on the backside, the dimensions are (6 mm$\times$3.5 μm). Data with courtesy from Pierre Jouy.

The performance of the device was tested in continuous-wave operation at -20 °C. The LIV of this dual-stack (see Figure 8.2) gives a threshold current densities of 1.5 kA/cm^{2}and the slope efficiency amounts to 1.7 W/A. The measurements were performed by Pierre Jouy.

As a result of the broad spectra and good performance, this dual-stack active region is well suited for frequency comb measurements (see Figure 8.3). In the first case we present the beating of a QCL frequency comb with another QCL frequency comb on the same chip. With this setup external noise parameters as thermal drifts are shared among the QCLs and do not interfere with the measurement. The RF beatnote measurement shows clearly two narrow beatnotes originating from the two QCL ridges. This setup can easily be modified for dual comb spectroscopy [33, 34].

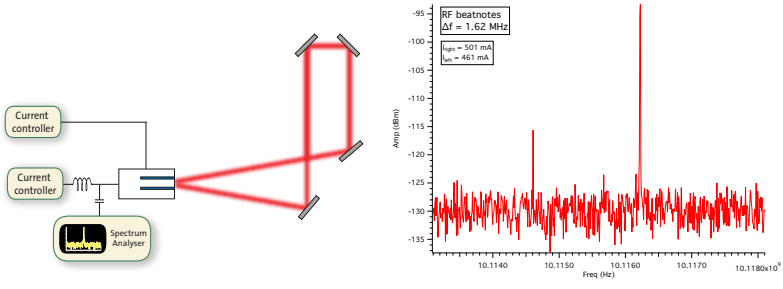

Figure 8.3: Left: Dual comb measurement setup. Right: RF beatnote measurement.The dimensions of the devices are (4.5 mm × 2 μm) and uncoated. Figure courtesy of Pierre Jouy.

The flat gain can also be utilised for multi-species trace gas analysers based on a dfb-grating. In our case two subsequent sections with different DFB gratings are used to adress CO_2 (including its major isotopologues). The laser design and performance can be seen in Figure 8.4. The detection of CO_2,

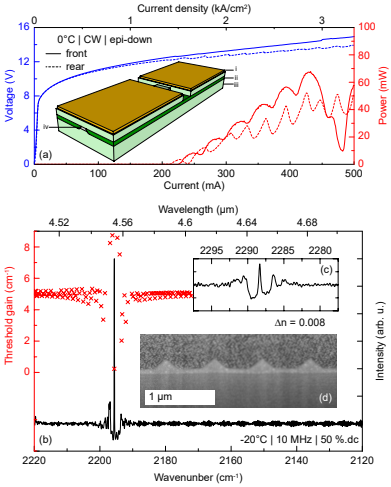

Figure 8.4: Device characteristics of the investigated dual-section DFB QCL. (a) LIV characteristic of a typical device with a device schematic in the inset. The color code for the inset is as follows: [i] yellow: Au electrode; [ii] dark green: insulating InP; [iii] light green: conducting InP; [iv] gray: dual-wavelength active region). (b) Sub-threshold electroluminescence revealing the stopband of the rear (b) and front (c) section. The spectrum is superimposed with a simulation of the threshold gain of each mode, highlighting that lasing occurs on the QWS. (d) FIB-SEM cross section through a laser revealing the wet-etched grating on top of the active region. The roughness seen in the upper part of this micrograph is ion-beam damage from the FIB preparation. Figure taken from Ref. [7].

CO and N_2O simultaneously with a precision of 0.16 ppm, 0.22 ppb and 0.26 ppb, respectively is presented in Figure 8.5. The integration time is 1s and the optical path length of the trace gas is 36 m. For more details, the reader is referred to the corresponding publication Ref. [7].

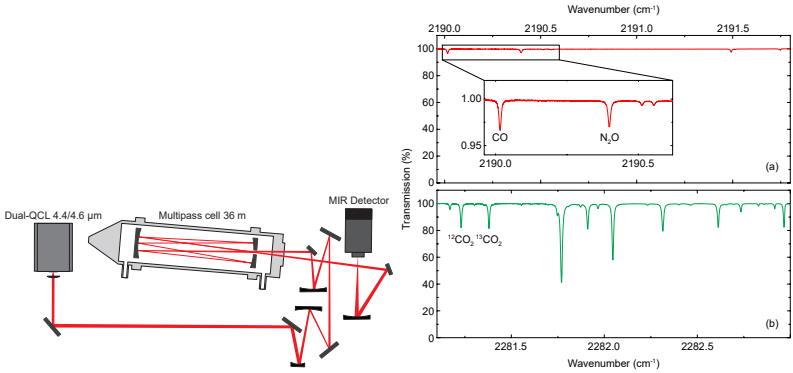

Figure 8.5: Schematic of the optical layout. Absorption spectra of dry air recorded at 50 hPa pressure. The absorption lines used for the concentration measurements are labelled. The inset in Figure 8.5(a) shows a close-up of the range with the absorption lines of CO and N_2O. Figure taken from Ref. [7].

8.2 Long Wavelength Lattice Matched QCL stacks

8.2.1 Broad Emission from 7 to 10 μm

For the long wavelength region we realized a lattice matched active region 3-color-design with gain around 1150 cm^{-1}(for simulations see Section 7.2.3). This work was done within the framework of the european project MIRIFISENS (see Ref. [141]). Our partner, the "Fraunhofer-Institut für Angewandte Festkörperphysik", used the 3-color active region in a μ-external cavity QCL setup (see Figure 8.6).

The devices are processed with the buried heterostructure technique [45]. The facet facing the grating has an anti-reflective coating, the other facet is coated with SiN for passivation. The devices reach over 700 mW peak power, as shown in Figure 8.7 a) with a threshold of 1.25 A (4.4 kA/cm^2). The bandwidth is $d\lambda/\lambda$ >33 % (330 cm^{-1}) (see Figure 8.7 b)). The external cavity system reaches a high scan rate (up to 1 $cm^{-1}/\mu s$) which enables

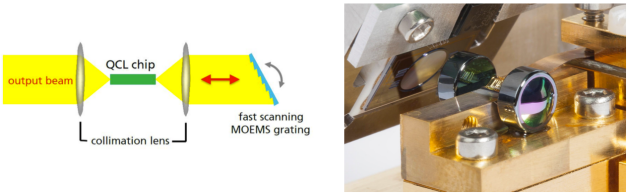

Figure 8.6: Left side: Schematic drawing of an EC-QCL with a MOEMS scanning grating in Littrow-configuration. Right side: Detailed photograph of the MOEMS EC-QCL with scanning grating. Figure taken from Ref. [21].

a fast, widely tunable, handheld external cavity detection system with MOEMS diffraction grating. Further details are presented in the corresponding publication, Ref. [21].

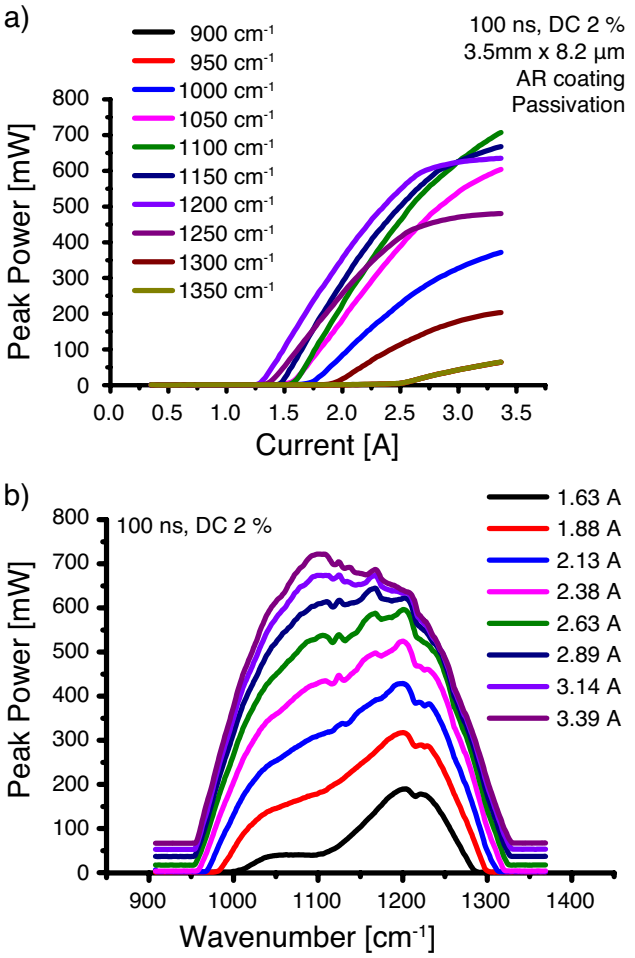

Figure 8.7: a) Power versus current for different grating positions. b) Spectral power measurements for different driving currents and different grating positions. Figures with courtesy from "Fraunhofer-Institut für Angewandte Festkörperphysik".

8.2.2 Broad Surface Emission from 8 to 10 μm

A on-chip alternative to the external cavity setup [21, 29, 122] are Distributed-Feedback (DFB) arrays [126, 142–146]. They consist of parallel ridges or rings on the same chip, where each of them contains a different DFB grating, therefore, each ridge / ring emits at a different wavelengths. In contrast to the external cavity setup the tuning is usually not continuous and the optical beam of parallel QCL arrays is shifted by the distance of the laser ridge facets. Here we would like to present an option which lifts the second restriction through surface emission.

A flat broadband emission from 8 to 10 μm is achieved with the two *genetic* active region designs from Section 7.2.2 and Section A.1.2, the electron sheet density is 7.7 and 10×10^{10} cm^{-2}, respectively. The MBE growth consists of 20 periods for the 8.5 μm emission and 30 periods for 10.4 μm. The top cladding is composed of (3.45/1.15) μm thick InP-Layers doped $(1/30) \times 10^{17}$ cm^{-3}. The simulated total modal gain is shown in Figure 8.8. We see that the gain is nicely equalized over a wide current range. The active region is processed similar to the inverted buried heterostructure (iBH) process, details thereof are found further below and in the corresponding publication Ref. [147].

FP Measurements

Results from a Fabry-Perot (FP) device with dimensions (1.5 mm $\times$ 7.5 μm) are shown in Figure 8.9 and compared with the simulations. The device has a HR coating on the back. The simulation parameters (listed in Table 2.2) were adapted to the device properties. The simulated device has a threshold of 1.7 kA/cm^2 and a slope efficiency of 1.5 W/A, compared to 2.4 kA/cm^2 and 0.9 W/A for the measurement.

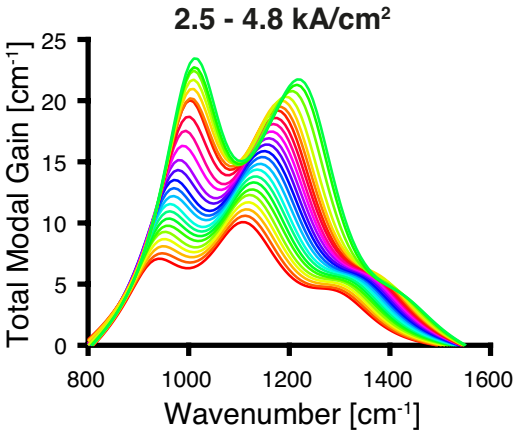

Figure 8.8: Simulated total modal gain for a dual-stack. The modal overlap is adapted according to waveguide simulations

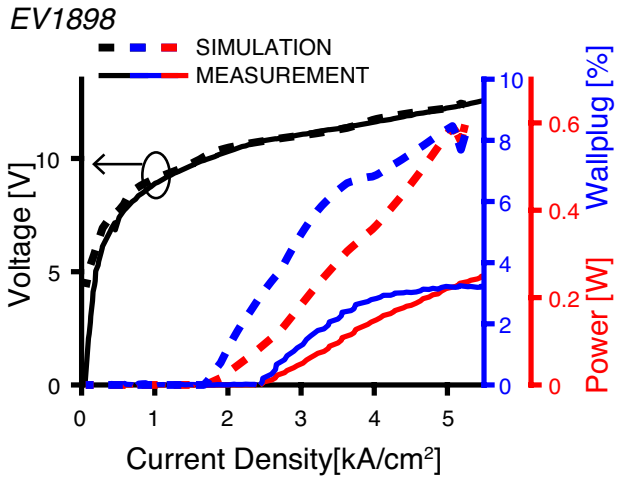

Figure 8.9: Comparison of the simulated (dashed lines) and measured (continuous lines) light(wallplug)-current density-voltage curve at -20 °C. The measured device was operated with 1 % duty-cycle, has the dimensions (1.5 mm×7.5 μm) and is high-reflectivity coated on the back-facet.

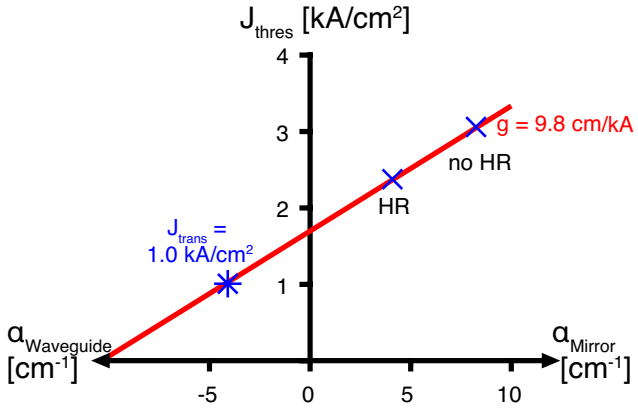

Figure 8.10: Device threshold current density as a function of mirror/waveguide losses. The crosses represent the measured threshold current densities with and without high-reflectivity coating. The line is the linear extrapolation. The transparency current is located on the x-axis at $-\alpha_{WG}$, indicated by the star.

To investigate this discrepancy further, we repeat the analysis from Section 3.2. The threshold current density is shown with respect to mirror losses in Figure 8.10. We find a transparency current density of $1.0\,kA/cm^2$ and a gain coefficient of $9.8\,cm/kA$. The simulation give $0.8\,kA/cm^2$ and $12.5\,cm/kA$, respectively. Even as the transparency current densities agree well, the reduced gain coefficient in the device increases the threshold current density. The dual-stack might suffer from unpredicted losses for example due to regrowth imperfections.

DFB Array Measurements

This active region was used to create a surface emitting multi-wavelength array of single frequency quantum cascade lasers. The work was published in Ref. [147]. The emission can

also be combined into a single ridge, which was shown on the same active region in Ref. [70].

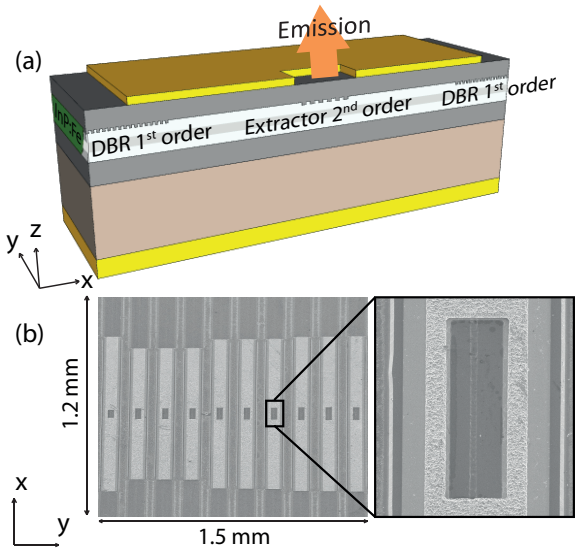

Figure 8.11: (a) Schematic drawing of a cut along the ridge of the buried heterostructure, surface emission device, showing the various functional elements. (b): Scanning electron microscope picture of a processed laser array with a zoom on the extraction window in the top contact. Figure taken from Ref. [147].

As shown schematically in Figure 8.11 a), our approach consists of a buried ridge, terminated by a pair of 360 periods long distributed Bragg reflectors (DBR) separated by a spacer of length $(60 + \frac{3}{4})\lambda/n_{eff}$, where λ is the target free space wavelength and n_{eff} the effective guided mode index. A unique defect mode is confined in the middle of the frequency gap. The extraction is realized by a second order Bragg grating in the middle of the spacer. The radiation escapes the structure through a rectangular aperture in the top metallic ohmic contact. The aperture is about

9 μm longer and wider than the extractor (see Figure 8.11(b)). This approach is immune to the phase relation between the mode and the reflection from the facets. The mode selection and extraction are achieved with two different gratings, unlike the recent proposal of Ref. [148] where both mechanisms are provided by the same grating.

The waveguide mode is computed for a trapezoidal buried ridge cross section featuring a 30° sidewall inclination and a 8 μm average ridge width. The gratings are formed by a 400 nm deep material etching of the InGaAs top cladding with a duty cycle of 50 %, ultimately the groves are refilled with InP. It results in an effective refractive index difference of 0.031 for the two parts of the grating according to COMSOL simulations, taking into account the Drude free carrier correction. The coupling constant of the first order grating is 69 cm^{-1}, the associated decay length is 142 μm. The total expected DBR reflectivity is 94 %. The modal overlap is 61 % for the fundamental mode and 52 % for the higher order lateral one, preventing the undesired lasing action of the latter.

To reduce the appearance of the side-lobes of the usual cardinal sine far-field, the near-field amplitude is apodized as shown in Figure 8.12(b). The periodicity of the extraction grating follows the rule $\Lambda_{extr} = \frac{N-0.5}{N} \lambda/n_{eff}$ where N is the number of grating periods. In this situation, the extraction is maximized in the middle of the grating (x=0) where the groove flanks fall at the maxima of the standing wave, and minimized at the edges of the grating where the groove flanks are on a node (Figure 8.12(a)). Assuming perfectly reflective DBRs the mode is a standing wave described by $E(x) = E_0 cos(2\pi x/\lambda)$. We select the subset of the grating positions $x_j = j \times \Lambda_{extr}$ where $j \in [-\frac{N}{2}, \frac{N}{2}]$, consequently the near-field follows this amplitude $E(x_j) = E_0 cos(\pi j/N)$. In other terms, the near-field is the baseband from the spatial

frequency demodulated by the grating. Thus, the near-field amplitude is shaped like the first half period of a sine function.

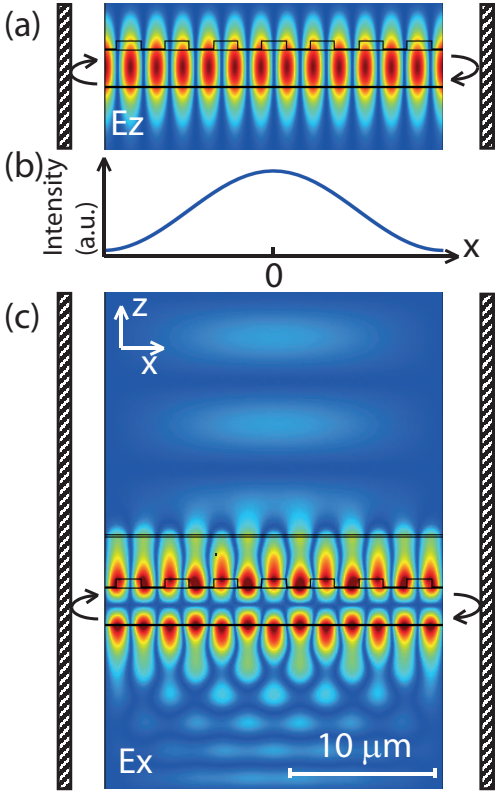

Figure 8.12: Finite element method simulation of the extraction of the mode of interest. (a) A vertical cut of the laser in the longitudinal direction with the absolute value of the electric field in the growth direction Ez is shown together with the grating of a 7-period extractor. The steps are positioned such that, the rises are at maxima of the field in the middle of the extractor and minima at the edges. The field is enclosed by a perfect mirror on the sides. (b): Resulting near-field intensity, computed at the top boundary of the simulation box. (c) Absolute value of the electric field in the longitudinal direction Ex. Figure taken from Ref. [147].

The efficiency of the second order grating and its optical mode profile is computed using the 2D eigenfrequency solver of

COMSOL, which solutions are shown in Figure 8.12. The guided standing-wave at the position of the second-order grating couples out vertically and has an electric field component along the x direction as in Figure 8.12(c) . The amplitude of the near-field at the top border of the simulation box has a bell shape consistently with the distance to the grating and the boundary conditions. The radiative efficiency of the grating expressed in terms of optical losses is 0.045 cm^{-1} per grating period at the maximum. It results in a total computed losses of 0.22 cm^{-1} and 0.64 cm^{-1} for the 7- and 20-period gratings respectively.

The resulting losses are then introduced as effective values in a one dimensional transfer-matrix simulation to compute the optical mode profile along the ridge. As shown in Figure 8.13, the optical field intensity of the mode presents a plateau in the second order grating and the spacer region while it exponentially decays in the first order DBR. The extraction grating induces a minor perturbation of the electric field in the middle of the plateau region. Its characteristic coupling strength $\kappa_{extr} L_{extr} \simeq 0.1 \ll 1$ is too weak to create an additional mode.

The outer halves of the DBRs are unpumped for the following two reasons. It provides an additional mode selection mechanism between the target mode and the two band-edge modes, because the latter have a 18 % overlap with the unpumped region, while the former has 1 %. Additionally, 40 % less power is dissipated in the ridge accounting for a better temperature management.

The arrays are constituted of 10 electrically separated lasers and have a footprint of 1.2 $\times$ 1.5 mm^2 per device. The periodicities of the gratings are tuned to cover the complete gain range by steps of 20 cm^{-1}. The radiation couples out through an opening in the electro-plated top contact of 70 μm x 27 μm and the facets are covered in absorbing insulating varnish.

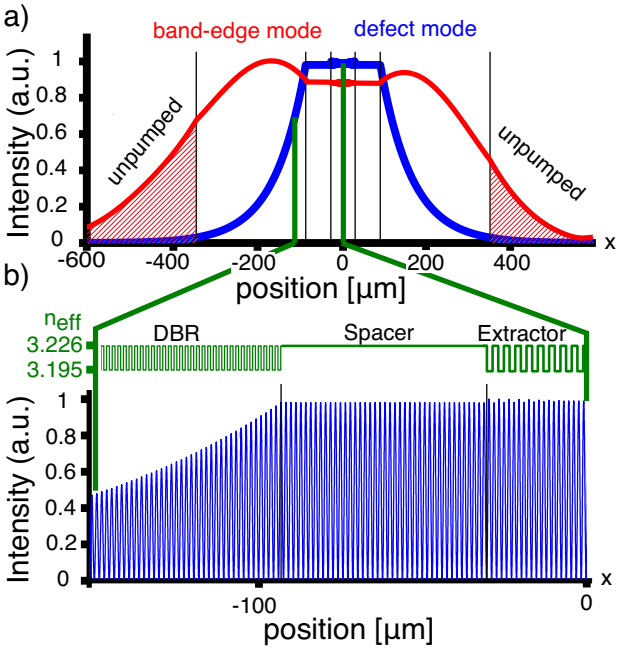

Figure 8.13: Transfer-matrix simulation of the optical mode intensity along the ridge. The different functional elements are marked with separation lines and labeled. (a) The envelope of the defect mode is plotted along with the one of the band edge mode. The defect mode is drawn in blue and the band-edge mode in red. (b) Close up view from the center of the defect mode showing the electric field intensity together with the effective refractive index. Figure taken from Ref. [147].

A high resolution electroluminescence spectrum of an extractor-less device, measured from the facet, is presented in Fig.8.14. The laser was driven below threshold by 30 ns long pulses at a duty cycle of 30%, to minimize the intra-pulse heating. The spectral peaks are the result of amplified spontaneous emission and are the signature of the optical cavity modes. From the measured value of 7.3 cm^{-1} stop-band, an index contrast of $\delta n = \frac{\pi}{2}\frac{\delta\omega}{\omega}n_{eff} = 3.2 \times 10^{-2}$ is deduced, in agreement with the design value of $\delta n = 3.1 \times 10^{-2}$. The high peak located at the center of the

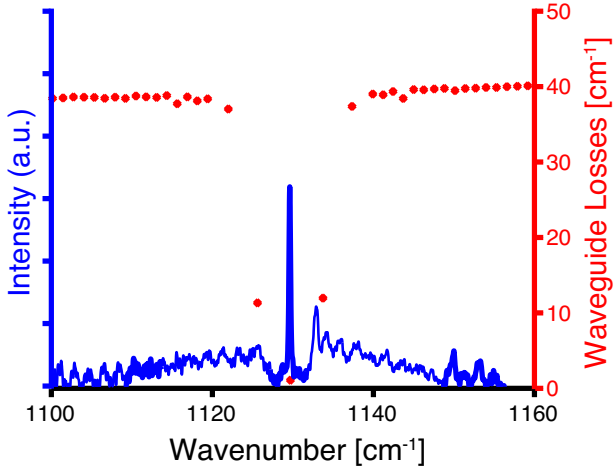

Figure 8.14: Electroluminescence from a device without second order grating measured below threshold, showing the laser mode in the middle of the stop band. Driving conditions are 345 mA at -10°C with 30 ns long pulses at a duty cycle of 30%. Also included are the waveguide losses from a transfer-matrix simulation. Figure taken from Ref. [147].

stop band is the defect mode that appears at the lasing frequency. The asymmetry of the band-edge mode intensity originates on the phase of the reflection induced by the cleaved facet. Figure 8.14 also displays the result of a transfer-matrix simulation of the same cavity where each mode and their respective losses are plotted over the electroluminescence spectrum. The observed frequency of the modes of the electroluminescence is in good agreement with the computation, the latter also predicts a mode discrimination of 10 cm^{-1} between the defect and the band-edge modes. Such a discrimination is consistent with the observed device behavior which lases consistantly at the defect mode.

Figure 8.15 shows a spectrum of an array of 10 lasers measured at room-temperature in pulsed mode with a high resolution (0.075 cm^{-1}) FTIR system. All the spectra are single mode and

emit from 1030 to 1205 cm^{-1}, spanning a region of 175 cm^{-1}. The side-mode suppression was found to be better than 20 dB. Nine out of ten lasers were operating on the desired defect mode, while the lasing on a band-edge mode is attributed to a fabrication imperfection. Also reported in Figure 8.15 is a spontaneous emission spectrum on the same active region. It features a flat broadband region from 1000 cm^{-1} to 1200 cm^{-1} in which all of the measured lasers are operating.

The threshold and maximum current at rollover are constant across the array. It is a sign of constant optical gain and losses and of their independence from the phase of the facet reflection. Concomitantly, the low device-to-device fluctuations of the maximum operation current reflect the reproducibility in the device ridge width. We attributed the remaining device-to-device power fluctuations to fabrication uncertainties and an uneven regrowth planarization of the device on top of the second order grating. The average threshold current density for the array is 5.2 kA/cm^2. The area used for the computation is the length of the top contact multiplied by the width of the ridge, and therefore neglects the current spreading into the unpumped region. The threshold current density is higher than the expected value below 3 kA/cm^2 and is attributed to current leakage paths in the iron-doped InP. The maximum device power was measured at 2 mW. This relatively low power is attributed to the leakage currents, to the relatively low radiative losses (0.2-0.5 cm^{-1}) and to the significant portion of the radiation which is emitted in the substrate.

In conclusion, we presented a design of QCL cavity that combines the advantages of buried heterostructure, a potential for low optical losses and efficient heat dissipation, together with the low threshold current from the high mirror reflectivity. The

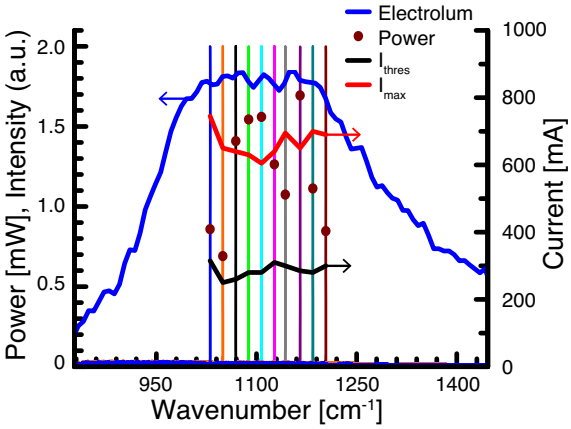

Figure 8.15: Performance of a ten-lasers array measured in pulsed operation. As shown by the high resolution spectra, the ten devices are operating in a single mode. For each device, the threshold and roll-over currents are reported, as well as the maximum peak power. The devices were measured at 1 % duty-cycle with 30 ns pulses at -20°C. On the same graph is shown the measured spontaneous emission of a similar device at room-temperature from the side to avoid any cavity or wave-guiding effects while driving the device at 13.5 V with a 6% duty cycle. Figure taken from Ref. [147].

approach is reliably generating equidistantly spaced emission lines for single mode operation and enables beam combining techniques with gratings, in stand-off applications. The laser array has the advantage of covering a broad spectral range with a high resolution. This geometry features an electrical tunability together with the possibility of sequential firing, enabling a fast acquisition rate. As the mode selection and extraction are achieved with different gratings, they can be tuned independently. The intrinsic limit of performances for these devices is set by the resonant losses and the free carrier absorption, thus a lower threshold current density. The limited performance in the presented case originates in fabrication imperfections and an increase by a factor ten on slope efficiency, with milliwatt level in continuous-wave operation

at room-temperature is expected for future realizations. We made compact arrays of surface emitting single mode devices with a high single mode yield at a deterministic wavelength and a bandwidth of 175 cm^{-1}.

8.3 Strained QCL stacks

To overcome the performance problems of the lattice matched structures shown above, strain-compensated active regions can be used for heterogeneous stacking. Using the *seed* active region from Section 7.2.2 (published in Ref. [76]) we created several strain-balanced active regions around 7.4, 7.8 and 9.5 μm (not shown in this work). The material system was changed to $In_{0.6}Ga_{0.4}As/Al_{0.665}In_{0.335}As$. They were successfully used as QCL stacks in a number of applications, amongst them dual-comb spectroscopy [33, 34] and comb dispersion engineering [35] to achieve the full gain bandwidth in the comb regime. For further details, the reader is referred to the publications. Here we will concentrate on two attempts to achieve octave spanning laser emission.

Octave spanning comb operation enables the determination of the offset frequency. It is also necessary for the self-referencing of the comb leading to a stable comb operation [149]. Octave spanning emission on QCLs was achieved in the THz wavelength region [150], but has not yet been shown in the mid-IR spectral region.

8.3.1 Towards Octave Spanning Emission

During the course of the master thesis of Nadja Walti[1], an octave spanning active region design was attempted. The active region designs are strained versions of Ref. [76]. The laser chip should finally reach emission from 1000 to 2000 cm^{-1}. In order to vary the band offset within the different active region designs, we use 3 material compositions to form composite wells [53]. The material system is $Al_{0.665}In_{0.335}As/In_{0.635}Ga_{365}As/In_{0.53}Ga_{0.47}As$ and the band offset spans from 770 to 820 meV for lattice matched and strained InGaAs, respectively. In Figure 8.16 we present the electron wavefunctions and the band diagram of an active region design.

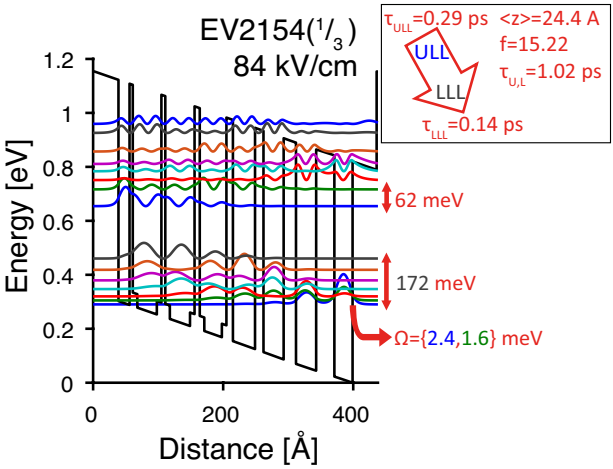

Figure 8.16: Band diagram and the squared electron wavefunctions offset by their energy with respect to the distance in growth direction. Data taken from [1].

[1]Design, Genetic Optimization and Characterization of Strain-Compensated Broadband Quantum Cascade Gain Regions. Master Thesis. Nadja Walti

3-color Design The measured emission spectrum of a preliminary, 3-color-design is presented in Figure 8.17. The threshold current density is 1.8 kA/cm^2 at 20 °C and the slope efficiency 0.5 W/A for a epi-down mounted device. Continuous-wave emission was aquired until 0 °C (see Figure 8.17).

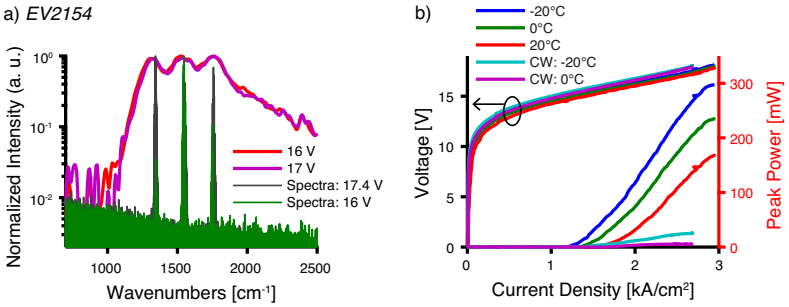

Figure 8.17: a) Spontaneous emission from a 250 μm long ridge, emission takes place perpendicular to the facet and spectral measurements of a 4 mm long device. The back facet was high-reflectivity coated. b) LIV measurements at different temperature for 1 % duty-cycle and for continuous-wave operation. Figures taken from [1].

5-color Design A version with 5 active region designs was designed and grown using 2 material compositions, which are adapted from one active region design to the next by means of growth interruptions. The periods per stack, waveguide losses and overlap factors are indicated in Table 8.2. The simulated gain for the single stacks including the overlap factor and the total modal gain for the 5-stack are shown in Figure 8.18. The crossabsorption was minimized by using wide minibands and separating the next upper levels (NULs) from the miniband states (see Figure 8.16). We find that the absorption of the single stacks is below 1.5 cm^{-1} in the wavelength range 1000 to 2900 cm^{-1}. The total modal gain at 2000 cm^{-1} is reduced by 0.4 cm^{-1} compared to the single stack

gain, due to crossabsorption. In contrast to that the gain at 1050, 1280, 1560 and 1820 cm^{-1} is increased compared to the single stack gain values due to the gain contribution of the neighboring stacks (see Figure 8.18).

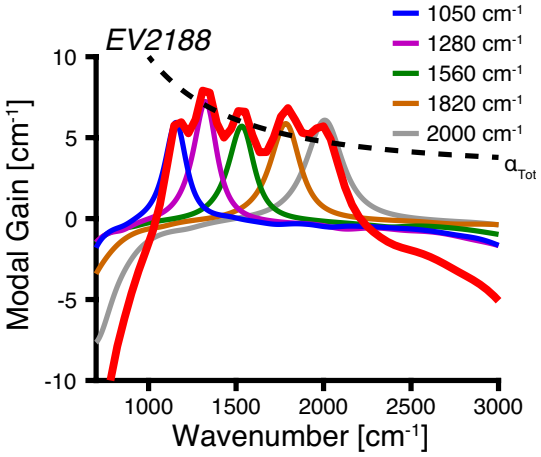

Figure 8.18: Simulated modal gain for the 5 stacks separately, the total modal gain (thick red line) for 3 kA/cm^2 and the total optical losses (dashed black line).

Peak Position [cm^{-1}]	N	Γ[%]
1050	14	13
1280	12	16
1560	8	13
1820	8	14
2000	10	18
	52	**74**

Table 8.1: Stacking values for the 5-stack device. N: Number of periods, Γ: modal overlap

The threshold condition is given by $g(\lambda) = \alpha_M + \alpha_{WG}(\lambda) + \alpha_{Trans}(\lambda) = \alpha_{tot}(\lambda)$ where g is the total modal gain evaluated at the wavelength λ and α_{Trans} is the resonant absorption term due to the transparency current (see Section 3.2). In order to reach threshold for all stacks simultaneously, the threshold condition needs to be fulfilled for all stacks at the same current density. We approximate the waveguide losses by the free carrier losses $\alpha_{WG}=e^2 * n * \lambda^2/(4 * \pi^2 * c^3 * \varepsilon_0 * n_{refr} * m^* * \tau)$ and we assume $\alpha_M+\alpha_{Trans}(\lambda) = 3\,cm^{-1}$. Here e is the electron charge, c the speed of light, ε_0 the vacuum permittivity, n=0.6 $\times 10^{17}$ cm^{-3} the doping of the waveguide, n_{refr}=3.4 the effective refractive index, m^*=0.0443 the effective electron mass and τ=170 fs the electron scattering time (inverse damping term). The total losses are shown in Figure 8.18 as dashed black line. We can see, that the condition is fullfilled well for the stacks, except for the stack at 1050 cm^{-1} which would need about 2 cm^{-1} more gain.

The device was processed with the BiBH technique, the layer sequence for the cladding is (0.020/0.360/0.020/0.020/4/**0.02**/0.5/0.1) μm InP doped (1/0.5/1/5/0.2/**1**/1/30) $\times 10^{17}$ cm^{-3}, where the bold layer is InGaAsP which can be used as an etch stop. The electron sheet doping density is 12 $\times 10^{10}$ cm^{-2}. The emission spectrum and LIV of the processed devices is shown in Figure 8.19. The simulated and measured positions of the active region gain agree reasonably. The threshold of the device at -20 °C is 3.2 kA/cm^2 with a slope efficiency of 0.44 W/A. The thresholds of the different stacks were measured using the emission spectra at different currents and are indicated in Table 8.2, together with the spectral position. The threshold values for the different stacks do not coincide with the prediction from Figure 8.18, especially the stacks lasing at 1790 and 1950 exhibit a high threshold current density, which

might be due to unpredicted absorption. The waveguide losses, including the losses from the transparency current (see Section 3.2) amount to 8.2 cm^{-1}. They are calculated from two neighboring device (6 mm $\times$ 5 μm/5.5 μm) using a length series (here: measured threshold current density with and without coating). A reduction in waveguide losses is necessary to decrease the threshold current density and enable a larger dynamical range.

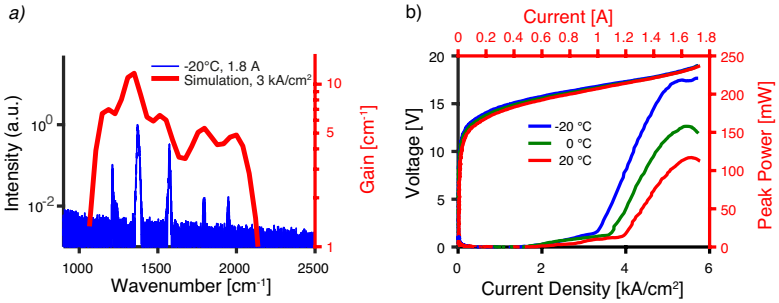

Figure 8.19: a) Emission spectrum of a lasing device with dimensions (6 mm $\times$ 5 μm). The back facet was high-reflectivity coated. The simulations of the active region gain, including the overlap factor is presented in red. We would like to thank to Dmitry Kazakov for the measurement. b) LIV of the same device for different temperatures. The increase in output power before the lasing threshold is due to a non-uniform pump puls.

Peak Position [cm^{-1}] -20 °C, 6 kA/cm^2	**Threshold Current Density[kA/cm^2]**
1220	**5**
1375	**3.2**
1575	**3.3**
1790	**5.7**
1950	**5**

Table 8.2: Analysis of the 5-stack measurements, the values are taken from the device in Figure 8.19.

8.3.2 Towards Octave Spanning Emission, the second

We also used the genetic optimized versions presented in the previous chapter to create a broadband active region. The QCL stack includes 7 strain balanced active regions with the material system $Al_{0.665}In_{0.335}As/In_{0.635}Ga_{365}As/In_{0.53}Ga_{0.47}As$. The emissions are centred at $1075/1235/1335/1515/1640/1755/1885\,cm^{-1}$ for the active regions presented in Appendix A.2.3 (*genetic*), Section 7.3.1 (*seed* and *genetic* design), Appendix A.2.2 and Appendix A.2.1. Additionally two strained active regions, designed from Prof. Dr. Jerome Faist at $6.25\,\mu m$ and $5.26\,\mu m$ (see Appendix B.28, Appendix B.29) were included.

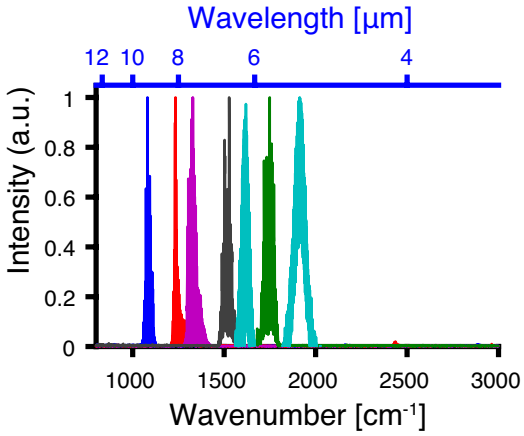

Figure 8.20: Normalised lasing emission from previously processed active regions, spectrally shifted according to their appearance in the broadband design.

This layers were grown and measured beforehand, either as single or dual-stack and showed good spectral and optical performances. According to measured emission spectrum and gain information, we adapted the active regions slightly. In

Figure 8.20, we present the laser spectra of these devices (hakki-paoli measurement in the case of 6.25 μm and 5.26 μm active region). In this figure, spectral adaptations for the broadband design are taken into account by shifting the measured data accordingly. The 7-stack is described in Table 8.3.

Peak Position [cm^{-1}]	N	overlap [%]
1075	16	17.3
1235	8	10.2
1335	5	7.8
1515	7	10.4
1640	5	9.8
1755	7	9.0
1885	6	12.2
	54	**76.7**

Table 8.3: Stacking values for the 7-stack device. N: Number of periods, Γ: modal overlap

Repeating the analysis from the previous section we present in Figure 8.21 the simulated gain for the different stacks weighted by the overlap factor and the total modal gain. In the same figure the total optical losses are shown as a dashed black line. As before, we assume $\alpha_M+\alpha_{Trans}(\lambda) = 3\,cm^{-1}$. Due to numerical problems and two optical transitions (not seen in the real device) on some of the stacks, the current density for the gain simulation was changed to $3.2\,kA/cm^2$ compared to $3.0\,kA/cm^2$ in the previous section. The stack at $1335\,cm^{-1}$ (see also Section 7.3.1(genetic)) gave outstanding performance as single stack, therefore, the overlap for this active region was sightly reduced compared to the other stacks. Due to the experiences from the previous section (see Table 8.2) we set the modal gain of the stack around $1074\,cm^{-1}$ as close as possible to the optical losses and we try to increase the

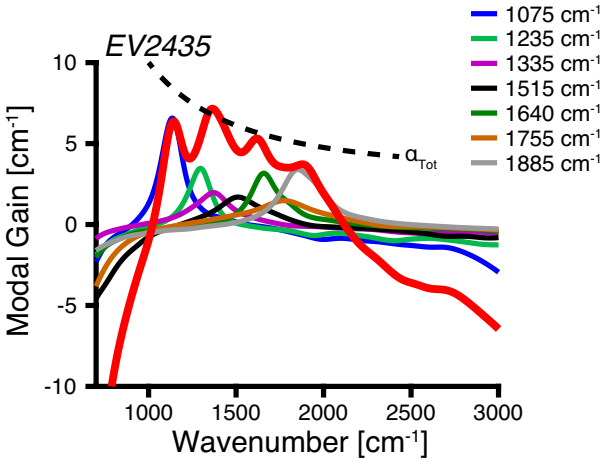

Figure 8.21: Simulated modal gain for the 7 stacks separately, the total modal gain (thick red line) for 3.2 kA/cm^2 and the total losses (dashed black line).

gain for the two stacks on the other end of the octave (1755 and 1885 cm^{-1}) compared to the stacks at 1640 and 1515 cm^{-1}. The total modal gain agrees well with the predicted optical losses.

The electron sheet density is 10×10^{10} cm^{-2}. Growth interruptions between the stacks were needed, as the material system differs slightly for some of the active regions. This layer was processed in a BiBH process, the cladding amounts to (0.02 /0.46 /0.04 /4.5 /0.5 /0.1) μm doped (1 /0.5 /1 /0.1 /1 /30) $\times 10^{10}$ cm^{-2}. The doping of the InGaAs layers surrounding the active region was reduced to 0.4×10^{17} cm^{-3} to reduce the waveguide losses. In Figure 8.22 the spontaneous emission at 80 K is shown, the device is 1.5 mm long without any facet coating. The spontaneous emission spans continuously from 1050 to 2030 cm^{-1}. The laser spectrum from a 3 mm device, with a high-reflectivity coating on the back facet, is presented in the same graph for the same temperature. Emission from nearly all stacks is visible,

where the stack at 1755 cm^{-1} does not reach threshold. Lasing emission is shown from 1090 to 1960 cm^{-1}. The peak position and threshold of the separate stacks are described in Table 8.4. The stacks marked with "?" could not clearly be distinguished from additional emission of the neighbor stack and would be shifted by 90 cm^{-1} from the designed spectral position. We can see that the different stacks reach threshold at nearly the same current densities (1.2-1.9 kA/cm^2).

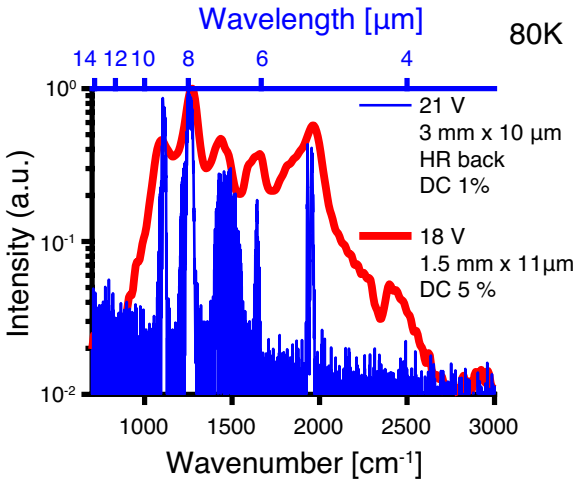

Figure 8.22: Spontaneous emission from the broadband design at 80 K and 18 V. Laser spectrum at 21 V at the same temperature.

Peak Position [cm^{-1}] 80 K	**Threshold Current Density[kA/cm^2]**
1066	**1.6**
1243	**1.2**
1395	**1.5**
1426?	**1.8**
1646	**1.2**
1930?	**1.9**
1960	**1.3**

Table 8.4: Analysis of the 7-stack measurements, the values are taken from the device in Figure 8.22.

Chapter 9

Conclusion and Outlook

The aim of this work is to optimize and automize active region designs for spectroscopic applications. This goal was separated into 4 main parts.

The validation of the Density Matrix (DM) model. The carrier transport using the tight binding model at the injector barrier and incoherent scattering within the active region period delivers accurate results for the current and the optical parameters. The analysis of the injector barrier delivered a technique to find the optimal injector barrier thickness. The comparison of two DM models, with and without inclusion of second order currents, Non-Equilibrium Green's Function (NEGF) and experimental measurements shows that our model is able to reproduce experimental results with low computation effort. Different interface roughness models where implemented with the DM and the NEGF model. We use a gaussian and a exponential interface roughness autocorrelation function. Provided that the different autocorrelation function matches at q values corresponding to the lasing transition, the results are in reasonable agreement.

The short wavelength design around 3-4 μm was optimized in

detail. Growth optimization took place using analytic methods like X-Ray, Transmission Electron Microscopy (TEM) and Scanning Electron Microscope (SEM). Subsequent optimization of the growth and regrowth conditions showed clear improvement in terms of defect locations, strain relaxation and laser performance. With the asymmetric active region design we subsequently reached single mode emission with a threshold dissipation of only 250 mW. We have shown pulsed operation up to 130 °C and threshold values of 30 mA in continuous-wave operation (-20 °C).

Genetic optimization in the wavelength range from 4-26 μm have been presented. The measured performances of the optimized designs give consistently better values compared to the *seed* designs. The optimization results were analyzed in detail. In most cases a diagonal design was preferred by the algorithm, as it gives better lifetimes and scattering times at threshold and at high current densities as well. Together with a reduction in electric field, due to a pocket injection this leads to increased wallplug efficiencies, which is our merit function.

Subsequently the design of broadband devices via heterogeneous stacking is discussed in detail. Gain equalization is reached by choosing similar active region designs, optimizing the modal overlap and the doping values. We show broad emission at different wavelength and their applications as Quantum Cascade Laser (QCL) frequency combs, Distributed-Feedback (DFB) (array) devices and μ-External Cavity QCL. Heterogeneous stacking reduced the gain per active region design considerably. In the last part we have discussed devices with 5 and 7 different active region designs, where the number of periods per active region design can be as small as five. Lasing operation for a full octave could not be shown so far.

The QCL is of growing importance for gas and liquid

spectroscopic in the Mid-Infrared (mid-IR) wavelength range. Improvements in power dissipation and gain equalization for broad devices needs to be continued, as well as the broadband mode locking which is required for QCL frequency combs.

9.1 Outlook

9.1.1 Measurement of the Wallplug Efficiency

Up to now, the thermopile detector is widely used for power and wallplug efficiency measurements in the mid-IR wavelength region. It was previously expected that power measurements between different devices vary by less than 5 %. In Figure 9.1 we present the comparison of averaged light-current density-voltage curves (LIVs) (2-9 measurements each) recorded with 5 different Ophir 3A thermopile detectors. The laser design is described in Section 7.3.1 (genetically optimized). The detector 1 delivers a signal increased by a factor of 2.1. The detector showed no sign of aging or contamination of the sensor. It is not possible to reproduce whether the signal increased gradually or abruptly, the detector was bought and calibrated in 2009, together with detector 7. We are not aware of publications adressing the inaccuracy of these detectors, furthermore a power difference of a factor of 2.1 would make comparisons between different detectors obsolete.

All power and wallplug measurements presented here are realized with a thermopile detector. Nevertheless to adress aforementioned problem, we would propose an alternative measurement technique for the wallplug efficiency, similar to the one presented in Ref. [151]. The measurement of the wallplug efficiency therein does not depend on the absolute measurement of output power, but on the relative change of the active region temperature. In Figure 9.2 we see a schematic representation of the

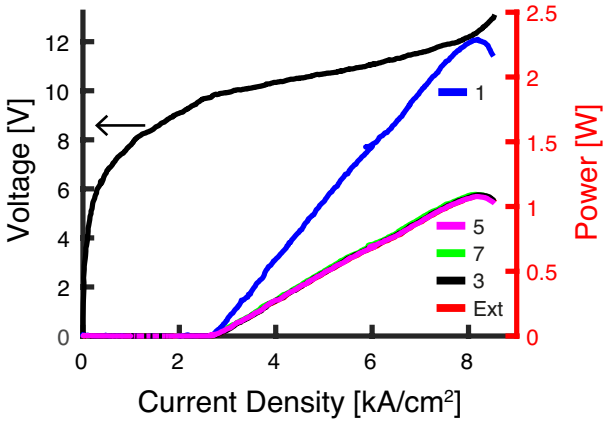

Figure 9.1: Comparison of different thermopile detectors at 20 °C and 1 % duty-cycle. Ext: Detector with courtesy from Alpes Lasers. The device is 2 mm long and 7.5 μm wide. No coating was applied to the facets of the tested lasers.

active region temperature versus the current density applied on a lasing and non-lasing device shown as continuous and dashed line, respectively. The linear relation is given by [16]:

$$G_{\text{thermal}} * T \quad = \quad \delta * V * J \tag{9.1}$$

where G_{thermal} is the thermal conductivity, T the temperature change due to dissipated heat, δ the duty cycle, V and J the voltage and current density applied on the device. At threshold (here: $25\,\text{kA/cm}^2V$), the lasing device emits part of the input power as optical emission. The emitted power does not contribute to the heating of the device (seen as continuous line in Figure 9.2). The temperature of the not lasing device increases according to Equation 9.1 for the whole current range.

The wallplug efficiency is therefore

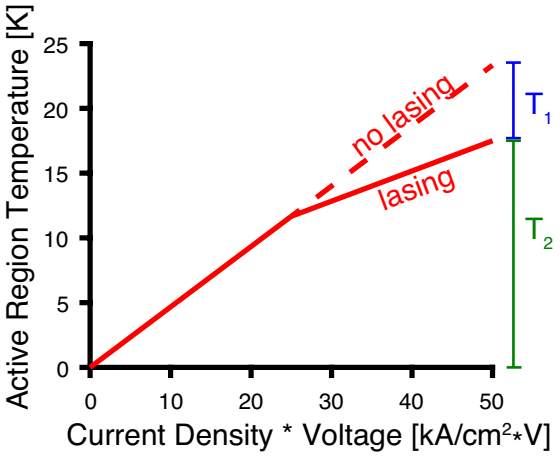

Figure 9.2: Temperature change of the active region with and without lasing.

$$\eta = \frac{P}{\delta * V * J} \tag{9.2}$$

$$= \frac{G_{\text{thermal}} T_1/\delta}{G_{\text{thermal}}(T_1+T_2)/\delta} \tag{9.3}$$

$$= \frac{T_1}{T_1+T_2} \tag{9.4}$$

Where T_1 and T_2 are marked in the graph. In order to measure the active region temperature of the device, termistors can be placed close to the active region (e.g. on top of the metal contact). In Figure 9.3 we present COMSOL simulations of a buried QCL device with dimensions $3\,\text{mm} \times 6\,\mu\text{m}$. The submount temperature is set to 293 K. The thermal conductivity is 74, 4.74 (see Ref. [16]) and 317 W/(m K) for Indium Phosphide (InP), the active region and the gold layer, respectively. The heat capacity at constant pressure is 310, 350 and 129 J/(kg K) for the same materials.

In Figure 9.3 a) we see the temperature map for a QCL driven with 12 V and 1 A (12 W). In Figure 9.3 b) the temperature of the active region is compared with the temperature on top of the gold contact versus the electrical input power. The measurement point for the temperature on top of the contact layer is displaced horizontally by 30 μm from the active region core and separated vertically from the active region by a 5 μm InP cladding layer and 4 μm of gold. Figure 9.3 b) shows a linear relation between the active region temperature and the temperature of the top contact. For 12 W input power the active region temperature increased by 100 K, on the gold contact the temperature increased 40 K. Therefore we assume the measured temperature follows the relation: $T^{\text{contact}} = \alpha T$ for a fixed submount temperature. Where α is the proportionality constant.

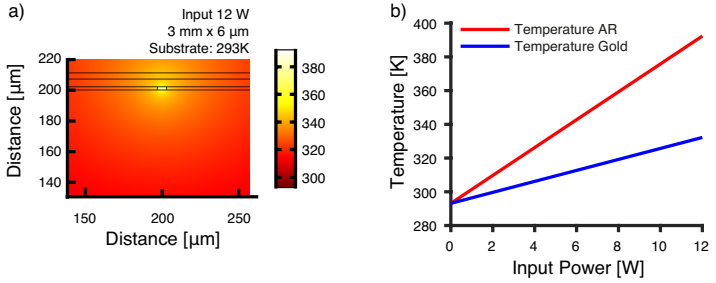

Figure 9.3: a) Temperature map of a buried QCL heterostructure. The electrical power input is 12 W. b) Comparison of the temperature of the active region and the temperature on top of the gold contact with respect to the electrical power input.

$T_1^{contact}$ is given by a linear interpolation of the T-JV curve(seen as dashed line in Figure 9.2), while $T_2^{contact}$ is measured directly. The wallplug efficiency is then

$$\eta = \frac{T_1^{contact}}{T_1^{contact} + T_2^{contact}}. \tag{9.5}$$

9.1.2 Reduction of Regrowth Defects

Due to the improvements discussed in Section 4 the processed samples are consistently less likely to have defects. Nevertheless, defects can still occur and considerably increase the optical losses of a QCL laser. We suspect that one of the sources for crystalline defects are sharp edges which are left after the lateral regrowth. These sharp edges are marked in red in Figure 9.4 a), where we present a schematic view of a processed QCL. At the beginning of the cladding regrowth, the growth directions at sharp edges are different, possibly leading to dislocations or crystalline defects (indicated with the red lines).

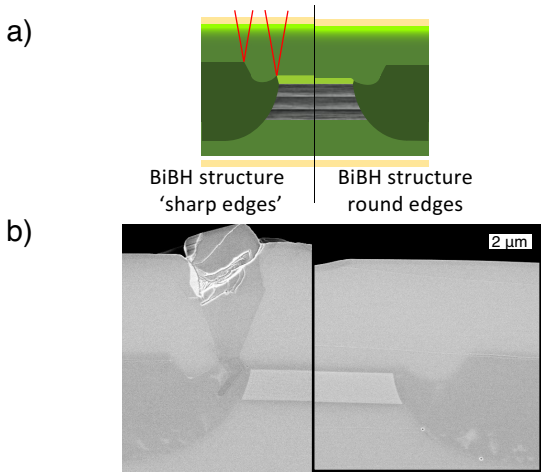

Figure 9.4: a) Schematic view of a processed BiBH laser with marked locations where defect growth might originate due to sharp edges on the beginning of the cladding regrowth. left: The same with a smoothing etch shortly before the cladding regrowth. b) SEM pictures of a processed superlattice, with and without the smoothing etch.

These corners after the lateral regrowth are not a result of the improvements mentioned in Section 4 and occur also in inverted

buried heterostructure (iBH) samples. The advantage of the new processing technique is, that a smoothing etch can be added shortly before the cladding regrowth (see right side of Figure 9.4 a)). Our test sample consists of a InGaAs/AlInAs superlattice which was processed according to Section 4.1. SEM pictures after the cladding regrowth are presented in Figure 9.4 b). The sample on the right side was smoothened by a 230 nm deep etch before the cladding regrowth. The sample without the smoothing etch shows ridges without visible defects, but at some ridges dislocations and defects occur, as shown in the left part of Figure 9.4 b).

In contrast to our assumption above the defect seems to originate in the lateral regrowth. It changes direction at the interface between lateral and cladding layer and is further translated into the cladding layer. On the sample with smoothing etch this kind of defect was not visible. As the regrowth of both samples showed dislocations originating from the sidewall of the ridge, we conclude that the superlattice was not completely strain-balanced and the test should be repeated.

Appendix A

Active Region Designs

A.1 Lattice Matched Long Wavelength Structures

A.1.1 Structure at 9.4 μm

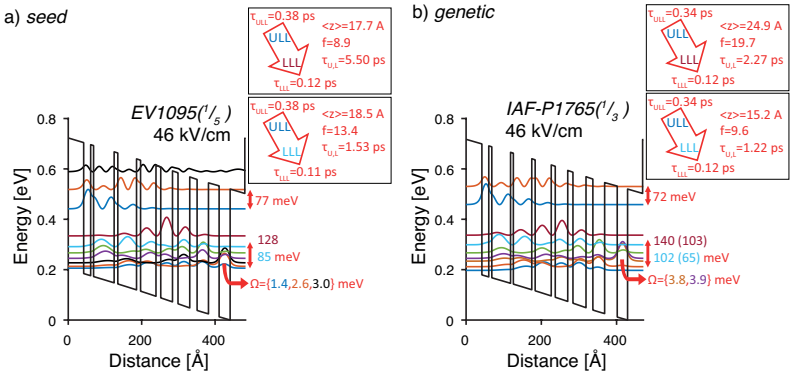

Figure A.1: Band diagram and the squared electron wavefunctions offset by their energy with respect to the distance in growth direction. Additional parameters of the design as described in Section 3.1.1. a) *seed* design (B.17). b) *genetic* design (B.18).

9.4 μm		*seed*	*genetic*
electron sheet density	10^{10} cm^{-2}	10	10
period length	A	439	427
max WP	%	25.7	21.2
Slope Efficiency	W/A	1.16	1.15
Gain Coefficient	cm/kA	10.22	15.29
τ_{eff}	ps	0.37,0.35	0.32,0.31
η_{tr}		0.76,0.76	0.73,0.72
Transparency Current Density	kA/cm^2	1.11	0.37
Threshold Current Density	kA/cm^2	2.00	1.02
Jmax	kA/cm^2	9.55	9.00
emission	μm	8.3, 10.4	9.5

Table A.1: Design, optical and electrical properties of the simulated structures.

The *seed* and *genetic* active region designs at threshold have two optical transitions, which needs to be taken into account (Figure A.1). While the *seed* design will maintain the two optical transitions also at higher fields, the *genetic* design

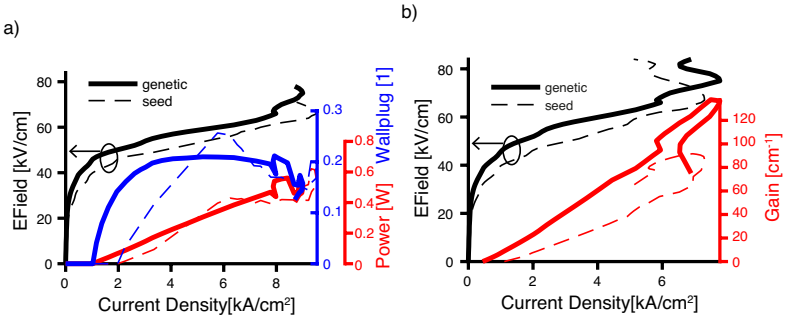

Figure A.2: Simulated a) LIV and b) GIV for the *seed* and *genetic* design in dashed and continuous line, respectively.

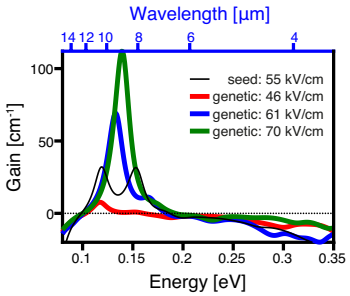

Figure A.3: Simulated gain spectrum for the *seed* and *genetic* design in dashed and continuous line, respectively.

will concentrate on one transition soon after threshold (verified by oscillator strength, electronic wavefunctions not shown). This can be seen in gain spectrum simulations (Figure A.3), where the *seed* design shows two gain peaks, whereas the *genetic* gives rise to one gain peak. As a consequence the gain coefficient is increased for the optimized design. The increased miniband in the *genetic* design has beneficial effects on the transparency current (Figure A.2 b)) and subsequently on the threshold current density (Figure A.2 a)) as presented in Section 3.2. This leads to a large dynamical range, but as the electric field is also increased in the *genetic* design, the

wallplug efficiency cannot overcome the values for the *seed* design.

A.1.2 Structure at 10.4 μm

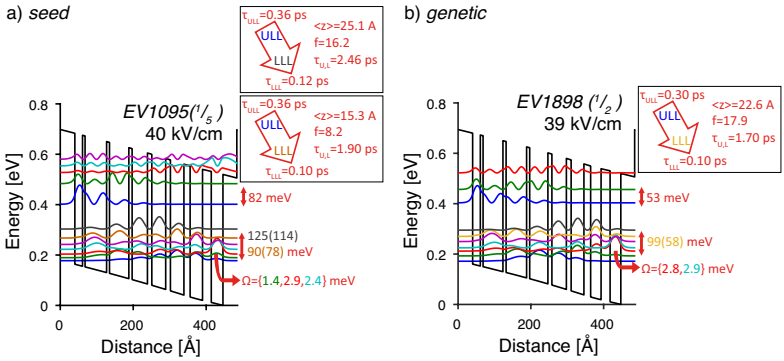

Figure A.4: Band diagram and the squared electron wavefunctions offset by their energy with respect to the distance in growth direction. Additional parameters of the design as described in Section 3.1.1. a) *seed* (Appendix B.19). b) *genetic* (Appendix B.20)

10.4 μm		*seed*	*genetic*
electron sheet density	10^{10} cm^{-2}	9.89	9.89
period length	A	444	445
max WP	%	13.7	23.8
Slope Efficiency	W/A	1.03	1.52
Gain Coefficient	cm/kA	14.5	17.5
τ_{eff}	ps	0.34,0.34	0.28
η_{tr}		0.74,0.77	0.74
Transparency Current Density	kA/cm^2	1.12	0.79
Threshold Current Density	kA/cm^2	1.66	1.60
Jmax	kA/cm^2	<7.7	<10.4
emission	μm	11.3	10.2

Table A.2: Design, optical and electrical properties of the simulated structures.

The optimization at 10.4 μm was done in order to create a heterogeneous active region stack used as Distributed-Feedback (DFB) array (see Section 8.2.2). Low dissipation and a broad spectral emission are the key requirements. The bandstructure

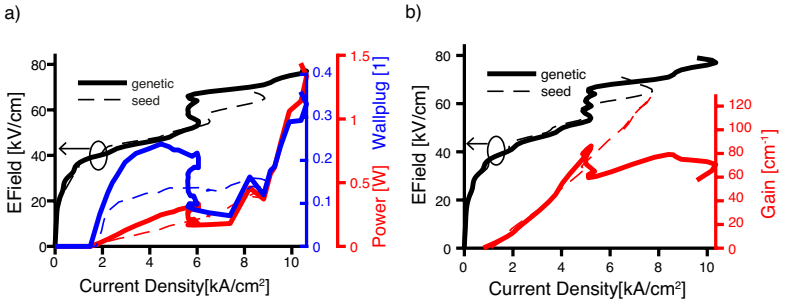

Figure A.5: Simulated a) LIV and b) GIV for the *seed* and *genetic* design in dashed and continuous line, respectively.

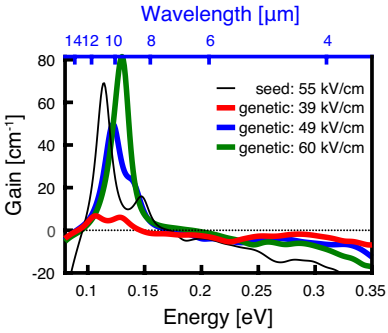

Figure A.6: Simulated gain spectrum for the *seed* and *genetic* design.

is shown in Figure A.4. The *genetic* design shows a more direct optical transition than the *seed* design. The optical transition is concentrated onto 1 upper laser level (ULL), instead of two for the *seed* structure, this is visible in the bandstructure, but also in the gain spectrum (Figure A.6). The gain-current density-voltage curve (GIV) (see Figure A.5 b)) shows an early negative differential resistance (NDR) at a current density around 5 kA/cm^2. The voltage and gain dependence for the two samples are similar. A clear improvement in slope efficiency for the *genetic* design is shown in the light-current density-voltage curve (LIV) (see

Figure A.5 a)), leading to a doubling of the wallplug efficiency. The increase in slope efficiency is not explained via the transition efficiency which is 0.74 for the *genetic* and 0.74 and 0.77 for the *seed* design.

A.1.3 Low Threshold Structure at 8.5 μm

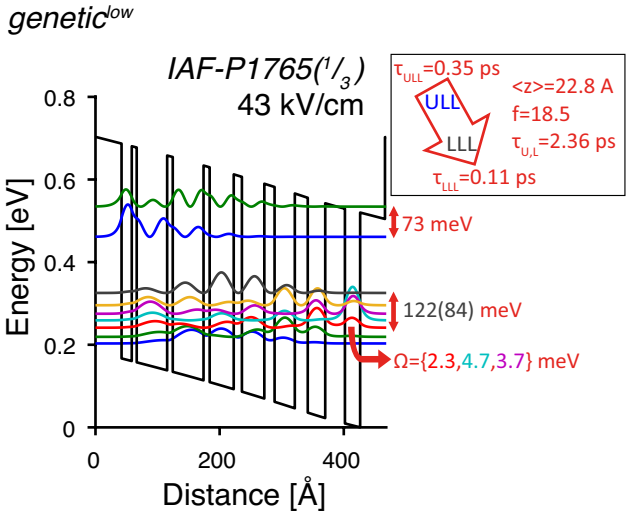

Figure A.7: Band diagram and the squared electron wavefunctions offset by their energy with respect to the distance in growth direction. Additional parameters of the design as described in Section 3.1.1. *genetic* (Appendix B.16).

We present the genetic optimization of a lattice matched 8.5 μm active region with the post-selection for low threshold (see Section 7.2.3). In Figure A.7 we see the band diagram of the *genetic* structure, the *seed* is presented in Section 7.2.2. The low threshold candidate has an increased miniband width and as a consequence also a lower transparency current density as can be seen in the GIV (Figure A.8b)). The optical transition

8.5 μm, low threshold		*seed*	*genetic*, low threshold	*genetic*
electron sheet density	10^{10} cm^{-2}	10	10	10
period length	A	449	424	417
max WP	%	20.87	25.87	26.74
Slope Efficiency	W/A	1.38	1.56	1.64
Gain Coefficient	cm/kA	14.9	15.2	13.9
τ_{eff}	ps	0.36	0.33	0.37
η_{tr}		0.77	0.75	0.79
Transparency Current Density	kA/cm^2	0.65	0.51	0.83
Threshold Current Density	kA/cm^2	1.31	1.06	1.55
Jmax	kA/cm^2	8.75	9.04	11.38
emission	μm	8.6	8.5	8.7

Table A.3: Design, optical and electrical properties of the simulated structures. Presented for the *seed* and the *genetic* design optimized for low threshold and the *genetic* design from Section 7.2.2.

of the *genetic* design is more vertical than the *seed* design, but the high current performance did not decrease as observed in other designs. On the contrary, the LIV (Figure A.8b)) shows an improvement of the maximum wallplug efficiency from 21 to 26 % for *seed* and *genetic* design, respectively. This active region is therefore considered a good alternative to the previous presented version (see Section 7.2.2)

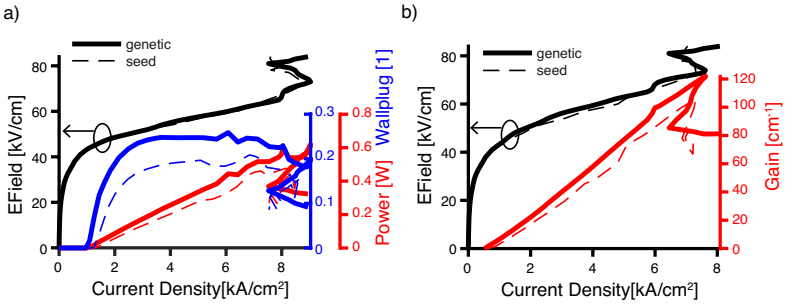

Figure A.8: Simulated a) LIV and b) GIV for the *seed* and *genetic* design in dashed and continuous line, respectively.

A.2 Middle and Long Wavelength Strained Active Regions

A.2.1 6 μm Strained Active Region

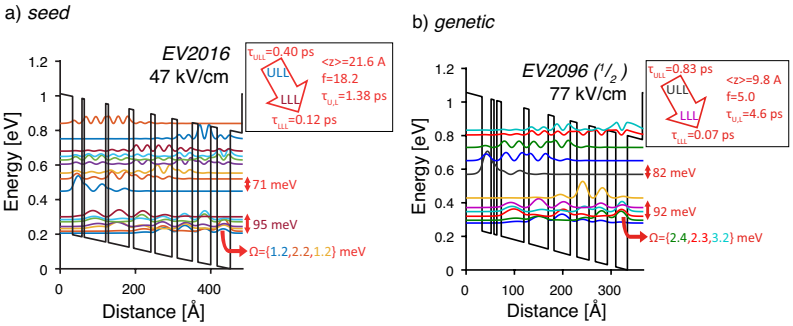

Figure A.9: Band diagram and the squared electron wavefunctions offset by their energy with respect to the distance in growth direction. Additional parameters of the design as described in Section 3.1.1. a) *seed* (Appendix B.24). b) *genetic* (Appendix B.22).

6 μm		*seed*	*genetic*
electron sheet density	10^{10} cm^{-2}	10	10
period length	A	450	332
max WP	%	17.2	43.5
Slope Efficiency	W/A	1.73	3.13
Gain Coefficient	cm/kA	16.0	10.0
τ_{eff}	ps	0.37	0.82
η_{tr}		0.76	0.92
Transparency Current Density	kA/cm^2	0.97	0.83
Threshold Current Density	kA/cm^2	1.54	1.67
Jmax	kA/cm^2	6.60	7.47
emission	μm	8.39	6.15

Table A.4: Design, optical and electrical properties of the simulated structures. Presented for the *seed* and the *genetic* design.

The optimization is based on a reproduction based on Ref.

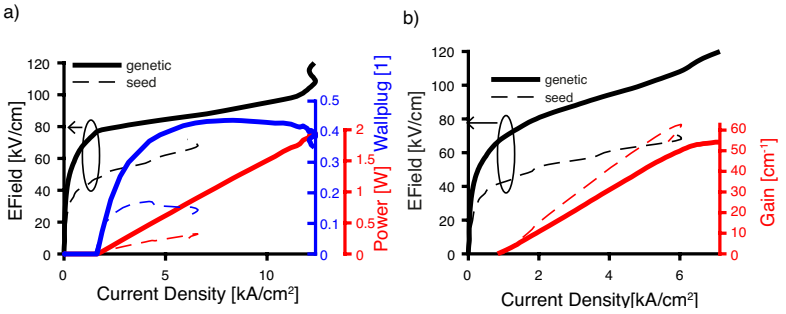

Figure A.10: Simulated a) LIV and b) GIV for the *seed* and *genetic* design in dashed and continuous line, respectively.

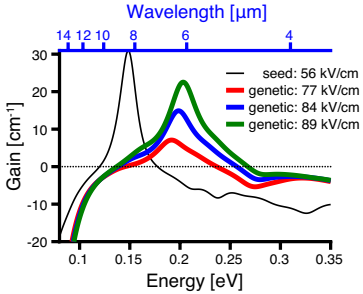

Figure A.11: Simulated gain spectrum for the *seed* and *genetic* design in dashed and continuous line, respectively.

[52]. The *seed* layer, emitting at 8.5 μm was modified prior to the optimization to roughly match the wavelength of 6 μm. In this section we present the comparison between the *seed* and *genetic* design, but as the emission wavelength is very different we will concentrate on the performance of the *genetic* design. In Figure A.9 the bandstructures are presented and the summary of performance parameters is given in Table A.2.1. The optical transition of the *genetic* design is very diagonal with a ULL of 0.83 ps. This can be seen in a high transition efficiency of 0.92 and therefore a slope efficiency that exceeds 3 W/A. The active region period

length is much shorter than the one given by the *seed* design. The second well is too thin for a bound state, this shows that the genetic optimised version would reduce the total number of wells in this design. Before growth this well and the subsequent barrier should be merged with the surrounding layers. In Figure A.10 we present the LIV and the GIV. The gain spectrum is presented in Figure A.11.

A.2.2 7-8 μm Strained Active Region

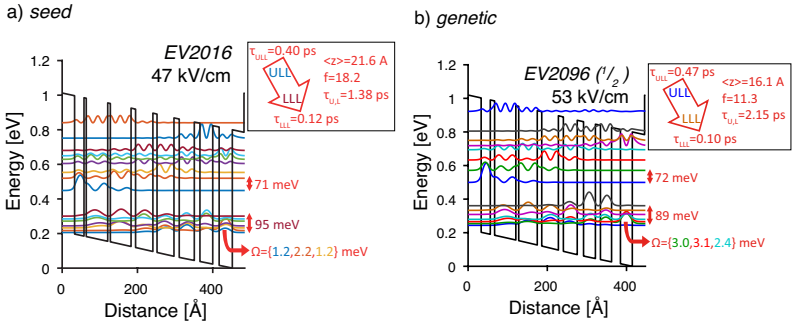

Figure A.12: Band diagram and the squared electron wavefunctions offset by their energy with respect to the distance in growth direction. Additional parameters of the design as described in Section 3.1.1. a) *seed* (Appendix B.24). b) *genetic* (Appendix B.23).

7 μm		*seed*	*genetic*
electron sheet density	10^{10} cm^{-2}	10	10
period length	A	450	413
max WP	%	17.2	36.1
Slope Efficiency	W/A	1.73	2.31
Gain Coefficient	cm/kA	16.0	10.2
τ_{eff}	ps	0.37	0.45
η_{tr}		0.76	0.82
Transparency Current Density	kA/cm^2	0.97	0.87
Threshold Current Density	kA/cm^2	1.54	1.68
Jmax	kA/cm^2	6.60	8.92
emission	μm	8.39	7.50

Table A.5: Design, optical and electrical properties of the simulated structures. Presented for the *seed* and the *genetic* design.

The band diagram of the *seed* and *genetic* structures are presented in Figure A.12. The *genetic* version has a more diagonal transition and larger coupling energies through the injection barrier. The LIV and GIV are shown in Figure A.13 a) and b),

respectively, the gain spectrum is given in Figure A.14. As for other diagonal designs a good performance is maintained even at higher currents and the slope efficiency increases, while the gain coefficient decreased. The performance values are summarised in Table A.2.2.

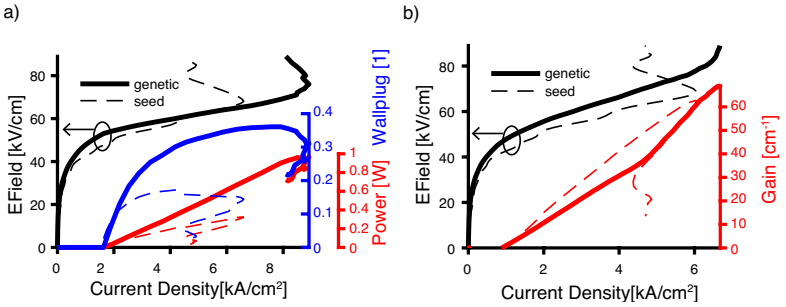

Figure A.13: Simulated a) LIV and b) GIV for the *seed* and *genetic* design in dashed and continuous line, respectively.

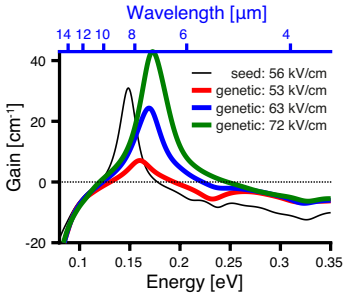

Figure A.14: Simulated gain spectrum for the *seed* and *genetic* design in dashed and continuous line, respectively.

A.2.3 9.6 μm Strained Active Region

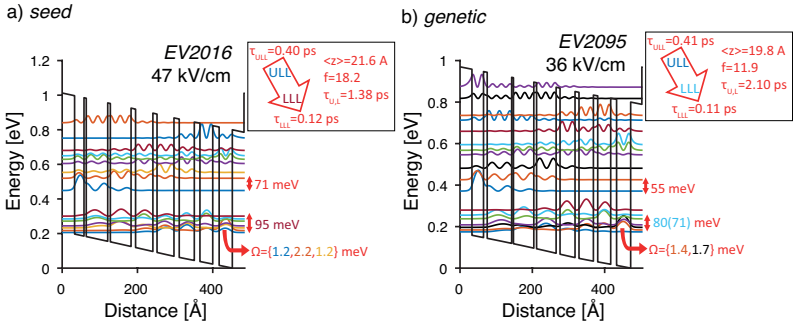

Figure A.15: Band diagram and the squared electron wavefunctions offset by their energy with respect to the distance in growth direction. Additional parameters of the design as described in Section 3.1.1. a) *seed* design (Appendix B.24). b) *genetic* design (Appendix B.26)

9.6 μm		*seed*	*genetic*
electron sheet density	10^{10} cm^{-2}	10	10
period length	A	450	470
max WP	%	17.2	24.0
Slope Efficiency	W/A	1.73	1.50
Gain Coefficient	cm/kA	16.0	12.8
τ_{eff}	ps	0.37	0.39
η_{tr}		0.76	0.78
Transparency Current Density	kA/cm^2	0.97	1.03
Threshold Current Density	kA/cm^2	1.54	1.64
Jmax	kA/cm^2	6.60	4.69, 6.91
emission	μm	8.39	10.14

Table A.6: Design, optical and electrical properties of the simulated structures.

The banddiagram for an optimization at 10 μm is presented in Figure A.15 a) and b) for the *seed* and the *genetic* structure, respectively. The performance parameters are summarized in Table A.6. We can see that the barrier separating the ULL and lower laser level (LLL) was increased for the genetic design to

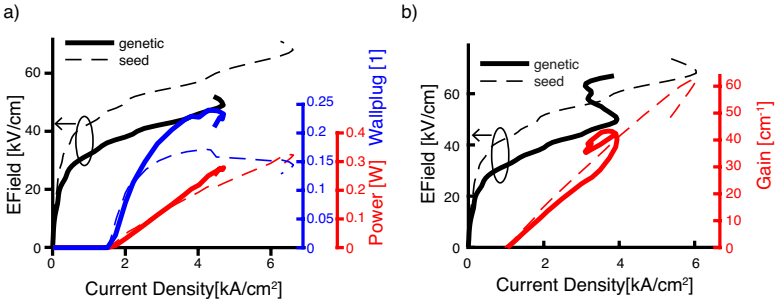

Figure A.16: Simulated a) LIV and b) GIV for the *seed* and *genetic* design in dashed and continuous line, respectively.

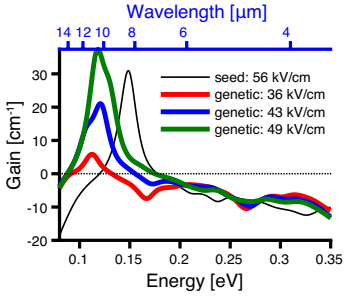

Figure A.17: Simulated gain spectrum for the *seed* and *genetic* design in dashed and continuous line, respectively.

10 μm (*seed* design: 6 μm). This leads to a slightly more diagonal transition as seen also in other designs. The transition efficiency improved only slightly from 0.76 to 0.78 (see Table A.6), as a consequence the slope efficiency (see Figure A.16 a)) improved slightly. The field is strongly reduced, due to a smaller separation of the LLL and the main injector state (MIS) leading to a wallplug efficiency of 24 % (*seed* 17 %). The GIV in Figure A.16 b) shows the same behaviour as previous designs with a reduced gain coefficient due to the more diagonal transition. This design shows a early NDR at around 4 kA/cm^2 whereas the *seed* design is lasing

until 6 kA/cm^2. The reason thereof is the reduced miniband, which is 15 meV smaller than the *seed* miniband and the reduced coupling energy (1.4 and 1.7 meV instead of 1.2 and 2.2 meV for the *seed* design). This is in contrast to other genetic optimizations, where the coupling strength was generally increased.

The gain spectrum, presented in Figure A.17 shows clearly two spectral contributions at 978 and 876 cm^{-1} (10.2 and 11.4 μm). They derive from the red and blue states just below the ULL (see Figure A.15b)). Due to the second transition the peak gain on the main transition is decreased.

Measurements of the *genetic* design were performed on buried inverted buried heterostructure (BiBH) processed devices mounted episide-down on NS submounts. The dimensions of the uncoated devices are 1.7 mm and 20 μm. The process and measurements were performed by Filippos Kapsalidis. The threshold current density at 20 °C is 2.4 kA/cm^2 and the slope efficiency amounts to 1.3 W/A for one facet. The devices show an early NDR at 4.2 kA/cm^2 similar to the simulations. Emission takes place around 9.5 μm instead of the designed value at 10.1 μm.

Appendix B

Active Region Specifications

The active region designs are listed in this section. The layer materials, compositions, thicknesses and dopings are given with respect to the simulations. As a reference the grown structures are identified by their growth identifier, e.g. EV2071. In case the structure was part of a heterogeneous stack this is indicated after the growth identifier: e.g. (1/7) indicates that the structure is one out of a 7-stack active region.

B.1 3 μm, strained Designs

Table B.1: Material parameters, discontinuity defined with respect to AlAs.

material	**discontinuity** [eV]	**relative mass**	**bandgap** [eV]
$Al_{0.48}In_{0.52}As$	0.78	0.0900	1.58
$In_{0.73}Ga_{0.27}As$	1.40	0.0443	0.82
AlAs	0	0.1240	3.00

Table B.2: EV2071: Asymmetric design, 3.3 μm, Section 6.1.

material	**thickness[Å]**	**doping [$\times 10^{18}$ cm^{-3}]**
AlAs	5	
AlInAs	7	
AlAs	10	
GaInAs	12	
AlAs	10	
GaInAs	34	
AlAs	10	
GaInAs	31	
AlAs	9	
GaInAs	27	
AlAs	9	
GaInAs	23	
AlInAs	2	
AlAs	8	
GaInAs	21	0.4673
AlInAs	3	
AlAs	7	
GaInAs	20	0.4673
AlInAs	4	
AlAs	8	
GaInAs	19	0.4673
AlInAs	4	
AlAs	8	
GaInAs	18	0.4673
AlInAs	5	
AlAs	8	
GaInAs	17	0.4673
AlInAs	7	
AlAs	9	
GaInAs	12	0.4673
AlInAs	10	
AlAs	10	
GaInAs	12	
AlInAs	13	
AlAs	10	
GaInAs	11	
AlInAs	13	

Table B.3: EV2072: Symmetric design, 3.3 μm, Section 6.1.

material	thickness[Å]
AlAs	6
AlInAs	5
AlAs	6
AlInAs	5
AlAs	6
AlInAs	3
GaInAs	11
AlInAs	2
AlAs	9
AlInAs	3
GaInAs	34
AlInAs	2
AlAs	9
AlInAs	2
GaInAs	30
AlInAs	2
AlAs	9
AlInAs	2
GaInAs	26
AlInAs	2
AlAs	9
AlInAs	2
GaInAs	24
AlInAs	2
AlAs	7
AlInAs	2

material	thickness[Å]	doping [$\times 10^{18}$ cm^{-3}]
GaInAs	22	0.4545
AlInAs	3	
AlAs	6	
AlInAs	3	
GaInAs	20	0.4545
AlInAs	3	
AlAs	7	
AlInAs	3	
GaInAs	19	0.4545
AlInAs	3	
AlAs	7	
AlInAs	3	
GaInAs	18	0.4545
AlInAs	3	
AlAs	8	
AlInAs	3	
GaInAs	17	0.4545
AlInAs	3	
AlAs	9	
AlInAs	4	
GaInAs	14	0.4545
AlInAs	5	
AlAs	10	
AlInAs	5	
GaInAs	13	
AlInAs	10	
AlAs	10	
AlInAs	3	
GaInAs	12	
AlInAs	9	

Table B.4: EV2135: Low strain design, 3.4 μm, Section 6.3.

material	**thickness[Å]**	**doping [$\times 10^{18}$ cm^{-3}]**
AlAs	5	
AlInAs	7	
AlAs	10	
GaInAs	13	
AlAs	10	
GaInAs	35	
AlAs	10	
GaInAs	32	
AlAs	9	
GaInAs	28	
AlAs	9	
GaInAs	24	
AlInAs	2	
AlAs	8	
GaInAs	22	0.4464
AlInAs	3	
AlAs	7	
GaInAs	21	0.4464
AlInAs	4	
AlAs	8	
GaInAs	20	0.4464
AlInAs	4	
AlAs	8	
GaInAs	19	0.4464
AlInAs	5	
AlAs	8	
GaInAs	17.5	0.4464
AlInAs	7	
AlAs	9	
GaInAs	12.5	0.4464
AlInAs	10	
AlAs	10	
GaInAs	12.5	
AlInAs	13	
AlAs	10	
GaInAs	11.5	
AlInAs	13	

Table B.5: EV2194: High strain design, 3.4 μm, Section 6.4,Section 6.3.

material	**thickness[Å]**	**doping [$\times 10^{18}$ cm^{-3}]**
AlAs	5	
AlInAs	7	
AlAs	10	
GaInAs	13	
AlAs	10	
GaInAs	35	
AlAs	10	
GaInAs	32	
AlAs	9	
GaInAs	28	
AlAs	9	
GaInAs	24	
AlInAs	2	
AlAs	8	
GaInAs	22	0.4464
AlInAs	3	
AlAs	7	
GaInAs	21	0.4464
AlInAs	4	
AlAs	8	
GaInAs	20	0.4464
AlInAs	4	
AlAs	8	
GaInAs	19	0.4464
AlInAs	4	
AlAs	9	
GaInAs	17.5	0.4464
AlInAs	6	
AlAs	10	
GaInAs	12.5	0.4464
AlInAs	9	
AlAs	11	
GaInAs	12.5	
AlInAs	12	
AlAs	11	
GaInAs	11.5	
AlInAs	13	

Table B.6: Full monolayer design, 3.4 μm, Section 6.4.

material	**thickness[Å]**	**doping [$\times 10^{18}$ cm^{-3}]**
AlAs	5.3	
AlInAs	6.1	
AlAs	10.5	
GaInAs	15.1	
AlAs	10.5	
GaInAs	39.4	
AlAs	13.2	
GaInAs	33.3	
AlAs	7.9	
GaInAs	30.3	
AlAs	7.9	
GaInAs	24.2	
AlAs	7.9	
GaInAs	24.2	0.4025
AlAs	7.9	
GaInAs	21.2	0.4025
AlInAs	3.1	
AlAs	7.9	
GaInAs	21.2	0.4025
AlInAs	3.1	
AlAs	7.9	
GaInAs	18.2	0.4025
AlInAs	3.1	
AlAs	7.9	
GaInAs	21.2	0.4025
AlInAs	3.1	
AlAs	10.5	
GaInAs	18.2	0.4025
AlInAs	6.1	
AlAs	10.5	
GaInAs	15.1	
AlInAs	9.2	
AlAs	10.5	
GaInAs	15.1	
AlInAs	9.2	

B.2 4 μm, strained Designs

Table B.7: Material parameters, discontinuity defined with respect to $Al_{0.665}In_{0.335}As$.

material	**discontinuity** [eV]	**relative mass**	**bandgap** [eV]
$Al_{0.665}In_{0.335}As$	0	0.090	1.68
$In_{0.635}Ga_{0.365}As$	0.82	0.044	0.82

Table B.8: EV1429, EV2137, EV2138 (1/2), EV2139 (1/2): 4 μm strained active region (*seed* design), Section 7.1.

material	**thickness[Å]**	**doping [$\times 10^{18}$ cm^{-3}]**
AlInAs	35	
GaInAs	11	
AlInAs	13	
GaInAs	38	
AlInAs	10	
GaInAs	35	
AlInAs	18	
GaInAs	27	
AlInAs	19	
GaInAs	26	
AlInAs	15	
GaInAs	23	
AlInAs	14	
GaInAs	21	0.099
AlInAs	22	0.099
GaInAs	19	0.099
AlInAs	20	0.099
GaInAs	19	0.099
AlInAs	19	
GaInAs	17	
AlInAs	24	
GaInAs	17	

Table B.9: EV2138 (1/2), EV2139 (1/2): 4 μm strained active region (*genetic* design), Section 7.1.

material	**thickness[Å]**	**doping [$\times 10^{18}$ cm^{-3}]**
AlInAs	35	
GaInAs	13.1	
AlInAs	14.8	
GaInAs	37.6	
AlInAs	10.3	
GaInAs	32.9	
AlInAs	19.9	
GaInAs	27.6	
AlInAs	14	
GaInAs	24.1	
AlInAs	14.8	
GaInAs	24.6	
AlInAs	13.3	
GaInAs	21.9	0.1554
AlInAs	15.8	0.1554
GaInAs	18.5	0.1554
AlInAs	19.7	0.1554
GaInAs	17.4	0.1554
AlInAs	20.6	
GaInAs	14.7	
AlInAs	21.7	
GaInAs	15.6	

B.3 Lattice Matched Designs

Table B.10: Material parameters, discontinuity defined with respect to $Al_{0.48}In_{0.52}As$.

material	**discontinuity** [eV]	**relative mass**	**bandgap** [eV]
$Al_{0.48}In_{0.52}As$	0	0.080	1.404
$In_{0.53}Ga_{0.47}As$	0.52	0.043	0.789

Table B.11: EV1095 (1/5): Structure at 7.3 μm (*seed* design), Section 7.2.1.

material	**thickness[Å]**	**doping [$\times 10^{18}$ cm^{-3}]**
AlInAs	40	
GaInAs	15	
AlInAs	10	
GaInAs	48	
AlInAs	12	
GaInAs	47	
AlInAs	13	
GaInAs	42	
AlInAs	15	
GaInAs	32	
AlInAs	17	
GaInAs	30	
AlInAs	18	
GaInAs	28	
AlInAs	23	0.2041
GaInAs	26	0.2041
AlInAs	34	
GaInAs	24	

Table B.12: Structure at 7.3 μm (*genetic* design), Section 7.2.1.

material	**thickness[Å]**	**doping [$\times 10^{18}$ cm^{-3}]**
AlInAs	40	
GaInAs	18.5	
AlInAs	15.5	
GaInAs	53.3	
AlInAs	13.7	
GaInAs	47.2	
AlInAs	19.4	
GaInAs	36.8	
AlInAs	16.6	
GaInAs	29.3	
AlInAs	15.7	
GaInAs	26.7	
AlInAs	20.1	
GaInAs	27.6	
AlInAs	26.5	0.198
GaInAs	24	0.198
AlInAs	24.4	
GaInAs	22.7	

Table B.13: IAF-P1765 (1/3): Low threshold structure at 7.3 μm (*genetic* design), Section 7.2.3.

material	**thickness[Å]**	**doping [$\times 10^{18}$ cm^{-3}]**
AlInAs	40	
GaInAs	15.5	
AlInAs	11.8	
GaInAs	44.7	
AlInAs	9.6	
GaInAs	45.5	
AlInAs	15.9	
GaInAs	40.5	
AlInAs	14.4	
GaInAs	33.2	
AlInAs	16	
GaInAs	28.1	
AlInAs	18.4	
GaInAs	24.5	
AlInAs	19	0.2415
GaInAs	22.4	0.2415
AlInAs	32	
GaInAs	21.3	

Table B.14: EV1095 (1/5) ,EV1140, EV2040, EV2103: Structure at 8.5 μm (*seed* design), Section 7.2.2.

material	**thickness[Å]**	**doping [$\times 10^{18}$ cm^{-3}]**
AlInAs	40	
GaInAs	18	
AlInAs	8	
GaInAs	53	
AlInAs	10	
GaInAs	48	
AlInAs	11	
GaInAs	43	
AlInAs	14	
GaInAs	36	
AlInAs	17	
GaInAs	33	
AlInAs	24	
GaInAs	31	0.1538
AlInAs	34	0.1538
GaInAs	29	

Table B.15: EV2041, EV2104, EV1898 (1/2), EV2102 (1/2): Structure at 8.5 μm (*genetic* design), Section 7.2.2.

material	**thickness[Å]**	**doping [$\times 10^{18}$ cm^{-3}]**
AlInAs	40	
GaInAs	16.7	
AlInAs	8.6	
GaInAs	50.6	
AlInAs	9.2	
GaInAs	46.6	
AlInAs	10.4	
GaInAs	39.3	
AlInAs	17.6	
GaInAs	32	
AlInAs	17.1	
GaInAs	28.4	
AlInAs	19.1	
GaInAs	27.4	0.181
AlInAs	27.8	0.181
GaInAs	25.5	

Table B.16: IAF-P1765 (1/3): Low threshold structure at 8.5 μm (*genetic* design), Section A.1.3.

material	thickness[Å]	doping [$\times 10^{18}$ cm^{-3}]
AlInAs	40	
GaInAs	16.4	
AlInAs	8	
GaInAs	49.1	
AlInAs	9	
GaInAs	49.6	
AlInAs	9.9	
GaInAs	38.8	
AlInAs	13.2	
GaInAs	36.1	
AlInAs	16.5	
GaInAs	32.6	
AlInAs	20.9	
GaInAs	28.1	0.167
AlInAs	31.7	0.167
GaInAs	24.5	

Table B.17: EV1095 (1/5): Structure at 9.4 μm (*seed* design), Section A.1.1.

material	thickness[Å]	doping [$\times 10^{18}$ cm^{-3}]
AlInAs	40	
GaInAs	19	
AlInAs	8	
GaInAs	56	
AlInAs	10	
GaInAs	51	
AlInAs	11	
GaInAs	42	
AlInAs	13	
GaInAs	32	
AlInAs	15	
GaInAs	32	
AlInAs	20	0.1961
GaInAs	31	0.1961
AlInAs	29	
GaInAs	30	

Table B.18: IAF-P1765 (1/3): Structure at 9.4 μm (*genetic* design), Section A.1.1.

material	**thickness[Å]**	**doping [$\times 10^{18}$ cm^{-3}]**
AlInAs	40	
GaInAs	18.3	
AlInAs	8.1	
GaInAs	49.8	
AlInAs	7.4	
GaInAs	49	
AlInAs	9	
GaInAs	42.8	
AlInAs	10.7	
GaInAs	33.2	
AlInAs	13.9	
GaInAs	34.7	
AlInAs	18.2	0.2019
GaInAs	31.3	0.2019
AlInAs	33.5	
GaInAs	27.5	

Table B.19: EV1095 (1/5): Structure at 10.4 μm (*seed* design), Section A.1.2.

material	**thickness[Å]**	**doping [$\times 10^{18}$ cm^{-3}]**
AlInAs	38	
GaInAs	21	
AlInAs	7	
GaInAs	59	
AlInAs	8	
GaInAs	53	
AlInAs	9	
GaInAs	42	
AlInAs	12	
GaInAs	38	
AlInAs	13	
GaInAs	37	
AlInAs	17	0.1961
GaInAs	34	0.1961
AlInAs	24	
GaInAs	32	

Table B.20: EV1898 (1/2), EV2102 (1/2): Structure at 10.4 μm (*genetic* design), Section A.1.2.

material	**thickness[Å]**	**doping [$\times 10^{18}$ cm^{-3}]**
AlInAs	38	
GaInAs	21.1	
AlInAs	7.6	
GaInAs	54.6	
AlInAs	8.7	
GaInAs	56.3	
AlInAs	8.5	
GaInAs	50	
AlInAs	11	
GaInAs	39.8	
AlInAs	13.1	
GaInAs	35.2	
AlInAs	18.5	0.2122
GaInAs	28.7	0.2122
AlInAs	24.8	
GaInAs	29.5	

B.4 5-10 μm, strained Designs

Table B.21: Material parameters, discontinuity defined with respect to $Al_{0.48}In_{0.52}As$.

material	discontinuity [eV]	relative mass	bandgap [eV]
$Al_{0.64}In_{0.36}As$	0	0.090	1.89
$In_{0.58}Ga_{0.42}As$	0.80	0.044	0.772

Table B.22: EV2023 (1/2), EV2096 (1/2): 6.3 μm, strained active region (*genetic* design), Section A.2.1.

material	thickness[Å]	doping [$\times 10^{18}$ cm^{-3}]
AlInAs	31.0	
GaInAs	18.8	
AlInAs	6.0	
GaInAs	5.9	
AlInAs	9.1	
GaInAs	46.8	
AlInAs	10.4	
GaInAs	39.9	
AlInAs	12.0	
GaInAs	33.6	0.13795
AlInAs	13.7	0.13795
GaInAs	25.1	0.13795
AlInAs	13.1	
GaInAs	24.9	
AlInAs	17.4	
GaInAs	24.1	

Table B.23: EV2023 (1/2), EV2096 (1/2): 7-8 μm, strained active region (*genetic* design), Section A.2.2.

material	**thickness[Å]**	**doping [$\times 10^{18}$ cm^{-3}]**
AlInAs	31.0	
GaInAs	23.1	
AlInAs	10.9	
GaInAs	53.6	
AlInAs	7.3	
GaInAs	46.8	
AlInAs	11.3	
GaInAs	42.0	
AlInAs	12.6	
GaInAs	35.0	0.12361
AlInAs	15.9	0.12361
GaInAs	30.0	0.12361
AlInAs	12.7	
GaInAs	28.1	
AlInAs	22.4	
GaInAs	29.9	

Table B.24: EV1907, EV2016: 8.5 μm, strained active region (*seed* design), Section 7.3.1.

material	thickness[Å]	doping [$\times 10^{18}$ cm^{-3}]
AlInAs	31	
GaInAs	25	
AlInAs	6	
GaInAs	57	
AlInAs	7	
GaInAs	55	
AlInAs	12	
GaInAs	46	
AlInAs	11	
GaInAs	45	0.10101
AlInAs	14	0.10101
GaInAs	40	0.10101
AlInAs	15	
GaInAs	34	
AlInAs	17	
GaInAs	35	

Table B.25: EV2017: 8.5 μm, strained active region (*genetic* design), Section 7.3.1.

material	thickness[Å]	doping [$\times 10^{18}$ cm^{-3}]
AlInAs	31.0	
GaInAs	25.2	
AlInAs	12.3	
GaInAs	57.7	
AlInAs	7.4	
GaInAs	50.0	
AlInAs	10.1	
GaInAs	44.9	
AlInAs	12.7	
GaInAs	37.9	0.120276
AlInAs	12.9	0.120276
GaInAs	32.3	0.120276
AlInAs	16.0	
GaInAs	28.9	
AlInAs	18.9	
GaInAs	30.1	

Table B.26: EV2095: 9.6 μm, strained active region (*genetic* design), Section A.2.3.

material	**thickness[Å]**	**doping [$\times 10^{18}$ cm^{-3}]**
AlInAs	31.0	
GaInAs	32.0	
AlInAs	10.2	
GaInAs	67.6	
AlInAs	5.0	
GaInAs	56.3	
AlInAs	7.7	
GaInAs	54.0	
AlInAs	10.8	
GaInAs	41.4	0.1084105
AlInAs	11.0	0.1084105
GaInAs	39.8	0.1084105
AlInAs	12.0	
GaInAs	35.9	
AlInAs	16.3	
GaInAs	38.9	

Table B.27: Material parameters, discontinuity defined with respect to $Al_{0.665}In_{0.335}As$.

material	**discontinuity** [eV]	**relative mass**	**bandgap** [eV]
$Al_{0.665}In_{0.335}As$	0	0.080	1.404
$In_{0.635}Ga_{0.365}As$	0.82	0.043	0.789

Table B.28: EV1815, EV2021, EV2435 (1/7): strained active region at 6.3 μm (courtesy of Prof. Dr. Jerome Faist), Section 8.3.2.

material	**thickness[Å]**	**doping [$\times 10^{18}$ cm^{-3}]**
AlInAs	31	
GaInAs	19	
AlInAs	9	
GaInAs	52	
AlInAs	9	
GaInAs	48	
AlInAs	10	
GaInAs	44	
AlInAs	11	
GaInAs	37	
AlInAs	11	
GaInAs	36	
AlInAs	12	
GaInAs	32	0.123
AlInAs	13	0.123
GaInAs	29	0.123
AlInAs	15	0.123
GaInAs	32	
AlInAs	21	
GaInAs	27	

Table B.29: EV1815, EV2021, EV2435 (1/7): strained active region at 5.3 μm (courtesy of Prof. Dr. Jerome Faist), Section 8.3.2.

material	thickness[Å]	doping [$\times 10^{18}$ cm^{-3}]
AlInAs	35	
GaInAs	15	
AlInAs	10	
GaInAs	45	
AlInAs	10	
GaInAs	41	
AlInAs	11	
GaInAs	38	
AlInAs	12	
GaInAs	33	
AlInAs	13	
GaInAs	29	
AlInAs	14	
GaInAs	26	0.123
AlInAs	15	0.123
GaInAs	24	0.123
AlInAs	16	0.123
GaInAs	26	
AlInAs	23	
GaInAs	23	

B.5 26 μm Designs

Table B.30: Material parameters, discontinuity defined with respect to $GaAs_{0.51}Sb_{0.49}$.

material	discontinuity [eV]	relative mass	bandgap [eV]
$GaAs_{0.51}Sb_{0.49}$	0	0.045	0.786
$In_{0.53}Ga_{0.47}As$	0.36	0.043	0.751

Table B.31: EP1519: Active Region design at 26 μm (*seed* design), Section 7.4.

material	thickness[Å]	doping [$\times 10^{18}$ cm^{-3}]
GaAsSb	48	
GaInAs	54	
GaAsSb	4	
GaInAs	86	
GaAsSb	5	
GaInAs	82	
GaAsSb	6	
GaInAs	81	
GaAsSb	7	
GaInAs	71	
GaAsSb	8	
GaInAs	61	
GaAsSb	14	
GaInAs	64	0.3906
GaAsSb	26	
GaInAs	71	

Table B.32: Active Region design at 26 μm (*genetic* design), Section 7.4.

material	thickness[Å]	doping [$\times 10^{18}$ cm^{-3}]
GaAsSb	48	
GaInAs	41.1	
GaAsSb	5.6	
GaInAs	84.2	
GaAsSb	5.1	
GaInAs	75.4	
GaAsSb	6.3	
GaInAs	74	
GaAsSb	4.9	
GaInAs	72.3	
GaAsSb	5.2	
GaInAs	51.1	
GaAsSb	8.6	
GaInAs	56	0.4465
GaAsSb	25.3	
GaInAs	69.2	

List of Figures

List of Tables

Literature

[1] T. Ashton, The Industrial Revolution: 1760-1830, Galaxy book, Oxford University Press (1948)

[2] G. Duxbury, N. Langford, M. McCulloch, S. Wright, "Quantum cascade semiconductor infrared and far-infrared lasers: from trace gas sensing to non-linear optics", Chem Soc Rev. 34 (2005), 921–934

[3] A. A. Kosterev, R. F. Curl, F. K. Tittel, C. Gmachl, F. Capasso, D. L. Sivco, J. N. Baillargeon, A. L. Hutchinson, A. Y. Cho, "Effective utilization of quantum-cascade distributed-feedback lasers in absorption spectroscopy", Appl. Opt. 39 (2000), 4425–4430

[4] B. Tuzson, K. Zeyer, M. Steinbacher, J. B. McManus, D. D. Nelson, M. S. Zahniser, L. Emmenegger, "Selective measurements of NO, NO_2 and NO_y in the free troposphere using quantum cascade laser spectroscopy", Atmos. Meas. Tech. 6 (2013), 927–936

[5] D. Nelson, J. Shorter, J. McManus, M. Zahniser, "Sub-part-per-billion detection of nitric oxide in air using a thermoelectrically cooled mid-infrared quantum cascade laser spectrometer", Appl. Phys. B 75 (2002), 343–350

[6] A. A. Kosterev, R. F. Curl, F. K. Tittel, C. Gmachl, F. Capasso, D. L. Sivco, J. N. Baillargeon, A. L. Hutchinson, A. Y. Cho, "Methane concentration and isotopic composition measurements with a mid-infrared quantum-cascade laser", Opt. Lett. 24 (1999), 1762–1764

[7] M. J. Süess, P. M. Hundt, B. Tuzson, S. Riedi, J. M. Wolf, R. Peretti, M. Beck, H. Looser, L. Emmenegger, J. Faist, "Dual-Section DFB-QCLs for Multi-Species Trace Gas Analysis", Photonics 3 (2016), 24

[8] J. R. Köster, R. Well, B. Tuzson, R. Bol, K. Dittert, A. Giesemann, L. Emmenegger, A. Manninen, L. Cárdenas, J. Mohn, "Novel laser spectroscopic technique for continuous analysis of N_2O isotopomers - application and intercomparison with isotope ratio mass spectrometry", Rapid Commun. Mass Spectrom. 27 (2013), 216–222

[9] T. H. Risby, F. K. Tittel, “Current status of midinfrared quantum and interband cascade lasers for clinical breath analysis”, Opt. Eng. 49 (2010), 111123

[10] “Hitran Database”, http://www.hitran.org

[11] J. Hecht, “Photonic Frontiers: Laser Countermeasures: Scaling down mid-IR laser countermeasures for smaller aircraft”, Laser Focus World (2014)

[12] T. Day, M. Pushkarsky, D. Caffey, K. Cecchetti, R. Arp, A. Whitmore, M. Henson, E. B. Takeuchi, “Quantum cascade lasers for defense and security”, Proc. SPIE 8898 (2013), 889802

[13] K. Karstad, A. Stefanov, M. Wegmuller, H. Zbinden, N. Gisin, T. Aellen, M. Beck, J. Faist, “Detection of mid-IR radiation by sum frequency generation for free space optical communication”, Opt Lasers Eng 43 (2005), 537 – 544, optics in Switzerland

[14] P. Corrigan, R. Martini, E. A. Whittaker, C. Bethea, “Quantum cascade lasers and the Kruse model in free space optical communication”, Opt. Express 17 (2009), 4355–4359

[15] E. Luzhansky, F.-S. Choa, S. Merritt, A. Yu, M. Krainak, “Mid-IR free-space optical communication with quantum cascade lasers”, Proc. SPIE 9465 (2015), 946512

[16] J. Faist, Quantum Cascade Lasers, Oxford University (2013)

[17] N. Bandyopadhyay, M. Chen, S. Sengupta, S. Slivken, M. Razeghi, “Ultra-broadband quantum cascade laser, tunable over 760 cm^{-1}, with balanced gain”, Opt. Express 23 (2015), 21159–21164

[18] Y. Bai, N. Bandyopadhyay, S. Tsao, S. Slivken, M. Razeghi, “Room temperature quantum cascade lasers with 27% wall plug efficiency”, Appl. Phys. Lett. 98 (2011), 181102

[19] B. Hinkov, A. Bismuto, Y. Bonetti, M. Beck, S. Blaser, J. Faist, “Single-mode quantum cascade lasers with power dissipation below 1 W”, Electron. Lett. 48 (2012), 646 –647

[20] A. Bismuto, S. Blaser, R. Terazzi, T. Gresch, A. Muller, “High performance, low dissipation quantum cascade lasers across the mid-IR range”, Opt. Express 23 (2015), 5477–5484

[21] R. Ostendorf, L. Butschek, A. Merten, J. Grahmann, J. Jarvis, S. Hugger, F. Fuchs, J. Wagner, “Real-time spectroscopic sensing using a widely tunable external cavity-QCL with MOEMS diffraction grating”, Proc. SPIE 9755 (2016), 975507

[22] “mirSense”, http://mirsense.com

[23] “Pendar Technologies”, http://www.pendartechnologies.com/

[24] B. Schwarz, C. A. Wang, L. Missaggia, T. S. Mansuripur, P. Chevalier, M. K. Connors, D. McNulty, J. Cederberg, G. Strasser, F. Capasso, "Watt-Level Continuous-Wave Emission from a Bifunctional Quantum Cascade Laser/Detector", ACS Photonics 4 (2017), 1225–1231

[25] R. Szedlak, A. Harrer, M. Holzbauer, B. Schwarz, J. P. Waclawek, D. MacFarland, T. Zederbauer, H. Detz, A. M. Andrews, W. Schrenk, B. Lendl, G. Strasser, "Remote Sensing with Commutable Monolithic Laser and Detector", ACS Photonics 3 (2016), 1794–1798

[26] A. A. Kosterev, R. F. Curl, F. K. Tittel, C. Gmachl, F. Capasso, D. L. Sivco, J. N. Baillargeon, A. L. Hutchinson, A. Y. Cho, "Effective utilization of quantum-cascade distributed-feedback lasers in absorption spectroscopy", Appl. Opt. 39 (2000), 4425–4430

[27] M. Fischer, B. Tuzson, A. Hugi, R. Brönnimann, A. Kunz, S. Blaser, M. Rochat, O. Landry, A. Müller, L. Emmenegger, "Intermittent operation of QC-lasers for mid-IR spectroscopy with low heat dissipation: tuning characteristics and driving electronics", Opt. Express 22 (2014), 7014–7027

[28] A. N. Chryssis, M. Dagenais, J. D. Bruno, J. L. Bradshaw, "Tunable External Cavity Interband Cascade Laser", in "Lasers and Electro-Optics Society Annual Meeting-LEOS", (2007)

[29] A. Hugi, R. Terazzi, Y. Bonetti, A. Wittmann, M. Fischer, M. Beck, J. Faist, E. Gini, "External cavity quantum cascade laser tunable from 7.6 to 11.4 μm", Appl. Phys. Lett. 95 (2009), 061103

[30] J. Reichert, R. Holzwarth, T. Udem, T. Hänsch, "Measuring the frequency of light with mode-locked lasers", Opt. Commun. 172 (1999), 59 – 68

[31] T. Udem, J. Reichert, R. Holzwarth, T. W. Hänsch, "Accurate measurement of large optical frequency differences with a mode-locked laser", Opt. Lett. 24 (1999), 881–883

[32] A. Hugi, G. Villares, S. Blaser, H. Liu, J. Faist, "Mid-infrared frequency comb based on a quantum cascade laser", Nature492 (2012), 229–233

[33] G. Villares, A. Hugi, S. Blaser, J. Faist, "Dual-comb spectroscopy based on quantum-cascade-laser frequency combs", Nat. Commun. 5 (2014), 5192

[34] G. Villares, J. Wolf, D. Kazakov, M. J. Süess, A. Hugi, M. Beck, J. Faist, "On-chip dual-comb based on quantum cascade laser frequency combs", Appl. Phys. Lett. 107 (2015), 251104

[35] G. Villares, S. Riedi, J. Wolf, D. Kazakov, M. J. Süess, P. Jouy, M. Beck, J. Faist, "Dispersion engineering of quantum cascade laser frequency combs", Optica 3 (2016), 252–258

[36] R. L. Terazzi, "Transport in quantum cascade lasers", Ph.D. thesis, ETH (2012)

[37] D. Indjin, P. Harrison, R. W. Kelsall, Z. Ikonić, "Self-consistent scattering theory of transport and output characteristics of quantum cascade lasers", J. Appl. Phys. 91 (2002), 9019–9026

[38] P. Harrison, D. Indjin, V. Jovanović, A. Mirčetić, Z. Ikonić, R. Kelsall, J. McTavish, I. Savić, N. Vukmirović, V. Milanović, "Carrier Dynamics in Quantum Cascade Lasers", Acta Physica Polonica, A 107 (2005)

[39] A. I. Mátyás, "Modeling of quantum cascade lasers by ensemble Monte-Carlo methods", Ph.D. thesis, Technische Universität München (2011)

[40] A. Wacker, M. Lindskog, D. O. Winge, "Nonequilibrium Green's Function Model for Simulation of Quantum Cascade Laser Devices Under Operating Conditions", IEEE J. Sel. Topics Quantum Electron. 19 (2013), 1–11

[41] R. F. Kazarinov, R. A. Suris, "Electric and electromagnetic properties of semiconductors with a superlattice", Sov. Phys. Semicond. 6 (1972), 120–131

[42] R. Terazzi, T. Gresch, A. Wittmann, J. Faist, "Sequential resonant tunneling in quantum cascade lasers", Phys. Rev. B 78 (2008), 155328

[43] D. O. Winge, M. Lindskog, A. Wacker, "Microscopic approach to second harmonic generation in quantum cascade lasers", Opt. Express 22 (2014), 18389–18400

[44] J. Faist, F. Capasso, D. L. Sivco, C. Sirtori, A. L. Hutchinson, A. Y. Cho, "Quantum Cascade Laser", Science 264 (1994), 553–556

[45] M. Beck, D. Hofstetter, T. Aellen, J. Faist, U. Oesterle, M. Ilegems, E. Gini, H. Melchior, "Continuous Wave Operation of a Mid-Infrared Semiconductor Laser at Room Temperature", Science 295 (2002), 301–305

[46] J. Faist, M. Beck, T. Aellen, E. Gini, "Quantum-cascade lasers based on a bound-to-continuum transition", Appl. Phys. Lett. 78 (2001), 147–149

[47] Y. Yao, W. O. Charles, T. Tsai, J. Chen, G. Wysocki, C. F. Gmachl, "Broadband quantum cascade laser gain medium based on a 'continuum-to-bound' active region design", Appl. Phys. Lett. 96 (2010), 211106

[48] Y. Yao, X. Wang, J.-Y. Fan, C. F. Gmachl, "High performance 'continuum-to-continuum' quantum cascade lasers with a broad gain bandwidth of over 400 cm^{-1}", Appl. Phys. Lett. 97 (2010), 081115

[49] A. Lyakh, R. Maulini, A. Tsekoun, R. Go, C. Pflügl, L. Diehl, Q. J. Wang, F. Capasso, C. K. N. Patel, "3 W continuous-wave room temperature single-facet emission from quantum cascade lasers based on nonresonant extraction design approach", Appl. Phys. Lett. 95 (2009), 141113

[50] Y. Bai, N. Bandyopadhyay, S. Tsao, E. Selcuk, S. Slivken, M. Razeghi, "Highly temperature insensitive quantum cascade lasers", Appl. Phys. Lett. 97 (2010), 251104

[51] R. Maulini, A. Lyakh, A. Tsekoun, C. K. N. Patel, "$\lambda \approx 7.1\ \mu$m quantum cascade lasers with 19% wall-plug efficiency at room temperature", Opt. Express 19 (2011), 17203–17211

[52] A. Lyakh, R. Maulini, A. Tsekoun, R. Go, C. K. N. Patel, "Multiwatt long wavelength quantum cascade lasers based on high strain composition with 70% injection efficiency", Opt. Express 20 (2012)

[53] N. Bandyopadhyay, Y. Bai, S. Slivken, M. Razeghi, "High power operation of $\lambda \approx 5.2$-$11\ \mu$m strain balanced quantum cascade lasers based on the same material composition", Appl. Phys. Lett. 105 (2014), 071106

[54] D. Botez, C.-C. Chang, L. J. Mawst, "Temperature sensitivity of the electro-optical characteristics for mid-infrared (λ = 3-16 μm)-emitting quantum cascade lasers", Journal of Physics D: Applied Physics 49 (2016), 043001

[55] A. Bismuto, R. Terazzi, B. Hinkov, M. Beck, J. Faist, "Fully automatized quantum cascade laser design by genetic optimization", Appl. Phys. Lett. 101 (2012)

[56] L. M. Rios, N. V. Sahinidis, "Derivative-free optimization: a review of algorithms and comparison of software implementations", J. Global Optim. 56 (2013), 1247–1293

[57] G. Venter, "Review of optimization techniques", Encyclopedia of aerospace engineering (2010)

[58] A. Mirčetić, D. Indjin, Z. Ikonić, P. Harrison, V. Milanović, R. W. Kelsall, "Towards automated design of quantum cascade lasers", J. Appl. Phys. 97 (2005), 084506

[59] A. I. Mátyás, R. Chashmahcharagh, I. Kovacs, P. Lugli, K. Vijayraghavan, M. A. Belkin, C. Jirauschek, "Improved terahertz quantum cascade laser with variable height barriers", J. Appl. Phys. 111 (2012), 103106

[60] A. Gajić, J. Radovanović, V. Milanović, D. Indjin, Z. Ikonić, "Genetic algorithm applied to the optimization of quantum cascade lasers with second harmonic generation", J. Appl. Phys. 115 (2014), 053712

[61] R. Terazzi, J. Faist, "A density matrix model of transport and radiation in quantum cascade lasers", New J. Phys. 12 (2010)

[62] J. Faist, "Wallplug efficiency of quantum cascade lasers: Critical parameters and fundamental limits", Appl. Phys. Lett. 90 (2007), 253512

[63] P. Offermans, P. M. Koenraad, J. H. Wolter, M. Beck, T. Aellen, J. Faist, "Digital alloy interface grading of an InAlAs/InGaAs quantum cascade laser structure studied by cross-sectional scanning tunneling microscopy", Appl. Phys. Lett. 83 (2003), 4131

[64] M. J. Süess, R. Peretti, Y. Liang, J. M. Wolf, C. Bonzon, B. Hinkov, S. Nida, P. Jouy, W. Metaferia, S. Lourdudoss, M. Beck, J. Faist, "Advanced Fabrication of Single-Mode and Multi-Wavelength MIR-QCLs", Photonics 3 (2016), 26

[65] A. Bismuto, "Mid-infrared quantum cascade lasers: active medium and waveguide engineering", Phd thesis, ETH Zurich (2011)

[66] B. Hinkov, "Radio-Frequency Modulation of Low-Dissipation Distributed-Feedback Quantum Cascade Lasers", Phd thesis, ETH Zurich (2015)

[67] J. M. Wolf, A. Bismuto, M. Beck, J. Faist, "Distributed-feedback quantum cascade laser emitting at 3.2 μm", Opt. Express 22 (2014)

[68] L. Cheng, J. Fan, D. Janssen, D. Guo, X. Chen, F. J. Towner, F.-S. Choa, "Analysis of InP Regrowth on Deep-Etched Mesas and Structural Characterization for Buried-Heterostructure Quantum Cascade Lasers", J. Electron. Mater. 41 (2012), 506–513

[69] Y. Chiu, Y. Dikmelik, P. Q. Liu, N. L. Aung, J. B. Khurgin, C. F. Gmachl, "Importance of interface roughness induced intersubband scattering in mid-infrared quantum cascade lasers", Appl. Phys. Lett. 101 (2012), 171117

[70] M. Süess, P. Jouy, C. Bonzon, J. Wolf, E. Gini, M. Beck, J. Faist, "Single-Mode Quantum Cascade Laser Array Emitting From a Single Facet", IEEE Photon. Technol. Lett. 28 (2016), 1197–1200

[71] J. M. Wolf, S. Riedi, M. J. Süess, M. Beck, J. Faist, "3.36 μm single-mode quantum cascade laser with a dissipation below 250 mW", Opt. Express 24 (2016), 662–671

[72] A. Bismuto, M. Beck, J. Faist, "High power Sb-free quantum cascade laser emitting at 3.3 μm above 350 K", Appl. Phys. Lett. 98 (2011), 191104

[73] D. Söderström, S. Lourdudoss, "Resistivity analysis on n-semi-insulating-n and p-semi-insulating-p structures exemplified with semi-insulating InP", J. Appl. Phys. 89 (2001), 4004–4009

[74] S. Nida, B. Hinkov, E. Gini, J. Faist, "Characterization of iron doped indium phosphide as a current blocking layer in buried heterostructure quantum cascade lasers", J. Appl. Phys. 121 (2017), 094502

[75] P. J. Corvini, J. E. Bowers, "Model for trap filling and avalanche breakdown in semi-insulating Fe:InP", J. Appl. Phys. 82 (1997), 259–269

[76] A. Bismuto, R. Terazzi, M. Beck, J. Faist, "Electrically tunable, high performance quantum cascade laser", Appl. Phys. Lett. 96 (2010), 141105

[77] E. Dupont, S. Fathololoumi, H. C. Liu, "Simplified density-matrix model applied to three-well terahertz quantum cascade lasers", Phys. Rev. B 81 (2010), 205311

[78] S. Barbieri, C. Sirtori, H. Page, M. Stellmacher, J. Nagle, "Design strategies for GaAs-based unipolar lasers: Optimum injector-active region coupling via resonant tunneling", Appl. Phys. Lett. 78 (2001), 282–284

[79] P. Friedli, H. Sigg, A. Wittmann, R. Terazzi, M. Beck, A. Kolek, J. Faist, "Synchrotron infrared transmission spectroscopy of a quantum cascade laser correlated to gain models", Appl. Phys. Lett. 102 (2013), 012112

[80] M. Lindskog, J. M. Wolf, V. Trinite, V. Liverini, J. Faist, G. Maisons, M. Carras, R. Aidam, R. Ostendorf, A. Wacker, "Comparative analysis of quantum cascade laser modeling based on density matrices and non-equilibrium Green's functions", Appl. Phys. Lett. 105 (2014), 103106

[81] C. Ndebeka-Bandou, A. Wacker, F. Carosella, R. Ferreira, G. Bastard, "Dopant engineering of inter-subband linewidth and lineshape in multiwell heterostructures", Appl. Phys. Express 6 (2013), 094101

[82] A. Kolek, G. Hałdaś, M. Bugajski, "Nonthermal carrier distributions in the subbands of 2-phonon resonance mid-infrared quantum cascade laser", Appl. Phys. Lett. 101 (2012), 061110

[83] H. Choi, L. Diehl, Z.-K. Wu, M. Giovannini, J. Faist, F. Capasso, T. B. Norris, "Gain Recovery Dynamics and Photon-Driven Transport in Quantum Cascade Lasers", Phys. Rev. Lett. 100 (2008), 167401

[84] R. Terazzi, T. Gresch, M. Giovannini, N. Hoyler, N. Sekine, J. Faist, "Bloch gain in quantum cascade lasers", Nat. Phys. 3 (2007), 329–333

[85] D. G. Revin, M. R. Soulby, J. W. Cockburn, Q. Yang, C. Manz, J. Wagner, "Dispersive gain and loss in midinfrared quantum cascade laser", Appl. Phys. Lett. 92 (2008), 081110

[86] P. Hyldgaard, J. W. Wilkins, "Electron-electron scattering in far-infrared quantum cascade lasers", Phys. Rev. B 53 (1996), 6889–6892

[87] M. F. Pereira, S.-C. Lee, A. Wacker, "Controlling many-body effects in the midinfrared gain and terahertz absorption of quantum cascade laser structures", Phys. Rev. B 69 (2004), 205310

[88] I. Shtrichman, C. Metzner, E. Ehrenfreund, D. Gershoni, K. D. Maranowski, A. C. Gossard, "Depolarization shift of the intersubband resonance in a quantum well with an electron-hole plasma", Phys. Rev. B 65 (2001), 035310

[89] T. Unuma, M. Yoshita, T. Noda, H. Sakaki, H. Akiyama, "Intersubband absorption linewidth in GaAs quantum wells due to scattering by interface roughness, phonons, alloy disorder, and impurities", J. Appl. Phys. 93 (2003), 1586–1597

[90] S. Tsujino, A. Borak, E. Müller, M. Scheinert, C. V. Falub, H. Sigg, D. Grützmacher, M. Giovannini, J. Faist, "Interface-roughness-induced broadening of intersubband electroluminescence in p-SiGe and n-GaInAs/AlInAs quantum-cascade structures", Appl. Phys. Lett. 86 (2005), 062113

[91] A. Leuliet, A. Vasanelli, A. Wade, G. Fedorov, D. Smirnov, G. Bastard, C. Sirtori, "Electron scattering spectroscopy by a high magnetic field in quantum cascade lasers", Phys. Rev. B 73 (2006), 085311

[92] A. Vasanelli, A. Leuliet, C. Sirtori, A. Wade, G. Fedorov, D. Smirnov, G. Bastard, B. Vinter, M. Giovannini, J. Faist, "Role of elastic scattering mechanisms in GaInAs / AlInAs quantum cascade lasers", Appl. Phys. Lett. 89 (2006), 172120

[93] Y. Chiu, Y. Dikmelik, P. Q. Liu, N. L. Aung, J. B. Khurgin, C. F. Gmachl, "Importance of interface roughness induced intersubband scattering in mid-infrared quantum cascade lasers", Appl. Phys. Lett. 101 (2012), 171117

[94] J. B. Khurgin, "Inhomogeneous origin of the interface roughness broadening of intersubband transitions", Appl. Phys. Lett. 93 (2008), 091104

[95] J. B. Khurgin, Y. Dikmelik, P. Q. Liu, A. J. Hoffman, M. D. Escarra, K. J. Franz, C. F. Gmachl, "Role of interface roughness in the transport and lasing characteristics of quantum-cascade lasers", Appl. Phys. Lett. 94 (2009), 091101

[96] T. Ando, A. B. Fowler, F. Stern, "Electronic properties of two-dimensional systems", Rev. Mod. Phys. 54 (1982), 437–672

[97] M. Franckié, D. O. Winge, J. Wolf, V. Liverini, E. Dupont, V. Trinité, J. Faist, A. Wacker, "Impact of interface roughness distributions on the operation of quantum cascade lasers", Opt. Express 23 (2015), 5201–5212

[98] S. M. Goodnick, D. K. Ferry, C. W. Wilmsen, Z. Liliental, D. Fathy, O. L. Krivanek, "Surface roughness at the Si(100)-SiO_2 interface", Phys. Rev. B 32 (1985), 8171–8186

[99] R. M. Feenstra, D. A. Collins, D. Z. Y. Ting, M. W. Wang, T. C. McGill, "Interface roughness and asymmetry in InAs/GaSb superlattices studied by scanning tunneling microscopy", Phys. Rev. Lett. 72 (1994), 2749–2752

[100] A. Y. Lew, S. L. Zuo, E. T. Yu, R. H. Miles, "Correlation between atomic-scale structure and mobility anisotropy in InAs/$Ga_{1-x}In_xSb$ superlattices", Phys. Rev. B 57 (1998), 6534–6539

[101] K.-J. Chao, N. Liu, C.-K. Shih, D. W. Gotthold, B. G. Streetman, "Factors influencing the interfacial roughness of InGaAs/GaAs heterostructures: A scanning tunneling microscopy study", Appl. Phys. Lett. 75 (1999), 1703–1705

[102] T. Saku, Y. Horikoshi, Y. Tokura, "Limit of Electron Mobility in AlGaAs/GaAs Modulation-doped Heterostructures", Jpn. J. Appl. Phys. 35 (1996), 34

[103] F. Lopez, M. R. Wood, M. Weimer, C. F. Gmachl, C. G. Caneau, "Direct Measurement of Interface Roughness in QCL Materials Grown by MOCVD", in "ITQW 2013", (1483)

[104] S. A. Cohen, "The Fourier Transform Asymptotic Behavior Theorem", IEEE Trans. Edu. 12 (1969), 56 – 57

[105] "NIST Chemistry WebBook", http://webbook.nist.gov/

[106] J. Jágerská, B. Tuzson, H. Looser, A. Bismuto, J. Faist, H. Prinz, L. Emmenegger, "Highly sensitive and fast detection of propane-butane using a 3 μm quantum cascade laser", Appl. Opt. 52 (2013), 4613–4619

[107] C. S. Kim, M. Kim, J. Abell, W. W. Bewley, C. D. Merritt, C. L. Canedy, I. Vurgaftman, J. R. Meyer, "Mid-infrared distributed-feedback interband cascade lasers with continuous-wave single-mode emission to 80 °C", Appl. Phys. Lett. 101 (2012), 061104

[108] W. W. Bewley, C. L. Canedy, C. S. Kim, M. Kim, C. D. Merritt, J. Abell, I. Vurgaftman, J. R. Meyer, "High-power room-temperature continuous-wave mid-infrared interband cascade lasers", Opt. Express 20 (2012), 20894–20901

[109] M. Kim, C. L. Canedy, W. W. Bewley, C. S. Kim, J. R. Lindle, J. Abell, I. Vurgaftman, J. R. Meyer, "Interband cascade laser emitting at λ=3.75 μm in continuous wave above room temperature", Appl. Phys. Lett. 92 (2008), 191110

[110] T. Hosoda, G. Belenky, L. Shterengas, G. Kipshidze, M. V. Kisin, "Continuous-wave room temperature operated 3.0μm type I GaSb-based lasers with quinternary AlInGaAsSb barriers", Appl. Phys. Lett. 92 (2008), 091106

[111] T. Hosoda, G. Kipshidze, L. Shterengas, G. Belenky, "Diode lasers emitting near 3.44 μm in continuous-wave regime at 300K", Electron. Lett. 46 (2010), 1455–1457(2)

[112] G. Belenky, L. Shterengas, G. Kipshidze, T. Hosoda, "Type-I Diode Lasers for Spectral Region Above 3 μm", IEEE J. Sel. Topics Quantum Electron. 17 (2011), 1426–1434

[113] J. Devenson, O. Cathabard, R. Teissier, A. N. Baranov, "High temperature operation of $\lambda \approx$ 3.3 μm quantum cascade lasers", Appl. Phys. Lett. 91 (2007), 141106

[114] D. G. Revin, J. W. Cockburn, M. J. Steer, R. J. Airey, M. Hopkinson, A. B. Krysa, L. R. Wilson, S. Menzel, "InGaAs/AlAsSb/InP quantum cascade lasers operating at wavelengths close to 3 μm", Appl. Phys. Lett. 90 (2007), 021108

[115] M. P. Semtsiv, M. Wienold, S. Dressler, W. T. Masselink, "Short-wavelength (μm $\approx$3.05μm) InP-based strain-compensated quantum-cascade laser", Appl. Phys. Lett. 90 (2007), 051111

[116] A. Bismuto, S. Riedi, B. Hinkov, M. Beck, J. Faist, "Sb-free quantum cascade lasers in the 3 μm spectral range", Semicond. Sci. Technol. 27 (2012), 045013

[117] N. Bandyopadhyay, Y. Bai, S. Tsao, S. Nida, S. Slivken, M. Razeghi, "Room temperature continuous wave operation of $\lambda \approx$ 3-3.2 μm quantum cascade lasers", Appl. Phys. Lett. 101 (2012), 241110

[118] D. Vaitiekus, D. G. Revin, K. L. Kennedy, S. Y. Zhang, J. W. Cockburn, "Quantum Cascade Laser With Unilateral Grating", IEEE Photon. Technol. Lett. 24 (2012), 2112–2114

[119] D. Revin, J. Commin, S. Zhang, A. B. Krysa, K. Kennedy, J. Cockburn, "InP-Based Midinfrared Quantum Cascade Lasers for Wavelengths Below 4 μm", IEEE J. Sel. Topics Quantum Electron. 17 (2011), 1417–1425

[120] J. P. Commin, D. G. Revin, S. Y. Zhang, A. B. Krysa, K. Kennedy, J. W. Cockburn, "High peak power 3.3 and 3.5 μm InGaAs/AlAs(Sb) quantum cascade lasers operating up to 400 K", Appl. Phys. Lett. 97 (2010), 031108

[121] N. Bandyopadhyay, S. Slivken, Y. Bai, M. Razeghi, "High power, continuous wave, room temperature operation of $\lambda \approx 3.4$ μm and $\lambda \approx 3.55$ μm InP-based quantum cascade lasers", Appl. Phys. Lett. 100 (2012), 212104

[122] S. Riedi, A. Hugi, A. Bismuto, M. Beck, J. Faist, "Broadband external cavity tuning in the 3-4 μm window", Appl. Phys. Lett. 103 (2013), 031108

[123] Ioffe Physico-Technical Institute, "New Semiconductor Materials. Characteristics and Properties", http://www.ioffe.ru/SVA/NSM/Semicond/index.html

[124] S. Oktyabrsky, P. Ye, Fundamentals of III-V Semiconductor MOSFETs, Springer US (2010)

[125] J. P. Commin, K. Kennedy, D. G. Revin, S. Y. Zhang, A. B. Krysa, J. W. Cockburn, "$\lambda \approx 3.36$ μm room temperature InGaAs/AlAs(Sb) quantum cascade lasers with third order distributed feedback grating", Appl. Phys. Lett. 97 (2010), 111113

[126] E. Mujagić, C. Schwarzer, W. Schrenk, J. Chen, C. Gmachl, G. Strasser, "Ring-cavity surface-emitting lasers as a building block for tunable and coherent quantum cascade laser arrays", Semicond. Sci. Technol. 26 (2011), 014019

[127] R. Cendejas, Z. Liu, W. Sánchez-Vaynshteyn, C. Caneau, C. Zah, C. Gmachl, "Cavity Length Scaling of Quantum Cascade Lasers for Single-Mode Emission and Low Heat Dissipation, Room Temperature, Continuous Wave Operation", IEEE Photon. J. 3 (2011), 71–81

[128] W. Streifer, D. R.Scifres, R. Bumham, "Coupling Coefficients for Distributed Feedback Single- and Double-Heterostructure Diode Lasers", IEEE J. Quantum Electron. 11 (1975), 867 – 873

[129] H. Haus, C. Shank, "Antisymmetric taper of distributed feedback lasers", IEEE J. Quantum Electron. 12 (1976), 532 –539

[130] A. Yariv, P. Yeh, Optical Waves in Crystals, John Wiley and Sons (1984)

[131] S. Blaser, L. Diehl, M. Beck, J. Faist, U. Oesterle, J. Xu, S. Barbieri, F. Beltram, "Characterization and modeling of quantum cascade lasers based on a photon-assisted tunneling transition", IEEE J. Quantum Electron. 37 (2001), 448–455

[132] K. Ohtani, M. Beck, M. J. Süess, J. Faist, A. M. Andrews, T. Zederbauer, H. Detz, W. Schrenk, G. Strasser, "Far-Infrared Quantum Cascade Lasers Operating in the AlAs Phonon Reststrahlen Band", ACS Photonics 3 (2016), 2280–2284

[133] M. Troccoli, "Quantum cascade lasers: high-power emission and single-mode operation in the long-wave infrared (> 6 μm)", Opt. Eng. 49 (2010), 111106

[134] R. P. Leavitt, J. L. Bradshaw, K. M. Lascola, G. P. Meissner, F. Micalizzi, F. J. Towner, J. T. Pham, "High-performance quantum cascade lasers in the 7.3- to 7.8-μm wavelength band using strained active regions", Opt. Eng. 49 (2010), 111109

[135] A. Wittmann, T. Gresch, E. Gini, L. Hvozdara, N. Hoyler, M. Giovannini, J. Faist, "High-Performance Bound-to-Continuum Quantum-Cascade Lasers for Broad-Gain Applications", IEEE J. Quantum Electron. 44 (2008), 36–40

[136] Y. Bai, S. Slivken, S. R. Darvish, M. Razeghi, "Very high wall plug efficiency of quantum cascade lasers", Proc. SPIE 7608 (2010), 76080F

[137] P. Q. Liu, A. J. Hoffman, M. D. Escarra, K. J. Franz, J. B. Khurgin, Y. Dikmelik, X. Wang, J.-Y. Fan, C. F. Gmachl, "Highly power-efficient quantum cascade lasers", Nat. Phys. 4 (2010), 95 – 98

[138] A. Lyakh, C. Pflügl, L. Diehl, Q. J. Wang, F. Capasso, X. J. Wang, J. Y. Fan, T. Tanbun-Ek, R. Maulini, A. Tsekoun, R. Go, C. Kumar N. Patel, "1.6 W high wall plug efficiency, continuous-wave room temperature quantum cascade laser emitting at 4.6 μm", Appl. Phys. Lett. 92 (2008), 111110

[139] F. Xie, C. Caneau, H. P. Leblanc, D. P. Caffey, L. C. Hughes, T. Day, C.-e. Zah, "Watt-Level Room Temperature Continuous-Wave Operation of Quantum Cascade Lasers With lambda > 10 μm", IEEE J. Sel. Topics Quantum Electron. 19 (2013)

[140] J. B. McManus, M. S. Zahniser, D. D. Nelson, J. H. Shorter, S. C. Herndon, D. Jervis, M. Agnese, R. McGovern, T. I. Yacovitch, J. R. Roscioli, "Recent progress in laser-based trace gas instruments: performance and noise analysis", Appl. Phys. B 119 (2015), 203–218

[141] MIRIFISENS, "Mid InfraRed Innovative lasers For Improved SENSors of hazardous substrances", http://www.mirifisens-project.eu

[142] B. G. Lee, H. A. Zhang, C. Pflugl, L. Diehl, M. A. Belkin, M. Fischer, A. Wittmann, J. Faist, F. Capasso, "Broadband Distributed-Feedback Quantum Cascade Laser Array Operating From 8.0 to 9.8 μm", IEEE Photon. Technol. Lett. 21 (2009), 914–916

[143] P. Rauter, S. Menzel, A. K. Goyal, C. A. Wang, A. Sanchez, G. Turner, F. Capasso, "High-power arrays of quantum cascade laser master-oscillator power-amplifiers", Opt. Eng. 21 (2013), 4518–4530

[144] P. Rauter, S. Menzel, A. K. Goyal, B. Gökden, C. A. Wang, A. Sanchez, G. W. Turner, F. Capasso, "Master-oscillator power-amplifier quantum cascade laser array", Appl. Phys. Lett. 101 (2012), 261117

[145] Y. Bai, S. Slivken, Q. Y. Lu, N. Bandyopadhyay, M. Razeghi, "Angled cavity broad area quantum cascade lasers", Appl. Phys. Lett. 101 (2012), 081106

[146] E. Mujagić, C. Schwarzer, Y. Yao, J. Chen, C. Gmachl, G. Strasser, "Two-dimensional broadband distributed-feedback quantum cascade laser arrays", Appl. Phys. Lett. 98 (2011), 141101

[147] P. Jouy, C. Bonzon, J. Wolf, E. Gini, M. Beck, J. Faist, "Surface emitting multi-wavelength array of single frequency quantum cascade lasers", Appl. Phys. Lett. 106 (2015), 071104

[148] C. Sigler, J. D. Kirch, T. Earles, L. J. Mawst, Z. Yu, D. Botez, "Design for high-power, single-lobe, grating-surface-emitting quantum cascade lasers enabled by plasmon-enhanced absorption of antisymmetric modes", Appl. Phys. Lett. 104 (2014), 131108

[149] S. A. Diddams, D. J. Jones, J. Ye, S. T. Cundiff, J. L. Hall, J. K. Ranka, R. S. Windeler, R. Holzwarth, T. Udem, T. W. Hänsch, "Direct Link between Microwave and Optical Frequencies with a 300 THz Femtosecond Laser Comb", Phys. Rev. Lett. 84 (2000), 5102–5105

[150] M. Rösch, G. Scalari, M. Beck, J. Faist, "Octave-spanning semiconductor laser", Nat. Phys. 9 (2015), 42–47

[151] M. S. Vitiello, T. Gresch, A. Lops, V. Spagnolo, G. Scamarcio, N. Hoyler, M. Giovannini, J. Faist, "Influence of InAs, AlAs δ layers on the optical, electronic, and thermal characteristics of strain-compensated GaInAs/AlInAs quantum-cascade lasers", Appl. Phys. Lett. 91 (2007), 161111

List of Publications

1. J. M. Wolf, S. Riedi, M. J. Süess, M. Beck, J. Faist, "3.36 µm single-mode quantum cascade laser with a dissipation below 250 mW", Opt. Express 24 (2016), 662–671

2. J. M. Wolf, A. Bismuto, M. Beck, J. Faist, "Distributed-feedback quantum cascade laser emitting at 3.2 μm", Opt. Express 22 (2014)

3. P. Jouy, J. M. Wolf, Y. Bidaux, P. Allmendinger, M. Mangold, M. Beck, J. Faist, "Dual comb operation of $\lambda \approx 8.2$ μm quantum cascade laser frequency comb with 1 W optical power", Appl. Phys. Lett. 111 (2017), 141102

4. R. Peretti, V. Liverini, M. J. Süess, Y. Liang, P.-B. Vigneron, J. M. Wolf, C. Bonzon, W. Metaferia, M. Balaji, S. Lourdudoss, E. Gini, M. Beck, J. Faist, "Room temperature operation of a deep etched buried heterostructure photonic crystal quantum cascade laser", Laser Photon. Rev. (2016)

5. M. Süess, P. Jouy, C. Bonzon, J. Wolf, E. Gini, M. Beck, J. Faist, "Single-Mode Quantum Cascade Laser Array Emitting From a Single Facet", IEEE Photon. Technol. Lett. 28 (2016), 1197–1200

6. M. J. Süess, P. M. Hundt, B. Tuzson, S. Riedi, J. M. Wolf, R. Peretti, M. Beck, H. Looser, L. Emmenegger, J. Faist, "Dual-Section DFB-QCLs for Multi-Species Trace Gas Analysis", Photonics 3 (2016), 24

7. M. J. Süess, R. Peretti, Y. Liang, J. M. Wolf, C. Bonzon, B. Hinkov, S. Nida, P. Jouy, W. Metaferia, S. Lourdudoss, M. Beck, J. Faist, "Advanced Fabrication of Single-Mode and Multi-Wavelength MIR-QCLs", Photonics 3 (2016), 26

8. G. Villares, S. Riedi, J. Wolf, D. Kazakov, M. J. Süess, P. Jouy, M. Beck, J. Faist, "Dispersion engineering of quantum cascade laser frequency combs", Optica 3 (2016), 252–258

9. M. Franckié, D. O. Winge, J. Wolf, V. Liverini, E. Dupont, V. Trinité, J. Faist, A. Wacker, "Impact of interface roughness distributions on the operation of quantum cascade lasers", Opt. Express 23 (2015), 5201–5212

10. P. Jouy, C. Bonzon, J. Wolf, E. Gini, M. Beck, J. Faist, "Surface emitting multi-wavelength array of single frequency quantum cascade lasers", Appl. Phys. Lett. 106 (2015), 071104

11. G. Villares, J. Wolf, D. Kazakov, M. J. Süess, A. Hugi, M. Beck, J. Faist, "On-chip dual-comb based on quantum cascade laser frequency combs", Appl. Phys. Lett. 107 (2015), 251104

12. M. Lindskog, J. M. Wolf, V. Trinite, V. Liverini, J. Faist, G. Maisons, M. Carras, R. Aidam, R. Ostendorf, A. Wacker, "Comparative analysis of quantum cascade laser modeling based on density matrices and non-equilibrium Green's functions", Appl. Phys. Lett. 105 (2014), 103106